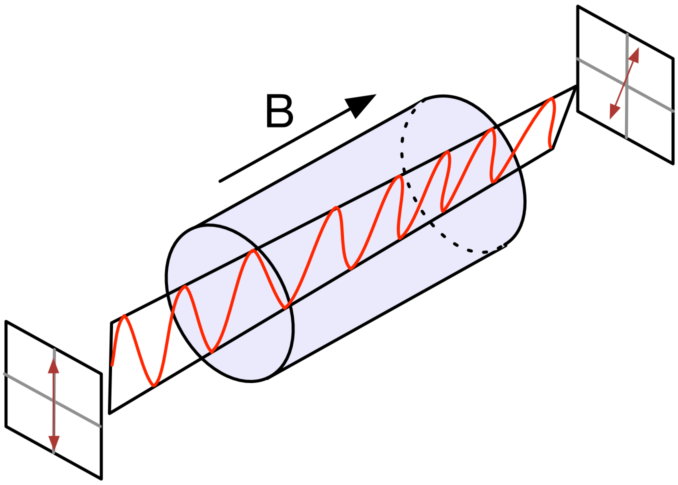

Optical fiber sensors technology for supervision, control and protection of high power systems

Ivo Maciel Nascimento

Física

Departamento de Física e Astronomia

2016

Orientador

Pedro Alberto da Silva Jorge, Professor Assistente Convidado do Departamento de Física e Astronomia, Faculdade de Ciências da Universidade do Porto e Investigador Sénior no INESC TEC

Coorientador

José Manuel Rocha Teixeira Baptista, Professor Associado na Faculdade de Ciências Exatas e da Engenharia, Universidade da Madeira e Investigador Sénior no INESC TEC

PhD

Optical fiber sensors technology for supervision, control and protection of high power systems

U. PORTO

FACULDADE DE CIÊNCIAS
UNIVERSIDADE DO PORTO

Doctoral Thesis

Department of Physics and Astronomy

University of Porto

This thesis was conducted under the supervision of

Prof. Dr. Pedro Alberto da Silva Jorge

Invited Assistant Professor of Department of Physics and Astronomy, Faculty of Sciences of University of Porto and Senior Researcher at INESC TEC

and

Prof. Dr. José Manuel Rocha Teixeira Baptista

Associate Professor of Faculty of Exact Sciences and Engineering of University of Madeira and Senior Researcher at INESC TEC

Ivo Maciel Nascimento

2016

FCT Fundação para a Ciência e a Tecnologia
MINISTÉRIO DA EDUCAÇÃO E CIÊNCIA

ACÇÃO CO-FINANCIADA AO ABRIGO DE:

PROGRAMA OPERACIONAL POTENCIAL HUMANO

QUADRO DE REFERÊNCIA ESTRATÉGICO NACIONAL PORTUGAL 2007.2013

Governo da República Portuguesa

UNIÃO EUROPEIA
Fundo Social Europeu

Bolsa de investigação da Fundação para a Ciência e a Tecnologia com a referência SFRH/BD/80056/2011, financiada pelo POPH – QREN – Tipologia 4.1 – Formação Avançada, comparticipada pelo Fundo Social Europeu e por fundos nacionais do MCTES.

"Our greatest weakness lies in giving up. The most certain way to succeed is always to try just one more time."

Thomas A. Edison (1847 – 1931)

Acknowledgements

I would like to express my sincere thanks to all those who in somehow enabled this work, in particular:

My parents, Eduardo Nascimento and Virgínia Nascimento, for all the support they have given me throughout life, especially in difficult times.

To my girlfriend, Cristina Gouveia, for the support and friendship.

To Dr. Pedro Jorge and Dr. José Manuel Baptista for the opportunity given to carry out this work, supervision and availability along this process.

The conditions provided by INESC TEC and friends: Luísa Mendonça, Carlos de Jesus, Luís Coelho, João Ferreira, Gaspar Pacheco, Dr. Ireneu Dias, Dr. José Luís Santos, Dr. Manuel Joaquim Marques, Dr. Paulo Marques, Dr. Serge Mendonça and Dr. Paulo Caldas.

To Dr. Jose Luis Cruz and Miguel Andrés for supervising me during six months in the University of Valencia, Spain.

The financial support of FCT (SFRH/BD/80056/2011), allowing me to work full time on my doctoral thesis.

To all professors of University of Porto that shared their scientific knowledge with me.

Abstract

This thesis, entitled “Optical fiber sensors technology for supervision, control and protection of high power systems” was developed in the scope of a PhD degree in Physics. It reports on the development of optical sensors, namely for current measurement in high power grids, using bulk optical glasses and optical fibers.

In this document, sensors based on the Faraday effect, the most common optical effect used in current sensing, were evaluated using polarimetric detection schemes. One approach consisted in a portable clamp-on sensing head with a bulk optical glass and an interrogation unit, developed for an industrial application. The sensor demonstrated to conform with accuracy class 1 considering nominal current equal or larger than 900 A_{RMS}, and the possibility of detecting transients under 10 μs. Simulations were also made in order to study its susceptibility to external magnetic fields, showing that strategic positioning of the sensors in the line may greatly reduce measurement errors.

Other configurations were investigated using optical fibers as the sensing medium, where sensing elements with conventional fibers were compared with two spun highly birefringent fibers. One of the fibers is commercialized by IVG and the other is a Photonic Crystal Fiber (PCF) developed by Gleb Wataghin physics institute from the University of UNICAMP, Brazil. The IVG fiber revealed good stability and robustness against linear birefringence effects, when compared with the standard fiber, operating as a class 0.5 device for nominal currents equal or higher than 600 A_{RMS}. The PCF fiber developed showed promising features but due to its fragility and reduced availability it was not possible to conduct conclusive tests.

Magnetostrictive effects were also evaluated by combining a magnetostrictive rod of Terfenol-D with all fiber optical lasers and a Long Period Grating (LPG). In the former

configuration the magnetostrictive material was used to modulate the laser fiber Bragg mirrors and consequently the laser wavelength emission. An interferometric detection scheme was also employed in one of the configurations to demodulate the wavelength information, containing the magnetic field information. Also, it was observed that if the laser linewidth is too narrow, its optical power becomes very susceptible to acoustic vibrations and can even pulse, which is an undesirable outcome. However, having this consequence into account, by tuning the laser bandwidth allowed the development of a laser whose optical power is modulated according to the applied magnetic field, eliminating the need for an interferometric readout system.

With the LPG sensor, the resonance amplitude modulation due to the magnetostrictive material, in the presence of the magnetic field, was explored. A resolution of 4.61 μT_{RMS} was achieved, however, due to limited range of operation and slightly larger errors this sensor could not fit any of the current sensors error classes. The LPG alone also proved to be sensitive to vibration, a capability required in detection of structures resonance frequencies, namely in the electric grid transmission towers, in order to prevent degradation therefor.

Resumo

Esta tese, intitulada “Optical fiber sensors technology for supervision, control and protection of high power systems” foi desenvolvida no âmbito de um programa doutoral em Física. Reporta o desenvolvimento de sensores óticos, com especial enfâse na medição de corrente em linhas de transmissão de alta potência, utilizando vidros óticos e fibras óticas.

Neste documento, sensores baseados no efeito de Faraday, o mecanismo mais utilizado na deteção de corrente através de meios óticos, foram avaliados utilizando esquemas de deteção polarimétrica. Uma das abordagens consistiu numa cabeça sensor portátil para ancoragem na linha de transmissão, utilizando vidro ótico de baixa birrefringência e uma unidade de interrogação, desenvolvida para uma aplicação industrial. O sensor demonstrou precisão de classe 1, para correntes nominais iguais ou superiores a 900 A_{RMS}, e a possibilidade de detetar impulsos na rede abaixo dos 10 μs. Simulações foram também efetuadas, a fim de estudar a sua suscetibilidade a interferências devido a campos magnéticos externos e verificou-se que o posicionamento estratégico dos sensores na linha pode ajudar a minimizar erros de medição.

Outra configuração testada envolveu o uso de fibras óticas como elemento transdutor, empregando, uma fibra convencional e duas fibras torcidas durante a sua fabricação (*spun*) e altamente birrefringentes. Uma das fibras foi proveniente da empresa IVG e a segunda é uma fibra de cristal fotónico desenvolvida pelo instituto de física *Gleb Wataghin* da Universidade UNICAMP, no Brasil. A fibra IVG revelou boa estabilidade e robustez contra efeitos de birrefringência linear, quando comparado com a fibra standard, enquadrando-se na classe 0.5 para correntes nominais iguais ou superiores a 600 A_{RMS}. A fibra PCF demonstrou algumas características promissoras, mas devido à sua fragilidade e disponibilidade limitada não foi possível obter resultados conclusivos.

Efeitos magnetoestrictivos foram também avaliados, combinando uma barra de um material magneto-restritivo, o Terfenol-D, com lasers em fibras óticas e também com uma rede de período longo em fibra. Na primeira configuração, o material magneto-restritivo foi utilizado para modular os espelhos (redes de *Bragg*) e por sua vez o comprimento de onda de emissão do laser. Um esquema de deteção interferométrico é utilizado em uma das configurações para desmodular as informações de comprimento de onda, que por sua vez contêm a informação de campo magnético. Foi também demonstrado que se a largura espectral do laser for demasiado estreita, a potência ótica de saída torna-se muito suscetível a vibrações acústicas, podendo mesmo entrar num regime de impulsos, uma consequência indesejável. No entanto, tento em conta esta consequência, o ajuste da largura de banda do laser, permitiu o desenvolvimento de um laser cuja potência ótica é modulada de acordo com o campo magnético aplicado, eliminado a necessidade de um sistema interferométrico de leitura.

Com o sensor de rede de período longo, a modulação de amplitude de ressonância resultante do material magneto-restritivo, na presença de um campo magnético, foi explorada. Resolução de 4.61 μT_{RMS} foi obtida com o sensor, no entanto, neste caso devido a limitações na gama de medição e erros mais elevados não foi possível enquadrar o sensor em nenhuma das classes de precisão dos sensores de corrente. O LPG por si só também mostrou sensibilidade a vibrações, uma aptidão necessária na deteção de deslocamentos da frequência de ressonância de estruturas, nomeadamente de torres empregues no transporte de energia e assim evitar a degradação das mesmas.

Keywords

Optical current sensor, passive interferometer, virtual instrumentation, prototype, optical fiber laser, spun fiber, optical glass, polarimetric detection, Faraday effect, magnetostriction, vibration sensor.

List of Symbols

B – Magnetic field intensity along light propagation

$\mathbf{B_L}$ – Linear birefringence

$\mathbf{B_p}$ – Parallel magnetic field intensity along light propagation

$\mathbf{B_r}$ – Magnetic field amplitude along a radius *r*

c – Velocity of light in vacuum

D – Coil diameter

d – Distance between a fixed pole and a moving pole in the curvature setup

$\mathbf{d_F}$ – Fiber diameter

$\mathbf{E_L}$ – Left circular polarization

$\mathbf{E_R}$ – Right circular polarization

$\mathbf{F_M}$ – Radial force exerted on the electron

$\mathbf{I_0}$ – Nominal current

$\mathbf{I_{AC}}$ – Alternating component of the current passing through the conductor

$\mathbf{I_P}$ – Current passing through the primary transformer

K – Transformation ratio of an electric current transformer

L – Length of the Faraday medium

$\mathbf{L_B}$ – Linear beat length

$\mathbf{L_E}$ – Elliptical polarization beat length

$\mathbf{L_{ind}}$ – Linear beat length due to winding

LP_{0m} – Linear polarized mode of the m cladding mode

L_S – Circular beat length or spin pitch

M – Mirror matrix

$n^{cl(m)}$ – Effective refractive indices of the cladding guided mode

n_{eff} – Effective refractive indices of the core guided mode

n_{fast} – Fast axis refractive index

n_L – Left axis refractive index

n_{low} – Slow axis refractive index

n_R – Right axis refractive index

P[α] – Polarizer oriented at α degrees from the horizontal axis matrix

P_1 – X polarization

p_{11} and p_{12} – Strain-optic constants

P_2 – Y polarization

r – Distance from the conductor to the sensor

S – Polarimetric quadrature signal

S_1 – X polarization after photodetection

S_2 – Y polarization after photodetection

S_{AC} – Alternating component of the quadrature processed signal

S_C – Sensitivity decay factor due to coiling a HiBi fiber

S_{SPUN} – Sensitivity decay factor of an ideal circularly birefringent fiber

U_S – Current passing in the secondary transformer

V – Verdet constant

α – Angle in relation to the horizontal plane

β – Linear birefringence expressed in rad/m

β_{ind} – Linear birefringence per meter due to fiber winding expressed in rad/m

δ – Angle of characteristic direction of birefringence

ΔL – Offset induced with the translation stage in the curvature setup

$\Delta\lambda$ – Linedwidth in wavelength

$\Delta\upsilon$ – Linewidth in frequency

ε – Strain

θ_F – Circular Birefringence due to Faraday rotation in rad/m

θ_{Ft} – Total circular Birefringence due to Faraday rotation in rad

θ_S – Circular birefringence expressed in rad/m

Θ_r – Reflection angle

Θ_t – Transmission angle

$\emptyset_{DC}$ – DC interferometer phase

$\emptyset(t)$ – Time varying interferometer phase

Λ – Fiber Bragg grating period or photonic crystal fiber pitch

λ – Wavelength

$\lambda/4$ – Quarter wave plate

λ_0 – Mean wavelength of the resonances in the UV

λ_B – Bragg wavelength

μ_0 – Vacuum permeability

ν – Poisson’s ratio

σ – Standard deviation

Acronymous

ANN – Artificial Neural Networks

BS – Beam Splitter

BW – BandWidth

CT – Current Transformer

CVD – Chemical Vapor Deposition

DAQ – Data AcQuisition

DFB – Distributed Feedback Laser

DOP – Degree of Polarization

EFPI – Extrinsic Fabry-Perot Interferometer

ESA – Electric Spectral Analyzer

FBG – Fiber Bragg Grating

FFT – Fast Fourier Transform

FP – Fabry-Pérot

FRM – Faraday Rotator Mirror

HiBi – Highly Birefringent

HWP – Half Wave Plate

LPG – Long Period Grating

OPD – Optical Path Difference

OSA – Optical Spectrum Analyzer

PBS – Polarizing Beam Splitter

PCF – Photonic Crystal Fiber

PMF – Polarization Maintaining Fiber

PZT – PieZoelectric Transducer

QWP – Quarter Wave Plate

RI – Refractive Index

RIU – Refractive Index Unit

RMS – Root Mean Square

SLD – Super Luminescent Diode

SMF – Single Mode Fiber

SNR – Signal to Noise Ratio

SOP – State Of Polarization

Contents

List of Figures

List of Tables

Chapter 1 Introduction

In this chapter the motivation and objectives for the work reported in this thesis are described along with its major scientific and technological achievements. A brief description of the main fundamental concepts and mathematical tools required to better understand the remaining document are also given; namely principles and tools to understand the Faraday effect and its effects on optical polarization when magnetic fields are present.

1.1 Motivation

The real time measurement of electric parameters is a fundamental requirement to fully characterize the energy flow in power grids and better understand its operation enabling the development of sustainable energy management systems. In this context, electric current sensors are one of the key requirements as they enable for instance, accurate measurement of power consumption or fast identification of failures on power systems.

Traditional electric current transformers (CTs) technology is typically used. However, in a high voltage environment these systems can easily achieve magnetic saturation, get damaged by heat, short-circuits or atmospheric electrical discharges, so it is necessary to employ protection circuits and insulation which demand for costly periodic maintenance. Furthermore these sensors have high dimensions and weight and cannot be suspended on the electric line, greatly increasing the installation logistics and the substation footprint. Therefore, in order to achieve smarter and more efficient power grids is necessary to improve the sensor technology [1, 2].

In conventional electric transformers, accuracy is not constant in all operating range. This happens due to phenomena of hysteresis and magnetic permeability and resistivity variations.

So, according to these characteristics, current sensors are defined in classes, where each class requires different maximum errors, as shown in Figure 1.1 [3]. These errors are calculated as

$$\text{Error} = \frac{\text{KU}_\text{S}\text{-I}_\text{P}}{\text{I}_\text{P}} \times 100\% \tag{1.1}$$

where K is the transformation ratio, U_S is the current passing in the secondary transformer and I_P is the current passing through the primary transformer. However, when dealing with optical current sensors, since there is no conventional transformer, the KU_S parameter relates to the optical sensor accuracy, after calibration. For instance, a class 0.5 sensor designed to operate with a nominal current of 1 kA, has a maximum error of ±0.5 %, for currents above 1 kA. According to IEC 60044-1 standard, classes 0.1 and 0.2 can be employed in precision measurement and classes 0.5 and 1 for standard metering.

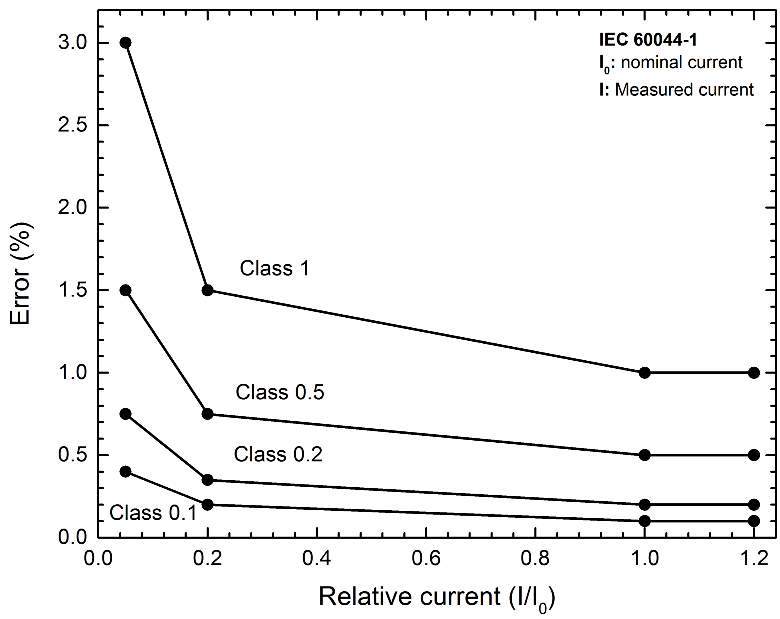

Figure 1.1 – Maximum errors according to the transformer class for IEC 60044-1.

Over the past decades, many product revolutions have taken place due to the growth of the optoelectronics and fiber optic communications industries. Along with this technology, the optical fiber sensors emerged, leading to fiber based sensing devices and components for many fields of application [4].

The high growth in the telecommunications industry led to material cost decrease of fiber sensor components. These types of sensors are quite attractive and have been gaining great interest since they can be light, small, immune to electromagnetic interference, presenting good performance in high temperature, having large bandwidth, high sensitivity, environmental ruggedness, and the ability for distributed sensing. Other important aspects are electrical passivity, not needing local electric power, and enabling the possibility of multiplexing of a large number of sensing elements [5].

A diversity of configurations and devices can be setup to couple the optical fiber with different transducing mechanisms. As result, fiber optic sensors can be used to measure a diversity of parameters and examples are reported in literature for measurement of rotation, acceleration, electric and magnetic field, temperature, pressure, acoustics, vibration, linear and angular position, strain, humidity, viscosity and even chemical and biological analytes [4].

One of the most successful and used optical fiber sensor developed up to date is the FBG (Fiber Bragg Grating) where the measurement information is encoded in wavelength and presents a linear response to temperature and strain. Its characteristics include being relatively inexpensive to produce, immunity to electromagnetic interference, and providing the capability of multiplexing several sensors, allowing several measurement points in a single fiber. This sensor includes a short section of a single-mode fiber (typically below 10 mm) where the core refractive index is modulated periodically. This structure acts as a highly selectively wavelength filter (λ_B - Bragg wavelength), dependent on the grating period and the effective refractive index of the propagating mode ($\lambda_B = 2.\Lambda.n_{eff}$). This periodical index modulation of the structure allows the light to be coupled from the forward propagating core mode into the backward propagating core mode. The refractive index modulation of an FBG is achieved by exposure of the core to an intense UV interference fringe pattern.

The sensing characteristics of an FBG derive from the sensitivity of the refractive index and the grating period to externally applied mechanical or thermal perturbations. Applied strain affects the response of an FBG directly, through the expansion and compression of the grating size and through the strain-optic effect (strain-induced modification of the refractive index). On the other hand, the temperature sensitivity is dependent on the thermal expansion coefficient and the thermo-optic coefficient of the fiber. The first parameter relates with the grating expansion and the latter one, is the main effect and depends on the induced refractive index change due to temperature. Some of their main applications include structural health monitoring (strain and accelerometer) in rods, rail bridges, tunnels and dams [5–7]. Furthermore, application in manufacturing optical fiber lasers [8] and accelerometers [9] can also be found in literature.

Another important sensor class, where fiber based solutions attained very high performance and reliability is in gyroscope systems. The fiber optic based gyroscope, is presently used in the most demanding applications in navigation guidance and stabilization. The simpler configuration is based on the Sagnac effect and the sensor forms a closed loop with two counterpropagating light waves. This sensor is only susceptible to non-reciprocal effects such as rotation and Faraday effect [5]. Indeed, the Sagnac configuration is also a very common approach for deployment of polarization based magnetic and electric field optical sensors and it is the most studied configuration, attaining better performances in different applications in the electric power industry [10].

A great diversity of other fiber optic based configurations such as in fiber interferometers or LPGs (Long Period Gratings) can also be used for very compact refractive index based (label-free) measurement of bio-chemical parameters [11,12].

The measurement of electric current, and other grid parameters, using optical methods is especially interesting for high power system applications. An optical current sensor is normally composed by an optical sensing element which measures the integral of the magnetic field along the sensing region and an optical fiber link, which connects the sensing element to the optoelectronic control and processing unit [13].

Comparing optical current sensors with conventional current transformers, they offer several advantages: large bandwidth, high linear response over a wide frequency, immunity to electromagnetic interferences, possibility of AC and DC measurements, possibility of multiplexing and compatibility with fiber optic communication technology, allowing long range remote detection. They are typically made from non-conducting materials, offering electromagnetic interference immunity. Depending on the configuration, they are hysteresis free and present higher dynamic range and wider bandwidth operation. In general, they are lighter, compact, simpler and cheaper [13–15], establishing a promising technology for more sustainable power grids, with reduced footprint, lower maintenance cost and ability of self-diagnostic. Nevertheless, in spite of great developments, with several industrial solutions of fiber optic based technology already probing the market, several challenges persist that still make worthwhile research topics, including temperature dependence, susceptibility to vibrations and long term reliability [16].

1.2 Objectives

The main goal of this PhD program is to develop new optical fiber sensors for current/magnetic field metering in energy systems. Specific and operational objectives are:

- Design, development and characterization of new optical fibers configurations based in standard, birefringent, and microstructured optical fibers for detection of electric current and magnetic fields.
- Exploitation of sensing mechanisms such as magneto-optic and magnetorestritive effects for the sensing head design.
- Development of strategies for interrogation of the developed sensors, including polarization, interferometric, wavelength and amplitude based.
- Application of virtual instrumentation for implementation of advanced and compact interrogation schemes.
- Investigation of strategies for packaging and integration of subsystems.
- Develop supporting sensors for the electric distribution network.

1.3 Document structure

This essay is organized in seven chapters. The current chapter addresses the work objectives, and the fundamental concepts explored, including light polarization, the Faraday effect and Jones matrix formalism.

In the second chapter, the state of the art of optical current sensors is reported, including sensors based on the Faraday effect, magnetostrictive and other magnetic effects, and hybrid.

In the third chapter, a clamp-on sensor based on the Faraday effect to monitor high voltage power lines was implemented. This work was developed within an international project between Brazil and Portugal named TECCON. The sensor uses a high Verdet bulk material encapsulated in a nylon casing and the prototype also includes a portable interrogation unit. The polarimetric bulk optical current sensor was also theoretically studied, considering the effects of external conductors.

In chapter number four, polarimetric optical current sensors using conventional and special fibers as the sensing medium are studied, namely highly birrefringent spun fibers.

In chapter five, fiber optic lasers combined with magnetostrictive materials were tested for magnetic field sensing. An interferometric detection scheme, using a passive interferometer, acts as a wavelength-to-intensity modulator and is used to retrieve the magnetic field information.

In chapter six, a long-period grating (LPG) was firstly proposed for vibration sensing of the electric grid towers and subsequently for magnetic field sensing, using the same sensing principle, but employing a magnetostrictive material.

In the last chapter, number six, conclusions of the developed work and future works suggestions are given. Also, throughout the document are made references to the appendix, where some complementary work is described.

1.4 List of publications

From the work carried out during the PhD program resulted several scientific publications, namely: five papers in international peer reviewed scientific journals and another one in submission, six articles in international conferences proceedings (corresponding to an oral presentation and five poster presentations). Furthermore, part of this PhD program consisted in developing a prototype for the high power electric grid, in optical current sensing, within an industrial project between Portugal a Brazilian company, namely a grid operator company

(TBE). In particular, resulted as project outputs: a prototype of an magneto-optic clamp-on sensing probe; a prototype of a portable industrial sensor interrogation unit; corresponding acquisition and control software with signal processing ability. The project was successfully evaluated by the very demanding regulator of the Brazilian electric sector (ANEEL), and is presently initiating the second stage, for development of an industrial prototype.

Articles in International Scientific Journals:

- A. C. S. Brigida, I. M. Nascimento, S. Mendonça, J. C. W. A. Costa, M. A. G. Martinez, J. M. Baptista, and P. A. S. Jorge, "Experimental and theoretical analysis of an optical current sensor for high power systems" Photonic Sensors, vol. 3, no. 1, pp. 26–34, 2012.

  This paper is related with Chapter 3 where its presented one the preliminary experimental results obtained with the bulk sensing head operating at 1550 nm. Here the sensor transfer function is calculated and interference errors due to external magnetic fields, in a tree-phase system was theoretically studied.

- R. M. Silva, H. Martins, I. Nascimento, J. M. Baptista, A. L. Ribeiro, J. L. Santos, P. Jorge, and O. Frazão, "Optical Current Sensors for High Power Systems: A Review" Applied Sciences, vol. 2, no. 4, pp. 602–628, 2012.

  This manuscript is related with the state of the art, Chapter 2, where a brief historical overview of the optical current sensors is presented, including the different physical principles and its main advantages and disadvantages.

- I. M. Nascimento, J. M. Baptista, P. A. S. Jorge, Jose L. Cruz, Miguel V. Andrés, "Passive interferometric interrogation of a magnetic field sensor using an erbium doped fiber optic laser with magnetostrictive transducer" Sensors and Actuators A: Physical, vol. 235, pp. 227-233, 2015.

This paper is related with Chapter 5, and explains the wavelength modulated Fabry-Pérot laser. Essentially, a pair of FBGs (cavity mirrors) is glued onto a magnetostrictive material (Terfenol-D rod) and when subject to a static or a time dependent magnetic field is applied, the laser wavelength is modulated. A passive interferometer was employed to measure the laser wavelength changes due to the applied magnetic field.

- I. M. Nascimento, J. M. Baptista, P. A. S. Jorge, Jose L. Cruz, Miguel V. Andrés, "Intensity modulated optical fiber sensor for AC magnetic field detection" IEEE Photonics Technology Letters, vol. 27, no. 23, pp. 2461-2464, 2015.

  This paper is also related with Chapter 5, but consists of another configuration, the intensity modulated laser. Its optical response is characterized using different bias fields, as function of alternating magnetic fields.

- I. M. Nascimento, A. C. S. Brígida, J. M. Baptista, J. C. W. A. Costa, M. A. G. Martinez, P. A. S. Jorge, "Novel Optical Current Sensor for Metering and Protection in High Power Applications", Instrumentation Science & Technology, vol. 44, no. 2, pp. 148-162, 2015.

  This paper is also connected with Chapter 3, but characterization of the bulk sensing head is made at different wavelengths, 650 nm, 830 nm and 1550 nm. Furthermore, the clamp-on prototype is introduced and evaluated.

Articles in International conferences with poster presentation:

- I. M. Nascimento, C. Gouveia, Sunirmal Janad, Susanta Berad, J. M. Baptista, Paulo Moreira, “High refractive index and temperature sensitivity LPGs for high temperature operation,” in *RIAO/OPTILAS 2013, VIII Iberoamerican Optics Meeting and XI Latinamerican Meeting on Optics, Lasers and Applications*, July 2013, pp. 1–5.

  This paper is related with accessory work of tailoring the sensitivity of LPG devices with special sol-gel coating. It has only a marginal relation with the work of Chapter 6, and was not included in this thesis.

- A. C. S. Brigida, I. M. Nascimento, G. Hesinid, J. G. Hayashid, J. M. Baptista, J. C. W. A. Costa, and C. M. B. Cordeiro, “Fabrication of a spun elliptically birefringent photonic crystal fiber and its characterization as an electrical current sensor,” in *Fifth European Workshop on Optical Fibre Sensors*, May 2013, vol. 2, no. 1, pp. 1–4.

  This manuscript is related with Chapter 4 and relates to preliminary characterization of the first batch of spun HiBi PCF fiber, using a polarimetric configuration in transmission, using a laser light source at 633 nm.

- I. M. Nascimento, G. Chesini, A. C. S. Brígida, J. G. Hayashi, J. M. Baptista, J. C. W. A. Costa, M. A. G. Martinez, P. A. S. Jorge, Cristiano M. B. Cordeiro, “Fabrication and characterization of spun HiBi PCF fibers for current sensing applications” in *23rd International Conference on Optical Fibre Sensors*, June 2014, pp.1-4.

  This conference article is associated with Chapter 4 and relates to characterization of the second batch of spun HiBi PCF fiber with distinct spin pitch (11.06 mm, 13.52 mm and 20.28 mm), using a polarimetric configuration in transmission and a SLD light source at 650 nm.

- I. M. Nascimento, J. M. Baptista, P. A. S. Jorge, Jose L. Cruz, Miguel V. Andrés, "Magnetic field measurement using a fiber laser sensor in ring arrangement" in *Optical Sensors 2015*, May 2015, pp. 1-6.

  This paper is correlated with Chapter 5, and shows the results obtained with the laser loop configuration, interrogated using a passive interferometer.

- I. M. Nascimento, J. M. Baptista, P. A. S. Jorge, Jose L. Cruz, Miguel V. Andrés, "Erbium doped optical fiber lasers for magnetic field sensing" in *24th International Conference on Optical Fibre Sensors*", September 2015, pp.1-4.

  This conference manuscript is also linked with Chapter 5, where two erbium doped optical fiber laser configurations for magnetic field measurement are compared, the loop configuration and the wavelength modulated Fabry-Pérot. Characterization is made when no bias field is applied, as function of alternating magnetic fields.

Oral presentation in an international conference:

- I. M. Nascimento, J. M. Baptista, P. A. S. Jorge, J. L. Cruz, M. V. Andrés, "Optical sensors for magnetic field measurement" in *International OSA Network of Students (IONS)*, 2015, Valencia (Spain).

  This presentation was a resume of the some of the work developed along this doctoral thesis, showing the main results obtained with the clamp-on prototype sensing head (Chapter 3), and the use of fiber lasers combined with magnetostrictive materials for magnetic field sensing (Chapter 5).

1.5 Fundamental concepts

In this section a brief description of the fundamental concepts and tools necessary to understand polarization based optical sensors are given.

1.5.1 Fiber optic sensors classification

Fiber optic sensors can be classified according to a diversity of criteria depending on the intended application or purpose. Major classes can be defined based on [4]:

- **Modulation and demodulation process**: intensity, phase or polarization.
- **Application**: physical (temperature, stress, magnetic field, etc.), chemical (refractive index, gas, pH, etc.) or biological (blood flow, glucose, etc.).
- **Intrinsic and Extrinsic**: In the former, one or more of the physical properties of the light travelling in the fiber experience a change (intensity, phase, polarization or wavelength). In the latter one the sensing occurs outside of the fiber and the fiber essentially channels the light into and out of the sensing region.
- **Measurement points**: Point-by-point, multiplexed or distributed. In the first one there is a single measurement point in the fiber optic cable, similarly to most electrical based sensors. Multiplexed sensors allow the measurement at multiple points along a single fiber line and distributed sensors are able to sense at any point along a single fiber line, typically every centimeters over many kilometers of length.

Typically, optical fiber current sensors can be classified as bulk, all-fiber, magnetostrictive or hybrids, depending on the sensing configuration. Characteristics and examples of each category are further detailed in the state of the art chapter.

1.5.2 Polarized light

Light can be modeled in terms of transverse electromagnetic waves and its polarization corresponds to the variation of the electric field as a function of time, in a determined point of space, in the direction of propagation. Considering polarized light propagating in the *z* direction, the electric field can be represented as two orthogonal fields [17]

$$\vec{E}(z,t) = \vec{E}_x(z,t)+\vec{E}_y(z,t) \tag{1.2}$$

For linear polarized light, the orthogonal electric field components have the same amplitude and a relative phase that is zero or multiple of π. For circular polarized light, the amplitude is the same but the relative phase is π/2, and for elliptic polarized light, the phases and amplitudes are generally different from the two previous cases, as shown in Figure 1.2.

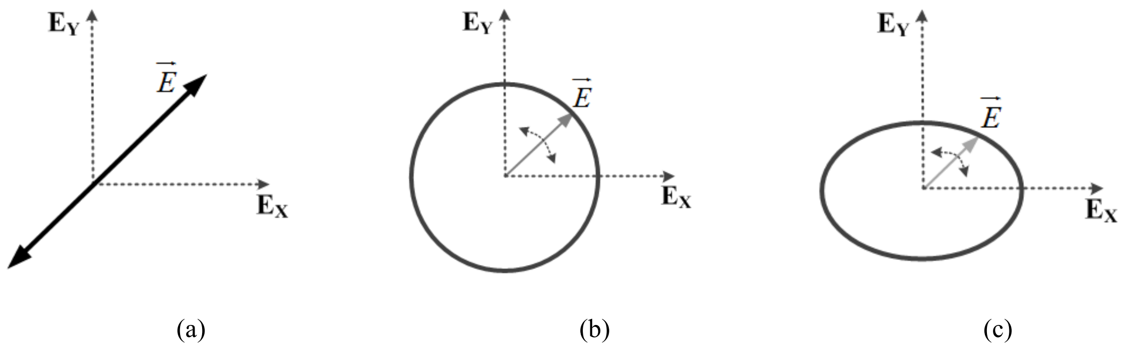

Figure 1.2 – (a) Linear, (b) Circular and (c) Elliptic Polarization.

On the other hand, when considering incoherent broadband sources, light can also be unpolarized or partially polarized, meaning that its polarization changes randomly over time. Unpolarized light from a white light or broadband optical source can be represented as the superposition of two, incoherent and orthogonal polarized states with the same amplitude. A perfect polarized light has 100 % degree of polarization (DOP), while the unpolarized light has 0 % [17]. In practice, more often a superposition of polarized and unpolarized components can be found, resulting in partially polarized light where the DOP is somewhere between 0% and 100%.

1.5.3 Linear and circular birefringence

Many crystalline substances present an anisotropic atomic distribution, resulting in anisotropic connection forces between atoms and consequently different optical properties in distinct directions. These structural changes result in different refractive indexes, corresponding to different propagation velocities for different polarization states. Such property is called birefringence.

In a medium with linear birefringence (β), the two orthogonal directions have different refractive indices where light propagates with different velocities. If linear polarized light is launched at an arbitrary angle in relation with one of the axis, both orthogonal states are excited and light will eventually become elliptic, due to a relative phase difference between the two orthogonal states.

In case of circular birefringence (θ_S), right and left circular polarized light propagate with different refractive indices. On the other hand, and considering that linearly polarized light can be described by the combination of two circular polarized waves of opposite handedness, in the presence of circular birefringence, a propagating linear polarized field will experience a rotation of its plane of vibration [17,18].

1.5.4 Polarizers

A polarizer is a device that transforms natural light into polarized light. There are several devices that produce this effect, and they can be based in dichroism or selective absorption; reflection; scattering; and birefringence or double refraction. As a common characteristic, they all have some form of asymmetry associated to the process of light propagation [17]:

- Dichroism - Works by selecting one of the two orthogonal linear polarized states being transparent to one field and absorbing the other field. In this group we have the Wire-grid polarizer, dichroic crystals and the polaroid.
- Birefringence - Normally a Glan-Foucault or a Wollaston prism. The first one uses two prisms made of calcite (a highly birefringent material) with an air gap between them or cemented, and each polarization follows perpendicular routes, after reaching the second prism. The Wollaston prism uses two prisms cemented, with the first one made of glass and the second of calcite. Light that passes the first prism, when it reaches the second one, separates in two orthogonal polarizations with an angle between them.

- Scattering - Considering an unpolarized light incident on a particle, some light is re-emitted in all directions, however the one perpendicular to the plane of incident is linearly polarized.
- Reflection - When unpolarized light reflects in a dielectric medium, with $\Theta_r + \Theta_t = 90°$ (r-reflection, t-transmission), only the reflected component is linearly polarized and its polarization direction is parallel in relation to the reflective surface.

In practice, if linear polarized light passes through a polarizer, the intensity at its output is described by Malus law

$$I_{OUT} = I_{IN}\cos^2\theta \tag{1.3}$$

where I_{IN} is the light intensity before the polarizer and θ is the relative angle between the linear polarized light direction and the polarizer axis. Therefore, if the relative angle is 90 degrees no light is transmitted, for an ideal polarizer. Additionally, if totally unpolarised light passes through a polarizer, at the output a linear polarized wave with half intensity is obtained.

1.5.5 Wave Plates

Wave Plates are devices that permit the modification of the state of polarization of a wave, by changing the relative phase of its linear polarized components, when propagating through a linearly birefringent material. The most commonly used are the half and quarter waveplates. The first one introduces a relative phase difference of π between orthogonal polarization states. This results into a simple rotation of the plane of polarization in case of incident linearly polarized light. For elliptic or circular polarized light this plate produces a change in the rotation direction. On the other hand, the quarter waveplate introduces a relative phase difference of π/2, transforming linear polarization states into elliptic or circular, as show in Figure 1.3. Notice that, if polarized light is oriented according to one of the two axis of the plate, the output polarization state will remain unchanged, because no relative phase difference is introduced [17].

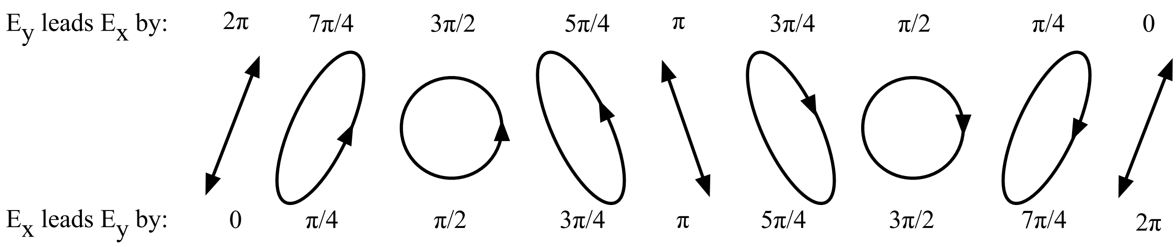

Figure 1.3 – Polarization rotation.

1.5.6 Faraday effect

Michael Faraday discovered in 1875 that light that propagates through a material medium can be influenced by the application of an external magnetic field. He has discovered that in the presence of a magnetic field (B), a rotation of the plane of vibration of linear polarized light takes place, that is proportional to the magnetic field parallel to light propagation and is given by

$$\theta_{Ft} = \int_L V.B.dl \tag{1.4}$$

where V is the Verdet constant that is an intrinsic property of the medium, and depends on the light wavelength and on the temperature [17]. This effect is called the Faraday effect or magnetic-optic effect. In diamagnetic materials and in the visible spectral range the Verdet constant is related to the medium properties by the following relation [19].

$$V = \frac{\pi}{\lambda}\left(a + \frac{b}{\lambda^2 - \lambda_0^2}\right) \tag{1.5}$$

In this equation, λ_0 is the mean wavelength of the resonances in the UV and a and b are the constants and in reference [19] these parameters can be found for several optical glasses.

The theoretical treatment of the Faraday Effect involves quantum-mechanical theory of dispersion, including the effects of the magnetic field on the atomic or molecular energy levels. In literature the Verdet constant can be expressed in rad/A or in rad/T.m and the conversion from the latter to the initial one is made by multiplication with the vacuum permeability (μ_0).

Considering only nonmagnetic materials, this effect can be approximately explained with a classic treatment. Knowing that linearly polarized light can be expressed by the combination of two circular polarized waves with opposite rotations, and supposing an incident circular and monochromatic light: as result, an elastically bound electron will take on a steady-state circular orbit, due to electric field rotation. When an external magnetic field, perpendicular to the plane of the orbit is applied, a radial force F_M is exerted on the electron. That force can be directed toward or away from the circle center, depending on the incident light rotation and magnetic field direction. The total radial force (equal to F_M plus elastic restoring force) can have two values. For a given magnetic field, there will be two possible values of the electric dipole moment, as well as two values of the refractive index, n_R and n_L (right and left). Therefore, the presence of the magnetic field induces circular birefringence in the medium and implies that light with right and left circular polarizations have different propagation velocities [17].

For a generic polarization state, which can be described as a combination of two orthogonal circular modes (left and right), the application of the magnetic field, translates into the accumulation of a relative phase between the two modes, proportional to the magnetic field. For linearly polarized light, this relative phase, results in a rotation of the polarization plane, as shown in Figure 1.4.

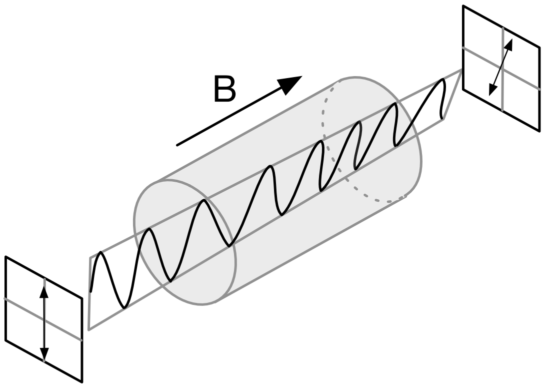

Figure 1.4 – Faraday effect in linearly polarized light.

The effect of the Faraday rotation is non-reciprocal, in other words, the rotation only depends on the magnetic field and not on the light propagation direction. Therefore, if the same light passes through the same medium, but with opposite propagation direction, the rotation of polarization will be cumulative (as is the phase delay between opposite circular components).

The Faraday effect is observed in diamagnetic, paramagnetic and ferromagnetic materials. In the case of diamagnetic materials, the Verdet constant is relatively low and its dependence with temperature is also reduced. For paramagnetic and ferromagnetic materials, their Verdet constant values are high but also change significantly with temperature. Also, these materials exhibit saturation effects. The highest Verdet constant values are found in ferromagnetic materials, however, changes with temperature and wavelength are also very high, and present undesirable saturation phenomena. Also, some paramagnetic materials do not exhibit a linear response with the magnetic field and may present some hysteresis. In Table 1.1 it is shown the Verdet constant of some materials [17,20].

Table 1.1 – Verdet constant of some materials.

λ = 633 nm	Material	Verdet constant (rad/T.m)
Diamagnetic	Air	6.27×10^{-6}
	SiO_2 (Silica)	3.67
	BK7	4.9
	SF57	21.8
	BSO	60.3
Paramagnetic	FR-5	-71.0
	EY-1	-41.9
Ferromagnetic	TGG	-134

1.5.7 Jones matrix formalism

The Jones Matrix is a mathematical tool suitable for the representation of linearly polarized light. It allows calculating the evolution of polarization as light travels through linear optical elements, permitting the calculation of the resulting electromagnetic field. This method is suitable for the calculation of the response of an optical current sensor built with such birefringent elements.

Considering a polarized light propagating along *z* direction, the electric field can also be defined as

$$\vec{E}(z,t) = \left(\hat{i}E_{0x}e^{i\varnothing_x} + \hat{j}E_{0y}e^{i\varnothing_y}\right)e^{i(kz-\omega t)} \tag{1.6}$$

In a matrix form, this field can be represented instead as

$$\vec{E}_0 = \begin{bmatrix} E_{0x}e^{i\varnothing_x} \\ E_{0y}e^{i\varnothing_y} \end{bmatrix} \tag{1.7}$$

In many applications it is not necessary to know the exact amplitudes and phases. Therefore, we can normalize the irradiance to unity and obtain simpler expressions, although some information is lost. This proceeding is done by dividing both elements in the vector by the same scalar (real or complex), such that, the sum of the squares of the components is one [17].

For a generic electric field with the plane of polarization oriented with an angle α in relation to the horizontal plane, the Jones vector is then

$$\vec{E}_0 = \begin{bmatrix} \cos(\alpha) \\ \sin(\alpha) \end{bmatrix} \quad 0 \leq \alpha < \pi \tag{1.8}$$

In case of right and left circular polarization, the normalized Jones matrices are

$$\begin{aligned} \vec{E}^R &= \frac{1}{\sqrt{2}} \begin{bmatrix} 1 \\ -i \end{bmatrix} \\ \vec{E}^L &= \frac{1}{\sqrt{2}} \begin{bmatrix} 1 \\ i \end{bmatrix} \end{aligned} \tag{1.9}$$

Suppose that a polarized wave E_0 passes through a series of optical elements, represented by $A_1, \ldots, A_n$, the corresponding electric field is then expressed as

$$\vec{E}_{out} = A_n \ldots A_1 \vec{E}_0 \tag{1.10}$$

where A_n is a 2×2 matrix that depends on the optical element it represents. In Table 1.1 are shown examples of the Jones matrices describing some of the most common linear optical elements [17].

Table 1.2 – Jones Matrices for some elements.

Linear optical element	Jones matrix
Polarizer oriented at an angle *α* with the horizontal axis	$P[\alpha] = \begin{bmatrix} \cos^2(\alpha) & \cos(\alpha).\sin(\alpha) \\ \cos(\alpha).\sin(\alpha) & \sin^2(\alpha) \end{bmatrix}$
Mirror	$M = \begin{bmatrix} 1 & 0 \\ 0 & -1 \end{bmatrix}$
Beam Splitter	$BS = \frac{1}{\sqrt{2}} \begin{bmatrix} 1 & 0 \\ 0 & 1 \end{bmatrix}$
Quarter-wave plate (λ/4), fast axis vertical	$QWP^V = e^{i\pi/4} \begin{bmatrix} 1 & 0 \\ 0 & -i \end{bmatrix}$
Quarter-wave plate (λ/4), fast axis horizontal	$QWP^H = e^{i\pi/4} \begin{bmatrix} 1 & 0 \\ 0 & i \end{bmatrix}$
Half-wave plate (λ/2), fast axis at angle *α*	$HWP[\alpha] = \begin{bmatrix} \cos(2\alpha) & \sin(2\alpha) \\ \sin(2\alpha) & -\cos(2\alpha) \end{bmatrix}$

In addition, propagation in a medium with both linear birefringence and circular birefringence induced by Faraday effect, can be described by [21]

$$F[\theta_F,\beta,\delta] = \begin{bmatrix} A+iB\cos(2\delta) & -C+iB\cos(2\delta) \\ C+iB\cos(2\delta) & A-iB\cos(2\delta) \end{bmatrix} \tag{1.11}$$

with $A = cos(pL/2)$, $B = \beta/p.sin(pL/2)$, $C = (2\theta_F/p).sin(pL/2)$ and $p = (\beta^2+4\theta_F^2)^{1/2}$. The parameters β, θ_F are expressed in *rad/m*, and relate to the linear and circular birefringence (due to Faraday effect), respectively. The δ is a characteristic direction of birefringence and L is the length of the medium.

In a HiBi spun fiber, whose preform is rotated during fiber fabrication, the matrix is then [22]

$$F[\theta_F,\beta,\delta] = \begin{bmatrix} i\theta_F & i\frac{\beta_{ind}}{2}+i\frac{\beta}{2}e^{i2L\theta_S} \\ i\frac{\beta_{ind}}{2}+i\frac{\beta}{2}e^{-i2L\theta_S} & -i\theta_F \end{bmatrix} \tag{1.12}$$

where L is the fiber length, θ_S the circular birefringence per meter due to fiber rotation and β_{ind} the linear birefringence per meter due to fiber winding and it is given by [23]

$$\beta_{ind} = 0.25\frac{2\pi}{\lambda}n^3\left(p_{11}\text{-}p_{12}\right)(1+\upsilon)\left(\frac{d_F}{D}\right)^2 \tag{1.13}$$

where n is the refractive index and depends on the wavelength, $p_{11} = 0.113$ and $p_{12} = 0.252$ are the strain-optic constants, $v = 0.17$ is the Poisson's ratio [24], d_F and D are the fiber diameters and winding diameter, respectively.

Chapter 2 State of the art

There are basically two linear effects by which the magnetic field can be measured by optical sensors: magneto-optic effect (Faraday effect), magnetostrictive and magnetic force (or Lorentz force).

In the case of the sensors, that use the Faraday effect, a rotation in the angle of polarization of the light propagating in magneto-optic material is induced by an external magnetic field. Two different groups of optical current sensors using this effect (all-fiber optic sensors and bulk-optics based sensors) are analyzed. A key aspect of the concept of all-fiber optic sensors is that the optical fiber acts both as the sensing element and as communication channel, which allows for simple solutions and reduces the losses in the fiber connections. By winding the optical fiber around the electric conductor, immunity to external currents or magnetic fields, as well as tunable sensitivity can be easily achieved. As for bulk-optics sensors, they usually present higher sensitivity and robustness, which are very important aspects in real applications. In both cases, saturation effects such as the ones that occur in ferromagnetic-based sensors are avoided allowing higher measurement ranges. Typically, these sensors can be interrogated using three kinds of interrogation techniques: basic polarimetric, quadrature polarimetric and interferometric.

As for the magnetostrictive sensors, it usually includes measuring the force induced by the magnetic field on the sensing element, usually by magnetostriction effects. The possibility of bonding or jacketing optical fibers with magnetostrictive materials to measure the intensity of the magnetic field is also discussed, with special emphasis to Terfenol-D, which has the highest magnetostriction of any alloy. With these types of sensors, multi-point magnetic field measurements are possible with a single optical fiber (optical multiplexing). Other solutions using magnetic fluids are also discussed.

Most of optical sensors described can be installed without the interruption of the current in the conductor, which is a very advantageous property when dealing with high voltage distribution systems.

Lastly, the possibility of hybrid solutions for current measurement, using both conventional technology and new (optical) technology, are also discussed. In this case, the first current transducer is done with conventional electromagnetic technology (such as, a Rogowski coil) but its interrogation and collection of information is done by an optical fiber system. Besides some operational advantages, these hybrid sensors may also be very important in the first step of implementing optical current sensors in the industry, before developing fully optical current measuring systems [25].

2.1 Bulk

In a bulk optical current sensor, a bulk piece of transducer material is used as the sensing media. In addition, besides forming a robust sensor element, depending on the material, much higher Verdet constant can be achieved when compared with silica. Furthermore, several bulk glass materials are available with very low linear birefringence and low elasto-optic coefficients, minimizing the deleterious effects of induced linear birefringence.

The simplest sensing configuration with bulk sensing elements is based on the basic polarimetric detection scheme shown in Figure 2.1. The first polarizer, has the objective of defining the initial polarization state of the light wave. The second polarizer is used as an analyzer, controlling the sensor sensitivity and transforming the polarization rotation into a light intensity modulation that can be measured using a photodetector.

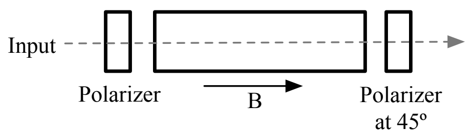

Figure 2.1 – Basic polarimetric detection scheme with bulk material.

According to Malus law, when two polarizers are in such arrangement, the electric field at the output is

$$E_{OUT} = P[\alpha].F[\theta_F].E_0 \tag{2.1}$$

where E_0 is the electric field amplitude after the first polarizer, θ_F is the Faraday rotation due to the applied magnetic field and α is the relative angle between the transmission axes of the polarizers. The intensity of the photodetected signal is then [17]

$$S = E_{OUT} \cdot E_{OUT}^{*} = \frac{1}{2} E_0^2 \sin(\alpha+\theta_F)^2 \tag{2.2}$$

Showing that maximum sensitivity is achieved when this angle is 45º. This means that with the polarizers having a relative angle of 45º, any small change in the plane of polarization of the light, induced by an external magnetic field, in the path between the two polarizers, will be transformed in a larger change of intensity at the output.

In order to eliminate the dependence of the sensor response to the input light intensity fluctuations, a processed output signal, read with a photodetector, can be obtained by dividing the AC component by the DC yielding the signal

$$S_N = 1+\sin(2\theta_F) \tag{2.3}$$

Another improvement of the processing scheme consists on replacing the output polarizer with a polarizer beam splitter (PBS) at ±45 degree from the input.

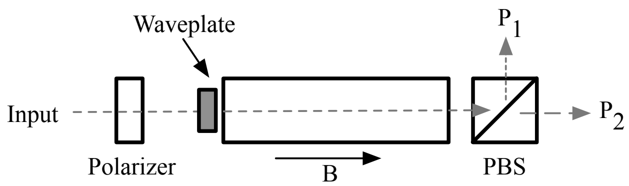

Figure 2.2 – Quadrature polarimetric detection scheme with bulk material.

In this case, the output light is divided into two orthogonal polarizations, through the use of a PBS, and these two signals are detected by two independent photodetectors (S_1 and S_2) and processed by an analog circuit that computes the output signal S, given by

$$S = \frac{S_1\text{-}S_2}{S_1+S_2} = \sin(2\theta_F) \tag{2.4}$$

Since the two signals S_1 and S_2 are in phase opposition, this scheme offers better common noise rejection than the previous one, and also makes the measurement independent of the optical power. Typically, in these bulk materials the linear birefringence (β) is negligible. Furthermore, if the elasto-optic coefficient is also extremely low, as it is for the SF57 material, it is practically invulnerable to induced birefringence owed to pressure with [13]

$$S = \sin(2\theta_F) \qquad \text{if } \beta << 2\theta_F \tag{2.5}$$

However if linear birefringence is considerable, the processed signal becomes

$$S \approx 2\theta_F \frac{\sin(\beta)}{\beta} \qquad \text{if } \beta >> 2\theta_F \tag{2.6}$$

While these can be very simple and sensitive configurations, suitable to act as a simple to install probe, with no need to interrupt the circuit, when operating at high currents, the magnetic crosstalk between different conductors can also be a relevant problem. This arises from the fact that in essence the device is sensitive to any magnetic field collinear with the propagation of light, independent of its origin. Schemes to reduce the magnetic crosstalk in three-phase electric systems have been proposed [26]. A compensation procedure that consists on having a sensor for each phase and determine a correction Matrix has been reported, nevertheless, it does not take into account the temperature dependence of the Verdet constant, requiring an extra temperature sensor to further compensate for the Verdet constant variation.

However, if the optical path can be made to forms a closed circuit around the electrical conductor, the effective Faraday rotation will not be sensitive to any external magnetic fields. Only current passing through the loop, will effectively contribute for the Faraday rotation. A big advantage of these kind of bulk sensors is that the sensor around the conductor does not have to be made from a single piece of material. This allows an easy installation without the need of interrupting the current in the conductor.

The main disadvantages are related to the fact that reflections need to occur inside the bulk optic material for light to go around the conductor. Since the reflection angle will be dependent on the refractive index of the crystal and outside surrounding medium (such as air), the sensor will be affected by a number of external factors such as humidity. This can be solved by isolating the reflection regions of the sensor from external factors but will add higher cost to installation and maintenance operation of the sensor [27]. Also, every internal reflection of the light that occurs at an incident angle, which is larger than the critical angle, will introduce an optical phase difference between the two polarizations, changing the overall state of polarization. In a polarimetric or interferometric scheme, this leads to an unavoidable error source [13,28]. The problem can be solved with the use of double reflections at 45 degrees in each corner of the bulk optic material, where the optical phase difference introduced in the first reflection is compensated by the second reflection. A patent describing this idea was registered in 1986 [29] and it is shown in Figure 2.3.

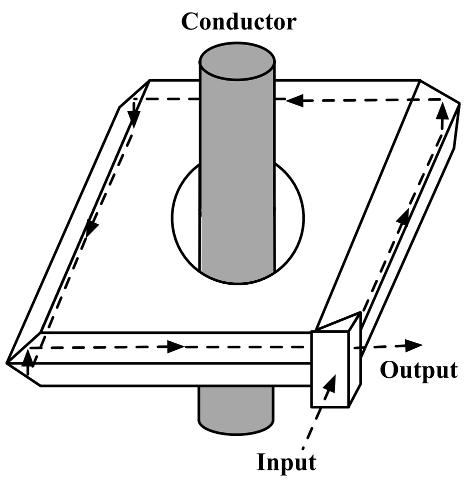

Figure 2.3 – Bulk optical current sensor with double reflection.

However, this idea presents another problem: in the optical path between the first and second reflections, the polarization state is elliptical and the signal will be non-linearly affected by any magnetic field component along that direction. This will cause the system to be affected by external magnetic fields. This problem takes special relevance when measuring current in three phase systems, since the three conductors are usually close to each other. Another possible solution is using a triangular shaped bulk optic material (SF6 glass) in which the light is always reflected at the critical angle [30], as shown in Figure 2.4.

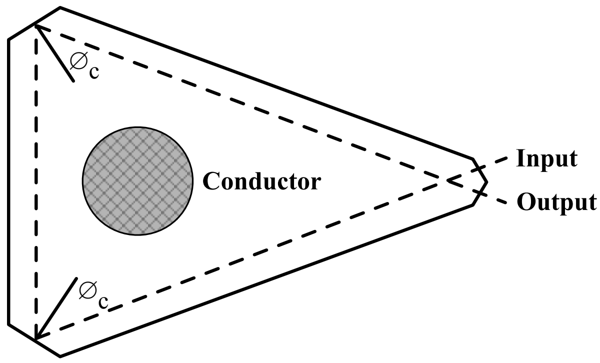

Figure 2.4 – Bulk optic triangular shape current sensor.

This configuration is simpler than the previous. At the input a multimode laser at 780 nm pigtailed to a HiBi fiber is used and the detection scheme applied is similar to the quadrature polarimetric detection but using a regular beam splitter (BS) at the output, instead of a PBS. In one of the BS outputs an analyzer at 45° is employed, obtaining an output with the Faraday rotation plus noise. In the other output, with no polarizer the overall noise is detected. The processing scheme subtracts both signals and the processed signal yields the Faraday rotation without noise. A sensitivity of $3.088 \pm 0.015 \times 10^{-5}$ rad/A was achieved from 0 to 600 A. Immunity to external magnetic fields was also tested with an error of 1 % for an external conductor at 200 mm [30]. Implementation of the quadrature polarimetric detection scheme was also tested using this configuration at 633 nm with a flint glass. A solenoid with 30 turns was wrapped around one of the sensing arms. A DC current measurement up to 3000 A was demonstrated and AC measurements from DC to 10 kHz where carried out with a resolution of 20 mA/√Hz [31].

However, this approach requires a precise reflection angle cut within ±0.01° and still needs isolation from external noise sources such as temperature. Several schemes have been proposed to further increase the sensitivities of these sensors, including extending the light optical path inside the crystal (by using total internal reflections before the light exits from the sensing element) [32]. For this purpose, a circular sensor head was developed (Figure 2.5), where light is injected through a prism and at specific angles, light travels five times around the conductor (with 15 reflections) before exiting the prism. This scheme enhances sensibility and it is not susceptible to external fields. Using the basic polarimetric detection scheme and a solenoid to provide magnetic field a resolution of 1 A/√Hz was reported [33].

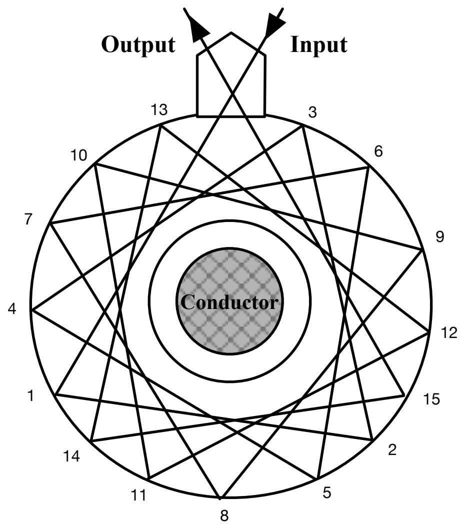

Figure 2.5 – Bulk optics ring shaped current sensor.

Other sensors are available in a square configuration where light passes around the conductor several times. A sensitivity of 6.57×10^{-5} rad/A and a minimum detectable current of 11.3 mA/√Hz have been achieved at 360 Hz with an optical source at 633 nm, using a quadrature polarimetric scheme. In this sensor the angle tolerance is ±0.16°, less rigorous than the triangle shape sensor [34].

The dependence of the Verdet constant with the optical source wavelength is also important, because it changes the sensitivity of the sensor [35]. Also, it was shown that the errors introduced by a small bandwidth optical source (up to 58.8 nm) are very small and therefore it is reasonable to use the models which assume a monochromatic light source [36]. In literature, studies of the Verdet constant changing due to temperature and sensitivity decreasing due to reflection induced retardance can be found for SF-6 glass from 1290 nm to 1315 nm [35]. Moreover, when the linear birefringence of the material is not negligible, and the sensor element is under an external stress, a temperature change from -40 ºC to 40 ºC, for instance, can change the linear birefringence by more than 1 % [37] .

Temperature compensation techniques were also developed for these types of sensors. One of them consists on changing the polarization state of the input with a waveplate of a specific retardance as presented in Figure 2.6, for diamagnetic materials. The introduced waveplate produces an opposite deviation of the sensor output with temperature, consequently compensating the Verdet constant variation [38]. For a SF57 glass, the introduction of a birefringent material with a retardace of 154º, demonstrated the temperature compensation for changes from 20 ºC to 120 ºC.

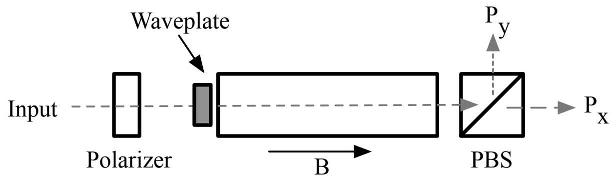

Figure 2.6 – Quadrature polarimetric detection scheme with waveplate added for temperature compensation.

Another solution is presented in [39] and requires knowing the Verdet constant dependence of the material with temperature and an optical temperature sensor. With processing, the temperature information is used to further compensate the sensor output change due to the Verdet constant. In reference [40] a solution employing the quadrature polarimetric detection scheme was developed and consists in filtering the DC part of the signal, containing only the linear birefringence and filter the AC component, which is a function of the linear birefringence and the Faraday rotation. This method involves simple arithmetic and uses the fact that the DC component of *S* (equation (2.6)) can be modified with a constant *k,* so that its temperature drift is equal to the one of the AC part

$$S' = \frac{S_{AC}}{1+k.S_{DC}} \tag{2.7}$$

For a square glass ring made of SF57 glass, operating at 850 nm, this method showed an error of 0.2 % for a temperature change from -20 ºC to 80 ºC.

Sensors using ferromagnetic materials have also been proposed for detecting very low currents. A square configuration similar to Figure 2.3 with four rods of Ga:Yig with 5 mm in length were arranged so that the optical path approximates a closed loop around a conductor with a resolution of 220 nA/√Hz (Figure 2.8). A linear response is attained up to 3 A and, saturation due to the ferromagnetic properties of the material occurs at 90 A. Moreover, hysteresis for currents above 10 A was reported [41]. A detailed review of the magneto-optic sensing parameters, including saturation, Faraday rotation per Ampere and frequency response is presented for ferromagnetic materials of YiG, Ga:YiG and another three non-commercial Iron Garnets crystals in reference [42].

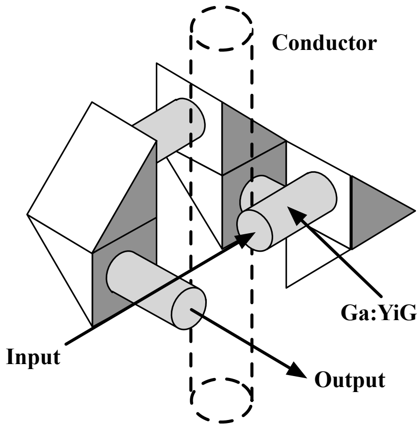

Figure 2.7 – Ferromagnetic bulk sensing head with Ga:YiG.

Commercial products using bulk materials for magnetic field measurement are available in the market. PowerSense [43] is a company having a commercial product named DISCOS (Figure 2.8 (a)), based on the sensing scheme like the one shown in Figure 2.1, which permits AC current measurement from 200 A to 20 kA. It employs a BK7 glass and it provides a maximum error of 2 % and ±2 A accuracy in the 5 A to 20 A range. Another company, AIRAK, developed an optical fiber based current sensor (Figure 2.8 (b)) for monitoring medium voltage electrical distribution lines, using the same principle of PowerSense. The sensor is very lightweight (about 1.25 lbs [0.57 kg]) and small size (about 11” × 7” × 6.25” [280 mm × 180 mm × 160 mm]). As for the technical details, the sensor meets the IEEE 36 kV insulation class, has a resolution better than 1 % f.s. (full-scale is 3 kA), an operating frequency range of 5 Hz to 20 kHz, temperature range of -40 ºC to +70 ºC, and has a full scale measurement of from 30 A to 30 kA [44,45].

.

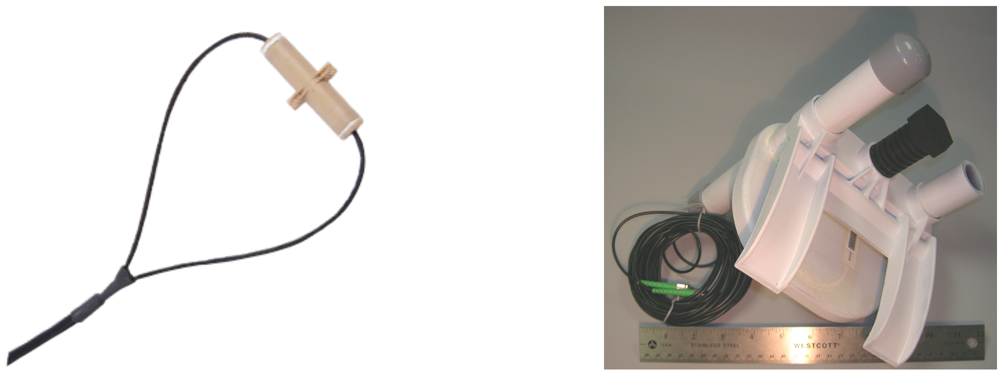

(a) (b)

Figure 2.8 – Commercial optical current sensors from (a) PowerSense [43] and (b) Airak [44].

2.2 All-fiber

All-fiber sensors use very simple configurations because the fiber can be easily coiled around the electric conductor to be measured. Also, the sensor sensitivity can be changed by simply changing the number of turns of the optical fiber around the conductor [46]. Since these kind of devices have much longer optical paths, usually using several meters of fiber, the sensors are more vulnerable to pressure and temperature gradients, mechanical vibrations and other environmental noises than smaller devices (such as bulk-optic).

Different detection schemes can be used with all-fiber optical current sensors, including polarimetric or interferometric schemes in a Sagnac configuration. Figure 2.9 shows schematically a current sensing Sagnac interferometer, which is commonly used in gyroscopes and it is sensitive to non-reciprocal effects [46]. This interferometer is interrogated by using a heterodyne detection scheme.

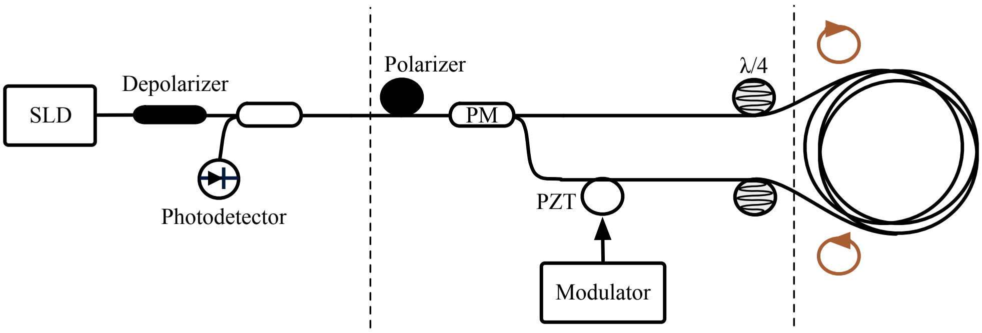

Figure 2.9 – Sagnac loop interferometer current sensor.

In this particular application, light from an optical broadband source, is first depolarized and then linearly polarized with a fiber polarizer and finally injected into the Sagnac loop with crossed quarter-wave plates (λ/4) mounted at an angle of 45º and -45º relative to the plane of polarization of the linearly polarized inputs, for the upper and lower plate, respectively. In this arrangement each of the counter propagating waves are converted to orthogonal circular states with opposite rotation directions. These two counter-propagating waves travel the Sagnac loop with different velocities, due to the circular birefringence induced by the external magnetic field. After crossing the loop they are converted back into linear polarization modes and interfere after crossing the output linear polarizer. The phase information is retrieved with the introduction of the phase modulator on the unbalanced Mach-Zehnder interferometer, which can be used to generate the phase carrier. Using either Pseudo-Heterodyne or Heterodyne processing schemes, the relative phase accumulated in the Sagnac loop, which is proportional to the magnetic field generated by the electric current on the conductor, can be recovered. Some disadvantages of using this type of interferometer include temperature and vibration dependent sensitivities.

An improved version of the above system can be done in a reflection configuration, as shown in Figure 2.10 [22,46].

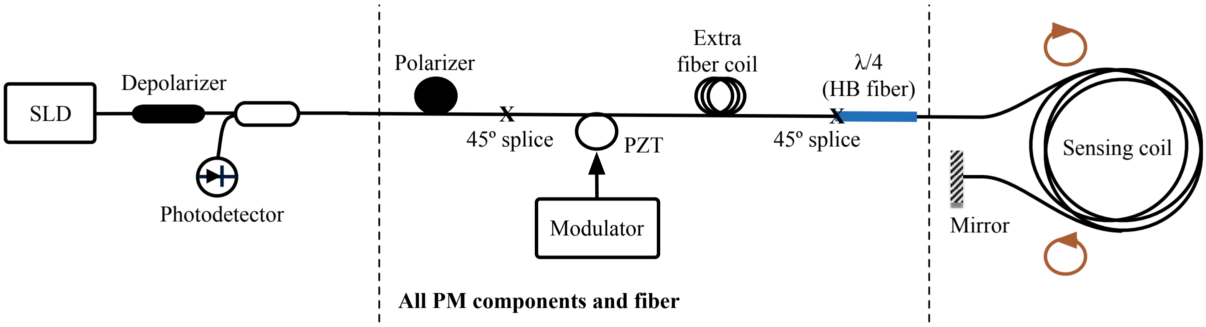

Figure 2.10 – In-line interferometer current sensor.

Between the optical source and the HiBi fiber acting as a λ/4-wave plate, the polarized light is injected at 45° into a polarization maintaining fiber (PMF). After crossing the PMF, the λ/4-wave plate which is oriented at 45° with respect to the birefringence axis of the PMF, transforms the two orthogonal polarization modes into circular polarization modes with opposite rotation directions. At the end of the fiber, reflection occurs and the reverse process occurs. However, with propagation now in the opposite direction, the same rotation direction that would be described as "right handed" for the incident beam, is "left-handed" for propagation in the reverse direction, and vice versa. The quarter-wave retarder converts the returning circular waves back to orthogonal linear waves. The new polarization directions are also interchanged, i.e., the forward waves polarized along X and Y become backward waves polarized along Y and X. At the end the phase difference proportional to the electric current is maintained. As a result of the polarization swapping at the reflector any small disturbances of the differential optical phase during forward propagation are largely cancelled on the return path. Also, due to the operation in reflection this scheme doubles the sensitivity in relation to the first one, for the same number of fiber turns around the conductor. The extra coil delay is required to increase the phase modulation efficiency.

The modulation introduced in the polarization interferometer (the length of PMF), near the 45° splice enhances the ability to detect the small phase differences, produced by small currents and these interferometric configurations require a stable optical source. Problems may occur in the phase difference introduced by the λ/4-wave plate that can have small deviations from the optimal value, which change with temperature, and therefore can change the system sensitivity [25]. However, as already mentioned, the Verdet constant is also temperature dependent. In [10] a passive compensation scheme taking advantage of both temperature dependencies is used to improve the sensor stability. It consists on introducing a phase retarder, in this case a piece of HiBi fiber, with a retardation between fast and slow axis of 100.4° rather than 90° (quarter-wave plate). The temperature dependencies of the Verdet constant and of the retarder have opposite effect on the sensor response and cancel out. Furthermore, in 2015, a similar approach was reported by Sasaki et al. [47]. In this case, a quarter waveplate made of Panda fiber with a metal coating is used. Both materials have different linear expansion coefficients ($\sim 10^{-5}$ K^{-1} and 10^{-7} K^{-1} to the metal and fiber, respectively) and therefore, different lateral stress is induced in the fiber as a function of temperature, changing the retardance of the waveplate. These effects combined with the Verdet constant variation with temperature compensate each other and a measurement error of 0.1 % in a temperature range from -40 °C to 80 °C was reported.

Both previous configurations described need PM components that are typically more expensive than the ones using standard fiber. Moreover, splices with these fibers require a highly accurate axial alignment, only possible with special splicing machine which is much more expensive than conventional ones. Therefore to avoid using PM fibers Takahashi et al. [48] proposed the Sagnac interferometer shown in Figure 2.11 requiring three depolarizers and a much more complex detection scheme with an active control of the modulation amplitude [49]. Extra fiber coils are wounded in opposite direction to reduce errors, 120 m each, to increase the time difference between clockwise and anti-clockwise light passing trough the PZT (PieZoelectric Transducer) modulator. Results showed errors of 0.2 % and its operation satisfies IEC class 0.5, with a linear response up to 100 kA.

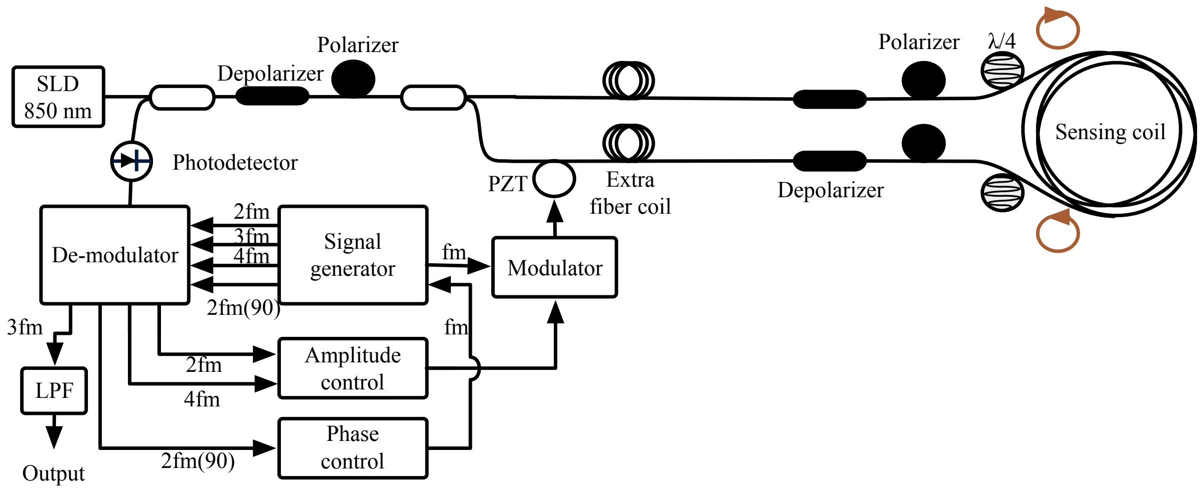

Figure 2.11 – Sagnac loop interferometer current sensor without PM components.

Another configuration using a 3×3 coupler was also reported [50]. Still, results have shown this configuration does not offer advantages over the configurations with a 2×2 coupler for electric current measurement.

Typically, standard silica fibers have a low Verdet constant when compared with bulk-optic glasses. Many studies have been done in order to increase the Verdet constant of the fibers. Materials such as flint glass have been tested and showed a Verdet constant six times higher than fused silica and much lower photo-elastic coefficient (780 times) at 830 nm [51,52]. A detailed review of current transducers using flint glass fibers can also be found in the literature [51]. The study provides specific information of the sensors (setup configurations, temperature dependence, accuracy, etc.) and the fibers used (Verdet constants, photo-elastic constants, wavelength dependence, etc.) as well as results of field tests performed. In Figure 2.12, a current sensor with flint fiber and using a quadrature polarimetric detection scheme is represented.

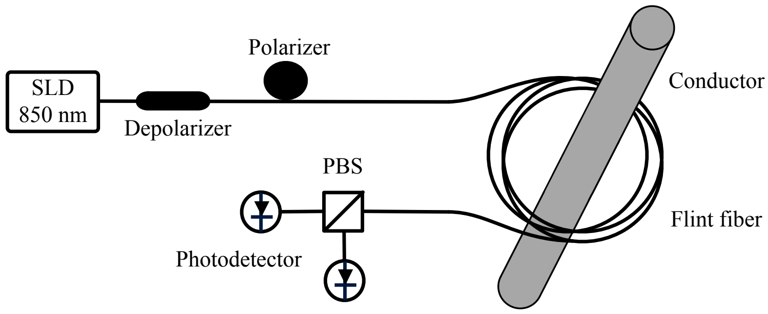

Figure 2.12 – Typical configuration of a quadrature polarimetric detection scheme using a flint sensing fiber.

A comparison between the performances of flint glass fiber and twisted single-mode fiber as a Faraday element was presented [53], and showed that the system with the flint glass fiber is more stable than the one with twisted fiber.

In 2009, a new optical glass for optical fibers with high refractive index for applications in optical current sensors was reported. The results showed that these fiber glasses could have ten times higher Verdet constant, smaller internal mechanical stress and higher refractive indices (1.6 to 2.2) [54].

Recently, a terbium-doped-core phosphate optical fiber with a Verdet constant six times larger than standard optical fibers was presented [55]. The same authors also presented in 2010 a high concentration of terbium-doped fiber with a record Verdet constant of -32 rad/(T.m) at 1064 nm, which is 27 times larger than standard optical fibers and corresponds to 83 % of the Verdet constant of commercially available crystals used in bulk optics–based isolators [56].

The most critical problem of using the fiber as the transducer is the effect of the linear birefringence that is induced by mechanical stress (when the fiber is bent for example), thermal stress, manufacture imperfections and other effects. The presence of linear birefringence significantly reduces the sensor sensitivity due to the polarization state degeneration. The linear birefringence can be neglected, however, if the circular birefringence is high enough.

A study using standard low birefringence fibers shows that when the linear birefringence is higher than 10^{-7}, the fibers are not adequate for current sensor applications [57]. The use of a twisted single mode fiber to impose a circular birefringence in the fiber has been demonstrated [58]. A similar approach and the most widely used up to now is to employ spun high birefringent fibers, which is twisted during fabrication. The method was proposed by Laming [59] and includes a complete description and equations of the sensor sensitivity as function of the fiber spin pitch (due to spun) and the intrinsic linear birefringence of the fiber. Moreover, in the same work, sensor stability was analyzed using three distinct setups with a laser source at 821 nm with quadrature polarimetric detection scheme, one in transmission and the other two in reflection, by using a conventional mirror and a Faraday rotator mirror (FRM). The more stable configurations were the ones in reflection, especially the one using the FRM as shown in Figure 2.13. A FRM is a device that works in reflection and rotates the plane of polarization of light by 90°. In this way, the state of polarization (SOP) of the forward and reflected light are always orthogonal to each other and any reciprocal SOP fluctuations that occur anywhere along the fiber are exactly compensated for, and their unwanted effects are neutralized. Fibrecore [60] is presently the main provider of such fibers, which are being incorporated in many of the optical current sensors commercial solutions available.

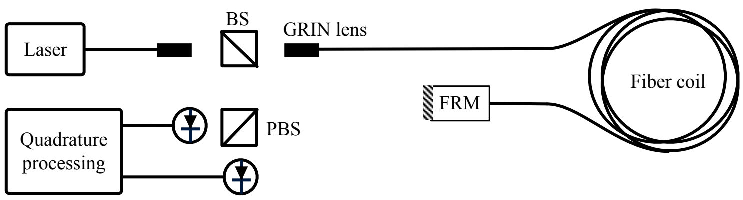

Figure 2.13 – Typical configuration of a quadrature polarimetric detection scheme in reflection, using a Faraday rotator mirror.

In order to have the maximum sensitivity, the ratio L_S/L_B has to be as small as possible, where $L_S = \lambda/\theta_S$ is the spin pitch and $L_B = \lambda/\beta$ is the beat length. Sensor susceptibility to pressure was also tested with the spun fiber (bow-tie fibercore with $L_S/L_B = 0.965$). Application of a distributed pressure along the fiber showed good stability, making possible to wound it in a 13 mm diameter with just 1 % sensitivity reduction. However, when the pressure was applied in a point load smaller than the fiber beat length, the sensitivity reduced drastically.

Furthermore, the fiber was found to be 40 dB less vibration sensitive than conventional fiber. A current resolution of 1 $mA_{RMS}\sqrt{Hz}$ was achieved using 100 turns of fiber.

Spun fibers have also been tested with an interferometric detection scheme using a broadband source at 1550 nm (15 nm bandwidth). Sensor performance showed a minimum detection limit of 70 mA/√Hz using 27 turns of spun HiBi Panda fiber with $L_S/L_B = 0.133$ [22].

A spun HiBi panda fiber acting as a quarter waveplate was also fabricated for electric current sensing to be used in an interferometric detection scheme. The quarter waveplate fabrication consists on heating (1650 ºC) and twisting a region of 0.25 m of the spun sensing fiber section with a gradual spin rate. Very good thermal stability with errors less than 0.1 % from -40 ºC to 70 ºC, were achieved [61].

Linear birefringence can also be reduced by fiber annealing process [62]. Theoretical models and experimental measurements for the Verdet constant dispersion in annealed silica based fibers have been presented for wavelengths ranging from 600 nm to 1550 nm [63].

Some methods for linear birefringence compensation in polarimetric detection schemes using reflected light propagation have been presented, such as the use of Faraday rotating mirrors in polarimetric detection schemes [59,64] or placing fiber polarization rotators [65] in the middle of the sensing coil with an interferometric detection scheme. A Faraday rotator mirror is a component that leads to a polarization shift of 90° and polarization components that propagate in one axis are coupled to the orthogonal axis, and vice-versa. Since the linear birefringence is a reciprocal effect, the phase difference introduced by the linear birefringence after propagation through the sensor full optical path will be compensated.

A sensor using reflected light propagation for linear birefringence compensation made of low-birefringent flint fiber with a very low photo-elastic constant, achieved the accuracy required for the 0.1% class of current metering transformers in the range of 1 kA [52].

It has also been shown that an FBG sensor can be made sensitive to magnetic field, if circular polarized light is used, with a sensitivity of around 200 pm/mT at 1300 nm [66]. If linear polarized light is used, the wavelength is insignificantly changed by 0.3 pm/T at

1550 nm [67]. This scheme relies on the Faraday effect to induce a slight change in the index of the fiber.

In 2011 a signal processing methodology based on artificial neural networks (ANN) using a quadrature polarimetric detection scheme in transmission was developed and tested for currents up to 1.2 kA. Acquisition includes processing signals from the optic current sensors and a thermometer, achieving higher accuracy with temperature and non-linearity compensation [68]. The great benefit of ANN is to get a transfer function for the measurement system taking in account all variables, even those from unwanted and unknown effects, providing a compensated output, after the ANN training session. An accuracy of 0.1 % was achieved under temperature variations between 22 ºC and 55 ºC.

Some optical electric current sensors are already commercially available from ABB, Alstom Grid (previous NXTphase) and Artche to measure electrical current on electrical potentials up to 800 kV with working principle identical to the one shown in Figure 2.10. The first company assures a range of operation up to 500 kA and ±0.1 % accuracy in DC measurements (Figure 2.14 (a)) [69]. Another sensor from the same company named MOCT from ABB (Figure 2.14 (b)), it also has a dynamic range from 1 A to 4 kA with accuracy performances that exceed IEC Class 0.2S and ANSI Class 0.15 S for metering applications. The system provides accurate waveform reproduction up to 100 kA. Different sensor weights, between 110 lbs (50 kg) for 72.5 kV and 410 lbs (186 kg) for 800 kV are also supplied [70].

The sensor NXCT from NxtPhase (bought by Alstom) shown in Figure 2.14 (c) for 362 kV has a dynamic range from 1 A to 4 kA with performances that exceeds the IEC Class 0.2S and IEEE Class 0.3 accuracy (0.15 %) for metering applications. The sensor is also able to measure up to 63 kA_{RMS} for short-time current (about 1 s) and accurate waveform reproduction up to 6 kHz. Different sensor weights, between 108 lbs (49 kg) for 72.5 kV and 210 lbs (95 kg) for 800 kV are supplied. The weight discrepancy is due to the isolation required and it has been showed the sensor can operate in a temperature range between -40 ºC to +55 ºC [71].

The latter company, Arteche, provides an all-fiber sensor named SDO OCT (very similar to Figure 2.14 (b)), for operation in the 100 A_{RMS} to 5000 A_{RMS} range, satisfying IEC class 0.2/0.2S This sensor works within a temperature range of -40 ºC to +55 ºC [72].

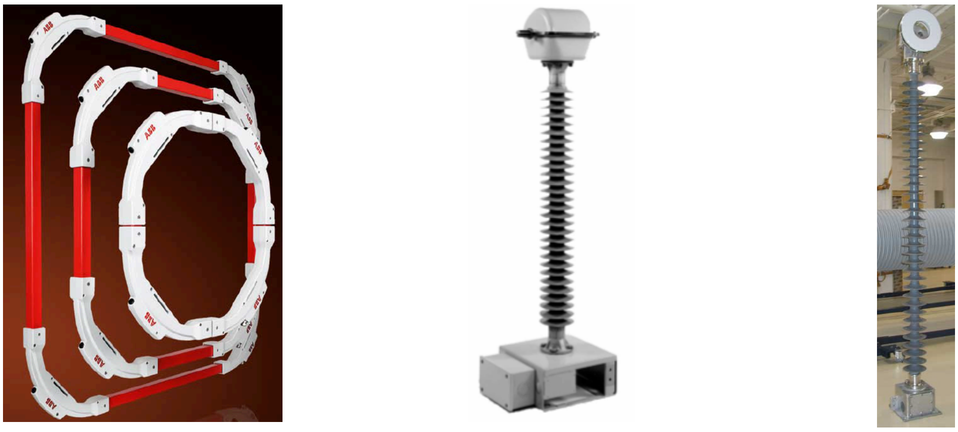

(a) (b) (c)

Figure 2.14 – (a) ABB [69], (b) ABB MOCT sensing head [70] and (c) NXCT NxtPhase for 362 kV [71].

In order to satisfy the high measurement requirements for the high power grid, advanced packing techniques for the sensing fiber coil is required, in order to avoid birefringence problems. To achieve a more stable performance, the sensing fiber must be placed without coating and inside a capillary filled with silicone oil to avoid internal friction during handling. A thin strip of fiber-reinforced epoxy serves as a robust protection of the capillary tube [10,69].

2.3 Magnetostrictive and other magnetic effects

Magnetostriction is the property that causes certain ferromagnetic materials to change shape in presence of a magnetic field [73]. This effect was first noticed in Nickel in 1842. Cobalt and iron alloys exhibit magnetostriction in the order of 10 ppm to 100 ppm (parts per million) [74].

During the 80's a great research effort was carried out for finding solutions to detect magnetic fields and/or electric current using optical fibers in combination with materials that exhibit magnetostriction effects. In 1980, Yariv et al. [75] studied the possibility of detecting weak magnetic fields by using magnetostrictive perturbation in optical fibers. A low loss optical fiber of length L with a nickel jacket suffers a longitudinal mechanical strain with a relation of -3×10^{-4} με/mT.

Other first experimental evidences of the magnetic field sensing characteristics of optical fibers jacketed with either nickel or metallic glass magnetostrictive materials was reported by Dandrige et al. [76]. Both bulk magnetic stretchers, as well as, thin films directly deposited on a single mode fiber (SMF) were analyzed. An all-fiber Mach-Zehnder interferometer was used to detect the magnetically induced mechanical changes in the optical path length that contained the magnetostrictive jacket. Figure 2.15 shows the schematic diagram of the magnetometer.

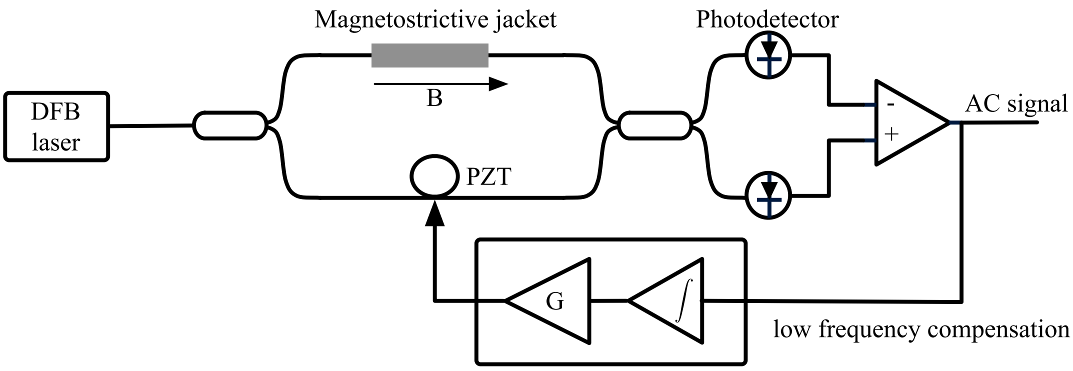

Figure 2.15 – Mach–Zehnder interferometer with a magnetostrictive jacket.

The sensor minimal detectable field achieved with the bulk nickel material was 8×10^{-9} mT/m. The response of the first generation thin film coated fiber optic sensors was about two orders of magnitude lower and was ruled by the thin-film thickness. Jarzynski et al. [77] investigated the mechanical strain induced by a weak axial magnetic field in an optical fiber with magnetostrictive jacket with different thicknesses. The sensitivity was calculated as function of jacket thickness for a variety of magnetostrictive materials.

In these configurations if the metallic cladding slips relatively to the silica fiber during thermal expansion, with time scales comparable to that of the magnetic field, the strain in the fiber core will not accurately reflect the magnitude of the field [78]. Heaton proposed a non-magnetostrictive metal-coated element (with similar thermal expansion) in the other arm of the interferometer, improving this way the response to magnetic field of fiber optic interferometers.

A SMF wounded under tension around a magnetically sensitive nickel cylindrical piece was proposed by Rashleigh with a quadrature polarimetric detection scheme as shown in Figure 2.16 [79]. The magnetic field changed the SOP of light in the fiber due to the birefringence, induced by nickel cylinder. An optical phase sensitivity of 1.76×10^{-1} rad/(mT.m) was achieved, allowing a detection of magnetic fields as small as 4.4×10^{-7} mT/m.

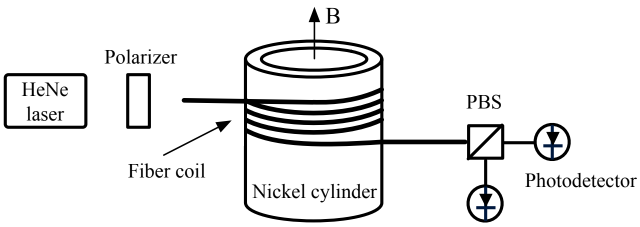

Figure 2.16 – Polarimetric detection scheme with nickel cylindrical piece.

The use of a metallic glass as sensing element for detection of very low magnetic fields was described by Koo and Sigel [80]. In their experiment, different metallic glasses were used in one arm of an all fiber Mach-Zehnder interferometer. In the presence of the magnetic field, the metallic glass increases its length and the interferometer output changes. A minimum detectable magnetic field of 5×10^{-10} mT/m was reported.

A technique for the measurement of weak DC and low frequency AC magnetic fields using an all fiber SMF magnetometer was described by Kersey et al. [81]. For the first time, the experimental scheme used, consisted in a Michelson interferometer where the two cleaved fibers ends were coated with silver film to form the mirrors. A minimum magnetic field of $\approx 10^{-4}$ T/m and $\approx 10^{-7}$ T/m at 20 Hz was detected with a bulk nickel and a metallic glass rod, respectively. Figure 2.17 represents the experimental configuration used.

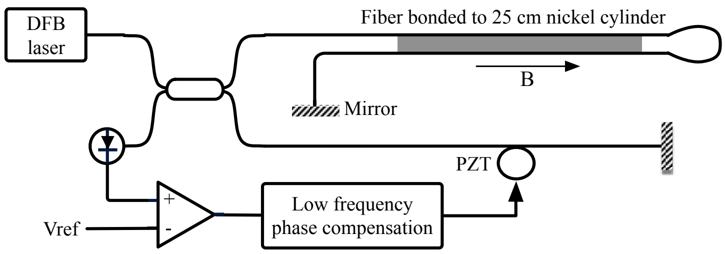

Figure 2.17 – Scheme of the all fiber magnetometer.

A fiber Mach-Zehnder interferometer passively stabilized using a 3×3 fiber coupler was used by Koo et al. [82]. The system response was examined by subjecting the metallic glass to a DC and AC fields. The sensor resolution was in the order of 1×10^{-7} mT/(m.√Hz) for a fiber length of 1 m.

The first demonstration of a closed-loop fiber optic magnetometer with dynamic magnetostrictive response was reported by Kersey et al. [83]. The sensor was capable of detecting low frequency and DC changes of magnetic field with a resolution of ≈2 nT at frequencies below 2 Hz.

One year later, the same group proposed a similar configuration, where the main difference in the magnetometer was that they kept at constant value the total local field (bias+ambient) [84]. By active-bias field stabilization they ensure that the magnetostrictive sensing element was temperature compensated, maintaining always the same operation point. This method eliminated any problems derived from the magnetic hysteresis of the metallic glass materials used (Metglass and Vitrovac). A minimum detectable field of 1×10^{-7} mT was observed over the frequency range from DC to 20 Hz using a small length of optical fiber (≈0.5 m).

In 1989, the first demonstration of the detection of magnetic fields at frequencies above 50 kHz using a fiber optic magnetometer was reported by Bucholtz et al. [85]. A Mach-Zehnder interferometer with a thick metallic glass cylindrical transducer and 31 m of fiber wounded in one of the interferometer arms was used (Figure 2.18). The technique consists in mixing two signals where the beat frequency, frequency difference between them,

($f_{TEST} - f_{LO}$) is maintained constant and a flat response up to 1 MHz is attained. The same group reported a minimum detectable AC magnetic field of 70 fT/√Hz at 34.2 kHz [86].

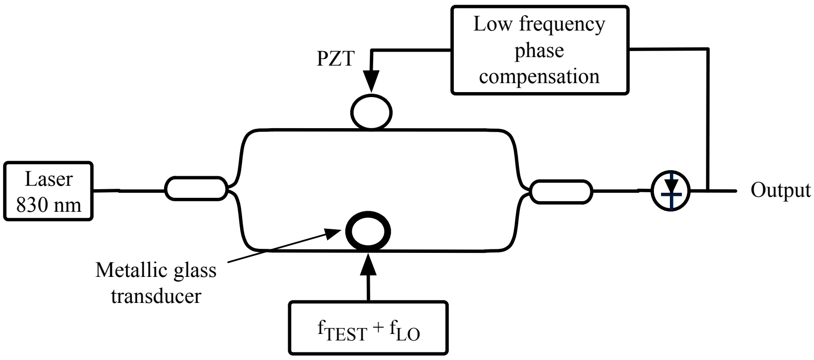

Figure 2.18 – Setup for mixing and detecting RF signals in fiber-optic magnetostrictive sensor.

Optical fibers coated with magnetostrictive ceramic films were tested by Sedlar et al. [87], by using a Mach-Zehnder interferometer operating in an close-loop configuration, where the sensor exhibited excellent linearity and good sensitivity. The materials used were magnetite, Fe_2O_3, nickel ferrite and cobalt doped nickel ferrite (NCF_2) jackets, with the later having the best response to magnetic field. They achieved a minimum detectable magnetic field of 4.02×10^{-6} mT (3.2×10^{-3} A/m) for optical fibers jacketed with 2 µm thick and 1 m long NCF_2 material.

A fiber optic sensor for measuring DC magnetic fields based on the extrinsic Fabry-Perot interferometer (EFPI) was proposed by Oh et al. [88]. A SMF and a Metglass wire magnetostrictive transducer constituted the input-and-output and reflector arms of the extrinsic Fabry-Perot interferometer (EFPI) sensor. Due to the sensor optical path geometric design, it showed a low vibration sensitivity and high compensation of thermal induced drift (better than 99%) for temperature fluctuations between 25.9 °C and 37.3 °C.

Pérez-Millán et al. [89] demonstrated a new approach for measuring electric current on high voltage systems. The fiber optic sensor employed the intrinsic magnetostriction of the ferromagnetic core of a standard current transformer and was interrogated with a Mach-Zehnder interferometer. In this setup the number of fringes during one period of the waveform is proportional to the current amplitude. Figure 2.19 represents the experimental configuration.

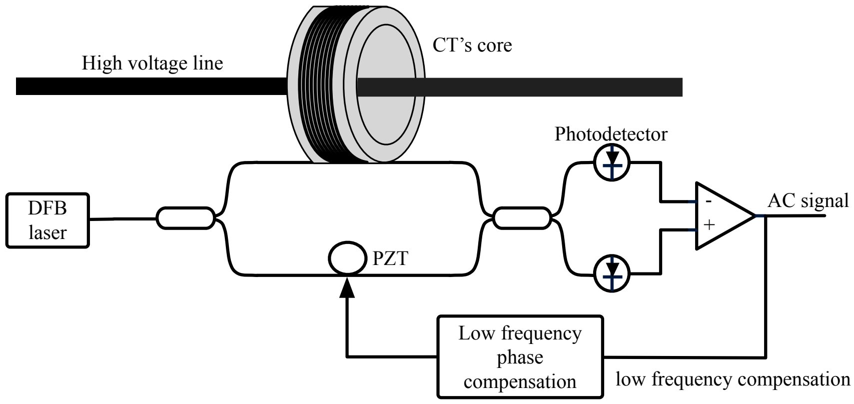

Figure 2.19 – Mach–Zehnder interferometer for measuring electric current on high voltage systems.

A magnetostrictive sensor capable of measuring both AC current and temperature using a single FBG bonded to a magnetostrictive material (unknown) of high magnetostriction was proposed by Reilly et al. [90] to withstand temperatures up to 100 °C. The detection system consists of a sawtooth modulated Fabry-Pérot tunable filter thermally stabilized using thermoelectric cooler controller. A bias magnetic field is induced via permanent magnetics to increase sensitivity to AC fields.

More recently, Djinovic et al. [91] presented results of measurement of AC and DC magnetic fields by using a fiber optic interferometric sensor for structural health monitoring. The principle of operation was based on changes in the optical path length of the cavity between a magnetostrictive wire and a fiber optic tip. The sensing configuration consisted of a Michelson fiber interferometer using a 3×3 single mode fiber coupler. It was possible to detect the instant separation between the wire and fiber end with an accuracy of 50 nm corresponding to a magnetic field in a range of 50 nT to 800 μT.

2.3.1 Terfenol-D

Since 2000, an intensive investigation on an alloy material with high magnetostriction coefficient (Terfenol-D) has been reported on literature. Terfenol-D is said to produce "giant" magnetostriction, with strains 100 times greater than classical magnetostrictive materials such as iron. Magnetic domains in the crystal rotate when a magnetic field is applied, providing proportional, positive and repeatable expansion in microseconds [89]. A rod of Terfenol-D with $Tb_{0.27}Dy_{0.73}Fe_2$ composition has a magnetostriction of 1500 ppm with 315 mT. However, depending on the composition a maximum magnetostriction of 2000 ppm can be reached [74].

The first work combining Terfenol-D alloy with optical fiber sensors to measure static magnetic fields was reported by Mora et al. [92]. The magnetostrictive sensor with temperature compensation scheme was composed by two different alloys with similar thermal expansion coefficient, being one of them Terfenol-D and the other Monel 400. The mechanical expansion of both materials due to temperature and magnetic field variations was detected by the two FBGs attached. The spectral difference between the two Bragg wavelengths was proportional to the amplitude of the magnetostriction, and the wavelength shift produced by the grating bonded to the non-magnetic alloy (Monel 400) was proportional to the temperature variation. For applied magnetic fields smaller than 59 mT a linear response of the fiber sensor was verified. The spectral sensitivity in this range was independent of temperature, having a value of $2.31 \pm 0.05 \times 10^{-10}$ nm/($A^2.m^{-2}$).

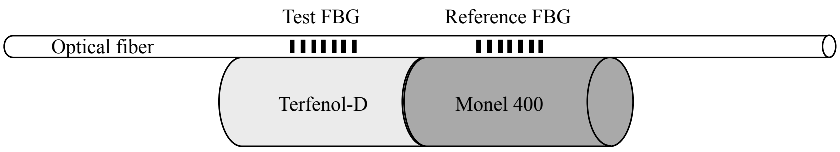

Figure 2.20 – Magnetostrictive sensor with temperature compensation proposed.

In order to compensate the temperature effects in the FBG based on magnetostrictive materials, two simple techniques were demonstrated by Yi et al. [93]. The first technique consisted of two FBGs placed perpendicular to each other and bounded onto a single Terfenol-D layer material. The second technique, two FBGs were stacked onto two different magnetostrictive bars (Terfenol-D and nickel) set physically parallel with each other. The materials used had similar thermal expansion coefficients but with magnetostrictive coefficients of opposite signs. The two techniques were capable of measuring the magnetostrictive effects with temperature insensitivity. The sensitivities due to the magnetic field were 2.44×10^{-4} nm/mT and 1.8×10^{-4} nm/mT, for the first and second techniques, respectively.

Li et al. [94] demonstrated a magnetic field sensor based on dual FBG configuration consisting essentially in a rod of Terfenol-D attached to the optical fiber. One of the gratings was fixed on both ends of the magnetostrictive alloy, while the other was only attached on one point, being the other end free to move. The configuration of dual FBGs was employed for point measurement reference and for easy temperature compensation. The maximum sensitivity achieved was 18 pm/mT when the applied magnetic field was smaller than 70 mT, decreasing the sensitivity for higher magnetic fields.

In 2006, Mora et al. [95] presented a fiber optic AC current sensor for high voltage lines based on an uniform FBG mounted on a Terfenol-D piece. An innovative way of processing the optical signal from the sensing head allowed a simultaneous measurement of temperature and the AC current. The first physical parameter was coded on wavelength shift, while the second one was coded on the amplitude of the signal. The sensor could also operate at long distances with capacity to be multiplexed.

Also a sensor for simultaneous measurement of AC current and temperature was reported by Reilly et al. [90]. The device was composed of a magnetically biased Terfenol-D piece fixed to one FBG (Figure 2.21). The sensor was capable of measuring AC current at temperatures from 18 ºC to 90 ºC. The nonlinear effects originated by the magnetostrictive alloy were identified and methods for compensating these effects were proposed.

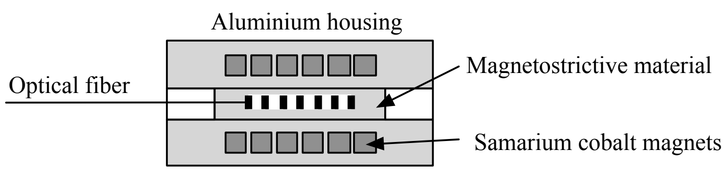

Figure 2.21 – FBG with magnetostrictive material for AC and temperature measurement.

A hysteresis compensation technique for a DC magnetic field sensor, containing a magnetostrictive alloy device, was presented by Davino et al. [96]. The sensing head integrated a rod of Terfenol-D and a FBG. Due to the nonlinear effects taking place in such materials, the magneto elastic material was accurately modeled in order to compensate for hysteresis, improving the sensor performance.

In 2009 and for the first time, a fiber optic magnetic field sensor with a thin film of Terfenol-D instead of the bulk magnetostrictive materials was reported by Yang et al. [97]. By magnetron sputtering deposition process, Terfenol-D thin films were deposited on etched FBGs. Two methods to improve the sensitivity were demonstrated. In one, the magnetostrictive alloy was deposited over different diameters of cladding-etched FBGs. The maximum sensitivity response to magnetic field was 0.95 pm/mT for an 85 µm diameter sensor. The other method consisted on coating FBGs with a layer of magnetostrictive alloys (FeNi and Terfenol-D) and a multilayer with both materials. The multilayer has the highest sensitivity of 1.08 pm/mT. In this experiment, the authors not only reduced the dimensions of the sensor, but also improved the sensitivity to magnetic field.

Liu et al. [98] proposed a transducer element composed by a mix of Terfenol-D particles with spurr epoxy, improving 60 times the sensitivity in respect to traditional monolithic Terfenol-D rods. The interrogation technique consists on illuminating the FBG with a tunable laser optical source, adjusted to the negative slope of the FBG spectrum. A photodetector is used to read the amplitude changes in the reflected signal, when a AC magnetic field is applied.

Recently Chen et al. [99] presented a quasi-balanced passive interferometer with a 3×3 coupler, where in one of the arms a loop of 82 mm and 115 fiber turns are stretched by a Terfenol-D rod with a sensitivity of 69.83 mrad/µT, providing a maximum resolution of 2.14 nT/√Hz at 200 Hz.

2.3.2 Magnetic fluid

In 2001, Yang et al. [100] investigated the physical mechanism of the optical transmission of magnetic fluid films under magnetic fields. Originally dispersed, the magnetic particles agglomerated forming magnetic columns in the presence of the magnetic field. The liquid phase was transparent, whereas the columns were opaque. Therefore, the liquid phase dominates the optical transmission of the magnetic fluid film. When the magnetic field strength was raised more columns were formed leading to a decrease in the optical transmission. Later on, the same group investigated the refractive index of the magnetic fluid film and found it to be magnetically modulated in the presence of an external magnetic field [101].

In 2007 Liu et al. [102] reported a magneto optic tunable filter based on a long period fiber grating (LPG) coated with magnetic fluid as surrounding media (Figure 2.22). Applying a variable magnetic field, the center wavelength of the attenuation band of LPG was shifted by about 7.4 nm with a field of 166.1 mT. The refractive index dependence of magnetic fluid on the external magnetic field intensity was measured exhibiting a good agreement with simulation results.

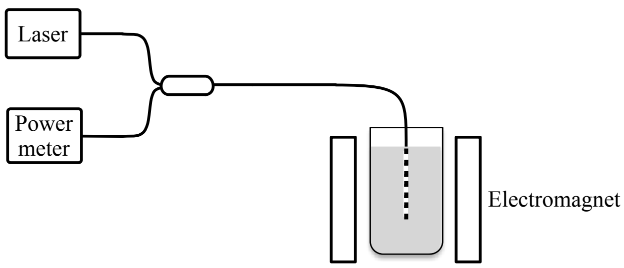

Figure 2.22 – Magneto optic tunable filter based on LPG immersed in magnetic fluid.

A fiber optic current sensor based on the magnetic fluid was developed by Hu et al. [103]. The magnetic fluid was used as the surrounding medium in a Fabry-Pérot (FP) resonant cavity. The refractive index characteristic of the magnetic fluid suffers variations due to the external magnetic field and the current was measured by the output wavelength of the FP fiber sensor. A signal demodulation method using a FBG wavelength measurement system was proposed. The results indicated a good linearity and, the thickness and initial concentration of the magnetic fluid affected the performance of the sensor.

Dai et al. [104] investigated a novel fiber optic sensor based on magnetic fluid and etched gratings. The nanoparticles of Fe_3O_4 (the magnetic fluid used) were injected into capillaries containing etched FBGs acting as sensing elements. The grating with smaller diameter (8.5 μm) exhibited a wavelength shift of 86 pm for a magnetic field of 25 mT, being the most sensitive. Experimental results showed a reversible response to magnetic field under 16 mT.

A magnetic field sensor consisting of a photonic crystal fiber and small amount of Fe_3O_4 magnetic nano-fluid trapped in the cladding holes of a polarization maintaining photonic crystal fiber were reported by Thakur et al. [105]. It was demonstrated that magnetic field of few mT can be easily and very well detected with a high sensitivity of 242 pm/mT.

Later on, a magneto optic modulator with a magnetic fluid film inserted on a Sagnac fiber interferometer was proposed by Zu et al. [106]. When the magnetic field was applied, the magnetic fluid exhibited a variable birefringence, leading to phase and polarization state variations.

Zhao et al. [107] reported the use of hollow core photonic crystal fiber (PCF) in the fabrication of the cavity of the FP sensor, which exhibits low transmission losses and insensitivity to temperature variations. The core of the fiber was filled with magnetic fluid allowing this way its use as a magnetic sensor (Figure 2.23). A shift of 5.5 nm of the pattern fringes was achieved for 28 mT.

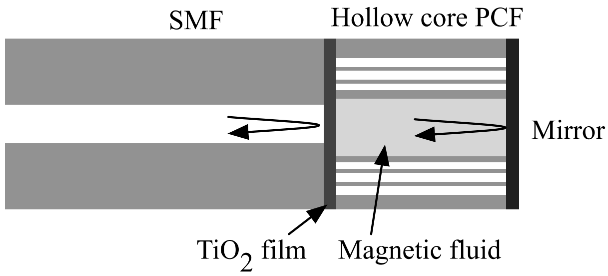

Figure 2.23 – Structure diagram of magnetic filled HC PCF FP sensor.

A microfiber knot resonator with magnetic fluid (water-based Fe_3O_4) was proposed by Li et al. Results have shown a resonance shift of 100 pm for 60 mT. Moreover, the sensor responding to the 50 Hz alternating magnetic field was also experimentally investigated, and a minimal detectable magnetic-field strength of 1 mT was successfully achieved [108].

Another sensor based on a tapered PCF coated with ferrofluid was proposed. It consists of a section of tapered PCF, which is spliced between two single-mode fibers with a waist diameter of 24 μm. The ferrofluid is filled in the capillary to coat the PCF taper. Experimentally, the refractive index (RI) of the ferrofluid increased under increasing magnetic field intensity with a sensitivity of 4×10^{-4} RIU/mT [109].

2.3.3 Sensing Fiber lasers

According to literature, optical fiber lasers can also be used for magnetic field sensing. Typically, the magnetic field disturbs the laser cavity by introducing birefringence and therefore the laser orthogonal modes are also affected. Moreover, the cavity mirrors, typically FBGs, can also be strained, changing the Bragg wavelength and consequently the laser wavelength emission.

In 1996 Park et al. [110] presented an erbium doped fiber laser. The cavity consisted of two mirrors, one conventional and the other a FRM (Faraday Rotator Mirror) to ensure temperature and strain stability. The magnetic field has to be applied near the output mirror where a non-reciprocal circular birefringence is induced and a linear analyzer following the laser output is used to interfere both circular polarizations with opposite rotation directions. The polarization mode beat is proportional to the magnetic field and is read using a fast photodetector and a spectrum analyzer.

Another configuration based on the Lorentz force was reported by Cranch et al. [111]. These sensors require another current carrying conductor (few milliamps) that will experience deformation in the presence of an orthogonal magnetic field. Although no hysteresis was observed, the deformation induced was very small; A Distributed feedback laser (DFB), with a π-phase shift FBG written in Er^{3+} fiber, and the wavelength changes are read with a Michelson interferometer with 25 m of optical path imbalance, as shown in Figure 2.24. Two Faraday rotator mirrors in the interferometer are used to compensate polarization-induced signal fading. A minimal detected field of 1.5 $\mu T/Hz^{1/2}$ was calculated.

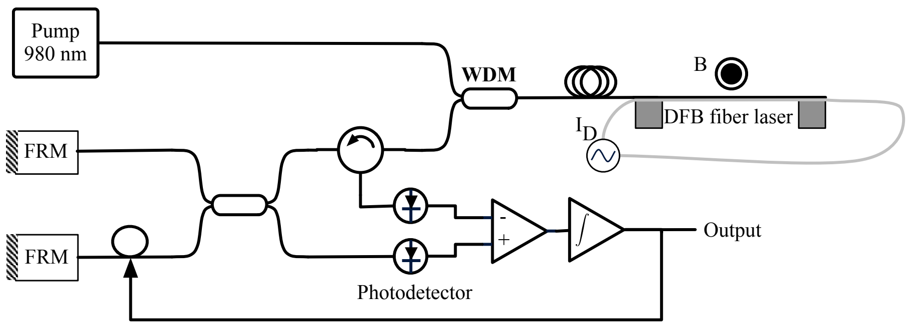

Figure 2.24 – DFB fiber laser magnetic field sensor based on the Lorentz force.

Another alternative reported consists on using a 60 mm long cavity laser with one longitudinal mode and two orthogonal polarizations [112]. Measurement of the beat frequency between these two polarizations is proportional to the laser birefringence and changes according to pressure exerted in the cavity due to the Lorentz force. Results showed relatively good linearity for magnetic fields between 4 and 20 mT.

A distributed sensor was firstly reported in 2014 [113] and consists in wounding a standard single mode fiber around a nickel wire. In the presence of the magnetic field the nickel wire stretches and the phase of the Rayleigh backscattered light changes according to it. A passive Mach-Zehnder interferometer with a 3×3 coupler and an OPD (Optical Path Difference) of 2 m (1 m spatial resolution) was used to read the phase changes.

2.4 Hybrid

This type of device tries to explore the combination of the optical fibers and the conventional current transducers. The main advantage is that the need for insulation is greatly reduced due to the intrinsic insulation provided by the fiber optic itself, therefore the overall cost of the insulation is reduced when compared with conventional current transducers. Sensing systems using hybrid devices consist mainly of a conventional electrical or electronic current sensor, a current transformer (such as Rogowski coil) or a photo-electronic device, but interrogated by an optical fiber system. The principal element of this combination is an electro-optic converter which transforms electrical current modulation into optical modulation [13].

For interrogating these sensing configurations, diverse optical modulation schemes were reported during last years, such as intensity modulation [114], frequency modulation [115], optical phase modulation [116], polarization modulation and chromatic modulation [13]. In Figure 2.25 an intensity modulation scheme is present and consists in converting the AC current signal, provided from the current clamp, into an AC optical modulated signal. The fiber is only used to transport the optical signal until the signal processing unit.

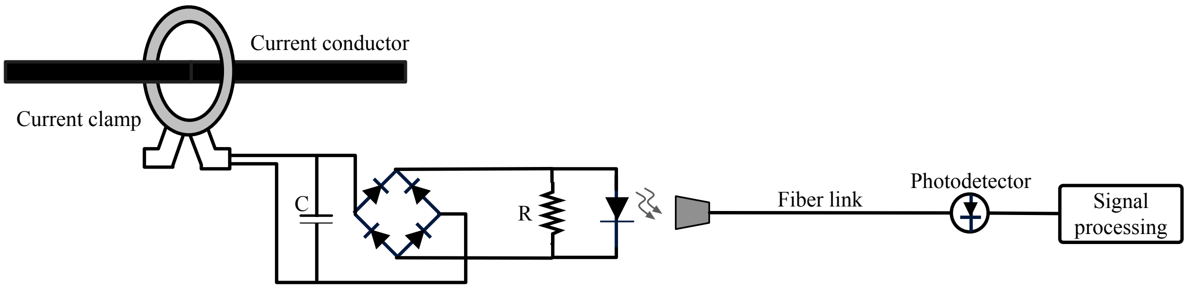

Figure 2.25 – Hybrid current sensing based on optical intensity modulation.

Another configuration, based on optical phase modulation is present in Figure 2.26. It uses a conventional CT as the primary transducer and a fiber optic Michelson interferometer acting as a secondary sensor. A high-wattage resistor is connected to the output of the secondary of the CT to convert the current into a corresponding voltage signal, which is then applied directly to the piezoelectric cylinder. This system works in a range up to 3000 A, providing an accuracy of 1 % and a frequency response up to 10 kHz [13].

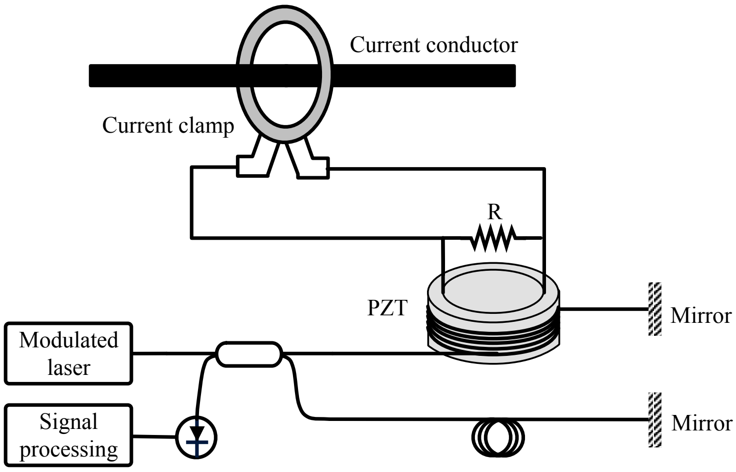

Figure 2.26 – Hybrid current sensor based on optical phase modulation.

2.5 Summary

In this chapter a complete description of the optical current sensors has been given, showing advantages and disadvantages of each group. In the industry, configurations employing bulk materials and particularly all-fiber sensors are the only ones commercially available for high power systems, providing better performances and depending on the configuration, immunity to external magnetic fields. In Appendix A it is summarized the main characteristics of the optical current sensors presented along the state of the art.

Typically, in Bulk configurations, the main advantage is the use of optical materials with low birefringence and low elasto-optic coefficient which enables the possibility to develop compact and portable sensing heads. These sensors are more robust when compared to all-fiber ones, being more protected against mechanical and thermal gradients and vibrations. Nevertheless, the all-fiber ones, provides the best performances of all, but with more complex settings due to the sensing coil protection requirement. Furthermore, its installation usually requires the interruption of the high power line. The third category comprises magnetostrictive sensors which are typically very compact configurations but with some intrinsic limitations. Indeed, magnetostrictive materials typically provide low dynamic range and also susceptibility to external magnetic fields. The latter group of sensors was the hybrid type, combining traditional CTs with optical fibers. The objective of these kind of sensors was to construct an interrogation system that takes advantages of the high level of electrical isolation offered by optical fibers and avoid difficulties associated with birefringence. A very important issue regarding hybrid sensors is that they can be used as a first step to start implementing optical current sensors in the industry, before all optical current sensors can be further developed, conforming to the industry requirements.

In order for this technology to be widely used in the future, some challenges still persist and need to be addressed, namely the development of spun HiBi fibers with higher Verdet constant, temperature compensation and long-term stability.

Chapter 3 Clamp-on optical current sensor

A clamp-on optical current sensor prototype for metering and protection applications in high power systems was developed and characterized. The system is based on the Faraday effect in a low birefringence, high Verdet constant, 80 mm long SF57 Schott glass prism. It is incorporated in a nylon encapsulation casing, suitable for clamp-on application in the power line. The sensor operation was tested at 630 nm, 830 nm and 1550 nm in order to access its applicability in remote interrogation via fiber links. The polarimetric bulk optical current sensor also was theoretically studied, and the effects of different sources of error considering practical deployment were estimated. In particular, the interference from external magnetic fields in a tree-phase system was analyzed. The work presented along this chapter was developed within an international project between Brazil and Portugal named TECCON.

3.1 Project TECCON

The project TECCON – "Fiber optic sensors technology for supervision, control and protection of electrical energy systems", had as main motivation the development of new systems based on optical sensors for monitoring and optimization of electric power networks in high voltage operation. Fiber optic sensor technology was chosen for its versatility, immunity to electromagnetic interference, low weight and remote monitoring capabilities; all appealing features for monitoring in real time, various quantities relevant for the operation of power systems.

Particularly TECCON intended to promote technological advances capable of providing network operators with tools to estimate in real time the load status of the transmission lines, allowing their most efficient and safe use. In this context, it was proposed the development of sensors for measuring in real time the temperature of the conductors, the state of the catenary and the electric current flowing in the conductor. Combination of these three measurements should provide a more detailed analysis of the load passing through the conductor. Moreover, it was also recommended the development of methods, algorithms and computer programs able to associate readings collected from the electric power grid, in order to identify and describe particular situations allowing to take prevention and optimization actions. In this context, the project included the development of an inclinometer, optical current and vibration sensors to monitor the power transmission line, and supervisory software system. The work developed in this thesis was, in the context of the project, focused, in particular, on the development of optical current sensors and a vibration sensor.

In the project different teams from Portugal and Brazil worked jointly, including UFPA (*Federal University of Pará*), Institute of Physics Gleb Wataghin of Unicamp, the institute *Tecnológico de Pesquisa da Baixada Santista* connected to the University *Santa Cecília* (UNISANTA) and INESC TEC - Institute for Systems and Computer Engineering. Furthermore, the client company, the TBE (*Transmissoras Brasileiras de Energia*) GROUP, supervised the progress of the project.

3.2 Sensing head configuration

The primary area of investigation of the project consisted on the development of new fibers for all-fiber current sensors. However, fiber fabrication is a complex process, subjected to many stringent lab conditions. This way a simpler and more versatile configuration, was necessary, for the project preliminary studies. Therefore, in order to ensure a working prototype to be available during the project span, a simpler setup was chosen. The configuration consisted on using a bulk optical glass as the sensing medium, allowing the possibility to be installed in the high power line, without interrupting it and also provide the chance to detect transients, which occur in the frequency range of tens to hundreds of kHz. For this prototype, a single prism of a diamagnetic material with high Verdet constant, possessing low intrinsic linear birefringence and low elasto-optic coefficient was selected for the sensing head [38]. The latter parameter was crucial in the prototype development, allowing to project an enclosure for the sensor, without introducing linear birefringence in the optical glass, due to pressure. Furthermore, the quadrature polarimetric detection scheme, already described in the state of the art, was also employed to ensure better performance, having a common noise rejection and a response independent off the optical power.

In Figure 3.1 it is presented a schematic representation of the bulk optical current sensor developed. Light from a depolarized broadband source is injected into the sensing head through a SM GRIN lens. The input polarizer is oriented at ±45° in relation to the output polarizing beam splitter (PBS) in order to operate with the highest sensitivity. While propagating through the 80 mm SF57 prism, the plane of polarization of the light rotates in the presence of a magnetic field. A high reflectivity mirror at the end of the glass reverses the direction of propagation, and the Faraday rotation accumulates due to its non-reciprocity. At the end, a beam splitter (BS) reflects the radiation towards a polarizing beam splitter (PBS) that separates the two orthogonal polarizations in two distinct outputs, which when combined produce a signal independent of undesirable optical power fluctuations. The two outputs are collected using two multimode GRIN lens instead of SM, becoming less susceptible to misalignments and collecting larger optical signals. To maximize the Faraday rotation the conductor must be placed perpendicularly and centered in relation to the SF57 prism as shown in Figure 3.1.

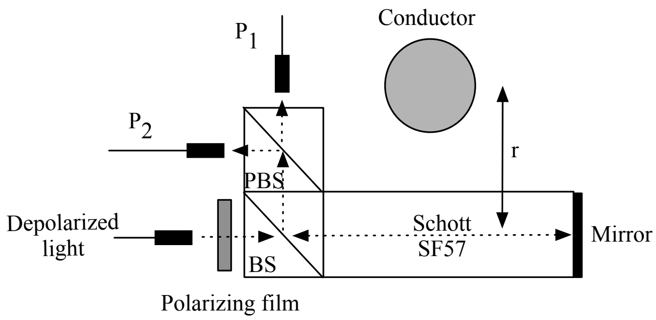

Figure 3.1 – Sensing head configuration.

The SF57 glass was chosen for having a high Verdet constant, low birefringence and a nearly zero elastic-optic coefficient. The Verdet constant of SF57 from 400-700 nm can be found in [19] (for a source at 650 nm is 21 rad/T.m, ~5.5 times greater than that of silica). To access the usability of the sensor with telecom based fiber links, the Verdet constants for 830 nm and 1550 nm are estimated next, based on the experimental results.

To estimate the sensor capability for monitoring transient signals, it is important to have an idea of its intrinsic bandwidth. In the optical domain, the maximum bandwidth is limited by the light propagation time inside the SF57, providing a maximum bandwidth of ~1 GHz. In this calculation we considered the refractive index of the Schott SF57 as 1.82164 with the sensor operating at 830 nm and a length of interaction of the light with magnetic field of 160 mm (due to reflection). In practice the sensor bandwidth will be therefore limited only by the characteristics of the optoelectronics components, namely the photodetectors and the sampling frequency.

3.2.1 Sensor transfer function

Using Jones formalism it is possible to obtain an analytical expression for the output response of the sensor, by defining a matrix for each component of the sensor. In a medium having both linear birefringence and circular birefringence induced by Faraday effect, the corresponding propagation matrix can be found in equation (1.11). Considering the configuration presented in Figure 3.1, the quadrature signals, after detection with a photodetector, are described by

$$\begin{aligned} S_1 &= |P[+\alpha].BS.M.F[-\theta_F].M.V[\theta_F].BS.E_{in}|^2 \\ S_2 &= |P[-\alpha].BS.M.F[-\theta_F].M.V[\theta_F].BS.E_{in}|^2 \end{aligned} \tag{3.1}$$

where the different matrixes represent a polarizer $P[\alpha]$ at an angle α, a beam splitter BS, a lossless mirror M and the sensing Faraday material $F[\theta_F]$. E_{in} stands for the vector representing the input polarization state. Assuming no linear birefringence is present

$$\begin{aligned} S_1 &= \frac{1}{16}E_0^2\left(1+\sin(4\theta_F)\right) \\ S_2 &= \frac{1}{16}E_0^2\left(1-\sin(4\theta_F)\right) \end{aligned} \tag{3.2}$$

These equations demonstrate that only 1/16 of the depolarized source power reaches each output. Applying the quadrature processing, a normalized output, independent of the input optical power is obtained

$$S = \frac{S_1\text{-}S_2}{S_1\text{+}S_2} = \sin[4\theta_F] \approx 4\theta_F \tag{3.3}$$

If linear birefringence is considered, the above equation becomes

$$S = 4\theta_F \frac{\sin\left[\sqrt{(\beta L)^2 + (4\theta_F)^2}\right]}{\sqrt{(\beta L)^2 + (4\theta_F)^2}} \tag{3.4}$$

This equation shows that in the presence of linear birefringence, the sensitivity is reduced. In the SF57 material the linear birefringence is residual with 0.38 rad/m at 633 nm and can be shown to have a negligible effect. Furthermore, the material possesses very small elasto-optic coefficient but its Verdet constant has a normalized temperature dependence at 633 nm of *[d(V.L)/(dT)]/(V.L)* = $1.35 \pm 0.08 \times 10^{-4}$ K^{-1}, corresponding to a drift of 0.0135 %/ºC of the Verdet constant [38,117].

In a high voltage environment, the measurement of the current implies the measurement of the magnetic field (*B*) due to the current passing through the conductor. Considering a sensing head of length *L*, centered and perpendicular to the conductor axis as shown in Figure 3.2, the amplitude of the parallel magnetic field intensity along the light propagation path is described as

$$B_p = B.\cos(\alpha) \tag{3.5}$$

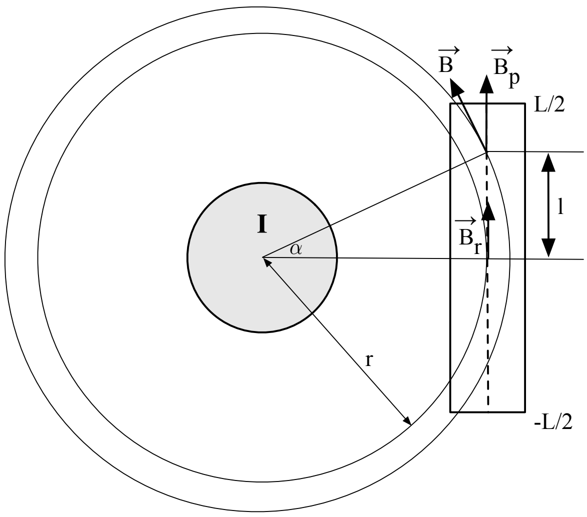

Figure 3.2 – Schematic of the magnetic field along the sensing head.

Considering that the magnetic field amplitude along a radius *r* is described as

$$B_r = \frac{\mu_0 I}{2\pi r} \tag{3.6}$$

where μ_0 is the vacuum permeability, the magnetic field intensity along light propagation is then

$$B = \frac{\mu_0 I}{2\pi\sqrt{r^2+l^2}} \tag{3.7}$$

Replacing equation (3.7) into (3.5)

$$B_p = \frac{\mu_0 I.r}{2\pi(r^2+l^2)} \qquad -L/2 \leq l \leq L/2 \tag{3.8}$$

and the resulting Faraday rotation expressed as $\theta_{Ft} = \int_{-L/2}^{L/2} V.B_p.\,dl$, is then

$$\theta_{Ft} = \frac{V\mu_0 I}{\pi}\,\mathrm{ArcTan}\left[\frac{L}{2r}\right] \tag{3.9}$$

In this equation *V* is the Verdet constant in rad/T.m, *L* is the SF57 prism length and *I* the current passing through the conductor, at an *r* distance, in relation to light propagation.

Since this sensor does not make a loop around the conductor it is sensitive to external magnetic fields. Nevertheless, for application in a three-phase electric grid, having a well known disposition, the errors can be estimated and offset using advanced signal processing. Moreover, strategic positioning of the sensors and shielding may be applied if necessary [118]. However, a theoretical analysis of the interference between conductors will be presented later on, in this chapter. Still, the perpendicularity and the distance of the sensing head in relation to the conductor needs to be maintained strictly constant. This can be attained through a suitable clamping system, with a robust fixation to the conductor. When the conductor is moving, all the system moves together with it, keeping the relative position of the sensors and the conductor unaltered. Due to the intrinsic large bandwidth of the sensor, harmonics and other superfluous noise present in the primary current, within the system bandwidth, can be detected and characterized. Nevertheless, filtering can be applied at the detection stage for measurement of the AC component of the nominal current.

3.3 Experimental results

A portable prototype comprising a light weight sensing head and a portable interrogation unit connected by a 20 m fiber optic cable were tested to assess their viability as a versatile metering and protection system in high-power grids. In Figure 3.3 it is shown the complete setup used for the experimental test of the prototype. The processing unit contains an SLD (Super Luminescent Diode) source and a depolarizer, used to excite the sensing head via a single mode fiber. For detection of the incoming optical signals, modulated by the magnetic field, two photodetectors with pre-amplification are used. A USB DAQ 6363 board is used for digital acquisition of the detected signals. Further signal processing is carried out in the digital domain using a PC and a specially developed LabVIEW program.

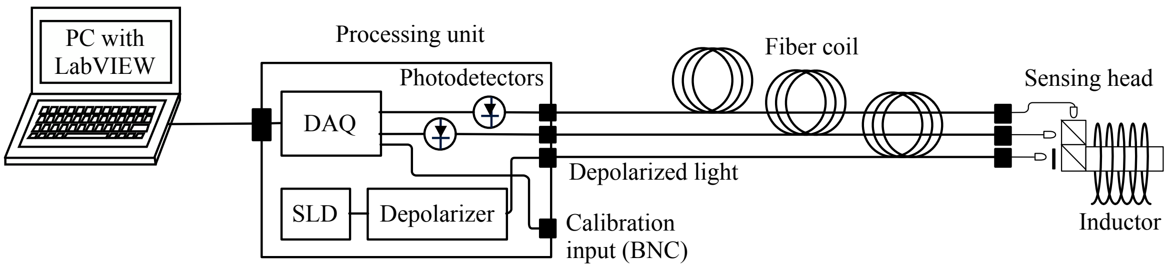

Figure 3.3 – Setup for magnetic field measurement.

3.3.1 Sensitivity in relation to the angle between input and output polarizers

A preliminary evaluation was made in order to access the tolerance of the sensing system to slight misalignments between the input and output polarizers. Considering their relative angle to be a generic angle α, equation (3.3) becomes

$$S = \cos[2\alpha - 4\theta_F] \tag{3.10}$$

Also, assuming a null Faraday rotation, the maximum sensitivity is accomplished for $\alpha_{max} = \pm 45$ degrees, as shown in Figure 3.4. Any deviation from this angle will result in decreasing sensitivity. The susceptibility of the sensor sensitivity according to misalignments of the input/output polarizers was tested with different optical sources and for a range of relative angles of $\alpha_{max} \pm 45$ degrees, showing no dependence on the optical source, including a DFB laser at 1570 nm, an amplified spontaneous emission (ASE) and a C+L band source (1530 nm until 1625 nm). For deviations between -9º and 9º, the resulting decrease in sensitivity was less than 5 %. However, out of this range, the sensitivity decreases rapidly. Therefore, since is it straight forward to ensure the alignment of the polarizers to less than a degree, this was not considered a critical setting of the sensor.

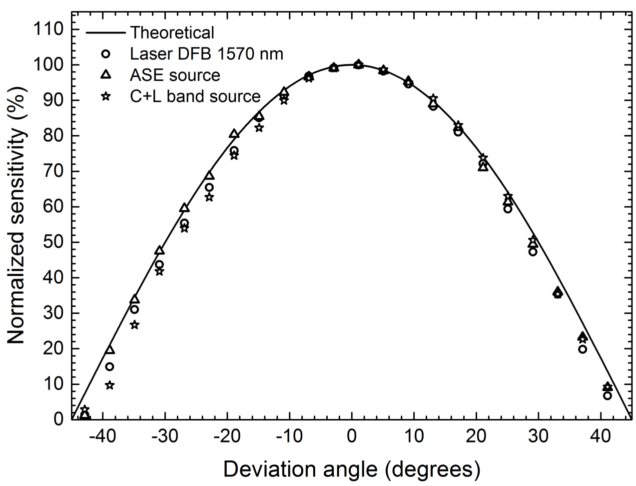

Figure 3.4 – Normalized sensitivity as function of the ideal angle between input and output polarizers, for different optical sources.

3.3.2 Sensor response at different frequencies

The sensor bandwidth at different frequencies was also investigated by submitting the sensing head to sinusoidal magnetic fields of 50 Hz, 60 Hz, 100 Hz, 250 Hz and 400 Hz. The magnetic field was generated with an inductor, a function generator and a current amplifier. For each frequency, the optical AC response was recorded, while incrementing the magnetic field amplitude, during 30 s steps (Figure 3.5 (a)). The sensor output provided a linear response as shown in Figure 3.5 (b). The latter plot was obtained by considering the average value measured at each applied current step. Due to practical limitation of the electronic components, the highest frequency tested was 400 Hz, nevertheless, considering the sensor intrinsic characteristics, the bandwidth will only be limited by the specification of the detection electronics.

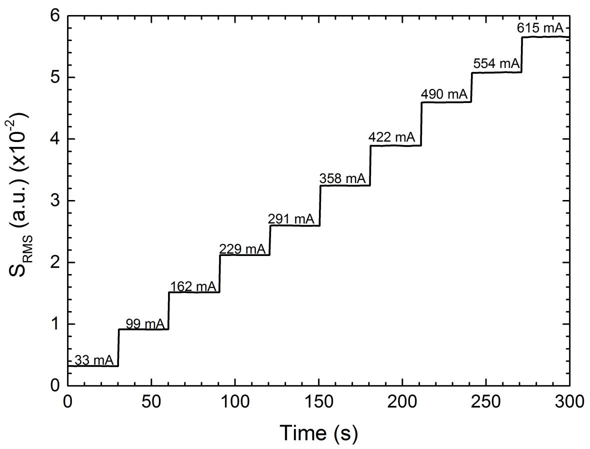

(a)

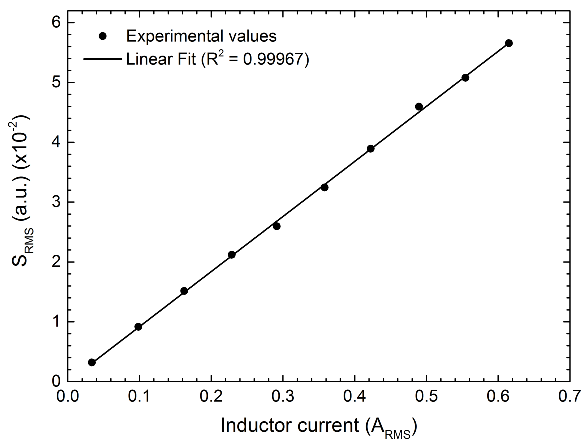

(b)

Figure 3.5 – (a) Sensor response to 30 s current increment steps and in (b) the respectively calibration curve.

In Figure 3.6 it is presented the combined results of all tests showing a very good linear response and independent of the signal frequency.

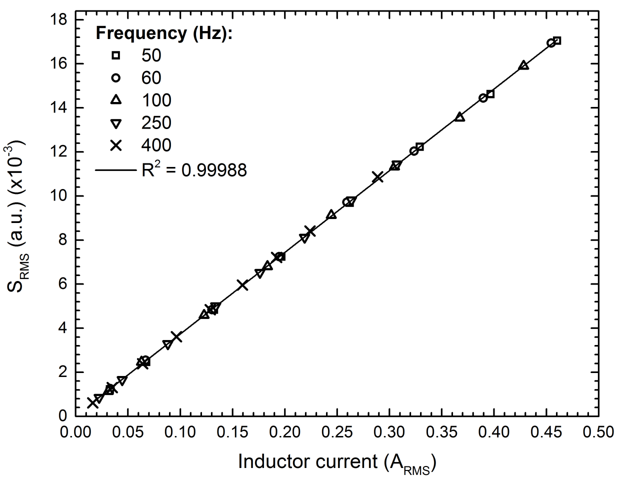

Figure 3.6 – Sensor response to magnetic fields with different frequencies.

3.3.3 Sensitivity and Resolutions obtained at different wavelengths

In order to evaluate the possibility of using this sensor configuration at telecom wavelengths, the prototype was tested with different broadband sources. Therefore, the sensor performance was tested at 630 nm, 830 nm and 1550 nm. The operational parameters of the optical sources tested and the corresponding sensor output powers are shown in Table 3.1. In the proposed sensing head configuration, most of the optical power is lost in the input polarizer (50 %), in the beam splitter (another 50 %) and in the GRIN lens (best case with 7 %), adding to these other residual losses in splices, connectors and parasitic reflections. As a result, the available optical signal reaching the photodetectors is relatively small leading to a degradation of the signal to noise ratio, requiring high gain amplification and filtering and imposing some limitations on the bandwidth.

Table 3.1 – Optical sources parameters and respective output powers.

Sources	Output power	3 dB Spectral bandwidth	Power at output S_1	Power at output S_2	Thorlabs detectors	Detector bandwidth
SLD 650	2.5 mW	6.2 nm	5,3 µw	2,8 µw	PDA100A-EC	20 kHz
SLD 830	7.8 mW	19.7 nm	19,12 µw	14,07 µw	PDA100A-EC	225 kHz
SLD 1550	22.5 mW	50 nm	434,10 µw	232,00 µw	PDA10-CS	775 kHz

An evaluation of the sensitivity and resolution of the sensor was performed, considering operation with the different optical sources and detection optoelectronics, using a 125 mHz bandwidth band-pass filter, at the detection stage, and submitting the sensor to six incremental current steps of 75 A_{RMS}, at 80 Hz, during 30 s each, ranging from 75 A_{RMS} up to 450 A_{RMS}. The optical sensor resolution was calculated as two times the standard deviation value of each incremental step, divided by the slope of the calibration curve. An inductor was used to generate a well-defined and stable sinusoidal magnetic field. From the measured magnetic field, it was calculated the equivalent current needed to generate such magnetic field considering a practical situation with a single conductor 40 mm apart from the sensor. With this procedure it was possible to obtain the sensor response and respective calibration curves while operating at different wavelengths. With this data, an estimate of the system sensitivity was done in all cases. A comparison of the results obtained with each optical source can be made in Figure 3.7 (a), where it is shown the normalized sensitivity as function of wavelength. In Figure 3.7 (b) the corresponding resolutions, taken for the quadrature signals (S_1 and S_2) and for the processed signal S, are given. These tests were performed before sensor encapsulation.

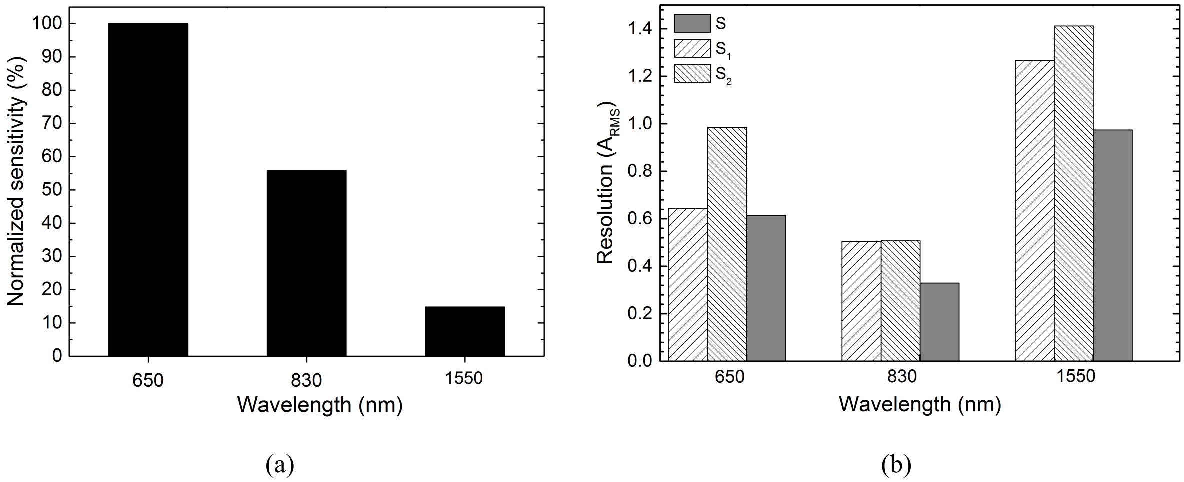

Figure 3.7 – Sensor performance, (a) sensitivity and (b) resolution for different optical sources.

As expected the sensitivity rapidly decreases with the increase of the wavelength, due to the decrease of the Verdet constant. The best resolutions are attained with the 830 nm source, having a 1.86 times improvement when comparing with the results obtained at 650 nm. This fact is justified by the higher optical power of the SLD at 830 nm in comparison with the one at 650 nm, leading to a better signal to noise ratio. Also, the photodetectors are around 1.29 times more sensitive to photons in the 830 nm wavelength than at 650 nm, due to the responsivity of silicon. However, although the optical source at 1550 nm had two times more power than the diode at 830 nm, the intrinsic sensitivity at this wavelength is 3.7 times lower, resulting in worst resolutions. Furthermore, from these results, it is seen that the dual quadrature processing gives better resolutions than the individual processed signals. Comparing S with S_1 there is a 4.6 %, 34.7 % and 23.1 % resolution improvement for the 650 nm, 830 nm and 1550 nm, respectively, demonstrating the effectiveness of the signal processing scheme.

As mentioned before, the Verdet constant of the SF57 material at 650 nm is 21 rad/(T.m). Based on the recorded sensitivities, it was possible to estimate the Verdet constant at the higher wavelengths obtaining 11.74 rad/(T.m) and 3.12 rad/(T.m) for 830 nm and 1550 nm, respectively.

Also, according to equation (3.4) the sensor transfer function is sinusoidal, but can be considered linear for the limited range of small angles. Setting the maximum tolerable error to 1 %, it can be defined a linear region considering $4\theta_F < 4\pi/180$. With $r = 40$ mm, $L = 80$ mm and $V(650\text{ nm}) = 21$ rad/T.m the linear response goes up to 9.7 kA. For operation at higher wavelengths, the sensor linear region increases up to 17.35 kA at 830 nm and 65.28 kA at 1550 nm. In all cases, adjustments can also be made to the sensitivity by controlling the distance to the conductor.

As stated before, the maximum intrinsic bandwidth of the transducer is around ~1 GHz. However, taking into account the limitations of the electronics systems (photodetectors, digital acquisition) and the impact of the available optical power in the signal to noise ratio, the bandwidth of the systems tested was limited to 100 kHz. Nevertheless, this value can be increased by using an optical source with higher output power that would allow reducing the gain requirements, thus increasing the bandwidth, and also using acquisition boards with better performance. In addition, such value of bandwidth, is already adequate for most application of metering and protection.

3.4 Sensor casing

After choosing the optimum operation wavelength at 830 nm, a protective casing for the sensing head was designed and built, where the bulk materials and GRIN lens alignment are protected and aligned. This way the sensor becomes portable, it can be transported and clamped to an external conductor from the electric grid or from other power system, without requiring alignment. In Table 3.2 it is shown a list of materials studied for the sensor enclosure. The casing material was chosen considering the need for a dielectric material that would not affect the magnetic field ($\mu_r \approx 1$) and capable of withstanding temperatures up to 80 ^{o}C. In addition, another important factor was the ability to machine the chosen material. Considering these restrictions and some limitations on the available materials, the protective casing system was implemented using nylon material, possessing a thermal expansion coefficient of *(dL/dT)/L* = $8 \times 10^{-5}\ K^{-1}$.

Table 3.2 – Analyzed materials for the sensor enclosure.

Material	**Temperature range (°C)**	**Melting point (°C)**	**Thermal expansion coefficient ($10^{-5}\ K^{-1}$)**	**Relative magnetic permeability (μ_r)**
Teflon	20 a 100	327	16.0	4,2
Acrylic		130	7.00	21
Glass	20 a 300	1600	0.86	4 a 10
PVC	-30 a 50	82,5	8.00	-
Aluminum		660	2.40	1
ZELLAMID® 1500 (PEEK)	up to 260		4.70	-
Wood			Fibers direction: 0.3 transverse direction of the fibers: 3	1
Fiber Glass			1.70	
Nylon	-70 a 99	216	8.00	~1

After selection of the material, a drawing of the encapsulation was performed using Autodesk Inventor. In Figure 3.8 it is shown the schematic of the sensing head setup, to be placed inside the enclosure, with a rotating input polarizer and the optical bulk materials: BS, PBS and SF57 prism. Also, it is presented the encapsulation that will make the sensor portable. It is composed by two nylon plates and a PVC plate in between with three holes where the FC/APC connectors are placed (one SM input and two MM outputs), enabling the connection of the sensing head to the interrogation unit. Inside the enclosure, the three FC/APC are connected to the GRIN lens. A third nylon piece it is also used to attach the enclosure to the conductor using three nylon screws. The big hole shown in the encapsulation is projected to support conductors with a maximum of 47 mm, but if a smaller diameter cable is used, rings with the desirable internal diameter can be fabricated to ensure the attachment. In Appendix B it is shown a detailed schematic of the enclosure, including dimensions and in Appendix C, Fig. C.1, the interior of the enclosure.

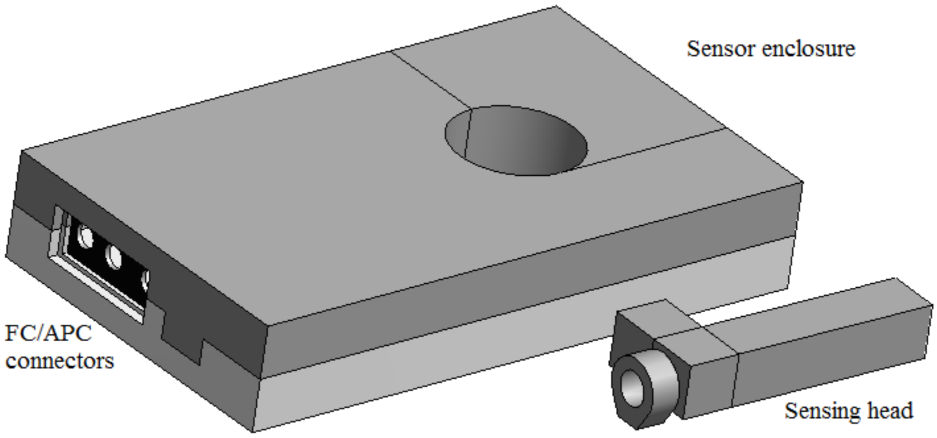

Figure 3.8 – Sensor enclosure and bulk sensing head.

Following design and parts machining, the BS, PBS and prism bulk components of Figure 3.8, were glued together with an optical epoxy EPOTEK-301 with 99 % transmittance at 830 nm, which cures within 24 h at 23 ^{o}C enabling to perform small alignment adjustments while curing. The same epoxy was used to glue the bulk components to the encapsulation. Furthermore, the input GRIN lens was glued to the encapsulation with acrylate glue and the output lens with hot-melt adhesive, after alignment. Small adjustments were made in the output lens during curing in order to maintain the alignment. The final arrangement of the encapsulation is shown in Figure 3.9 (a) and in (b) is illustrated the encapsulation interior, showing the sensor and the GRIN lens responsible for injecting and re-collecting the light. A more detailed description of the sensor assembly in the enclosure is done in Appendix C.

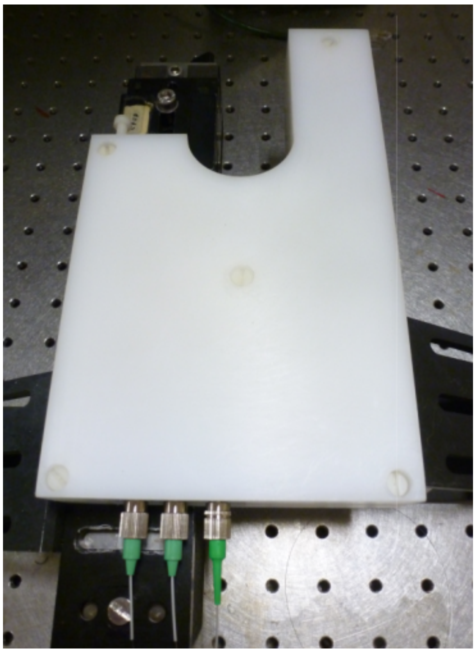

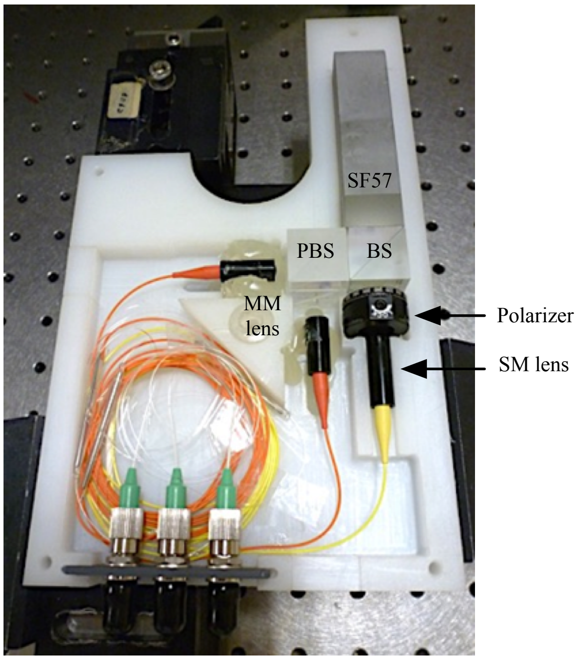

(a) (b)

Figure 3.9 – Sensor encapsulation (a) outside and (b) inside view.

3.4.1 Interrogation unit

The portability of the interrogation system was also considered in order to make the whole system transportable. An industrial PVC box with 650 × 500 × 250 mm dimension was used as protective casing for all the optoelectronics systems. It contains the SLD optical source followed by an optical depolarizer necessary to reduce its degree of polarization. It also holds the detection set composed by two photodetectors Thorlabs PDA100A-EC and a NI DAQ USB-6363 acquisition board, as shown in Figure 3.10. The box has two decks, the lower one for the power supply and voltage transformers and the upper one for the optics and electronic components.

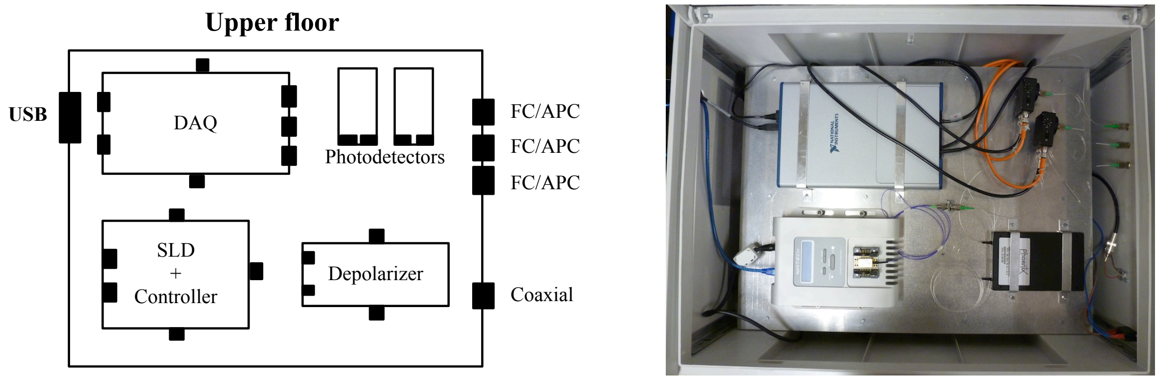

(a) (b)

Figure 3.10 – (a) Schematic and (b) photo of the interrogation unit inside.

All the optical components are connectorized, with the unit having one optical input and two optical outputs, enabling the necessary optical link between the system and the sensing head (Figure 3.11 (a)). There is also an electrical input port with a range of -12 V to 12 V which can be used as a reference input, for triggering purposes, or to receive a signal proportional to the current passing in the conductor, thus enabling calibration procedures. On the back, Figure 3.11 (b), the system also has an USB connection, enabling control via a PC with custom made LabVIEW program, where all the digital control and signal processing takes place. Three 20 m long optical cables were used to connect the sensor head to this interrogation unit.

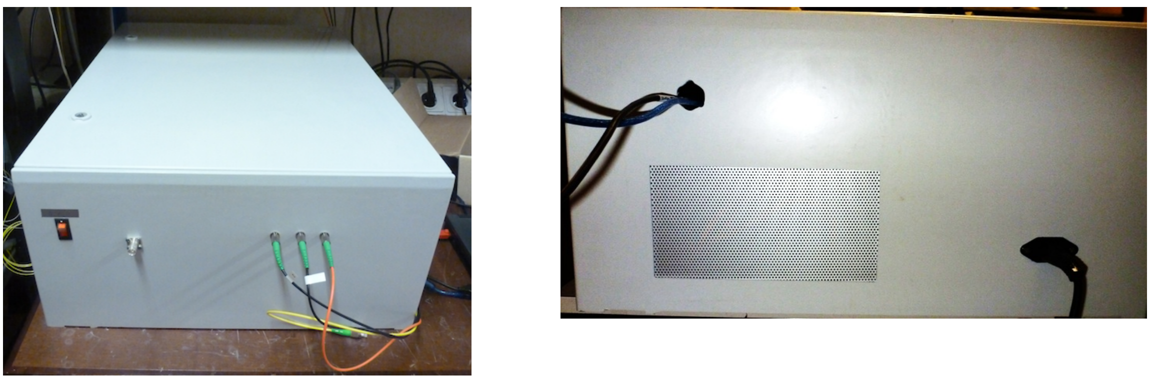

(a) (b)

Figure 3.11 – (a) Front-end and (b) back-end of the acquisition system.

In Figure 3.12 it is presented the front panel of the developed LabVIEW program, used to record and analyze the bulk optical current sensor. The program shows the acquired quadrature signals in the DAQ tab, the signals after passing through the band-pass filter (Filtered Sig. tab) and the AC response as function of time of the quadrature and processed signals (Sensor Resp. tab). The buttons “SaveData” and “Save Values to File” are used to record the sensor response and export the recorded data to a text file, respectively.

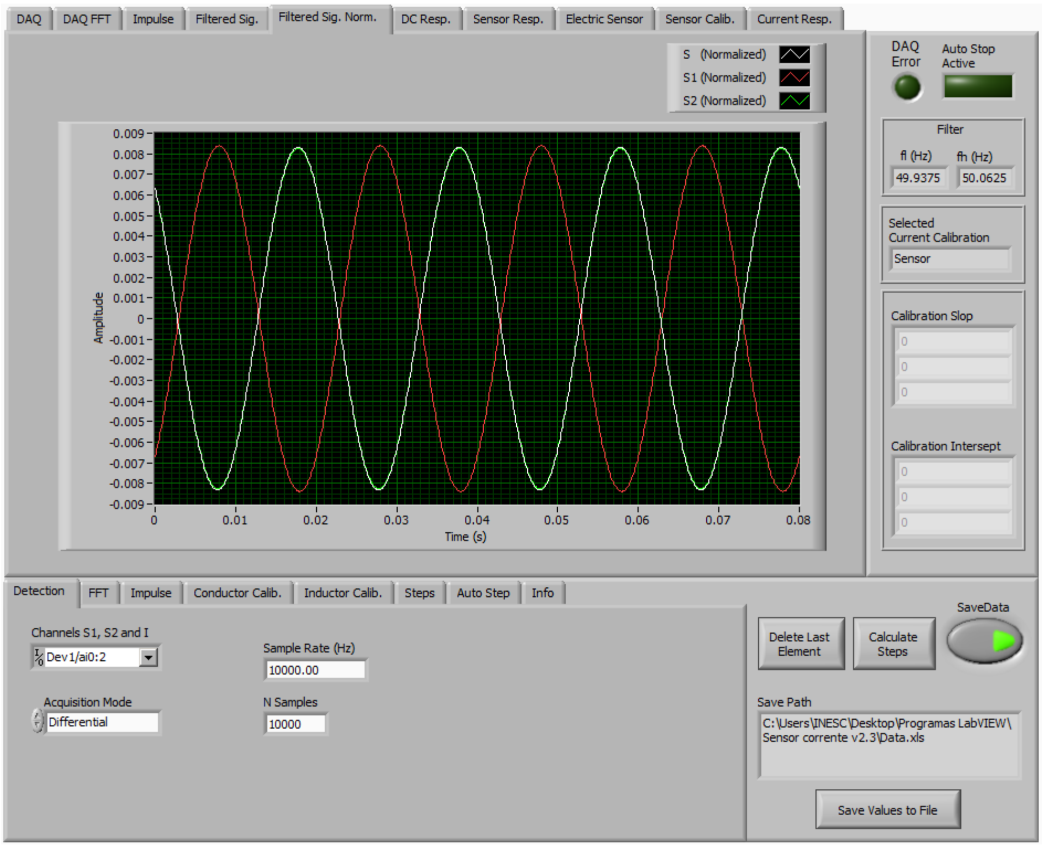

Figure 3.12 – Screenshot of the front panel of the LabVIEW program developed for the interrogation unit of the clamp-on optical current sensor.

Although it was not tested in this prototype, a custom photodetector system was developed to replace the commercial ones. The schematic can be found in Appendix D and basically consists of a low noise transimpedance circuit followed by two other gain circuits with an output containing the DC plus AC signal and the other with only the AC component, but having higher gain. This last circuit was projected to test the sensor performance with low currents, where the AC needs higher amplification before being read by the DAQ.

3.4.2 Prototype calibration

After the sensor encapsulation process, the obtained portable prototype was submitted to calibration procedures and additional tests. Again an inductor was used to apply a stable sinusoidal magnetic field at 19 Hz. In the digital acquisition system a sample frequency of 1 kHz and a 125 mHz bandwidth band-pass detection filter was defined. During six consecutive days the prototype was submitted to 12 identical calibration procedures. From the results an average sensitivity of $1.2789 \pm 0.0070\ A^{-1}$ was found giving an error of ±0.55 %, calculated as the standard deviation divided by the average sensitivity. This error was related with minor temperature dependent misalignments between the bulk sensor and the GRIN lens, when performing the quadrature polarimetric detection scheme.

Measurement errors were evaluated for a range of current between 0 and 1.2 kA, with the sensor presenting a resolution of 0.455 A_{RMS}. Accuracy errors provided by the optical sensor were calculated according to equation (1.1), as the difference between the optical sensor response (after calibration) and the equivalent current, divided by latter parameter. In Figure 3.13 it is shown the modulus of the error obtained for the prototype and it is compared with the industry accuracy classification (normative IEC 60044-1). The sensor satisfies class 1 operation with ±1 % error for a nominal current of 900 A_{RMS}. Due to experimental limitations, higher current values could not be tested. Nevertheless, considering the sensor intrinsic linear range, it is expected that accuracy class 1 will hold for much higher currents.

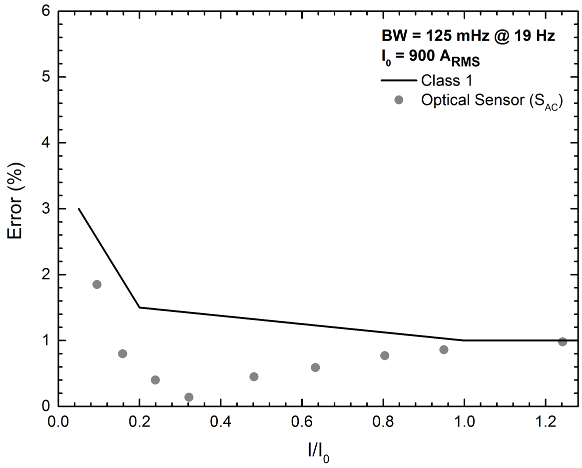

Figure 3.13 – Prototype classification according to metering accuracy classes. Fitting of sensor accuracy to metering class 1, for nominal current of 900 A_{RMS}. Operation at 830 nm.

Sensor accuracy, depends not only on its intrinsic precision but also on the stability of its relative position to the conductor, and the stability of the Verdet constant, which is temperature dependent. These parameters can be optimized and/or accounted for in the signal processing, contributing, in principle, to further optimize the sensor performance. Indeed, looking at the sensor intrinsic precision error, considering two times the standard deviation value (2σ) divided by the average, it can be seen (Figure 3.14) that, potentially, the sensor can fit accuracy classes 0.1 and 0.2 for nominal currents of 1.2 kA_{RMS} and 0.3 kA_{RMS}, respectively.

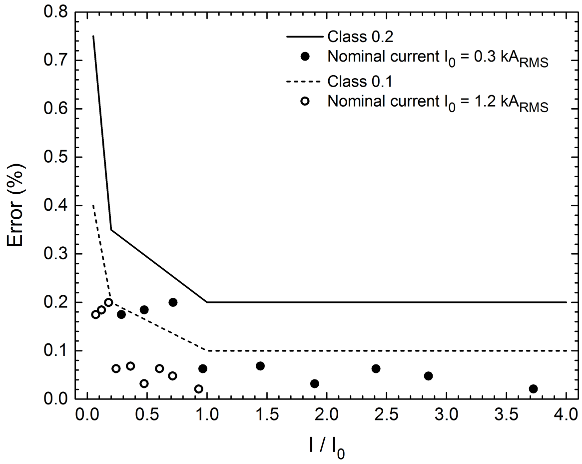

Figure 3.14 – Sensor precision error fitted to metering accuracy classes 0.2 and 0.1, considering nominal currents of 300 A_{RMS} and 1200 A_{RMS}. Operation at 830 nm.

3.4.3 Transient detection

Some preliminary tests were performed in order to evaluate the sensor response to transient current peaks in Eletronorte, Belém, Brazil. An industrial current source from *Multi-amp* was manually set on and off, while operating at ~300 A_{RMS}. During the switching operation, very fast transients could be observed. For these tests, the gain of the detector was reduced, allowing to increase the detection bandwidth. The transient behavior was due to sliding of the contact bars. In Figure 3.15 (b) a zoom of the transient signals detected during turn-on can be observed. From the data in Figure 3.15 (b), it can be estimated that the sensor was able to detect transient peaks with 3.62×6.02 μs (rise time at 90 % amplitude vs decay time at 50 % amplitude). This data clearly indicates the suitability of the proposed sensor system to be used in protection applications, where fast detection of transient peaks is required.

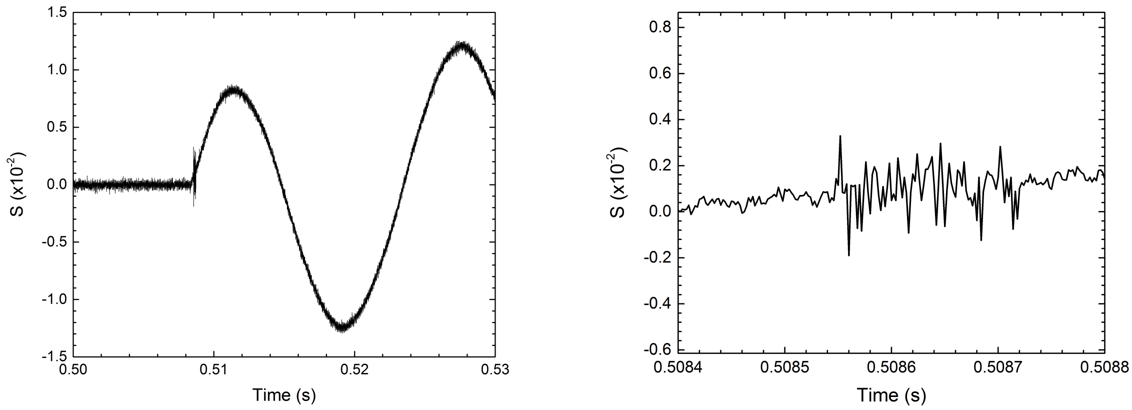

(a) (b)

Figure 3.15 – (a) Sensor output signal when turning on the conductor with 600 A_{RMS} and in (b) a zoom of the detected transient pulses.

3.4.4 Temperature dependence

Sensor stability with temperature was also evaluated using an oven while applying a constant magnetic field. In the present configuration, each of the system parts (prisms and coupling lens) was solidary with the nylon casing, allowing to test different coupling angles and distances. Unfortunately, in such arrangement the thermal expansion of the casing led to some temperature induce misalignment which resulted in degradation of the coupling efficiency and decrease of the signal to noise ratio. In spite of this, the signal processing was able to compensate most of the power loss. However, for temperatures changes larger than ~20 ºC, the power loss was too high compromising the sensor operation. Therefore, at the present configuration it can be stated that the sensor operation range was 25 ºC ± 15 ºC. While this is unacceptable for most practical applications, it was adequate for characterizing and validating the sensor prototype. In addition, this situation can be easily solved by implementing a monolithic solution, where sensing prisms can be glued together permanently to the GRIN lens using suitable optical grade epoxy glues (eg. Epoxy EPO-TEK 301 [119] can withstand temperatures up to 430 ºC). With such approach, the sensors intrinsic properties will allow stable operation in much broader temperature range. In such situation, however, the Verdet constant temperature dependence must be accounted for, to avoid fluctuations of the sensors calibration function. Nevertheless, the Verdet constant has a linear temperature dependence [117] that can be easily compensated by including a temperature sensor inside the sensor enclosure (a Fiber Bragg Grating, for instance), and using a proper calibration matrix. Moreover, this effect can also be compensated by varying the polarization state of the input light as a function of temperature and this can be done including a waveplate with a precise linear retardance [38].

3.5 Simulation of interference from external conductors

As mentioned previously the proposed sensing head is susceptible to external magnetic fields. In Figure 3.16 it is shown the schematic of one of the support towers of the high-power transmission line proposed in the TECCON project and two alternative positions where the sensor can be placed. In both cases the distance between adjacent conductors is the same and the distance between the sensor and the conductor is 40 mm. The objective of this analysis is to estimate the error in each optical sensor, positioned around each conductor due to the external magnetic fields.

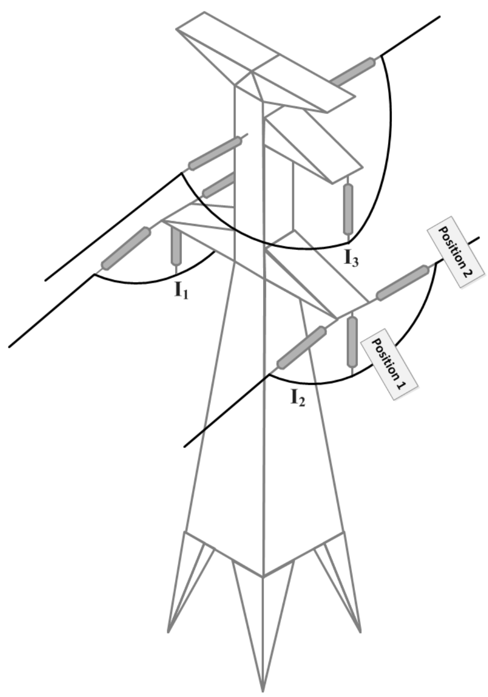

Figure 3.16 – High power grid from TECCON project.

For each case, distinct sensor positioning in relation to the conductor can be defined as presented in Figure 3.17 (a). Proper choice of relative position of the sensors can eventually be used to minimize the measurement errors. According to the power line specifications the minimum distance between conductors are $d_{12} = 4$ m, $d_{23} = 2{,}73$ m and $d_{13} = 3.88$ m. On the other hand, in Figure 3.17 (b) two variables are defined, the offset (h) and the distance to the conductor (r), to be used in the general expression for the Faraday rotation.

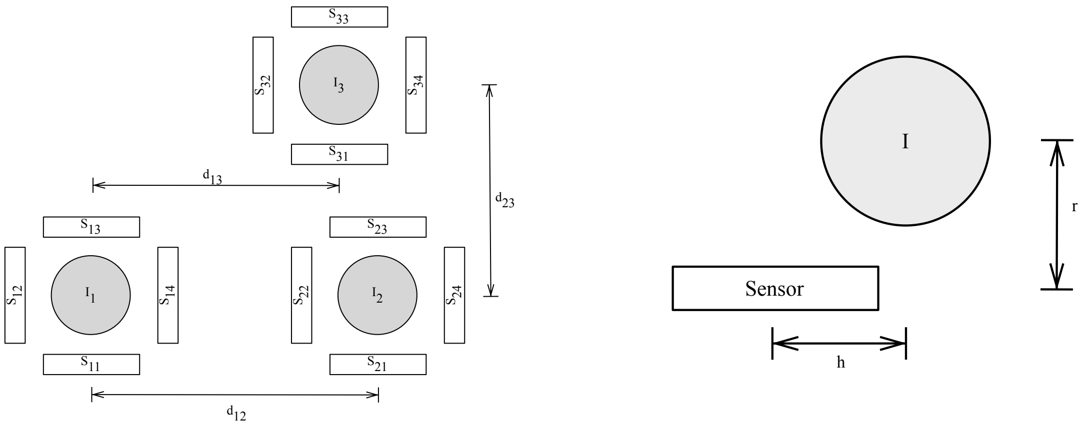

(a) (b)

Figure 3.17 – (a) Relative arrangement of conductors in a three-phase transmission line with different sensors positioning possibilities and (b) schematic of sensor positioning in relation to the conductor.

Considering the schematic presented in Figure 3.17 (b), a more generic expression for the Faraday rotation was derived, considering the dependency on the relevant geometrical parameters. This way, instead of the simplified expression describing the Faraday rotation in (3.9), the more generic expression becomes

$$\theta_{ijz}[r,h,I_z(t)] = \left(\mathrm{ArcTan}\left[\frac{h+L/2}{r}\right] - \mathrm{ArcTan}\left[\frac{h-L/2}{r}\right]\right) V \frac{\mu_0}{2\pi} I_z(t) \tag{3.11}$$

where ij corresponds to the sensor position according to the possibilities shown in Figure 3.17 (a) and z is the magnetic field generated by the conductor 1, 2 or 3. The variable $I_Z(t)$ is the time dependent current signal passing in each conductor and is given by

$$\begin{aligned} I_1(t) &= A_1 \,\mathrm{sen}(2\pi ft+0°) \\ I_2(t) &= A_2 \,\mathrm{sen}(2\pi ft+120°) \\ I_3(t) &= A_3 \,\mathrm{sen}(2\pi ft+240°) \end{aligned} \tag{3.12}$$

In the simulation a current of 2 kA is considered for the conductor being measured and a change of ±2 kA (0 to 4 kA) is defined for the other two conductors that generate interference, where the errors are calculated as

$$\mathrm{Error} = \frac{|S_{ij} - S_{i0}|}{S_{i0}} \times 100\ \% \tag{3.13}$$

with S_{ij} and S_{i0} being the peak values of the temporal signals read with the sensor, with and without interference and given by equation (3.3). In the simulation, the Faraday rotation caused by each conductor is considered independently and the total effect is calculated by adding the individual contribution of each conductor. For instance, the total Faraday rotation measured with the sensor in position ij = 11 is given by

$$\theta_{11}[r,h,I] = \theta_{111}[r,0,I_1]+\theta_{112}[r,d_{12},I_2]+\theta_{113}[(r+d_{23}),d_{13},I_3] \tag{3.14}$$

The behavior of the Faraday rotation measured in each sensor position due to the three conductors is thoroughly described in Appendix E. The interference due to the magnetic fields generated by the currents flowing in the other conductors will change the peak amplitude of the measured signal and its relative phase, as demonstrated in Figure 3.18. The signal S_{10} correspond to the magnetic field measured with a single sensor around the conductor and considering no interfering magnetic field is generated by the other conductors. On the other hand, the other two signals, S_{12} and S_{14}, are the output read with sensor two and four, respectively, around the first conductor and includes the interference due to the external conductors (2 and 3).

In Figure 3.18 a peak current of 2 kA is considered for conductor 1 and 10 kA for the other two conductors which generate interference. Although the average current of each phase is typically the same, to visually enhance the amplitude and phase errors due to interference, five times more current was defined for the interfering conductors (otherwise it wouldn't be visible graphically). As previously mentioned, the distance between the sensor and the conductor is 40 mm. However, the distance between the main conductor and the external conductors is at least 4 m, so the contribution of the external magnetic fields is relatively low. Furthermore, depending on the sensor positioning, the external fields can be perpendicular in relation to the sensor and therefore the resulting Faraday rotation is extremely weak.

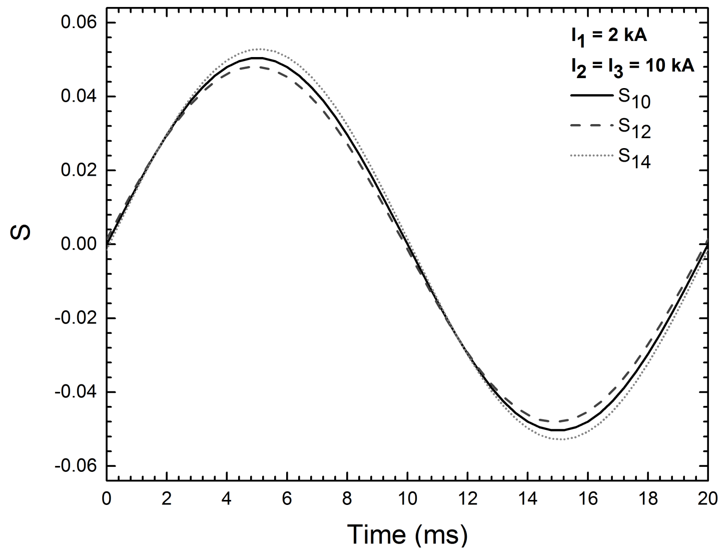

Figure 3.18 – Signals measured by sensors in different position around conductor 1, S_{10}, S_{12} and S_{14}, where a current of 2 kA was flowing. For S_{10}, no additional current is present in the system. For S_{12} and S_{14} a current of 10 kA is considered flowing in the two additional conductors.

The phase error in degrees is calculated by detecting the peak time of the signal read by each sensor with and without interference and its temporal difference *Δt (s)* relative to a phase change of

$$\Delta\theta = \Delta t.f.360° \tag{3.15}$$

In Figure 3.19 (a) and (b) it is shown the current amplitude and phase errors for each sensor, respectively, when considering a peak current of $I_1 = 2$ kA passing through the main conductor and the peak current of the external conductors changing from 0 to 4 kA (relative current changing by a factor from 0 to 2). The relative current is the peak current passing athwart the external conductors, normalized by the peak current of the main conductor (the one to be measured). Simulation results show that the amplitude errors are smaller with the sensor at position S_{13} with ±0.32 % and ±0.6 % for a relative current of 1 ($I_2 = I_3 = 2$ kA) and

2 ($I_2 = I_3 = 4$ kA), respectively. However, for this sensor the phase error is higher with 0.31 degrees and 0.6 degrees, respectively. Nevertheless, the lowest phase error is attained with sensor at positions S_{12} and S_{14} with 0.19 degrees and 0.39 degrees, respectively. The combination of the four signals read in each sensor (S_{AVG}) provides immunity to the external magnetic fields in phase and amplitude, an outcome already expected, since the sensing area is an approximation of a closed loop configuration. This normalized signal is obtained by adding the four time varying signals, S_{11}, S_{12}, S_{13} and S_{14}, and then dividing by four. Afterwards, the signal is compared with S_{10}, the one without interference, and the amplitude and phase parameters are calculated.

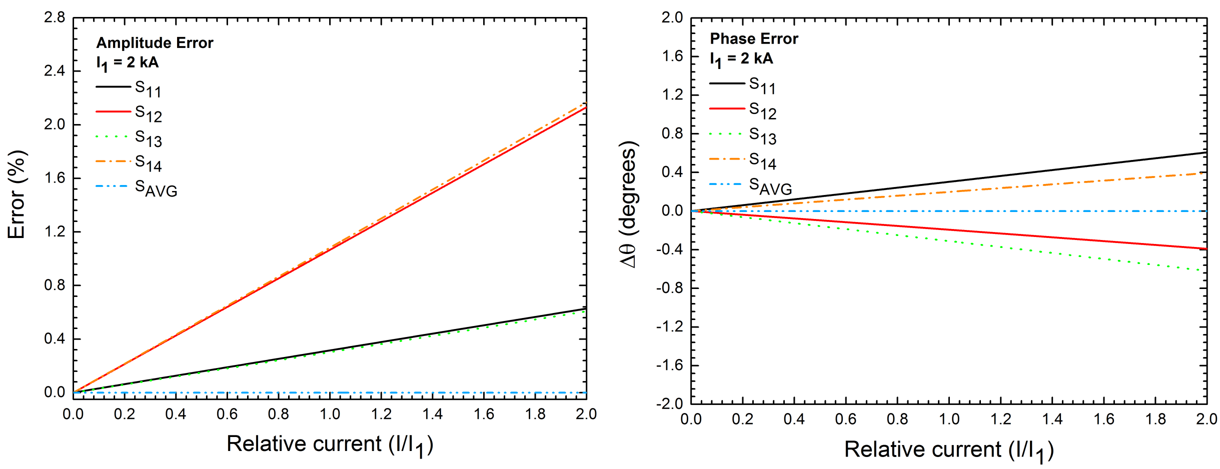

(a) (b)

Figure 3.19 – (a) Amplitude and (b) phase errors of the current measured by sensors around the main conductor, while changing the current flowing in the external conductors. It was considered an alternate current of $I_1 = 2$ kA flowing in main conductor, while interfering relative currents where changed from 0 to 2.

Considering the worst case scenario with maximum and minimum errors in amplitude, further analysis of Figure 3.19 (a) and (b) indicate that for a relative current of 1, there is an improvement of 70.9 % from sensor S_{13} to S_{14} for the measurement of amplitude and of 38.7 % in the phase measurement, from S_{12} to S_{13}. Also, the amplitude error of ±0.32 % for sensor S_{13} indicates a maximum performance at 0.5 class, where the error is ±0.5 % at nominal current. However, in a practical situation, the errors due to external magnetic fields can be attenuated by proper shielding of the sensing head, attached around the conductor.

Errors were also estimated for the sensors around the other conductors and the results are compiled in Figure 3.20 and Figure 3.21 for conductor 2 and 3, respectively. For conductor 2 minimal errors in amplitude and phase are obtained with the sensor at position S_{24} (±0.68 % for amplitude and 0.58 degrees for phase), considering a relative current of 1 (all conductor with the same peak current).

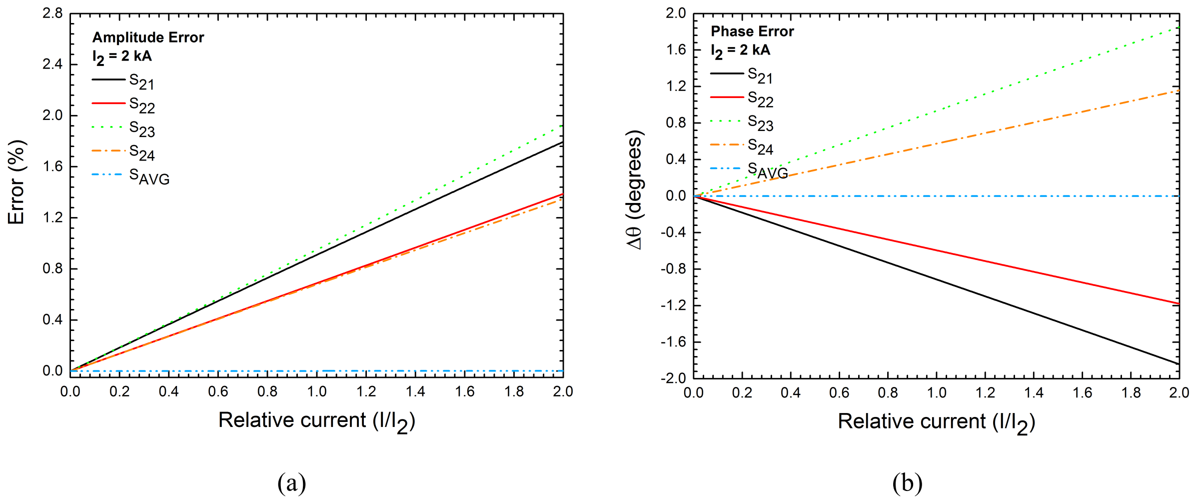

Figure 3.20 – (a) Amplitude and (b) phase errors of the current measured by sensors around the main conductor, while changing the current flowing in the external conductors. It was considered an alternate current of I_2 = 2 kA flowing in main conductor, while interfering relative currents where changed from 0 to 2.

A more detailed analysis of Figure 3.20 (a) and (b) indicates that for a relative current of 1, there is an improvement of 25.6 % in the amplitude error from sensor S_{24} to S_{21} and 38.7 % in the phase error from S_{24} to S_{23}. Also, an amplitude error of ±0.68 % for sensor S_{13} indicates a maximum performance conforming with class 1 operation.

However, for conductor three (Figure 3.21), the best result in amplitude and phase was obtained with sensors at positions S_{32} and S_{34} with ±0.4 % and 0.47 degrees error in amplitude and phase, correspondingly. Meticulous analysis of Figure 3.21 (a) and (b) indicate that for a relative current of 1, there is an improvement of 68.8 % in the amplitude error from sensor S_{32} to S_{31}, and of 25.4 % in the phase error from S_{34} to S_{31}. Also, the amplitude error of ±0.39 % for sensor S_{13} indicate a maximum performance at class 0.5.

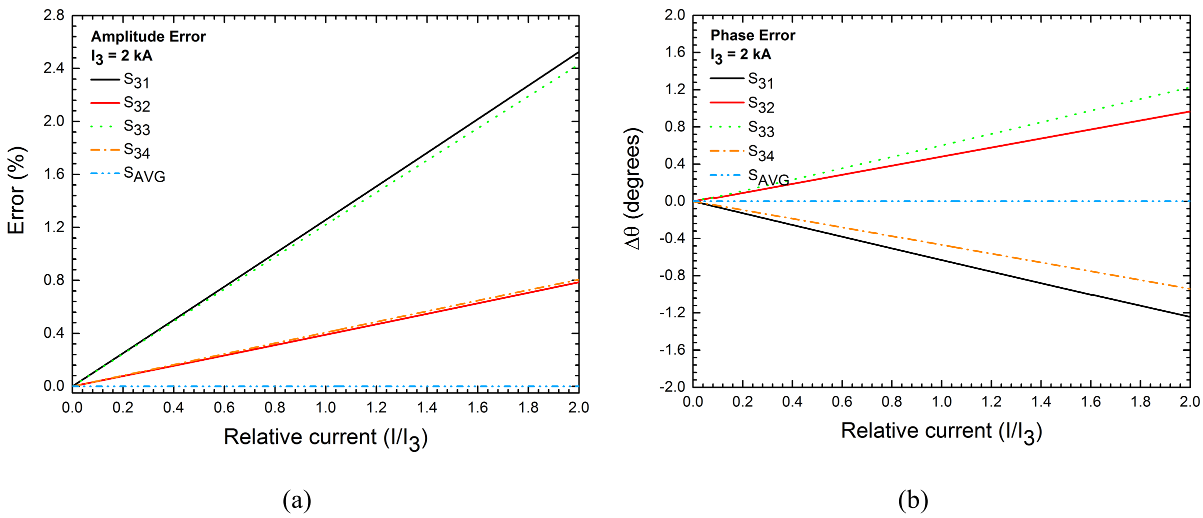

Figure 3.21 – (a) Amplitude and (b) phase errors of the current measured by sensors around the main conductor, while changing the current flowing in the external conductors. It was considered an alternate current of I_3 = 2 kA flowing in main conductor, while interfering relative currents where changed from 0 to 2.

These results have shown that the strategic positioning of the sensor can reduce the error due to interferences of external conductors. Furthermore, if four sensors around each conductor are combined, the amplitude and phase errors could be greatly minimized, because the setup makes a quasi-closed loop configuration. In Table 3.3 it is shown a summary of the best and the worst amplitude and phase errors obtained for each conductor, considering a peak current of 2 kA passing through each conductor, and considering the sensors at different positions.

Table 3.3 – Summary of the errors obtained in the simulation of interfering conductors, with $I_1 = I_2 = I_3$ = 2 kA.

Conductor	Amplitude		Phase	
	Best	**Worst**	**Best**	**Worst**
1	S_{13} = ±0.32 %	S_{14} = ±1.10 %	S_{12} = 0.19°	S_{13} = 0.31°
2	S_{24} = ±0.68 %	S_{21} = ±0.91 %	S_{24} = 0.57°	S_{23} = 0.93°
3	S_{32} = ±0.39 %	S_{31} = ±1.25 %	S_{34} = 0.47°	S_{31} = 0.63°
	S_{34} = ±0.40 %	S_{33} = ±1.22 %	S_{32} = 0.48°	S_{33} = 0.60°

3.6 Summary

An optical current sensor prototype composed by a portable sensing head and interrogation unit was successfully developed and characterized. Preliminary experimental results indicated the possibility of the sensor to operate at different wavelengths, showing that using a broadband optical source at 830 nm yielded a resolution improved by a factor of 1.86, when compared with operation at 650 nm. This outcome was due an improved SNR derived from having a source with 3.1 times more optical power and also due to the higher responsitivity of the photodetectors at the 830 nm wavelength. The sensitivity at 830 nm was also 3.8 times higher than obtained at 1550 nm, because of the Verdet constant wavelength dependence. Furthermore, applying the quadrature demodulation scheme, it was possible to reject most of the common mode noise, improving the resolution by at least 4.6 %.

In the optical domain a ~1 GHz intrinsic bandwidth could be estimated which was defined by the light propagation time inside the optical glass. In practice, combining the sensing head with the available electronics, the bandwidth was reduced to 100 kHz. For the sensing head, an encapsulation was implemented and tested, appropriate for direct clamp-on to a conductor. The results demonstrated the possibility to use the sensor for metering applications as an accuracy class 1 device considering nominal currents equal or higher than 900 A_{RMS}. Also, long-term stability was explored by performing twelve calibrations during six days showing an error of ±0.55 %. This error was connected to the stability of the alignment of the GRIN lens with the bulk components that was strongly dependent on temperature. This was an intrinsic problem of the materials used and can be easily solved by implementing a monolithic solution, where sensing prisms can be glued together permanently to the GRIN lens using suitable optical grade epoxy glues. Also minor temperature changes could have contributed to changes in the Verdet constant, affecting the calibration. Therefore, considering the sensor intrinsic precision error, it can be seen that, provided factors like positioning, and Verdet constant temperature dependence, are accounted for in the signal processing, its performance can increase to fit classes 0.2 or even 0.1, depending on the nominal currents.

Detection of transient pulses was demonstrated by monitoring the switch-on operation of a current source, where several pulses under 10 μs were detected. Overall the results demonstrate the viability of single prism bulk optical sensor to be used both as a metering and a protection device in high power systems applications.

As mentioned along the chapter, the proposed sensing head is sensitive to external magnetic fields. A simulation of an electric grid configuration being installed in Brazil in the scope of project TECCON was analytically studied by testing the positioning of the sensing head in distinct locations around the conductor. Considering a three-phase system with a peak current of 2 kA passing through each conductor, the minimal amplitude error obtained was ±0.32 %, ±0.68 % and ±0.49 % for the sensor in positions S_{13}, S_{24} and S_{32} respectively. However, results demonstrate that a minimal amplitude error not always corresponds to a minimal phase error. In any case, considering the sensor in positions 1 to 4 around each conductor, upper and lower phase error obtained was 0.57 degrees and 0.19 degrees for sensor in position S_{24} and S_{12}., respectively. When power measurements are involved the phase error is important. According to the IEC 60044-1 standard, at nominal current operation, the acceptable phase errors are 0.083, 0.166, 0.5 degrees and 1 degree for the class 0.1, 0.2, 0.5 and 1, respectively [3]. Having these values into account and considering the worst case scenario, without shielding of the sensing head, the instrument error is less than 1 %.

Chapter 4 Fiber sensing coil

All-fiber sensors employing optical fibers as the sensing medium present themselves as a good solution to be employed in the high power grid, since the fiber can be wounded around the conductor, making it immune to external magnetic fields. However, coiling the fiber induces linear birefringence, degrading the sensor performance. In order to overcome this disadvantage, special optical fibers have been investigated along the years.

One of the first approaches included fibers made of flint glass, possessing higher Verdet constant and lower photo-elastic coefficient than conventional fibers [51,52]. Another method for reducing this undesirable effect was performing the annealing, where the fiber is first coiled and then heated to reduced fiber internal stress [62].

Other methods to minimize linear birefringence effects, consists in introducing circular birefringence (θ_S) in the fiber by twisting it during coiling [58] or preferably during fiber drawing, making it permanent [59]. In these two cases, if the circular birefringence is much higher than linear birefringence (β), the effect of the induced birefringence can be negligible. Essentially, the spun averages all fiber non-uniformities, effectively cancelling the total fiber linear birefringence.

Typically, when dealing with spun HiBi fibers the linear and circular beat lengths parameters are used instead of linear and circular birefringence, to describe the fiber features. The beat length (L_p) is the length (in meters) over which a 2π phase retardation is introduced between the two orthogonal components, while the circular beat length or spin pitch (L_S) is the the longitudinal period of fiber rotation (in meters).

In this chapter a standard conventional fiber and two distinct spun HiBi fibers are studied. One of the HiBi fibers was a home-produced PCF (Photonic Crystal Fiber) and the other was a commercial fiber with an elliptically-stressed cladding manufactured by IVG, especially designed for optical current sensors applications. Birefringence is strongly dependent on temperature because most fibers use at least two different glass materials with different thermal expansion coefficient. In this context, the use of PCF fibers for magnetic field sensing arises as a promising solution [120,121] and also has the potential advantage of single mode operation at multiple wavelengths [122].

Although most commercial setups employ an interferometric detection scheme (Figure 2.10), the quadrature polarimetric detection scheme was preferred instead, due to more straightforward implementation, still suitable to compare the different fibers. The interferometric scheme requires using PM fibers at precise relative orientations and consequently demands for a special and very expensive splice machine, which was not available at laboratory.

For the purpose of comparing three distinct fibers, a polarimetric interrogation scheme was implemented and tested in transmission and reflection, using three distinct coiling diameters, with various fiber turns, in order to evaluate the effects of induced linear birefringence due to winding. In the reflection setup, a conventional silver mirror and a FRM were used, with the latter providing better performance, where all reciprocal linear and circular birefringence in the fiber is compensated. However, with the standard mirror, only the circular birefringence is compensated and the induced linear birefringence, which is temperature dependent, is not [59]. Furthermore, susceptibility to vibrations and external linear birefringence related with pressure in the sensing coil was studied.

4.1 Standard single mode fiber

A conventional SM fiber, having a Verdet constant at 1550 nm of around 0.5 rad/T.m [123], was first evaluated using a polarimetric quadrature detection scheme. According to equation (2.6), whenever the linear birefringence is higher than the circular birefringence (due to the Faraday effect), the sensor is expected to be highly susceptible to induced linear birefringence due to winding and pressure, with the first one being described as [23]

$$L_{ind} = \left(\frac{0.25}{\lambda} n^3 \left(p_{11}-p_{12}\right)(1+\nu)\left(\frac{d_F}{D}\right)^2\right)^{-1} \quad (4.1)$$

and it is dependent on the effective refractive index of the fiber (n), the strain optic coefficients (p_{11} and p_{12}), the poison ratio (v), the fiber diameter d_F, and the winding diameter D. For instance, for silica, the effective refractive index at 1550 nm *is* n = 1.4440, p_{11} = 0.113, p_{12} = 0.252 and v = 0.17.

4.1.1 Setup in transmission

The first experiment was carried out by implementing the transmission setup exhibited in Figure 4.1. A low coherence broadband source was used instead of a laser light source in order to avoid problems related with unwanted reflections that could lead to potential degradation of the sensor response due to interference. The light passes a rotating polarizer used to polarize the light and control the orientation of the input polarization plane. Afterwards it is injected into the sensing fiber using a microscope objective. When light propagates through the fiber, describing a circular path around the conductor it experiences the Faraday effect, in proportion to the current going through the loop, and thereby resulting in a corresponding rotation of its polarization plane. At the end, light is collimated and the two orthogonal polarization components are retrieved through a Polarization Beam Splitter (PBS) and detected by the photodiodes. A program in LabVIEW was developed to acquire and implement the quadrature polarimetric detection scheme, filtering the detected signals with a Butterworth band-pass filter with 1 Hz bandwidth. A NI DAQ 6343 (1.92 mV resolution), working as an analog-digital converter is used to record the photodetected signals and the reference signal, I_{AC} (corresponding to the current passing along the conductor, measured by an inductor). The magnetic field was generated with a high current source, which is basically an autotransformer with variable current control, enabling currents passing through the conductor in the range from 0 to 600 A_{RMS} at 50 Hz.

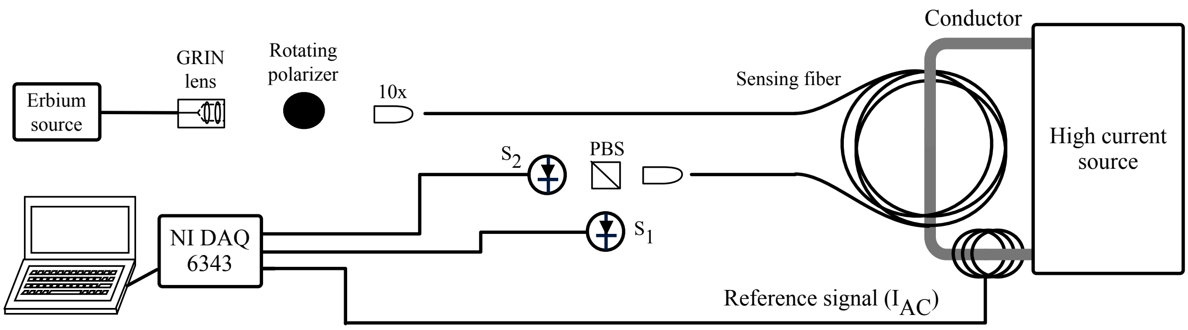

Figure 4.1 – Characterization setup of an optical fiber current sensor operating in transmission.

As described in Chapter 3, the polarimetric detection scheme provides maximum sensitivity when the output polarizers are at ±45 degrees in relation to the input. Theoretically, the Faraday rotation is directly proportional to the number of fiber turns (*N*) around the conductor and can be expressed as

$$\theta_F = \mu.V.N.I \tag{4.2}$$

being μ the relative permeability of the medium inside the coil, *V* the Verdet constant in rad/(T.m) and *I* the current passing in the conductor.

The first set of experiments consisted on evaluating the sensor SNR and stability of the recovered AC component of the quadrature processed signal (S_{AC}), when a current of 374 A_{RMS} was flowing through the conductor. In order to achieve that, a fiber coil with 12 turns having 180 mm in diameter was set around the conductor. During a 4 h measurement the optical sensor showed variations of ±11.14 % while the current source fluctuated ±1.84 %. The fluctuation was calculated as half the difference between the maximum and the minimum, divided by the average value. A SNR of 13 dB was obtained for the signals detected directly, S_1 and S_2. On the other hand, the processed signal *S*[1] yielded a SNR of 31 dB. In this assemble, therefore, the quadrature polarimetric processing scheme improved the SNR by 18 dB. The current source available was shown to have a high instability, therefore it was hard to maintain a constant current passing through the conductor. This way, in the remaining tests the calculated precision of the sensor is going to be shown alongside

[1] $S = \dfrac{S_1 - S_2}{S_1 + S_2} \approx 2\theta_F \dfrac{\sin(\beta)}{\beta}$

with the fluctuations of the current were recorded. Looking at the previous figures it can be seen that, in this particular case, the optical sensor poor stability is the major source of error.

The DOP was also measured at the output of the sensor, providing information related with the susceptibility of the polarization state, after passing through the optical fibers. This parameter changes from 0 to 100 % and should be maintained as high as possible. It is calculated as $(P_{MAX} - P_{MIN})/(P_{MAX} + P_{MIN}) \times 100\ \%$ where the minimum and maximum average powers were read with a photodetector and were obtained by rotating the input polarizer by 90 degrees. Linearly polarized light is injected in to the sensing fiber with a DOP of 99.5 % and, ideally this value should be maintained, otherwise, it means that the medium (sensing fiber) is making light elliptical and consequently diminishing the sensor sensitivity. In this configuration, the DOP at the output was 85 %. Having into account the poor SNR and large error attained in the stability analysis it was decided not to proceed with the current measurements. According to literature, these results were already expected, especially in terms of stability and are related with uncompensated changes of the SOP, not related with the Faraday effect, but rather to intrinsic and induced linear birefringence of various origins.

4.1.2 Setup in reflection

A much simpler and better approach than an active input polarization compensation can be obtained by arranging the sensor to operate in reflection by placing a mirror at the distal fiber tip, using either a silvered fiber tip or a FRM as depicted in Figure 4.2. The circulator employed at the input retrieves the reflected light and directs it to an in-fiber PBS. Notice that the reciprocal effects happening along fiber section at the second output of the circulator will in principle be compensated, especially when employing a FRM, where the thermal and mechanical perturbations affecting the SOP will be compensated, by swapping the polarization axis after reflection. Another benefit in using the sensor in reflection is to theoretically double the sensitivity for the same fiber length, due to the non-reciprocal nature of the Faraday Effect. This way, reciprocal effects can be canceled out while non-reciprocal effects are doubled.

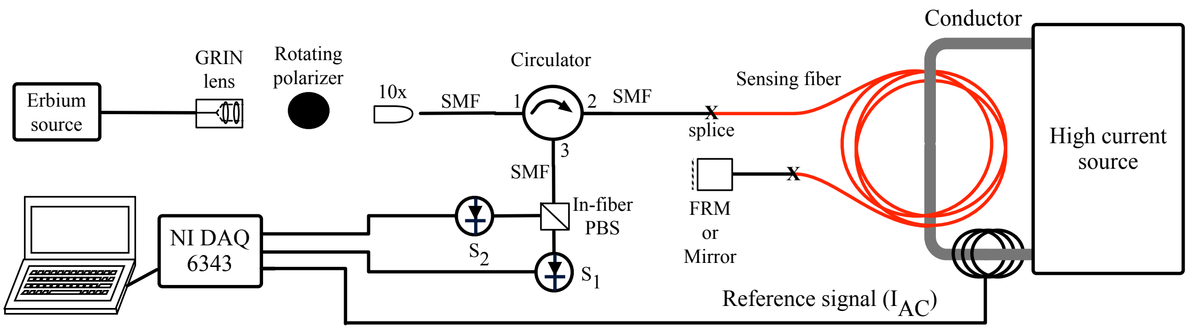

Figure 4.2 – Characterization setup of an optical fiber current sensor in operating in reflection.

The first approach consisted on using a conventional silver mirror and the same fiber coil as before (12 turns of fiber with 180 mm diameter). A DOP of 84 % was estimated for the output polarizations, with the optical sensor and the current source showing fluctuations of ±41.35 % and ±2.75 %, respectively, during a 4 h measurement, with an average current of 399 A_{RMS} passing through the conductor. In the same period, the normalized parameter S_{AC}/I_{AC} presented fluctuations around ±41.25 %. Moreover, the SNR was 35 dB, 28 dB and 29 dB for the S_1, S_2 and S signals, respectively.

Nevertheless, replacing the standard mirror with the FRM the output polarization degree increased to 98.8 % with a SNR of 48 dB, 45 dB and 47 dB for the S_1, S_2 and S signals, respectively. An error of ±26.19 % and ±1.53 % was calculated for the S_{AC} and I_{AC} signal, respectively (±26.80 % for S_{AC}/I_{AC}), during a 4 h measurement. In spite of improvements, in comparison with the transmission configurations, the great susceptibility of SMF fiber to induced birefringence still dominates the sensor operation.

In spite of all, with the configuration with the FRM providing the best results in terms of stability and SNR, the next stage consisted on calibrating the sensor response with 30 s current increments of approximately 60 A_{RMS} and up to 550 A_{RMS}, as present in Figure 4.3. The signals S_{1N} and S_{2N} correspond to the normalized orthogonal polarization (AC divided by the DC component) and S the quadrature processing. These calibrations were performed for coiling diameters of 180 mm, 120 mm and 60 mm, and distinct fibers turns.

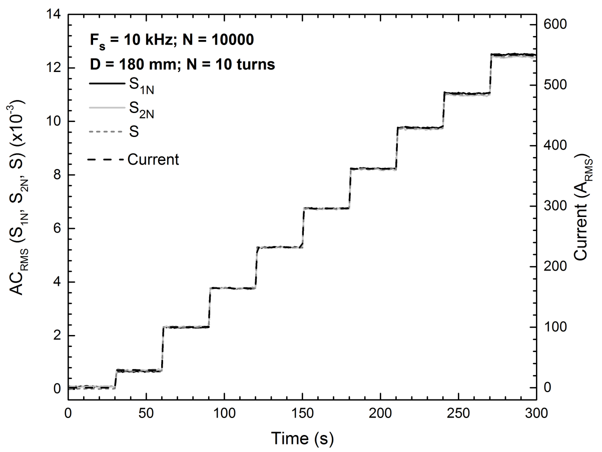

Figure 4.3 – Sensor response to step changes in the applied current using the SMF in reflection with the FRM.

For each possible measurement, two calibrations were performed and the average and standard deviation of both curves were calculated. Furthermore, the results were normalized as function of the number of fiber turns. This way according to equation (4.2), the normalized sensor response should be dependent on the number of turns, if linear birefringence is negligible. The results are presented in Figure 4.4 (a) and the fluctuations observed clearly shows that induced linear birefringence affects the sensor response, particularly for smaller coil diameters. For a coil diameter of 120 mm and 180 mm the normalized sensitivity does not change too much, contrary to the 60 mm diameter coil, where the linear birefringence due to winding increases highly and sensor response is highly degraded as function of the number of turns. According to equation (4.1) the induced linear beat length is 2.92 m, 11.67 m and 26.26 m, for the 60 mm, 120 mm and 180 mm coiling diameters, respectively. In order to better quantify the variability of the previous measurements, the average and standard deviations of the normalized sensitivities were calculated and gathered in Figure 4.4 (b). Results reveal the sensitivity is slightly higher with a coil diameter of 120 mm rather than with 180 mm, and it decreases drastically for 60 mm. The fact that the sensitivity with a coil of 180 mm diameter was lower than at 120 mm (3.94 % less) is most probably related with the coiling procedure. This process is done manually and because of it, different pressures might have been applied between the fiber and the support, leading to slightly distinct linear birefringence values. The precision error (calculated as two times the standard deviation and divided by the average value) was ±20.28 %, ±13.00 % and ±154.33 % for a coil diameter of 180 mm, 120 mm and 60 mm, respectively.

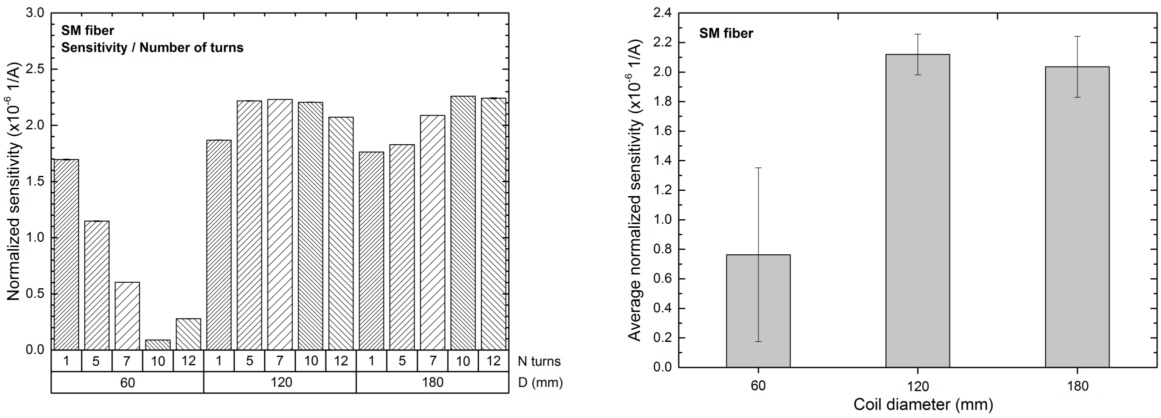

(a) (b)

Figure 4.4 – (a) Normalized sensitivity for different number of turns and (b) average normalized sensitivity for different coil diameters for the SMF.

Another set of measurements were performed in order to demonstrate the susceptibility of this fiber to induced linear birefringence. It consisted on repeating the previous measurements, but recoiling the fiber in each support before each measurement. The average and standard deviation values of the normalized sensitivity of both sets of measurements are shown in Figure 4.5. The variation shown for each bar clearly indicates that winding the fiber a second time, induced different linear birefringence. The precision error was calculated for each bar, showing an average of ±27.3 %. This result clearly suggests the fiber is extremely susceptible to induced linear birefringence due to coiling and pressure of the fiber against the support. As previously, for the smallest coiling diameter, the normalized sensitivity decreases the most with the increase of the number of turns. These results are related with a higher induced linear birefringence, when increasing the number of fiber turns.

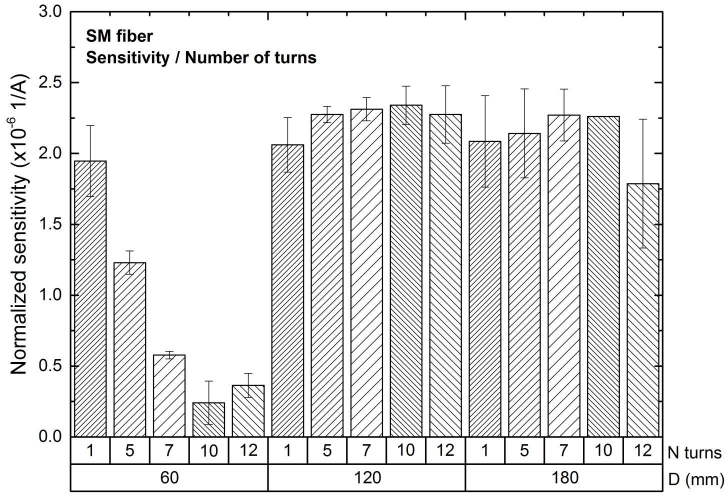

Figure 4.5 – Normalized sensitivity for a different number of turns obtained in two coiling procedures for the SM fiber.

Instability of the sensor response during the 30 s step as function of current was also calculated for the distinct coil diameters and fiber turns. However, variability of the current source was present, showing maximum fluctuations of ±0.61 %, ±11.13 % and ±0.85 %, with a coiling diameter of 180 mm, 120 mm and 60 mm, respectively, and currents up to 550 A_{RMS}. This way, the average precision (±2σ) of the optical sensor is displayed alongside the current source error in Table 4.1. Results revealed the best performance was attained with 10 fiber turns in a 180 mm coil diameter. Although it was expected a precision increase while incrementing the number of fiber turns, the experimental data did not reveal a trend for coiling diameters of 180 mm and 60 mm. This fact is due to the fiber being highly susceptible to linear birefringence and since there is not a precise pressure control of the fiber against the support, the induced linear birefringence also changes. Furthermore, the reference signal shows high instability, limiting the stability of the applied electric current during each current step, and sometimes showing fluctuations higher than the ones achieved with the optical sensor. Thereby, given the test conditions, it is not possible to estimate the intrinsic sensor resolution.

Table 4.1 – Average optical sensor and current source precision (±2σ) during each current step as function of the number of turns, obtained with the SM fiber.

Diameter (mm)	**Number of turns**					**Current source precision**
	12	**10**	**7**	**5**	**1**	
180	±2.61 A_{RMS}	±0.97 A_{RMS}	±1.63 A_{RMS}	±2.86 A_{RMS}	±12.23 A_{RMS}	±0.81 A_{RMS}
120	±0.98 A_{RMS}	±1.02 A_{RMS}	±1.16 A_{RMS}	±2.07 A_{RMS}	±9.14 A_{RMS}	±1.17 A_{RMS}
60	±6.02 A_{RMS}	±22.99 A_{RMS}	±4.53 A_{RMS}	±3.30 A_{RMS}	±10.69 A_{RMS}	±0.80 A_{RMS}

Sensor classification was also evaluated according to the electric grid requirements, using the best results obtained with the sensor with 10 fiber turns and 180 mm coil diameter. The results were calculated through equation (1.1) and are present in Figure 4.6 (modulus of the accuracy error), showing that it can be used as a class 1 sensor, with a nominal current of 700 A_{RMS}. The system used in this characterization, namely the current source, is the limiting factor in the setup, disabling the assessment of the true performance of the optical sensor performance.

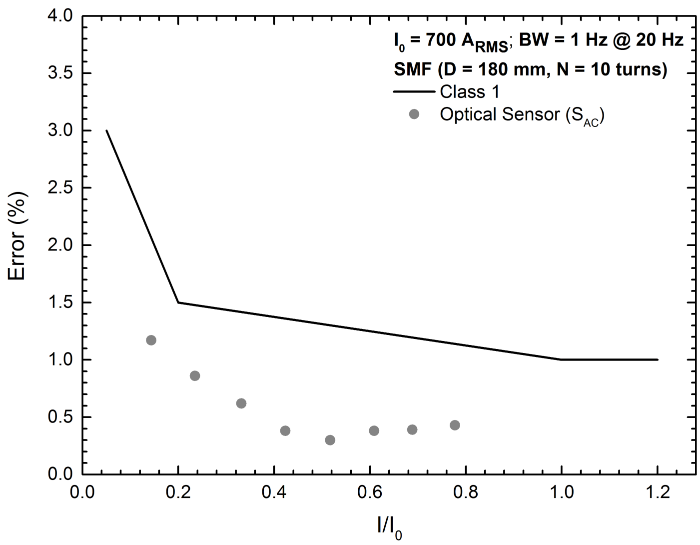

Figure 4.6 – Current sensor classification with SM fiber.

4.2 Spun HiBi fibers theory

Before introducing the sensor with the spun HiBi fibers, a brief description of the theory behind these fibers is presented, which will be further used to compare the theoretical and the experimental results. According to literature, the use of linear and circularized birefringent fibers in current sensors decreases the maximum sensitivity, in relation of an ideal fiber without birefringence (equation (4.2)), by the factors $S_{SPUN}.S_C$. However, this factor is only valid if quasi monochromatic radiation, such as provided by a single mode laser light source. For a broadband optical source, the theoretical sensitivity is given instead by $(S_{SPUN}.S_C)^2$. The first parameter depends on the linear (L_B) and circular beat length (or spin pitch), L_S, and it is expressed as [59]

$$S_{SPUN} = \frac{4\,L_B^2/L_S^2}{1+4\,L_B^2/L_S^2} \tag{4.3}$$

The second parameter, S_C, is another factor which depends on the elliptical polarization beat length (L_E) and the induced linear birefringence related with coiling the fiber (L_{ind}) and given by

$$S_C = \frac{L_{ind}^2/L_E^2}{1+L_{ind}^2/L_E^2} \tag{4.4}$$

The other parameter of S_C is the elliptical polarization beat length and it is defined as

$$L_E = \frac{L_B.L_S}{\sqrt{\left(4L_B^2+L_S^2\right)}-2L_B} \tag{4.5}$$

Nevertheless, a Jones matrix describing a Spun HiBi fiber medium in the presence of Faraday rotation, can be found in literature and it was already presented in equation (1.12).

4.3 IVG Spun HiBi Fiber

A commercial fiber designed for electric current sensors was evaluated. It is an IVG spun HiBi fiber, reference LB1300, possessing a Verdet constant at 1550 nm of around 0.5 rad/T.m [123]. The birefringence is achieved with an elliptically stressed cladding and the manufacturer certifies the fiber has a linear beat length and a spin pitch of 13 mm and 3 mm, respectively.

4.3.1 Setup in transmission

The first experiment with the IVG fiber involved assembling a setup in transmission as shown in Figure 4.1. Two broadband sources were used, an SLD with 40 nm bandwidth and an ASE (Amplified Spontaneous Emission) erbium source with 50 nm bandwidth, which was completely unpolarized. Using both sources the experiment showed it was not possible to measure any Faraday rotation, with currents up to 500 A_{RMS}, because the DOP at the output was only 0.3 %, indicating the light becomes totally unpolarized. The same setup was verified without the IVG fiber and the DOP increased to 99.4 %, validating that the remaining the components were working properly.

Replacing the broadband source with a DFB laser at 1500 nm, 1550 nm or 1600 nm in the setup of Figure 4.1, Faraday rotation could be measured with both orthogonal polarizations and a DOP of 81 % was calculated. This outcome reveals that in a transmission setup the HiBi spun fiber affects all wavelengths differently resulting in a totally unpolarized average measured signal, disabling the system measuring ability. Using a laser, on the other hand ensured the stability of the output polarization.

Sensor behavior was analyzed with 12 fiber turns in a 180 mm diameter coil. Defining a current of 442 A_{RMS} at 50 Hz passing through the conductor, the orthogonal signals of Figure 4.7 (a) were obtained having a SNR of 22 dB, 24 dB and 24 dB for S_1, S_2 and S, respectively. In Figure 4.7 (b) it is shown the optical sensor response to changing current steps of 30 s each. Results revealed high instability in each polarization, however, employing the polarimetric processing scheme improves the overall instability.

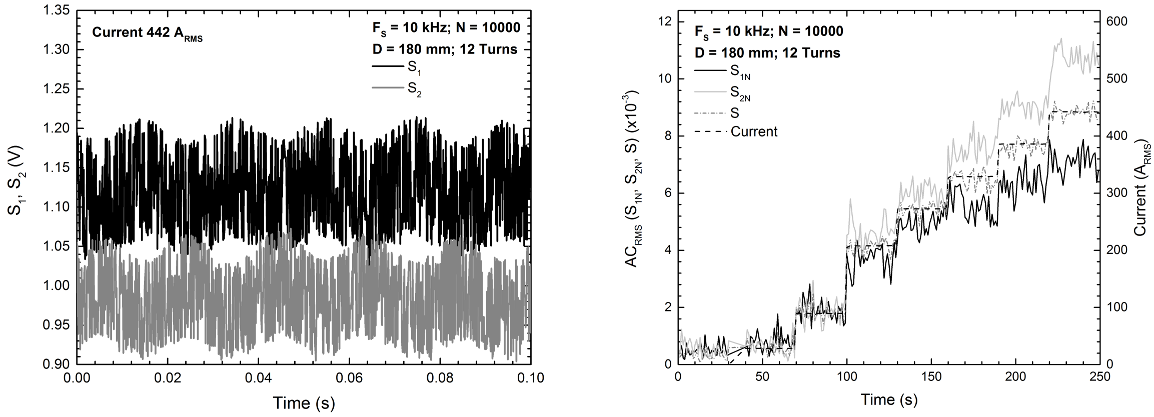

(a) (b)

Figure 4.7 – (a) Orthogonal polarizations read in the photodetectors and (b) Sensor response to step changes in the applied current using the IVG fiber in transmission.

Stability of the recovered optical AC signal was analyzed during 4 h measurement showing an error of ±101.9 % and reaching a zero response after 4 h and 8 minutes. During this experiment, fluctuations of ±3.60 % were observed in the current source, for an average current of 380 A$_{RMS}$. The normalized parameter analysed during the same period (S_{AC}/I_{AC}) showed fluctuations of ±97.63 %. This figures suggests that, in this case the limiting factor is the optical sensor stability. Indeed, it seems the relative angle between the input and output PBS is drifting and consequently affects overall sensitivity. For this kind of transmission configuration, an active compensation scheme was required to control the input polarizer and achieve better performances.

4.3.2 Setup in reflection

Using the setup already described, the IVG fiber was tested in reflection using a mirror and a FRM as demonstrated in Figure 4.8 (a). However, replacing the SMF fiber with the IVG fiber, only at the sensing coil was not sufficient to eliminate the instability in the DOP. Measurements of the DOP and of the calibration function of the sensor were performed along different days and it was verified that the polarization degree changed between 97 % and 66.4 %, and the calibration was changing by as much as ±37.5 %. These results indicate that some components of the system were still causing drift in the polarization state.

The same problems were observed when replacing the circulator (which has some polarization dependent components) with a conventional SMF coupler. After several tests, it was verified that the source of drift could be attributed to the segments of standard SMF fiber still remaining in the system.

The solution would be to replace all the SMF segments with PM fiber. However, due to lack of a suitable splice machine, to work with such fibers, the next best alternative was to reduce to minimum the SMF components, even using bulk components. Following these guidelines, the setup in Figure 4.8 (b) was implemented. It consisted in removing all the single mode fiber components, except for a short section of fiber with 300 mm containing the mirror or the FRM. The IVG fiber required a cut with an angle at the input, right after the objective, in order to prevent back reflection that was inducing some noise in the quadrature signals. With this new setup, a good stability in the DOP was observed, with a maximum and a minimum of 99.8% and 99.5 %. Also, the error in the calibration curve was also much lower and around ±0.1 %. Another configuration, similar to Figure 4.8 (b) was also tested and included splicing a single mode fiber with a GRIN lens to the IVG fiber, to replace the objective. However, during the experiments the sensor sensitivity showed a high dependence on the curvature applied to this SM fiber, so this solution was discarded, showing that even a short segment of SMF (around 2 m) can seriously compromise sensor operation.

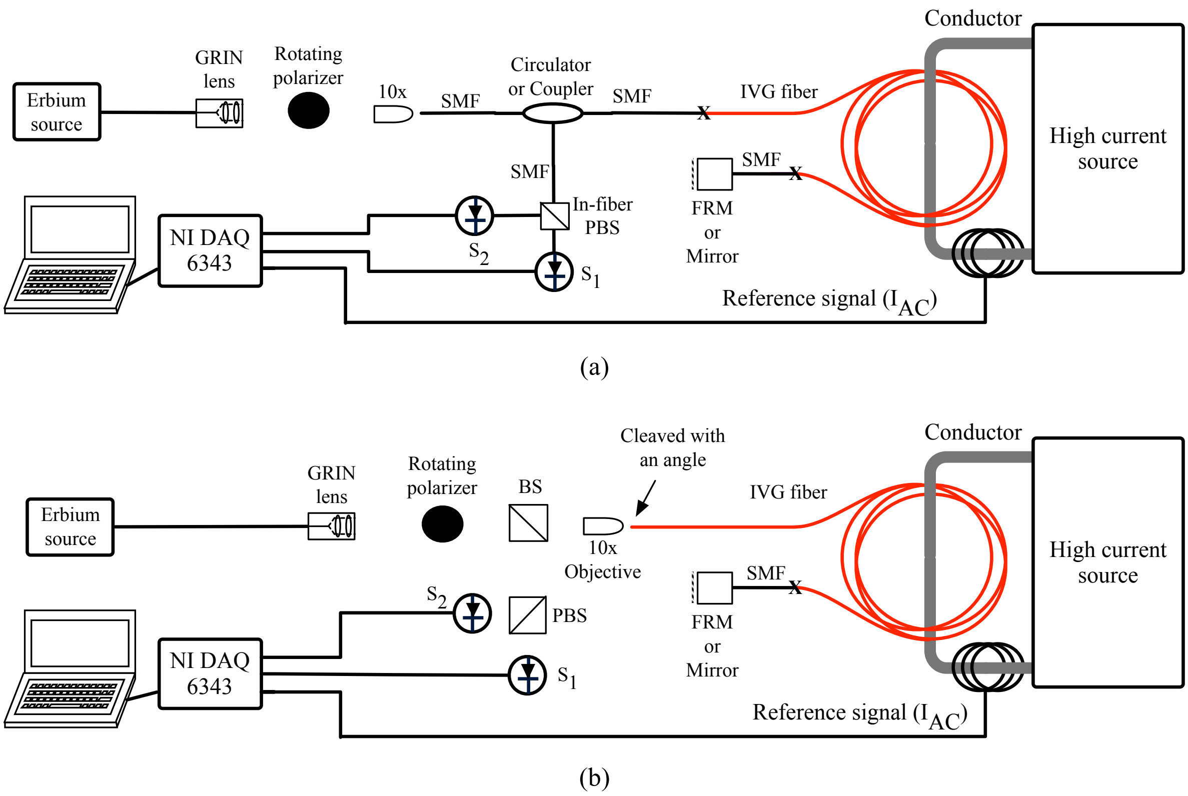

Figure 4.8 – (a) initial and (b) final characterization setup of an optical fiber current sensor in reflection for the IVG fiber.

Testing the sensor using a silvered mirror (Figure 4.8 (b)), a DOP of 90.4 % was attained and stability during 4 h measurement indicated an error of ±3.72 % and ±3.77 % for S_{AC} and I_{AC}, respectively. In addition, it was observed that in the same period the normalized parameter S_{AC}/I_{AC} showed fluctuations no larger than ±0.48 %. The SNR was also measured to be 50 dB, 51 dB and 50 dB for S_1, S_2 and S, respectively, with a current of 373 A_{RMS} at 50 Hz flowing in the conductor.

Replacing the mirror with the FRM, the DOP increased to 99.5 %, and a 4 h stability analysis revealed lower errors with ±2.13 % and ±1.98 % for S_{AC} and I_{AC}, respectively. Due to the high instability of the current source, therefore, it is not possible to evaluate properly the intrinsic response of the optical sensor. In any case, by considering the ratio between measured and applied signal S_{AC}/I_{AC}, during the tests, it was observed that it presented fluctuations no larger than ±0.38 %. This result clearly indicates the high accuracy of the optical sensor, which in this case is severely limited by the intrinsic fluctuations of the current source. The SNR was 53 dB, 54 dB and 54 dB for S_1, S_2 and S, respectively and the photodetected signals are shown in Figure 4.9 (a) corresponding to sensor response to an applied signal of 374 A_{RMS}. Comparing the SNR with the previous configurations, an improvement of 4 dB and 30 dB was obtained for the S signal, in relation to the configuration with a standard mirror and the one in transmission with the laser source. This improvement can also be seen when comparing Figure 4.9 (a) with Figure 4.7 (a), where S_{1N} and S_{2N} present much lower instability during the application of current steps than what was observed in Figure 4.7 (b) and also better agreement with the S response. This result also proves that if both orthogonal polarizations are more stable, the processed signal S will provide a better response.

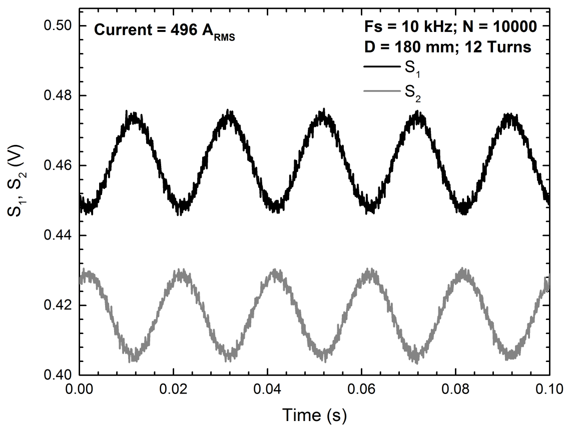

(a)

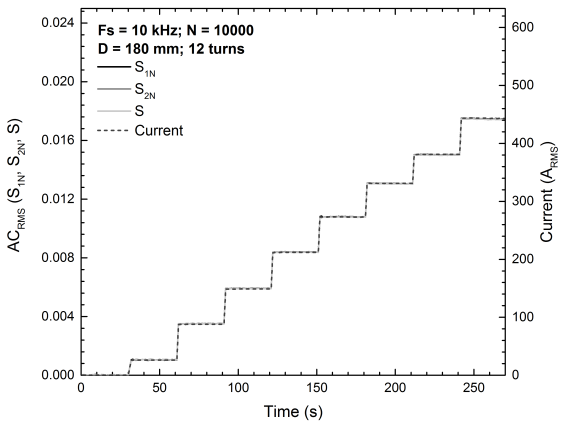

(b)

Figure 4.9 – (a) Orthogonal polarizations read in the photodetectors and (b) sensor response to step changes in the applied current using the IVG fiber and the FRM.

For each coiling diameter, the sensor response was evaluated using two independent tests with 12, 10, 7, 5 and 1 fiber turns as disclosed in Figure 4.10 (a). In Figure 4.10 (b) the average and standard deviation are calculated using a different number of turns, showing a precision error of ±0.26 %, ±0.45 % and ±1.38 %, for 180 mm, 120 mm and 60 mm coil diameter, respectively. According to equation (4.2), these errors should be close to zero, because the Faraday rotation is linearly dependent on the number of turns. However, because the sensor response is shown to be linearly dependent of number of turns and independent of the coil diameter these results prove that the spun HiBi fiber is much more robust against induced linear birefringence than the SMF.

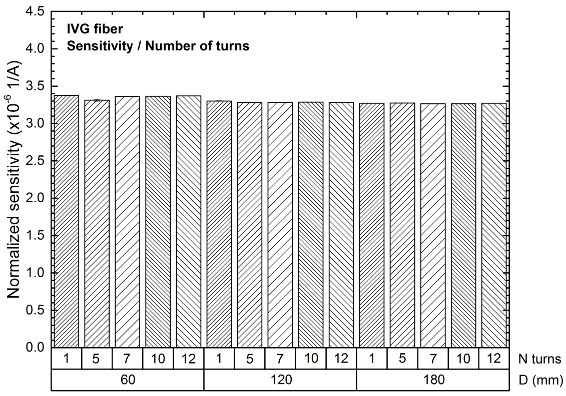

(a)

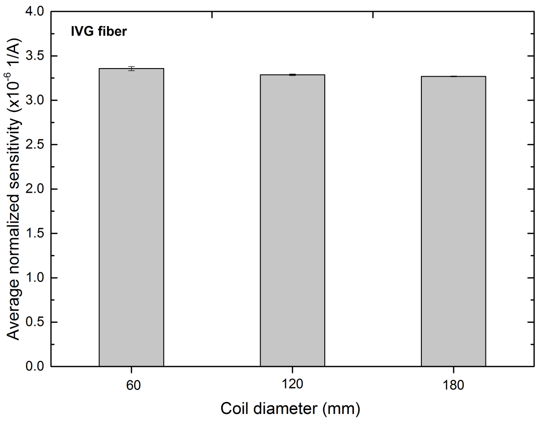

(b)

Figure 4.10 – IVG fiber (a) normalized sensitivity for different number of turns and (b) average normalized sensitivity for different coil diameters.

Susceptibility of the IVG fiber induced linear birefringence was also tested by performing two independent windings. The results (shown in Figure 4.11) demonstrated very good agreement in the calibration achieved with the two independent coiling procedures, with an average precision error of ±0.9 %. These results indeed indicate the fiber is pretty robust, contrary to the SMF fiber, where the error was as large as ±27.3 %.

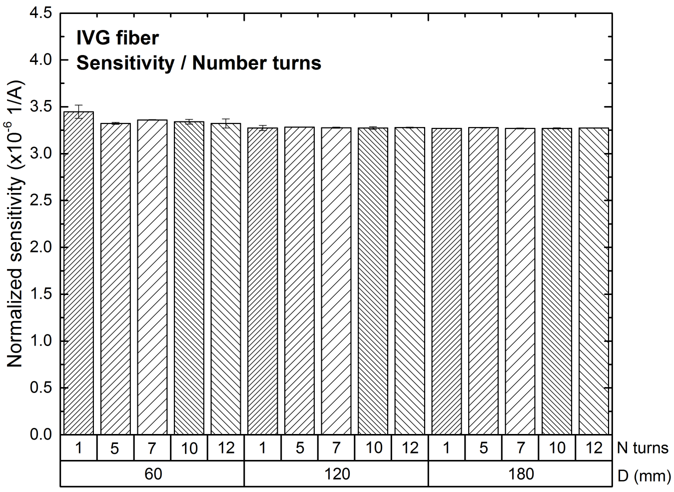

Figure 4.11 – Normalized sensitivity for a different number of turns obtained in two coiling procedures for the IVG fiber.

A theoretical study was also performed and a comparison made with the experimental results which is shown in Figure 4.12, where the normalized sensitivity is plotted as a function of the coil diameter, where the experimental values at 180 mm diameter were considered as reference. Since a broadband source is being used, the theoretical curves were calculated as $(S_{SPUN}.S_C)^2$, where each parameter is given by equations (4.3) and (4.4). Experimental results show reasonably good agreement with the experimental data with only the 60 mm coil showing a larger deviation. Indeed, experimental sensitivity is larger than expected by 3.34 %. The discrepancy in these results is probably due to fact that the induced linear birefringence is larger for smaller coiling diameters. Therefore, it is expected that the larger experimental variability is also observed in this range. Nevertheless, overall results show good agreement with the theory, in the range tested. Stronger decrease on the sensitivity should have been observed for smaller coiling diameters, however, practical limitations including the large diameter of the conductor, precluded such tests.

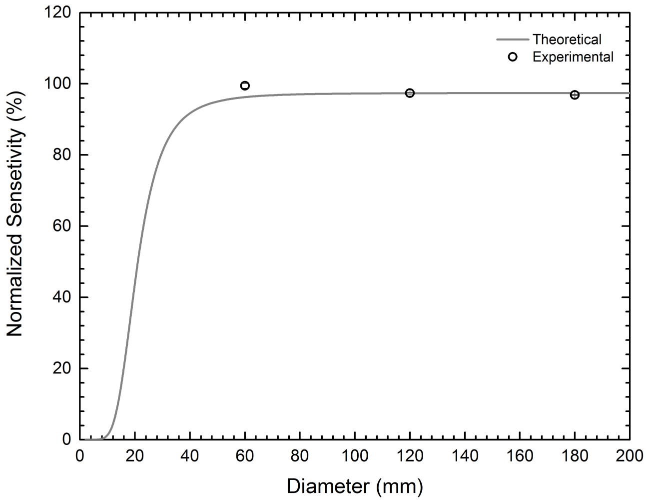

Figure 4.12 – Theoretical and experimental sensitivity.

The precision of the optical sensor and of the current source are shown in Table 4.2, as a function of the number of turns for distinct coil diameters. During the experiments, a maximum fluctuation of ±0.37 %, ±0.79 % and ±0.45 % was observed for the current source in the tests with coil diameters of 180 mm, 120 mm and 60 mm, respectively. Table 4.2 clearly shows the average estimated precision is higher with more fiber turns. However, overall, the precision of the current source are within the same order of magnitude of the estimated optical sensor precision, limiting the insight into the intrinsic sensor performance.

Table 4.2 – Average optical sensor and current source precision (±2σ) during each current step as function of the number of turns, obtained with the IVG fiber.

Diameter (mm)	**Number of turns**					**Current source precision**
	12	**10**	**7**	**5**	**1**	
180	±0.59 A_{RMS}	±0.69 A_{RMS}	±0.86 A_{RMS}	±1.11 A_{RMS}	±4.2 A_{RMS}	±0.77 A_{RMS}
120	±0.86 A_{RMS}	±0.86 A_{RMS}	±1.06 A_{RMS}	±1.27 A_{RMS}	±5.25 A_{RMS}	±1.12 A_{RMS}
60	±0.60 A_{RMS}	±0.65 A_{RMS}	±0.88 A_{RMS}	±1.08 A_{RMS}	±4.82 A_{RMS}	±0.78 A_{RMS}

Considering this data, and the sensor calibration function, the measurement accuracy was calculated and the sensor classified according to the electric grid requirements. Results shown in Figure 4.13, indicate that the sensor conforms with class 0.5 operation considering a nominal current of 600 A_{RMS}. This result was obtained with 12 turns of fiber in a 180 mm coil diameter. As previously, the system used to assess the optical sensor performance, was the limiting factor in the setup, and its intrinsic precision should allow fitting into more stringent precision classes.

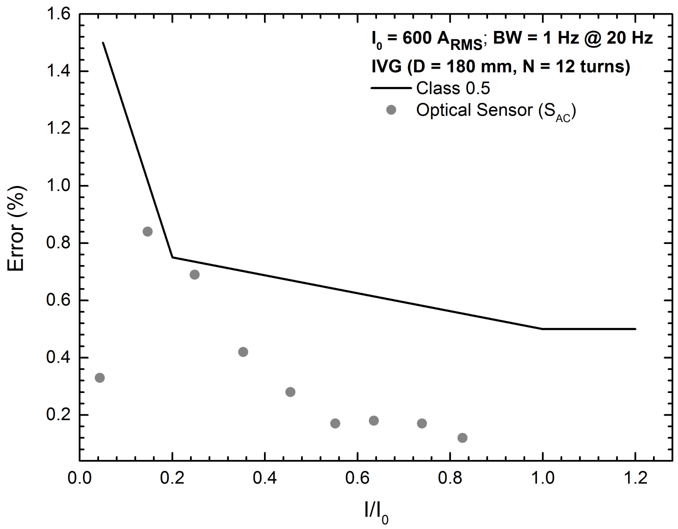

Figure 4.13 – Current sensor classification according to accuracy class. Data obtained with the IVG fiber.

4.4 Spun HiBi PCF

The preform of the photonic crystal fiber tested was fabricated by the stack-and-draw process in *Instituto de Física "Gleb Wataghin", Universidade Estadual de Campinas, UNICAMP, Campinas, SP, Brazil.* The resulting fiber design consists of five rings of periodic air holes around a central solid core of 2.6 μm diameter. The air holes have the same diameter except for two larger holes in the vicinity of the core that have 3.9 μm (Figure 4.17). The lattice parameter (diameter of the holes divided by their center-to-center distance or pitch, *d/Λ*) is approximately 0.6 and it was chosen to guarantee single-mode operation at 633 nm and consequently at 1550 nm also. The internal pressure used to control the diameter of the air holes and the ratio *d/Λ*, during fabrication, was around 100 mbar and the fiber final diameter was around 127 μm.

The spun fibers were produced by rotating this structured preform during the fiber drawing. Spin rates selected for production were 6 rps, 9 rps and 11 rps (rotations per second) and drawing velocity around 7.3 m/min resulting in a circular pitch (length of a 2π fiber rotation) L_S of 20.28 mm, 13.52 mm and 11.06 mm, respectively. These fibers originate a circular birefringence ($\theta_S = 2\pi/L_S$) of 309.9 rad/m, 464.8 rad/m and 568.1 rad/m, respectively. The linear birefringence was measured to be 2.5 × 10^{-5} (248.15 rad/m or L_B = 25.32 mm) and at 1550 nm was 3.1 × 10^{-4} (1256.64 rad/m or L_B = 5 mm) for the fiber without spun. It was assumed this value remains the same for the equivalent spun fibers. The ratio L_S/L_B gives a S_{SPUN} of 0.862, 0.933 and 0.954 for the fiber with 6 rps, 9 rps and 11 rps. For this silica fiber, the Verdet constant at 650 nm is around 3 rad/(T.m) [123].

The linear beat length was measured by the scanning wavelength method and consists in implementing an all-fiber Sagnac interferometer. A section of PCF fiber is spliced to the two outputs of the 50:50 coupler and the interference spectrum is measured with the OSA, when a broadband source is used at the input [124]. The wavelength spacing of each fringe ($\Delta\lambda$), is proportional to its central wavelength (λ) and inversely proportional to the linear birefringence, $B_L = n_{fast} - n_{slow}$ (n_{fast} and n_{low} is the slow and fast axis refractive index, respectively) and length (L) of the HiBi fiber [125]

$$\Delta\lambda = \frac{\lambda^2}{B_L L} \tag{4.6}$$

In this case, when linear birefringence is expressed as the difference between refractive indexes, the corresponding linear beat length is defined as $L_B = \lambda/B_L$.

A preliminary test was firstly done with the first batch of spun fiber possessing a circular spin pitch of 20.28 mm, using transmission setup and a laser light source at 633 nm instead of 1550 nm, because the Verdet constant is higher (around 6 times more) at this wavelength and there was not much length of fiber available. Also, it was verified that for this particular batch of fiber, guiding in the 1500 nm was very poor. Furthermore, the fragility of the PCF fiber makes it difficult to wound around the coiling supports without breaking it, and due to the air holes it was not straightforward to splice it in a reproducible fashion. The setup used is shown in Figure 4.14 and its configuration is quite similar to the one presented in Figure 4.1. However, since the laser was linearly polarized, the rotating polarizer was replaced with a half wave-plate to allow adjusting the orientation of polarization at the input fiber. The results obtained with the PCF spun fiber were also compared with a conventional single mode fiber at 630 nm from 3M (reference SM630), using the same setup.

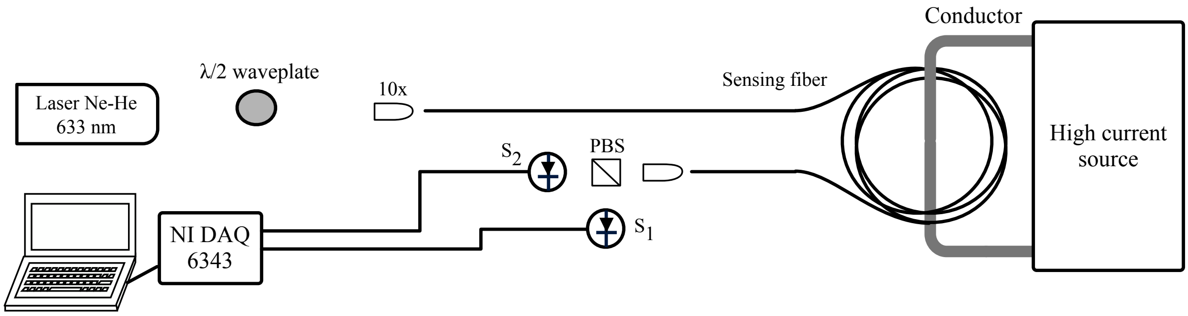

Figure 4.14 – Characterization setup in transmission of the first batch of spun PCF fiber using a laser light source.

The preliminary tests included evaluating the sensor sensitivity as function of the coil diameter and the number of turns, using the PCF and the SM630 fiber. In Figure 4.15 (a) it is revealed the sensor response as function of the applied current. High instability was observed for both orthogonal polarizations, but the processed signal *S* gave better response, as already expected. The difference in amplitude between orthogonal polarizations comes from the fact that a transmission configuration is being used, worsened by the use of a coherent source, where interference problems may increase the instability in sensor response.

In the first set of experiments a coil diameter of 60 mm was defined and the number of fiber turns was changed between 6 and 3 turns. The sensor normalized response (by the number of fiber turns) obtained with the SM630 and PCF fiber it is show in Figure 4.15 (b). In general, the PCF fiber is more robust against induced linear birefringence than the SM630, because the normalized sensitivity changes much less, with increasing number of turns (which creates increased linear birefringence).

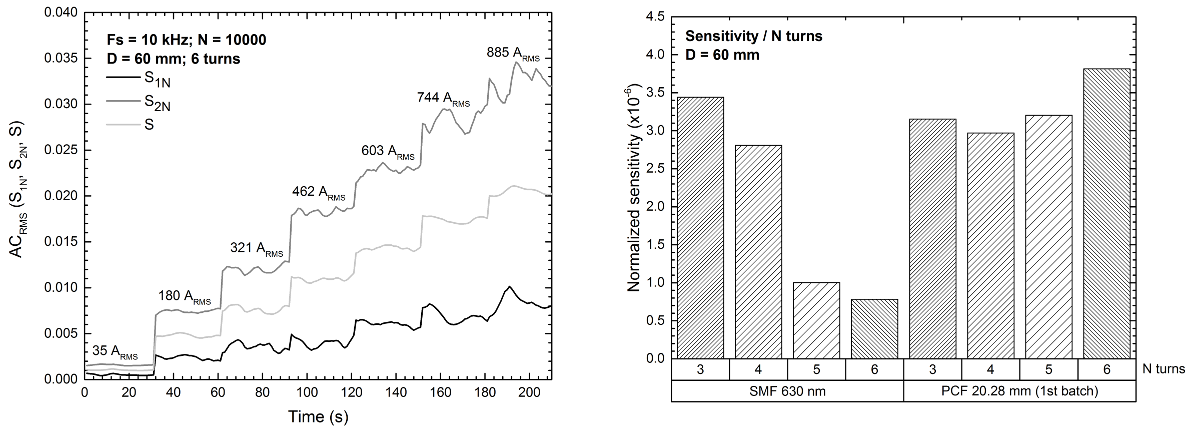

(a) (b)

Figure 4.15 – (a) Sensor response with the first batch of spun HiBi PCF fiber as function of current steps and in (b) SM630 and PCF fiber normalized sensitivity as function of the number of turns.

In order to better exemplify the variations in Figure 4.15 (b), in Figure 4.16 (a) the average and the variability of the normalized sensitivity for different number of turns is presented, showing precision errors of ±113.59 % and ±19.36 % for the SMF and the PCF fiber, respectively. Furthermore, the average normalized sensitivity was also calculated when the number of turns was fixed at 3 turns and the diameter changed between 180 mm, 120 mm and 60 mm. Precision errors of ±52.29 % and ±9.91 % were calculated for the SM630 and PCF fiber. The overall results indicate the spun PCF fiber is far more robust against linear birefringence effects than the SMF at 632 nm.

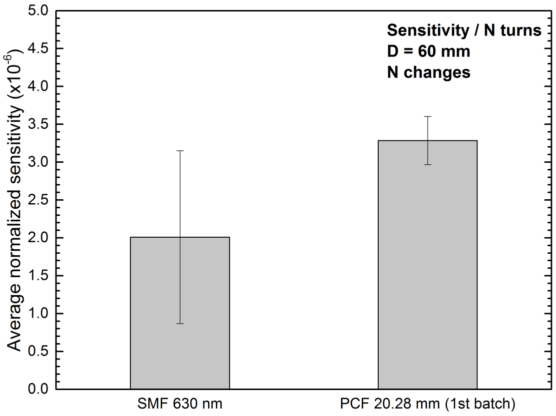

(a)

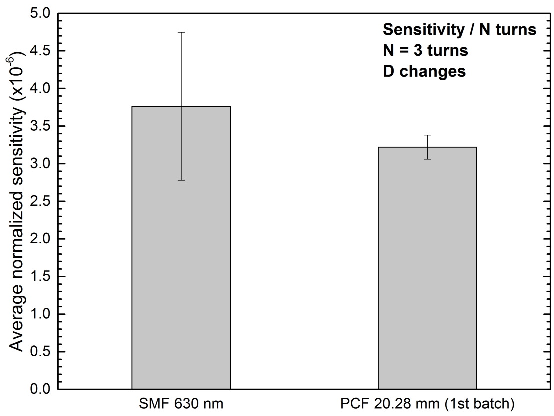

(b)

Figure 4.16 – First batch of spun PCF fiber and SMF 630 average normalized sensitivity obtained (a) with a coil diameter of 60 mm and different number of turns around the conductor (N = 6, 5, 4 and 3) and in (b) with 3 turns of fiber around the conductor, using supports with different diameters (180 mm, 120 mm and 60 mm).

These preliminary results indicated that the induced linear birefringence effects could be greatly minimized by using the spun PCF HiBi fiber fabricated has described. In spite of the encouraging results, several problems had to be solved concerning physical robustness of the fiber, and guiding at larger wavelength in the 1550 nm range. Therefore, the works proceeded and several new batches of fibers with distinct spin pitch were fabricated. In Figure 4.17 it is shown the straight section of each fabricated fiber and the corresponding mode profile at 633 nm, presenting mono-mode propagation. As observed, the fiber holes surrounding the core are not uniform and this could lead to slightly different linear birefringence values.

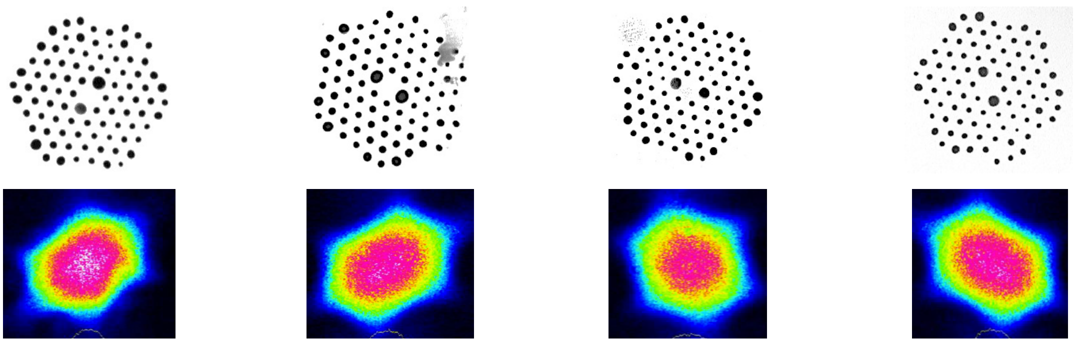

L_S = 11.06 mm L_S = 13.52 mm L_S = 20.28 mm no spin

Figure 4.17 – Straight section of each PCF fiber and corresponding mode profile at 633 nm.

For characterizing the new fibers further experiments were carried out. In tests that followed the setup shown in Figure 4.1 was used. Relatively to the previous tests performed with the first batch of fiber, the laser light source was replaced with a SLD source at 650 nm, in order to avoid interference problems that could lead to unwanted fluctuations of the orthogonal polarizations.

Previously, with the IVG HiBi fiber it was mention that no Faraday rotation could be measured in transmission with broadband sources (both an ASE and an SLD were tested). However, with the PCF fiber and using an SLD at 650 nm with only 6.2 nm of bandwidth, Faraday rotation could be measured. The DOP estimated at the system output changed according to the fiber and number of turns. For instance, for the 11.06 mm fiber, the DOP altered from 36.4 % to 46.9 %. On the other hand, for the 13.52 mm fiber, the DOP fluctuated between 15.1 % and 29.5 %. Nevertheless, for the 20.28 mm fiber, a change from 19.3 % to 53.6 % in the DOP was observed. This result clearly indicates that the HiBi fiber must also have a depolarizing effect that is dependent on the optical source bandwidth, as was observed with the IVG fiber. Nevertheless, because the SLD used had a somewhat more limited bandwidth, it was still possible to measure the Faraday rotation, which at this wavelength is much higher due to the increased Verdet constant. Similarly to what was observed with the IVG and SMF at 1550 nm, full compensation of the birefringence effects should be attained only when the sensor operates in reflection, using a FRM. Although it was not possible to effectively couple the mirror to the PCF fiber, in this particular case, it was still possible to perform a course characterization of the fibers in transmission mode.

Sensor characterization was performed by incrementing the current passing in the conductor in a step fashion at every 30 s interval. Figure 4.18 shows the calibration curves obtained for the spun fibers with 11.06 mm, 13.52 mm and 20.28 mm of circular pitch with 3 fiber turns around the conductor. The sensitivity (slope of the linear fit) decreases when reducing the coiling diameter. The unspun PCF fiber was also verified, but as expected, no measurements could be made due to its extremely high linear birefringence in relation to the small circular birefringence owing to the Faraday effect. The SNR was calculated with 750 A_{RMS} passing through the conductor, with 49 dB, 41 dB and 31 dB being obtained with the fibers with 11.06 mm (9 fiber turns), 13.52 mm (9 fiber turns) and 20.28 mm (4 fiber turns) spin pitch, respectively. The SNR reduction with the increase of the spin pitch is associated with the decrease of the intrinsic circular birefringence.

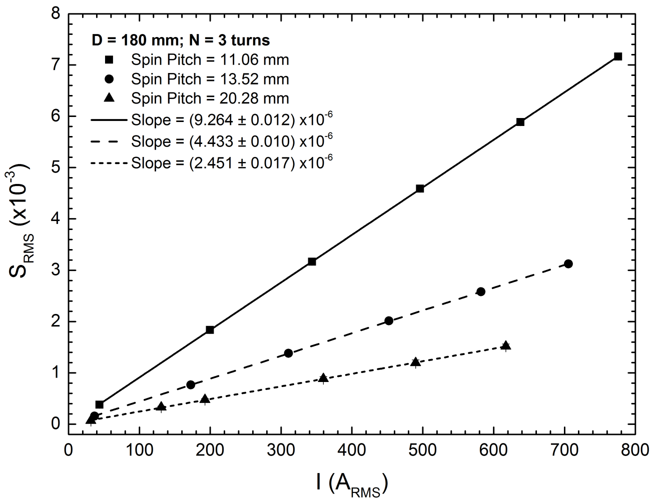

Figure 4.18 – Sensor response as function of the current for the PCF fibers with different spun rates.

In Figure 4.19 it is shown the normalized sensitivity in relation to the number of fiber turns around the conductor using different fibers and coiling diameters. For each test, two independent measurements were performed and the average and standard deviation values are indicated. For the fibers with 11.06 mm and 13.52 mm circular pitch, turns of 1, 3, 6 and 9 were tested. However, for the 20.28 mm circular pitch fiber the maximum number of turns was four due to the lack of available fiber length. Results have shown that the normalized sensitivity changes drastically as function of the number of turns.

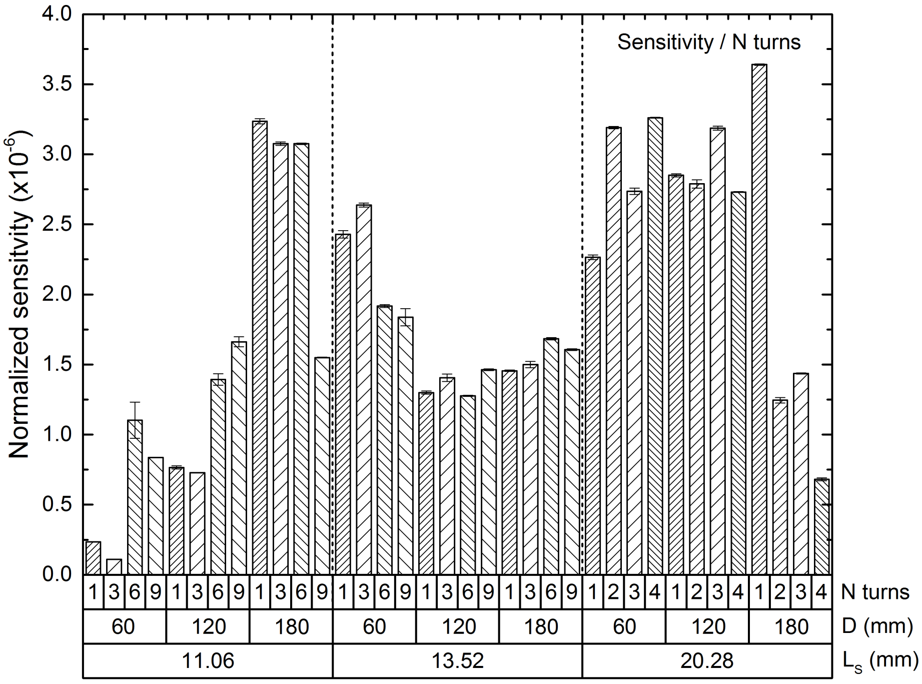

Figure 4.19 – Sensor normalized sensitivity for the three different circular pitch fibers, as function of the number of turns around the conductor for the diameters of 180 mm, 120 mm and 60 mm.

To simplify our analysis, the average of the normalized sensitivity obtained with different turns is shown in Figure 4.20. From the data, one can see that the standard deviation value in each bar is relatively high. Ideally the normalized sensitivity should have been similar for each winding diameter and fiber, but it was not the case, because the errors in each bar are excessive. The average precision error was ±54 % and the maximum and a minimum was ±144 % (60 mm coil diameter and 11.06 mm fiber) and ±11 % (120 mm coil diameter and 13.52 mm fiber), respectively. Depending on the fiber, the highest sensitivity depends on the winding diameter. Furthermore, it was expected a sensitivity decrease when reducing the coiling diameter, however this fact was only verified for the 11.06 mm fiber.

While this fiber was intended to provide immunity to induced linear birefringence, it should be taken into account, that operation in transmission works against this goal, as was demonstrated with the IVG fiber. Indeed, from the results obtained it is not clear a tendency, showing that the measurements are affected by random birefringence induced noise that should be canceled out in a reflection configuration, providing a much better performance.

Unfortunately, due to limited stock of fiber length together with its relatively high fragility, even with protective buffer, it was not possible to perform the analysis of the sensor performance in reflection.

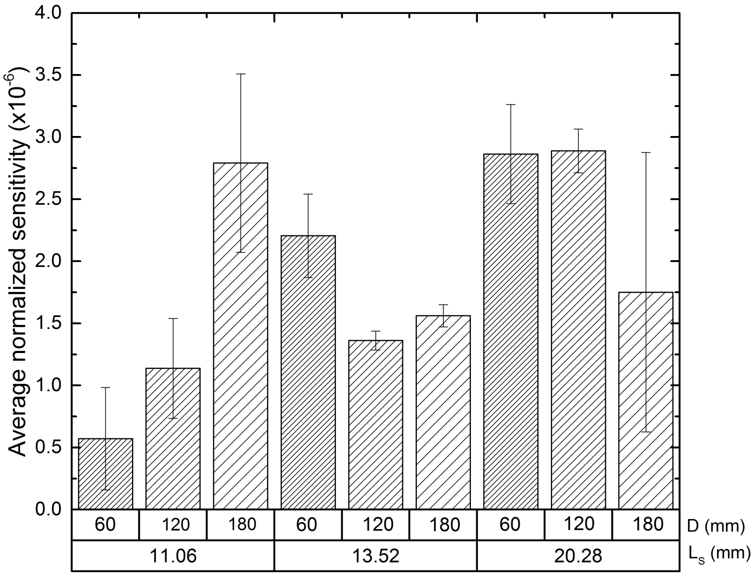

Figure 4.20 – Sensor normalized sensitivity for the three different circular pitch fibers, for the diameters around the conductor of 180 mm, 120 mm and 60 mm.

A theoretical analysis was also carried out and compared with the experimental data. In Figure 4.21 it is shown the theoretical normalized sensitivity in relation to an ideal fiber without birefringence, according to the fiber type and coil diameter. The theoretical curve was obtained by $(S_{SPUN}.S_C)^2$ and plotted along the experimental values (from Figure 4.20) for comparison purposes, with experimental values at 180 mm diameter considered as the reference. It can be seen that the theoretical and experimental results do not agree, again because due to the great variability of the experimental results it was not possible to identify any clear tendency.

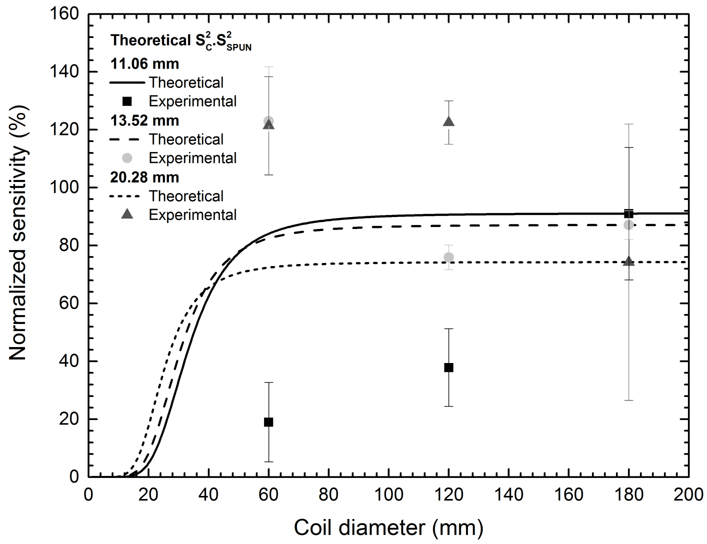

Figure 4.21 – Spun HiBi PCF theoretical normalized sensitivity in relation to an ideal circular fiber.

As with the previous fibers, the average precision of the optical sensor and the current source are shown in Table 4.3, as function of the number of fiber turns. During the experiments, precision errors as high as ±5.56 %, ±14.83 % and ±4.67 % were observed for the current source, when testing the 11.06 mm, 13.52 mm and 20.28 mm fibers, respectively. In general, the optical sensor provided worst resolutions with the fiber possessing the lower spin pitch, however, the current source presented fluctuation of the same order of magnitude. In this conditions it is therefore once more not straightforward to pinpoint any trends of the sensor performance, independent of the current source. To truly quantify the optical sensor precision, a more stable optical current source is required.

Table 4.3 – Average optical sensor and current source precision (±2σ) during each current step as function of the number of turns, obtained with the HiBi PCF, for the 180 mm diameter support from 25 A_{RMS} - 550 A_{RMS}.

L_S (mm)	Number of fiber turns; Optical sensor precision (A_{RMS}); Current source precision (A_{RMS})				
11.06	Number of turns	N=9	N=6	N=3	N=1
	Optical sensor	±3.73 A_{RMS};	±4.93 A_{RMS};	±3.10 A_{RMS};	±6.61 A_{RMS}
	Current source	±3.42 A_{RMS}	±4.73 A_{RMS}	±2.41 A_{RMS}	±4.93 A_{RMS}
13.52	Number of turns	N=9	N=6	N=3	N=1
	Optical sensor	±4.72 A_{RMS}	±2.12 A_{RMS}	±5.42 A_{RMS}	±15.74 A_{RMS}
	Current source	±4.33 A_{RMS}	±1.04 A_{RMS}	±5.38 A_{RMS}	±9.61 A_{RMS}
20.28	Number of turns	N=4	N=3	N=2	N=1
	Optical sensor	±15.41 A_{RMS}	±6.51 A_{RMS}	±12.99 A_{RMS}	±5.62 A_{RMS}
	Current source	±9.00 A_{RMS}	±4.52 A_{RMS}	±10.20 A_{RMS}	±3.65 A_{RMS}

As previously mentioned, a configuration working in reflection should improve the results. However, in order to assemble a reflective configuration with a SMF possessing a conventional mirror or a FRM is very tricky. If the arc charge is too strong, the air holes from the PCF fiber collapse easily and attenuation increases extremely. This situation was studied using the schematic shown in Figure 4.22 (a). It consists on using a conventional splicer machine to perform the fiber alignment and measure the transmission loss (the ratio of the optical power before and after the splice). In Figure 4.22 (b) it is displayed the image seen in the Sumitomo Electric Type-71C splicer machine.

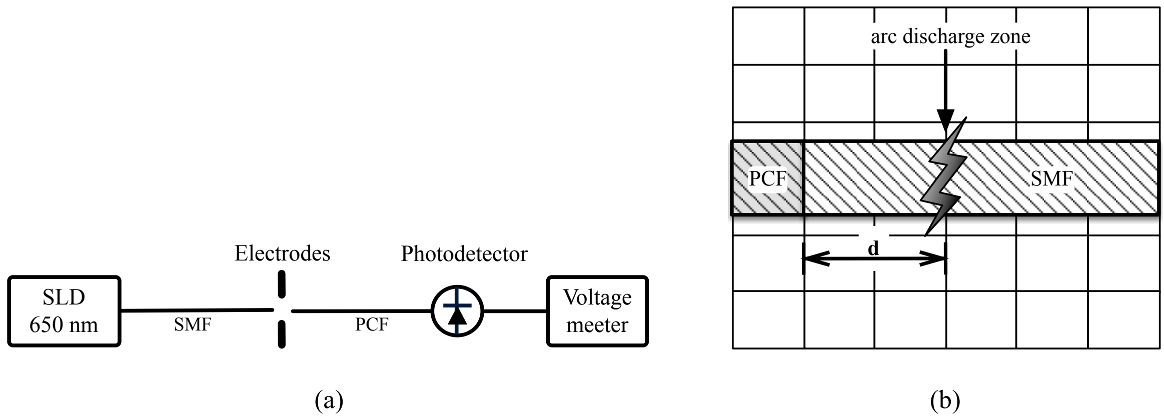

Figure 4.22 – (a) Setup for measuring the losses in the SMF-PCF splice and (b) image from the splicer.

In order to control all the splicing parameters, the machine was set in manual, including the alignment of the fibers. The duration and the arc intensity were fine-tuned until minimum loss was achievable, and for each parameter four measurements were performed. The best result was a loss of 25 % (1.25 dB) with a distance of $d = 34$ mm and a minimum arc power of -100 (unit-less parameter of the splicer). Furthermore, the splice time was 0.2 s and the duration of each arc was 15 µs. In Figure 4.23 (a) and (b) it is shown a photo of a bad and a good splice, respectively, between a PCF and SMF fiber, whereas on the left it can be seen the collapsed holes.

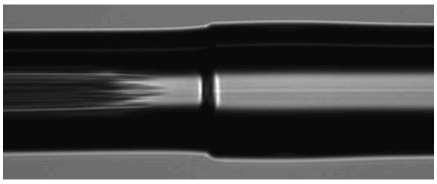

(a)

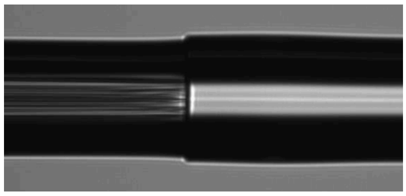

(b)

Figure 4.23 – Photo of a (a) bad and (b) a good splice between a PCF and SMF.

The results lead us to conclude that even in a reflective configuration it is still possible to perform a splice of the PCF fiber with a standard fiber, with an approximate loss 2.5 dB (43.75 %). On the other hand, contrary to SMF-PCF fusion, where the arc power was set to minimum and directed applied in the SMF (distant from the PCF), splicing PCF with PCF fibers is not an option, because the air holes of one of the fibers will collapse. The next set of experiments would be the implementation of a reflection configuration. However, due to the fragility of the fiber, breaking easily when handling and the short lengths available, no further tests were possible with these fibers. New batches are in production, in the framework of TECCON that will be used in future experiments.

4.5 Comparison

In this section a brief comparison of the results obtained with the distinct fibers is made in Table 4.4. Relatively to SMF fiber the lower error of the optical sensor was observed in transmission, followed by the FRM and the conventional Mirror. However, the DOP and SNR was much better with the FRM.

The overall results showed better performances (with enhanced DOP and SNR) in the reflective configuration using the FRM, for the IVG fiber, which means, a better precision can be achieved. Contrary to the SMF, for the IVG one, no Faraday rotation could be measured in a transmission setup using a broadband source, being only possible to measure when a laser light source was used instead. The lowest stability error was ±2.13 % and was accomplished with the IVG fiber while using the FRM, exhibiting an improvement of 7 dB of SNR in relation to the SMF. These results were clearly limited by the error of the current source, where it can be seen that the sensor was following the applied current with fluctuation of less than ±0.38 % during a 4 h measurement.

Preliminary results obtained with a first batch of fabricated spun HiBi PCF fibers, revealed that this fiber was more robust against linear birefringence than a standard SM630 fiber, being a promising candidate for all-fiber current sensors, mainly because it is expected a low temperature dependence of the Verdet constant. Moreover, with the second batch, where fibers of different spin pitch were fabricated, it was seen a SNR increased of 18 dB when the circular birefringence increased, corresponding to a spin pitch decrease from 20.28 mm to 11.06 mm.

Table 4.4 – Summary of the main characteristics of the fiber optical sensors obtained with quadrature polarimetric detection scheme.

Fiber	**Setup**	**Faraday rotation**	**DOP (%)**	***S* SNR (dB)**	**S_{AC} Error (%)**	**I_{AC} Error (%)**	**S_{AC}/I_{AC} Error (%)**
SM (1550 nm)	Transmission	Yes	85	31	±11.14	±1.84	±9.82
	Mirror	Yes	84	29	±41.35	±2.75	±41.25
	FRM	Yes	98.8	47	±26.19	±1.53	±26.8
IVG (1550 nm)	Transmission (Laser source)	Yes	81	24	±101.9	±3.60	±97.63
	Transmission	No	0.5	-	-	-	-
	Mirror	Yes	90.4	50	±3.72	±3.77	±0.48
	FRM	Yes	99.5	54	±2.13	±1.98	±0.38
PCF spun HiBi (650 nm)	Transmission	Yes			-	-	
Ls = 11.06 mm			36.4 to 46.9	49 (9 turns)	-	-	
Ls = 13.52 mm			15.1 to 29.5	41 (9 turns)	-	-	
Ls = 20.28 mm			19.3 to 53.6	31 (4 turns)	-	-	

The average normalized sensitivity achieved with both fibers are compiled in Figure 4.24. The errors in each bar accounts for the variability of the normalized sensitivity as function of the number of fiber turns around the conductor. The overall results indicate the spun HiBi fiber provides higher sensitivity and lower errors than the SMF, because it is less susceptible to induced linear birefringence effects.

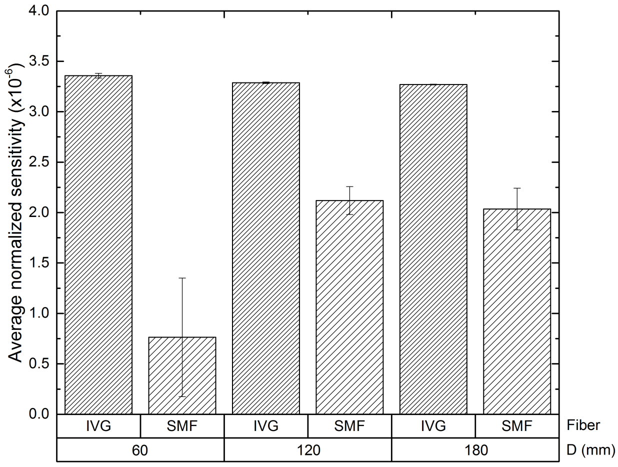

Figure 4.24 – (a) Average sensitivity divided by the number of fiber turns as function of the coil diameter.

Classification of the sensor accuracy with both fibers according to the accuracy classes of the electric grid are combined in Figure 4.25. The IVG fiber showed better performance, satisfying 0.5 class operation with a nominal current of 600 A_{RMS} while the SMF presents as a class 1 sensor with a nominal current of 700 A_{RMS}. Again, these results can certainly be improved considering that the intrinsic precision of the sensor, is much higher than the observed accuracy, which was limited by the intrinsic fluctuation of the current source.

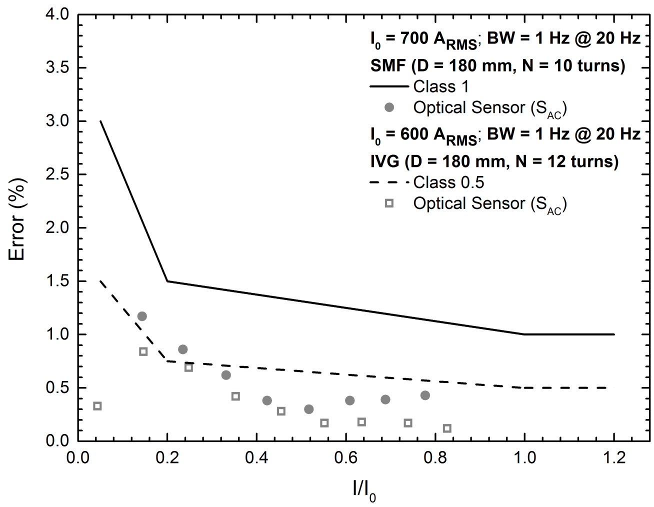

Figure 4.25 – Current sensor classification with IVG and SMF fiber.

Additionally, to verify that the linear birefringence plays an important role on the sensor response, deformation was applied to a coil having 12 fiber turns and 60 mm in diameter as presented in Figure 4.26. The pressure was done against the 12 fiber turns, using a rod of 12 mm cross-section, attached to a translation stage.

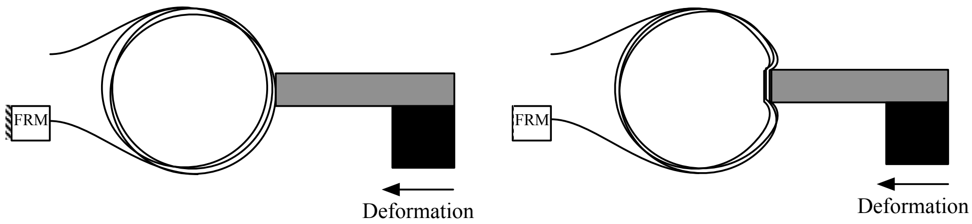

Figure 4.26 – Setup used to apply deformation in the IVG and SMF fiber, using a rod of 12 mm cross-section attached to a translation stage.

For each fiber, three independent measurements were performed, where the optical sensor response, *S*, was recorded while deforming the coil, with a constant current passing throw the conductor. The results are shown in Figure 4.27, and the IVG fiber proved to be quite robust against deformation, decreasing to 99 % with 1.5 mm deformation and to 96 % with 4 mm. However, the standard fiber is very susceptible to deformation above 1 mm, decreasing to 50 % with only 3 mm deformation.

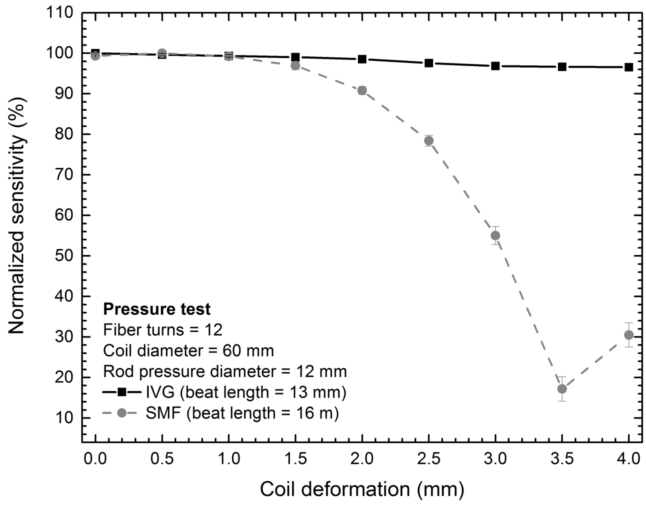

Figure 4.27 – Optical sensor normalized sensitivity as function of the applied deformation for the IVG and SMF fiber.

Fibers susceptibility to vibration was also analyzed using the setup in Figure 4.28. It consists of a speaker that applies a sinusoidal modulation with 0.62 V_{RMS} amplitude. The stability was tested with both fibers with frequencies of 120 Hz, 600 Hz, 700 Hz and 1000 Hz, but no resonances in the FFT spectrum of the processed signal (*S*) were found.

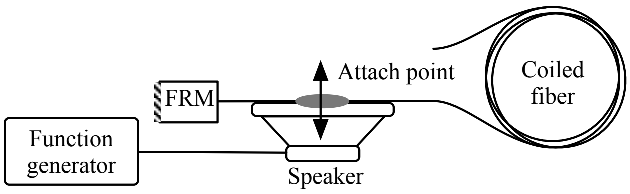

Figure 4.28 – Setup used to apply vibration to the fiber.

4.6 Summary

In this chapter a quadrature polarimetric interrogation scheme was implemented in order to evaluate standard and spun HiBi fibers in optical current sensing. Results revealed much better performances (stability and SNR) while operating in a reflection setup with the IVG fiber, a commercial spun HiBi fiber. The use of a FRM mirror is highly recommended instead of a conventional one, because perturbations in the SOP owed to reciprocal linear and circular birefringence effects are compensated. As already expected from the literature, the use of SMF is not adequate for this kind of sensor, because it is very susceptible to induced linear birefringence, owed to coiling and pressure, with the sensitivity reducing 50 % with 1 mm deformation. On the other hand, the sensitivity only decreased by 1 % with 1.5 mm deformation, with the IVG fiber.

Nevertheless, with the SMF fiber, the results could comply with a class 1 sensor for a nominal current equal or higher than 700 $A_{RMS.}$ Best performance was accomplished with the IVG fiber, however, with results complying with class 0.5 for a nominal currents higher than 600 A_{RMS}.

A new fiber, a spun HiBi PCF, which is expected to have low temperature dependence and monomode propagation in a wide range of wavelengths, was also tested, but only in a transmission configuration, due to experimental constrains. The results revealed this fiber is more robust against linear birefringence than the standard one, but due to its fragility and lack of fiber, it was not possible to implement a reflective configuration.

Increasing the number of turns should also improve the sensitivity and resolution of the sensors, but in order to prove it a more stable current source is needed, but at the time no better equipment was available at the laboratory.

Nevertheless, promising results were achieved with PCF HiBi fibers, where it was observed that higher circular birefringence (lower spin pitch) fibers were preferable, providing better precision. In general, the optical sensor provided higher SNR with the fiber possessing the lower spin pitch (higher circular birefringence), however, the current source precision was also better, contributing to better results with the optical sensor. As a future work new batches of highly spun HiBi fibers are going to be fabricated, in the TECCON II project, and tested in a reflective configuration, with a conventional silver mirror and a FRM. Moreover, a more stable optical current source will be acquired to truly quantify the sensor precision.

Chapter 5 Laser based sensors for magnetic field measurement

Fiber optic lasers are attractive elements for magnetic field sensing since they provide high SNR (Signal to Noise Ratio) and narrow bandwidth. In this chapter, erbium doped optical fiber laser configurations are proposed and characterized as magnetic field sensor devices. Erbium doped fibers were used as the active medium, with emission in the 1520 nm to 1570 nm range. The goal is to build optical fiber lasers modulated in wavelength or in emission power according to the magnetic field to be measured. To accomplish this, a magnetostrictive rod is attached to the FBG based cavity mirrors, stretching them as function of the applied magnetic field and consequently modulating the laser emission accordingly.

Laser wavelength changes are then analyzed by feeding the laser output into a passive interferometer built with a 3×3 coupler, acting like a wavelength-intensity converter and providing a very accurate and low cost solution. Additionally, an alternative demodulation technique is proposed using an LPG instead of the interferometer.

Finally, for configurations where the magnetic field information is encoded in a modulation of the emission power, a much simpler acquisition setup is implemented by measuring the ratio between the detected AC and DC power.

5.1 Wavelength-intensity converters

Before introducing the optical fiber laser configurations developed in this work, a description of the two strategies used to perform a wavelength-intensity conversion, in order to enable the readout of the laser output using simple photo detection, is made.

5.1.1 Interferometric readout system

Figure 5.1 shows the schematic of the interferometric readout system that was assembled. It consists on a passive interferometer with an OPD of 3.96 mm resulting in a free spectral range of 594 pm and 602 pm between interferometric fringes at 1534 nm and 1544 nm, respectively.

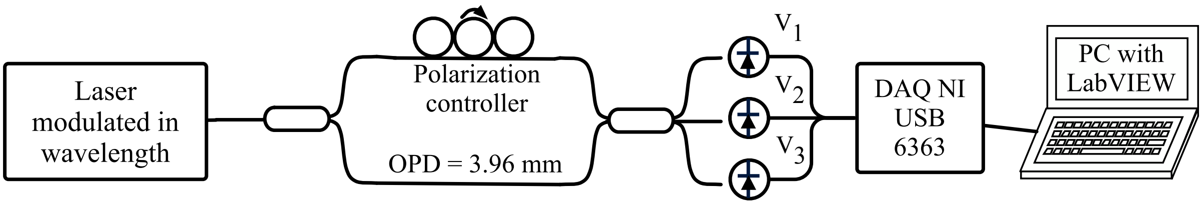

Figure 5.1 – Passive acquisition set-up based on a three port interferometer.

By using a 3×3 coupler at the interferometer output, three signals are obtained at the output ports having a 120 degrees relative phase difference which are described by [126]

$$V_n = A_i + B.\cos\left[\varnothing(t)+\varnothing_{DC}-(n-1)\frac{2}{3}\pi\right] \tag{5.1}$$

where n is the output 1, 2 and 3, A_i is the DC component obtained when sweeping one period of the interferometer, B is the visibility of the fringes which is maximized by a polarization controller (PC), $\varnothing(t)$ and $\varnothing_{DC}$ is the time varying and DC interferometer phase, respectively. The parameter $\varnothing(t)$ is related with the laser wavelength modulation and $\varnothing_{DC}$ is dependent on the laser DC wavelength and slow temperature fluctuation in the interferometer. In such configuration, any change in the laser emission wavelength results in a change of the interferometer optical output phase ($\varnothing(t)$ and $\varnothing_{DC}$), proportional to the OPD. This way, the interferometer acts like a wavelength-to-intensity converter enabling to track the wavelength changes, induced by the magnetic field, very accurately and with low cost instrumentation.

This interferometer has the advantage of not needing an active element to avoid total output fading. The relative phase of the three outputs and the signal processing can always retrieve the relevant output information, independent of the random drift of the interferometer. Nevertheless, the interferometer drift is mixed with the DC phase changes, also affecting the output intensity and limiting the application of this scheme to AC measurements. In any case, magnetic field measurements were performed in a temperature-controlled environment, in order to avoid thermal drifts.

A 16 bits analogue-digital converter from NI (National Instruments) with 305 μV resolution and 2 Mbps bandwidth is used to read the three outputs of the interferometer. The same system was also used to read the current signal from the inductor that was generating the magnetic field to be measured. In this way, the use of virtual instrumentation allows a straightforward way to test and implement any signal processing algorithm, by simply adjusting the software, offering a much higher versatility and scalability. Therefore, to test the versatility of virtual instrumentation systems, a LabVIEW program was developed to process the interferometric signals, and to implement, interchangeably, two distinctive demodulation methods. For this interferometer, a modular receiver system containing three photodetector circuits with adjustable gain were developed (schematic is shown in Appendix D). For each photodetected signal, two outputs were available, one with the DC and AC signal and the other with only the AC information but with higher gain.

The schematic of the first signal processing scheme (type I) is presented in Figure 5.2 and consists on performing derivatives and an integration as demonstrated in reference [126]. The output only contains the varying phase information and, in order for this method to work properly, the values of A_i must be the same for the three outputs, which is achieved by introducing an adjustable gain in each photodetected signal. Considering the previous assumption, the parameter A_i is subtracted from each interferometric signal, obtaining signals a, b and c. Performing the derivate of each of them, followed by some simple arithmetic calculations, the signals g, h and i are added, attaining

$$\mathrm{N} = \frac{3\sqrt{3}}{2}\mathrm{B}^2\varnothing'(\mathrm{t}) \tag{5.2}$$

where $\varnothing'(t)$ is the derivative of the signal of interest. This result also shows that the DC phase information was lost. The visibility, B, varies as a function of the laser intensity, temperature and polarization, and it is retrieved by summing the squares of a, b, and c, obtaining

$$D = \frac{3}{2} B^2 \tag{5.3}$$

The visibility dependence is then removed by performing the ratio of *N* by *D* and after the integration, the time varying signal (containing the wavelength information) is recovered.

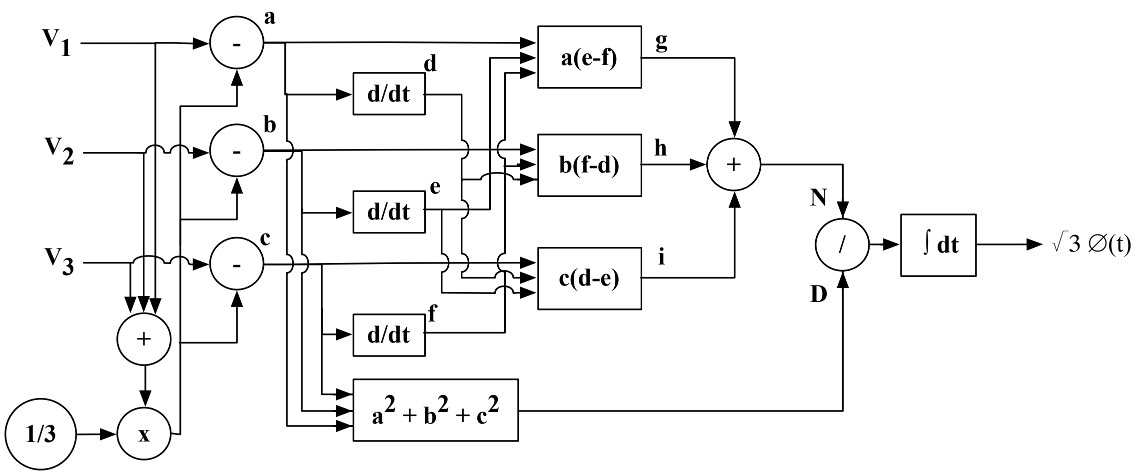

Figure 5.2 – Type I processing diagram.

The alternative algorithm (type II) consists on simply performing the Arc tangent function of the signals provided by the detectors [127]

$$\emptyset(t)+\emptyset_{DC} = \mathrm{ArcTan}\left[\frac{\sqrt{3}(\alpha_3 V_2-\alpha_2 V_3)}{\alpha_3 V_2+\alpha_2 V_3-2\alpha_2\alpha_3 V_1}\right] \tag{5.4}$$

where $\alpha_2 = A_2/A_1$ and $\alpha_3 = A_3/A_1$. If the three outputs have the same gain then $\alpha_2 = \alpha_3 = 1$. Although in this case it is also possible to recover the static phase information, the interferometer drift is also present, furthermore this method also requires an unwrapping algorithm to compensate phase changes larger than $\pm\pi$.

The laser emission wavelength is temperature dependent, due to the intrinsic FBGs response to temperature and also the strain induced by the Terfenol-D rod due to its thermal expansion. At the output of the interferometer this effect will be mixed with the random drift of the interferometer. Using type I method this DC effects are automatically excluded, on the other hand, with type II method the output will still contain the slow drifts induced by the temperature effects, which can, nevertheless be removed by filtering the AC response.

5.1.2 LPG readout system

Another approach consists on replacing the passive interferometer readout system with a plain LPG. The configuration is shown in Figure 5.3 (a) and involves an LPG with a steep transmission curve, whose slope overlaps with the laser wavelength (Figure 5.3 (b)). S_{MOD} is the signal transmitted through the LPG, containing the AC information and S_{REF} is obtained bypassing the LPG, and used as a reference to compensate any power fluctuations. Since the LPG is temperature dependent, it is maintained at constant temperature with a homemade peltier system, capable of providing 0.5 ºC stability.

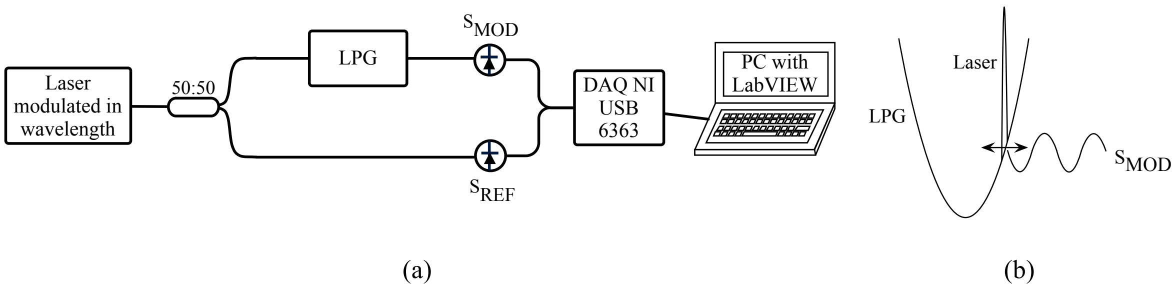

Figure 5.3 – (a) Setup for laser interrogation using an LPG; (b) LPG and Laser spectral profile.

5.2 Magnetostrictive material

The transducer used in the laser sensor applications is a magnetostrictive rod of Terfenol-D (composition $Tb_{0.27}Dy_{0.73}Fe_2$) having a cross-section of 5 mm and 100 mm in length. In Figure 5.4 it is shown the Terfenol-D rod response as function of the applied magnetic field. The Up and Down curves indicate the material response when incrementing and decreasing the field, respectively. According to the manufacturer the saturation of the material is around 510 mT and the frequency response, subject to the material thickness, is around 100 kHz. The material expansion in the presence of a magnetic field is non-linear and independent of the negative and positive sign of the magnetic fields.

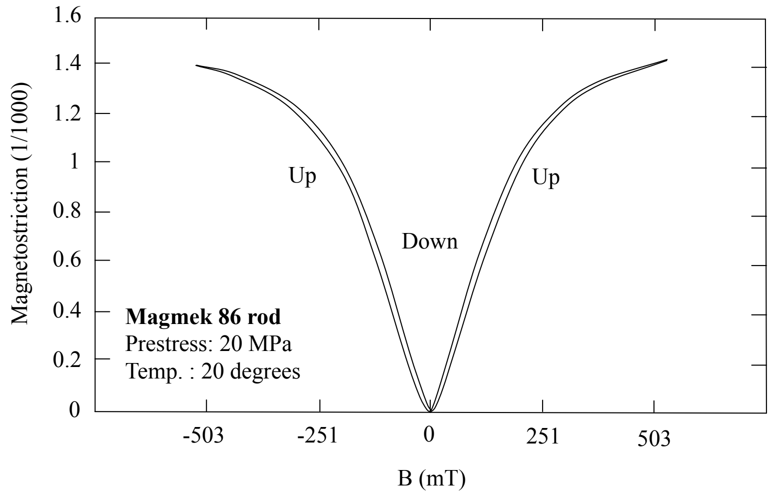

Figure 5.4 – Manufacturer Terfenol-D response.

5.3 Loop configuration

The first sensor tested was an optical fiber laser in a loop configuration, the corresponding schematic setup is shown in Figure 5.5. The laser cavity is constituted by 6.8 m of erbium-doped fiber (Fibercore M5) acting as the gain medium, a circulator, a polarization controller and an in-fiber polarizer, defining a total cavity length of 23 m. The polarization controller (PC) in conjunction with the fiber polarizer is responsible for introducing losses in a controlled fashion, enabling the possibility to operate in a single polarization. The transducer is the Terfenol-D rod described earlier and it is glued to a HiBi FBG (which acts as a selective mirror) in two points, 60 mm apart. A function generator, a current amplifier and an inductor are used to generate an average magnetic field with a relation of 11.9 mT/A along 60 mm. In the presence of a transverse magnetic field the rod stretches and, consequently, the laser wavelength operation changes accordingly. The FBG was inscribed by sequential writing in a HiBi fiber (Fibercore HB1250) using a 1067 nm period phase mask with a UV laser.

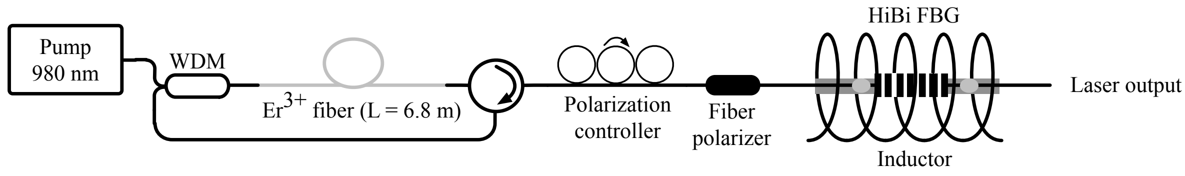

Figure 5.5 – Optical fiber laser setup based on a loop configuration.

In Figure 5.6 it is shown the transmission spectrum of each polarization, acquired with a 20 pm resolution, obtained by polarizing a broadband source and controlling the polarization state. The spacing between both polarizations is 377 pm and it is associated with the linear birefringence of the fiber. A reflectivity of 2.9 dB (48.7 %) and 2.5 dB (43.8 %) was attained for *X* and *Y* polarizations, respectively and the spectral bandwidth of each polarization is around 40 pm at -1 dB.

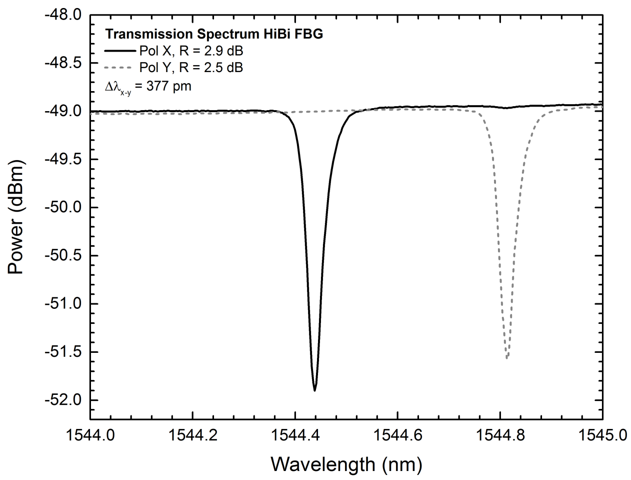

Figure 5.6 – Transmission spectrum of HiBi FBG showing both polarization modes.

By adjusting the polarization controller of the laser setup (Figure 5.5) it is possible to select the polarization mode of operation and setting the laser emission wavelength accordingly, as displayed in Figure 5.7.

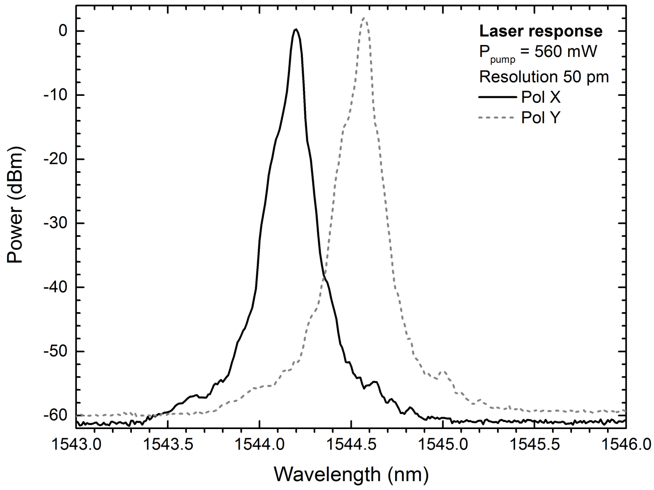

Figure 5.7 – Laser loop spectrum with polarization *X* and *Y*.

Since each polarization has distinct reflectivity, depending on the selected polarization mode the output power was different as can be observed in Figure 5.8. A maximum laser power of 3.9 mW and 5.5 mW was achieved for *X* and *Y* polarizations, respectively, with a 377 mW pump power and a threshold of 80 mW. For pump levels above 380 mW the laser also starts to lase at 1532 nm, despite the FBG being centered around 1544 nm. This happens because erbium has the peak emission cross section at this wavelength, and at high pump levels the laser reaches the threshold level very easily with unwanted small reflections.

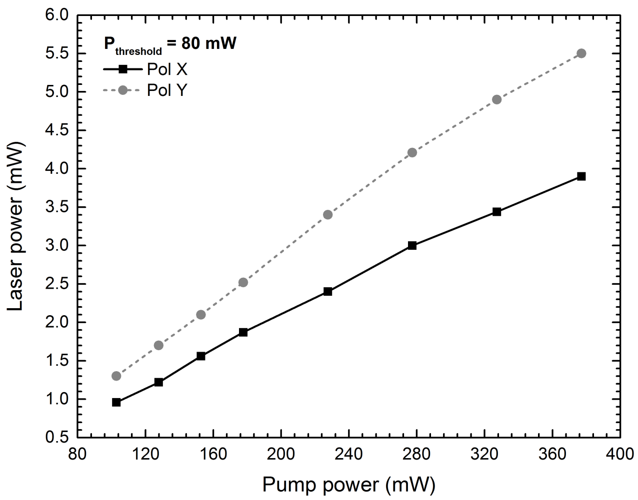

Figure 5.8 – Laser loop output power as a function of the pump power.

The laser spectral width was measured by coupling a tunable laser (100 kHz bandwidth) with the developed laser sensor. In the frequency domain, the convolution of both incoherent signals is read with a 50 GHz photodetector and an Electric Spectral Analyzer (ESA). Since the spectral width of the tunable laser is very narrow when compared to the fiber laser, the result output yields the spectral shape of the fiber laser, centered at the beat frequency of both lasers [128]. In Figure 5.9 it is shown the laser spectrum obtained with the ESA, with a spectral width of 25.8 MHz (0.20 pm at 1544 nm), observing at least three longitudinal modes in each polarization.

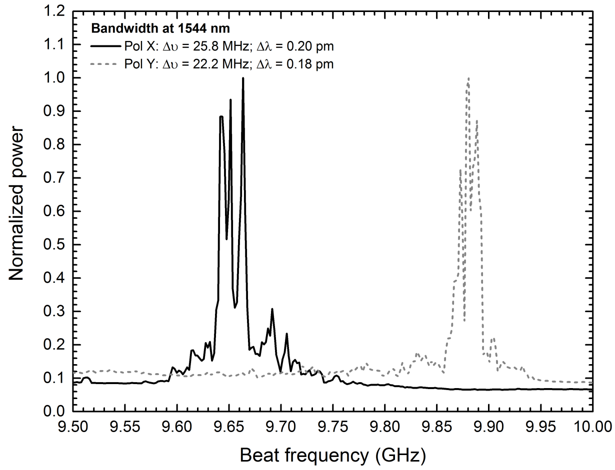

Figure 5.9 – Loop laser spectral width.

The corresponding linedwidth ($\Delta\lambda$) in meters is calculated using the following expression

$$\Delta\lambda = \Delta\upsilon \frac{\lambda^2}{c} \tag{5.5}$$

where $\Delta\upsilon$ is the laser linewidth in frequency.

Laser stability tests were also conducted during one hour for each polarization state, using a photodetector and an oscilloscope connected to a computer. Recording at a sampling frequency of 2 Hz, during one hour, low power fluctuations of ±3 % and ±3.4 % could be estimated, for polarization *X* and *Y,* respectively. These fluctuations were calculated as half the difference between the maximum and the minimum, divided by the average value. This laser showed high power stability and since it is intended to measure alternating magnetic fields, these slow frequency power fluctuations do not influence the processed signal, resulting from the read out interferometer.

5.3.1 Terfenol-D response for DC magnetic field

Although the Terfenol-D response as function of the magnetic field had already been described considering the manufacturer specifications, the set of laser and magnetostrictive material was also characterized by applying several DC magnetic fields from 0 to 18 mT, with an inductor, and measuring the laser response with a wavelength meter (Burleigh WA-1650 with 0.5 pm resolution). Figure 5.10 shows the magnetostrictive response of Terfenol-D driving the laser emission wavelength, the hysteresis cycle was obtained with three independent tests when the magnetic field goes up and down. The error bars correspond to the standard deviation of the three independent measurements, and account for the repeatability of the sensor, or the measurement precision. The worst precision (±2σ) registered was of ±4.5 pm at B = 5.95 mT (±11.76 % precision error) for the up curve and ±10.7 pm at B = 8.33 mT (±12.74 % precision error) for the down curve. Due to limitations of the experimental instrumentation it was not possible to attain magnetic fields higher than 17.85 mT, resulting in a maximum attainable wavelength shift of 258.5 pm, a first order sensitivity of ~14.48 pm/mT.

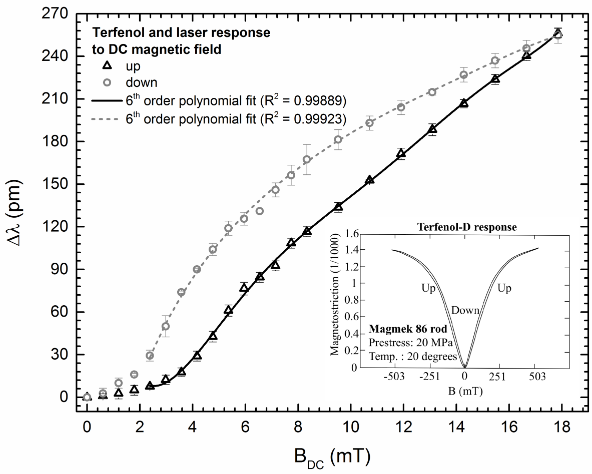

Figure 5.10 – Loop laser wavelength shift due to the applied magnetic field. In the inset the material response according to the manufacturer.

The non-linear behavior of the calibration curve is intrinsic to the Terfenol-D response to DC magnetic fields, as can be seen in the inset of Figure 5.10, where a representation of the manufacturer Data-sheet is given (notice that an rod without prestress/compression of the bar, was used, therefore saturation is reached with an applied field smaller than the one presented in the inset of Figure 5.10). The material expansion in the presence of a magnetic field is non-linear and independent of the negative and positive sign of the magnetic fields. Therefore, when no bias magnetic field is applied, the application of an AC magnetic field results in a response that is doubled in frequency. Moreover, since the transducer is intrinsically non-linear, different DC biasing points will result in different sensitivities to AC fields. Hysteresis is an additional problem for DC measurements that can be overcame with specific setups [129].

5.3.2 Response to distinct bias magnetic fields

The laser response to alternate magnetic fields (AC) at 20 Hz was characterized using different constant magnetic fields (DC), with the setup presented in Figure 5.1. This frequency was chosen as a compromise between SNR and magnetic field amplitude, avoid higher noise from the grid frequency (50 Hz), and compromising with the fact that the inductor impedance increases with frequency, limiting the maximum current provided by the amplifier and therefore the magnetic field amplitude.

The acquisition system was set with 10 kHz sample frequency and 10000 acquisition samples, also a low pass filter with 200 Hz cut-off was applied to each input signal, before processing the three outputs of the interferometer. The AC RMS value was then retrieved after filtering the demodulated signal with a second order Butterworth band-pass filter of 5 Hz bandwidth.

Figure 5.11 shows the RMS AC response for different AC steps during 30 s each, when no DC magnetic field is applied. The results were obtained with the demodulation process type II and the label values shown in each step correspond to the average value. The alternating signal is filtered using a band-pass filter with 5 Hz bandwidth at the second harmonic of the modulation frequency, due to the symmetric response of the magnetostrictive material as function of the magnetic field. The maximum and minimum precision error was ±3.43 % for 8.10 mT_{RMS} and ±1.73 % for 12.03 mT. A more detailed analysis is present later, including distinct bias fields.

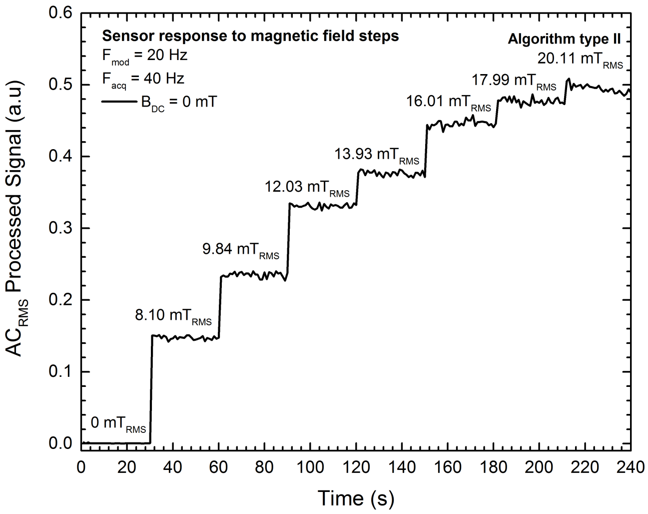

Figure 5.11 – Loop laser response to steps of AC magnetic field with no applied bias field.

In Figure 5.12 it is exhibited the waveform of the applied magnetic field signal and the sensor response after demodulating the interferometer output, showing the frequency doubling. Moreover, the sinusoidal form is also distorted due to the hysteresis.

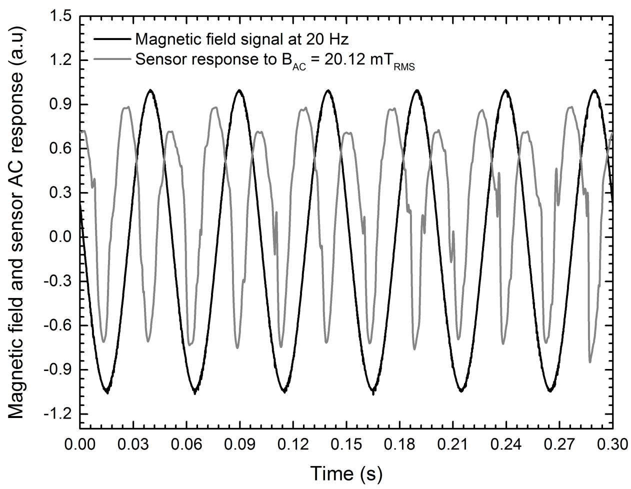

Figure 5.12 – Response of the Loop laser when an AC magnetic field of 20.12 mT_{RMS} is applied, obtained with demodulation algorithm type II, with no bias field.

In Figure 5.13 it is shown the average and the standard deviation value of the demodulated AC signal, acquired using two independent measurements. The results show good repeatability between both measurements. Furthermore, better sensitivity is attained for a bias magnetic field of 7.14 mT, followed by 9.52 mT, 11.9 mT and 0 mT. For each date set distinct fittings curves were applied, obtaining a good fitting with the experimental values. The worst sensitivity was found when no bias magnetic field was applied, with 50 % less than the one found with a constant field of 7.14 mT. In this calculation an average first order sensitivity, calculated from a linear fit of each individual curve, was considered.

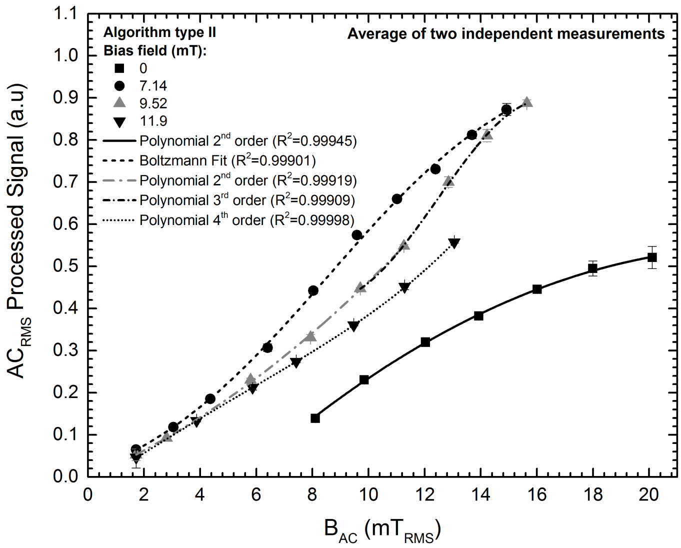

Figure 5.13 – AC RMS signal obtained at the output of the demodulation interferometer when the loop laser emission wavelength is under the influence of an AC magnetic field, using distinct bias fields.

The same measurements were performed simultaneously with type I algorithm but the plots taken with the two algorithms were indistinguishable, so the results have been numerically compared and are displayed in Table 5.1. The precision errors correspond to the average of the measured deviations. Similar errors were obtained with both algorithms but in average the error using algorithm type II is slightly lower. For instance, the maximum average precision error found with no bias field was ±2.70 % and ±2.68 %, for type I and II, respectively. For the type II algorithm, the maximum and minimum improvement/decrease was 2.19 % for a bias field of 9.52 mT and 0.38 % for a field of 11.9 mT, respectively.

Table 5.1 – Precision errors obtained with different bias magnetic fields, with the loop laser.

B_{DC} (mT)	Type I (%)	Type II (%)	Type II improvement (%)
0	±2.70	±2.68	0.81
7.14	±2.20	±2.19	0.43
9.52	±2.56	±2.51	2.19
11.9	±2.72	±2.71	0.38

The measured magnetic field resolution was also calculated as being two times the standard deviation value, divided by the sensitivity (which was derived from the fitting curves displayed in Figure 5.13). These results are represented graphically in Figure 5.14, where each value is normalized by the measurement bandwidth. As expected, the best resolutions were attained for bias fields of 7.14 mT and 9.52 mT, where the sensitivity is higher, according to Figure 5.13. Additionally, alternating magnetic fields ranging from 4 mT_{RMS} to 13 mT_{RMS} result in a maximum resolution of 57.76 $\mu T_{RMS}/\sqrt{Hz}$ (13.75 $A_{RMS}/\sqrt{Hz}$) and 60.11 $\mu T_{RMS}/\sqrt{Hz}$ (14.31 $A_{RMS}/\sqrt{Hz}$) for a bias of 7.14 mT and 9.52 mT, respectively. Out of these ranges, the sensitivity was reduced, leading to worst resolutions. The equivalence between magnetic field and current is presented right after Figure 5.14.

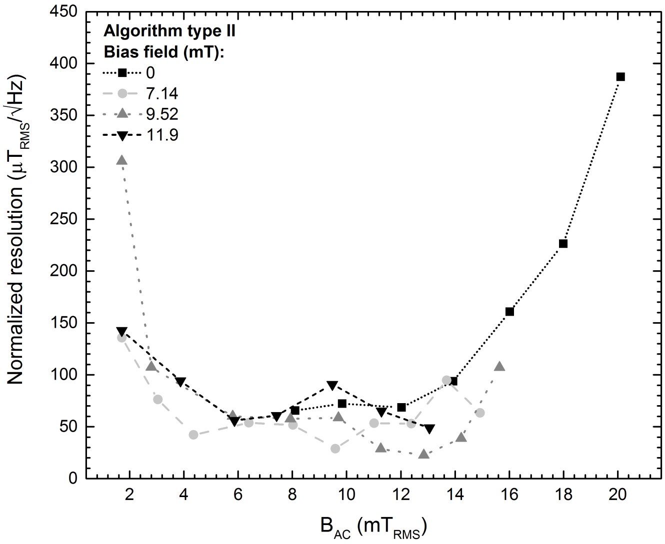

Figure 5.14 – Normalized resolution in relation to the measurement bandwidth as a function of the alternating magnetic field, using distinct bias fields, obtained with the loop laser.

Analyzing these results in the framework of a hypothetical application in the electric grid, the applied magnetic field can be converted to an equivalent current created by a conductor, given by

$$B_{AVG} = \frac{1}{L}\int_{-L/2}^{L/2} \frac{\mu_0.I}{2\pi}\frac{r}{r^2+l^2}\,dl = \frac{\mu_0.I}{L.\pi}\,\mathrm{ArcTan}\left(\frac{L}{2r}\right) \tag{5.6}$$

with the Terfenol-D section centered relative to the conductor (Figure 5.15). Assuming a distance between the Terfenol-D rod and the conductor of $r = 40$ mm and $L = 65$ mm, this expression results in a current-magnetic field relation of 238.16 A/mT.

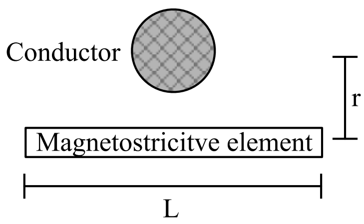

Figure 5.15 – Magnetostrictive element centered in relation to the conductor at a distance *r*.

According to Figure 5.13 and Figure 5.14 the sensor full-scale output response is within the range of 4 mT_{RMS} until 13 mT_{RMS}. Having into account the previous current-magnetic field relation, the range can be converted to an equivalent current from 953 A_{RMS} until 3096 $A_{RMS.}$ this is somewhat limited and not suitable for complying the sensor with any of the standard error classes. Moreover, the resolution of the sensor, expressed in Figure 5.14, still needs improvement.

In order to further understand the nature of poor resolution values, the laser power stability was investigated without the interferometer and the results have shown the presence of an AC power modulation of ±15.4 % when the sensor is submitted to an alternating magnetic field of 6.63 mT_{RMS} and a bias of 9.52 mT. The FFT of the laser output shows a peak at the same frequency of the applied magnetic field (20 Hz) with a SNR of -35.81 dB. This result implies that the signals read at the output of the interferometer will contain a 20 Hz modulation due to the interferometer wavelength-to-power modulation, combined with the laser 20 Hz power noise, decreasing the magnetic field resolution. Other sources of noise, such, power fluctuations coming from the pump power will not be a problem, since it does not match with the first and second harmonic of the modulation frequency.

5.3.3 LPG readout system

The laser sensor performance was also studied when the readout interferometer was replaced by a single LPG, stabilized in temperature with a peltier controller. The interrogator LPG was written in single mode Boron codoped Photosensitive fiber using a UV laser and had 14.87 nm bandwidth at half power and a peak attenuation band of 25 dB. The period of 299 µm was chosen in order to obtain a resonant loss with a transmission slope that matched the loop laser emission wavelength, as shown in Figure 5.16. The spectrum represented in this plot was obtained by illuminating the LPG with a broadband source and combining it with the laser, using a 50:50 coupler.

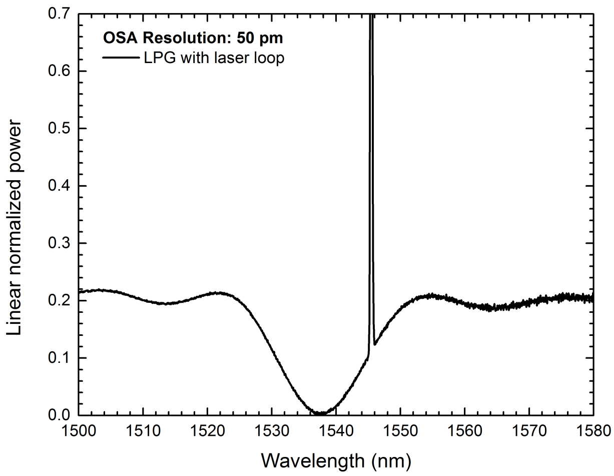

Figure 5.16 – Overlap of the LPG transmission spectrum with a the loop laser emission line.

An evaluation test, without bias magnetic field, and applying three current steps was carried out and the results can be observed in Figure 5.17. From this data, precision errors of ±3.93 % and ±6.9 % for an alternating magnetic field of 12.18 mT_{RMS} and 20.13 mT_{RMS} were recorded, respectively, which is considerably worse than the results obtained with the interferometer readout scheme (±1.87 % and ±2.15 %, respectively). In order to reduce the error it is crucial to decrease the LPG sensitivity to temperature, for instance inscribing the

LPG on a PCF, or assembling it over an athermic support. Furthermore, higher sensitivity can only be obtained having a steeper transmission spectrum. However, in practice, with the LPG fabrication setup used it is extremely difficult to reduce its bandwidth. Having these facts into account and the errors obtained using this technique, it is preferable to use the passive interferometer setup as a wavelength-intensity converter.

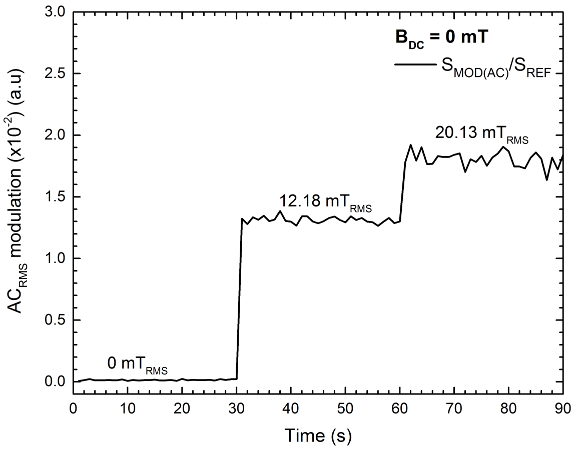

Figure 5.17 – LPG readout setup response to three AC magnetic field steps using the loop laser.

5.4 Wavelength modulated Fabry-Pérot

In order to improve the laser power stability when modulating the cavity Bragg mirror, another configuration has been tested which is represented in Figure 5.18. The laser setup consists of two FBGs, one at 1534.17 nm with 150 pm spectral bandwidth and 82 % reflectivity, and the other at 1534.21 nm with 160 pm spectral bandwidth and 87% reflectivity, written in single mode Boron codoped photosensitive fiber, using a phase mask (period of 1058 nm). In between the two FBGs, a piece of 6.8 m of Fibercore Erbium doped fiber M5 is used as the gain medium, resulting in an 8 m cavity length.

Each FBG was glued side by side at two fixation points, distant apart by 20 mm, in the Terfenol-D rod. Magnetic field was generated using the same inductor, referred earlier, which at its center, can deliver an average magnetic field of 12.2 mT/A along 20 mm length. Because this laser operates in reflection rather than in a transmission, it has no residual pump power at the output, resulting in a much more stable emission.

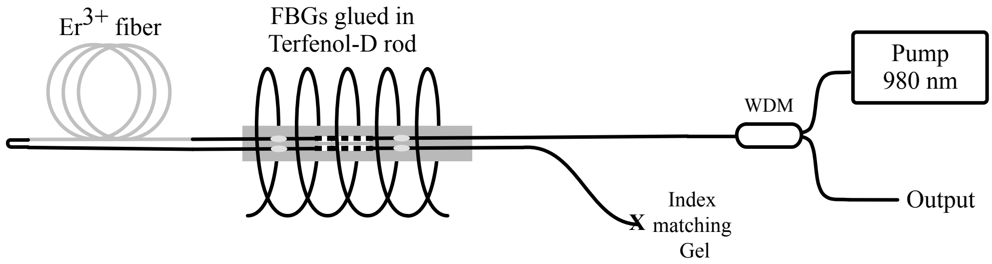

Figure 5.18 – Experimental setup of the wavelength modulated Fabry-Pérot laser.

A simpler setup could also be implemented by replacing the higher reflectivity FBG with a broadband mirror, such as silvered fiber tip. In this cases only a single FBG would have to be fixed to the Terfenol-D rod. However, due to experimental limitations the next simpler alternative was used, which consisted in the application of two very similar FBGs.

This laser spectral width was measured using the same method described above and the results are shown in Figure 5.19. A spectral width at half power of 1.87 GHz (14.7 pm at 1534 nm) was obtained for the multimode laser. The laser linewidth is around 40 times smaller than the free spectral range of the interrogation interferometer assuring adequate readout sensitivity.

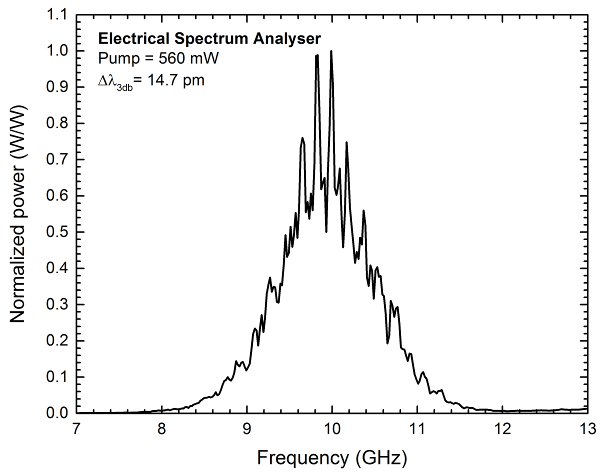

Figure 5.19 – Wavelength modulated Fabry-Pérot laser emission spectrum measured in the optical spectral analyzer.

The laser emission response was also characterized for distinct pump power (Figure 5.20), and a maximum laser power of 4.7 mW was achieved for 560 mW pump with a threshold of 50 mW.

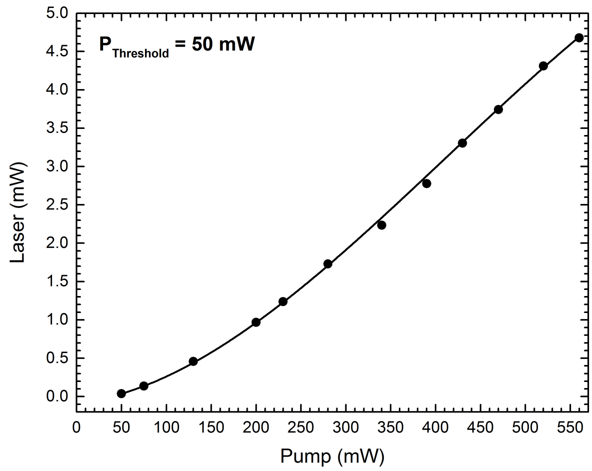

Figure 5.20 – Wavelength modulated Fabry-Pérot laser emission power as a function of the pump power.

Laser power stability was also recorded at 10 kHz sample rate and an output power modulation below ±1.2 % at 50 Hz was observed which was caused by the electronics driving the pump diode. Long term power fluctuations of about ±4 % where observed as well, however the detection setup compensates for this slow variation.

5.4.1 Response to distinct bias magnetic fields

The sensor response was again tested using different AC magnetic field increments at 20 Hz and distinct bias magnetic fields, using both demodulation algorithms and the passive interferometer. The same acquisition parameters of the former work were used, including the 200 Hz low pass filter applied to the three outputs of the interferometer.

In Figure 5.21 it is shown the waveform of the applied magnetic field signal and the sensor response, without a bias magnetic field, as demodulated at the interferometer output. The demodulated waveform yields a signal with much lower noise than the one obtained before (Figure 5.12) and consequently will provide better measurement stability. This result indicates that the sensor is much more stable in power, while being modulated in wavelength, than what was observed with the previous configuration. As will be detailed later in this chapter, this stability results from the higher bandwidth of the laser, as compared with the former configuration.

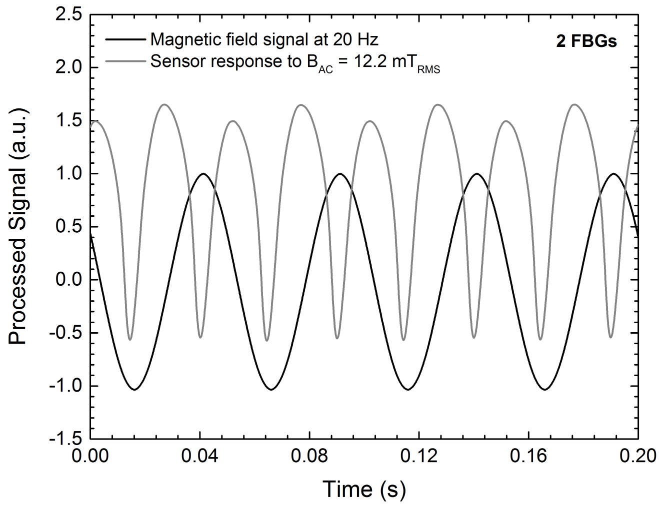

Figure 5.21 – Wavelength modulated Fabry-Pérot laser response to steps of AC magnetic field using demodulation algorithm type II.

Compilation of the sensor response in different measurement conditions, obtained using demodulation algorithm type II and different DC magnetic fields is present in Figure 5.22. For each case, two independent tests were conducted and the results showed good repeatability. Also, a standard deviation error is represented at each step, but they are too small to be observed in the plot. For AC magnetic fields up to 12.2 mT_{RMS} a DC bias field of 4.88 mT yields the best response. On the other hand, for values higher than 12.2 mT_{RMS}, a DC magnetic field of 8.54 mT is preferable, measuring fields up to 18.2 mT_{RMS}. Moreover, the worst sensitivities were found for a DC bias field of 0, 13.42 mT and 16.47 mT, which also corresponded to the worst sensitivity region of Figure 5.22.

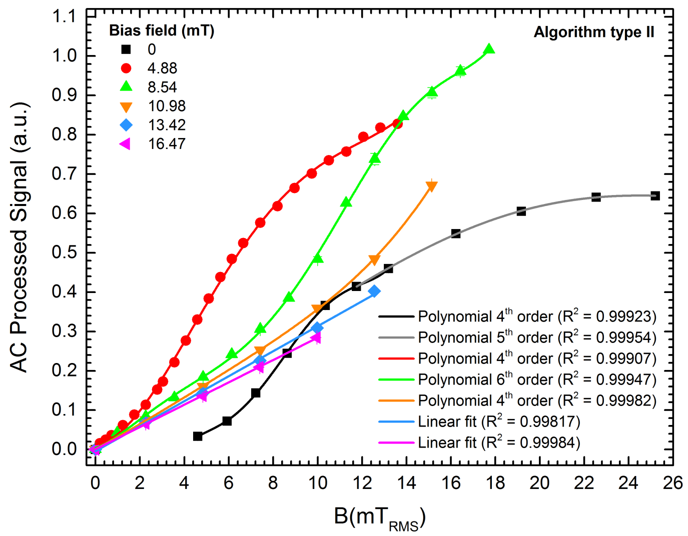

Figure 5.22 – AC response of type II demodulation algorithm, using different DC Bias magnetic fields, obtained with the wavelength modulated Fabry-Pérot laser.

In agreement with the DC response of the laser shown in Figure 5.22, the best response of the AC current sensor is achieved with a low but non-zero biasing field, however the best linearity is obtained for moderate bias fields because the transducer works still far from saturation.

As before, the same measurements where performed simultaneously with algorithms I and II and numerically compared in Table 5.2. The maximum precision errors found were ±0.62 % and ±0.63 % with a bias field of 4.88 mT, for type II and I algorithms, respectively. Results show slightly lower errors with type II algorithm, which makes use of the Arc tangent function. However, an isolated case, for a bias of 16.47 mT, type II processing gave a slightly higher error. The maximum and minimum improvement obtained with type II was 17.31 % and 0.4 %, respectively. As observed in the previous setup, lower errors are in general achieved in type II rather than in type I method because the latter one employs more complex functions such as derivatives and integration, translating into an increased noise.

Table 5.2 – Precision errors obtained with different bias magnetic fields for variant magnetic fields, obtained with the wavelength modulated Fabry-Pérot laser.

B_{DC} (mT)	Type I (%)	Type II (%)	Type II improvement (%)
0	±0.58	±0.48	17.31
4.88	±0.63	±0.62	0.98
8.54	±0.40	±0.40	0.40
10.98	±0.30	±0.29	1.89
13.42	±0.42	±0.42	0.61
16.47	±0.46	±0.46	-0.62

In another perspective, in Figure 5.23 it is presented the normalized resolution as function of the alternating magnetic field. In the range of 0 to 9 mT_{RMS} the best resolution is achieved using a 4.88 mT bias with 6 $\mu T_{RMS}/\sqrt{Hz}$. However, up to 14 mT_{RMS} the resolution worsens drastically to 20.93 $\mu T_{RMS}/\sqrt{Hz}$. For higher operating ranges, a bias magnetic field of 8.54 mT or 10.98 mT is preferable. Although higher sensitivity is attained with a bias field of 8.54 mT rather than at 10.98 mT as shown in Figure 5.22, the instability was slightly worst and consequently presented worst resolution. Moreover, the worst case is observed for a zero bias magnetic field with 25.78 $\mu T_{RMS}/\sqrt{Hz}$. From the FFT spectrum of the laser output a SNR of -63.04 dB was estimated at 20 Hz.

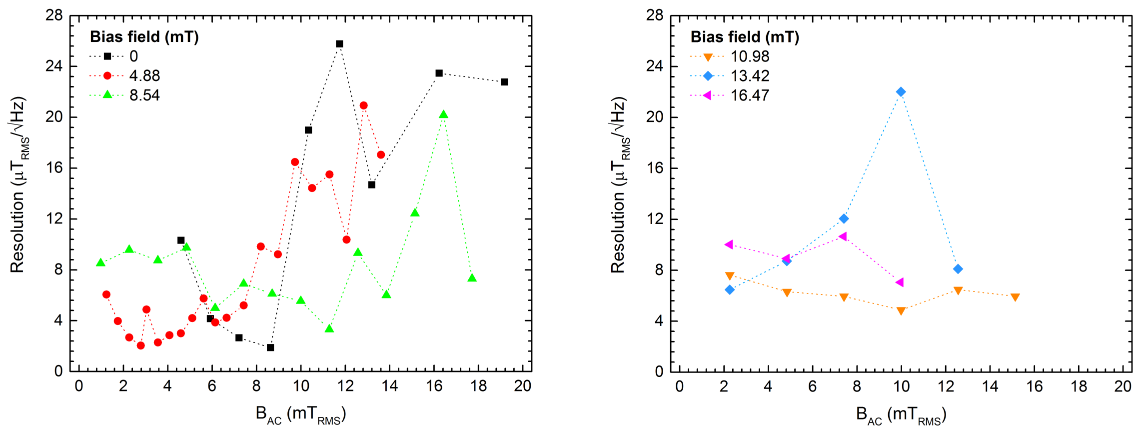

(a) (b)

Figure 5.23 – Normalized resolution in relation to the measurement bandwidth as a function of the alternating magnetic field, using distinct bias fields, obtained with the wavelength modulated Fabry-Pérot laser.

Accuracy errors were also estimated for this sensor, considering a bias filed of 4.88 mT, which corresponds to the best result obtained in Figure 5.22 (better sensitivity at lower fields) and in Figure 5.23 (a) (better resolutions at lower fields). The equivalence between current and magnetic field was calculated according to equation (5.6) and the modulus of the error (equation (1.1)) it is presented graphically in the plot of Figure 5.24. Unfortunately, the sensor does not comply any precision class, because accuracy errors were above ±1 % in the displayed range of 93.28 A_{RMS} until 2776 A_{RMS}. Although not displayed in the graph, an error of ±24.7 % was attained if an equivalent current of 40.68 A_{RMS} is considered. Therefore, the sensor is only suitable for detection of large currents, in limited ranges of operation. Due to its small size and ability to operate remotely, it can be useful, for instances, to monitor large currents inside big engines or turbine generators.

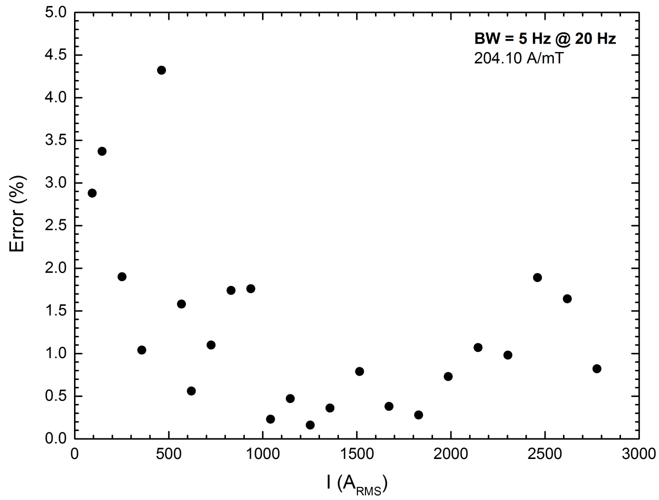

Figure 5.24 – Sensor classification according to the electric grid requirements, obtained with the wavelength modulated Fabry-Pérot laser.

5.5 Intensity modulated configuration

Having achieved a stable laser, the next step consisted on improving the laser linewidth by changing the cavity fiber Bragg mirrors overlap. A new configuration was tested, where the setup is the same as the one shown in Figure 5.18, but using two narrowband FBGs instead. The first one had 88 % reflectivity, 36 mm in length at 1530.94 nm and the second FBG had a 98 % reflectivity and 67 mm in length at 1531.07 nm, both written in single mode Boron codoped Photosensitive fiber. Spectral bandwidths of 27.58 pm and 37.24 pm were measured for the FBG with higher and lower reflectivity, respectively. The wavelengths were chosen near the Erbium gain peak where a small variation of their spectral characteristics will result in a large variation of the output power. In order to have lasing, the FBGs spectral overlap had to be tuned with strain, so that their reflection wavelengths can coincide. Moreover, in order to manufacture narrowband FBGs with a high reflectivity, the modulation index contrast had to be lower and consequently the FBGs length had to be increased from 5 mm to a minimum of 35 mm.

Between both FBGs, a piece of Fibercore Erbium doped fiber was used as the gain medium. Two fibers of different Erbium concentrations were tested, the M5 and the M12; and, as it is explained later, best immunity to vibrations was achieved with the M5 fiber. The final prototype had a piece of 6.8 m of M5 fiber resulting in a cavity length of 9 m. Each FBG was glued side by side at two fixation points, 90 mm apart, in the Terfenol-D rod. The laser output was seen reflection, free of pump power.

The gratings were partially overlapped using the setup in Figure 5.25. A tunable laser controlled with a computer, via GPIB was used to simultaneously scan both FBGs spectrum in transmission with 1 pm resolution. A third arm of the 3×3 coupler was used as a reference, to eliminate dependence on any laser output power variation.

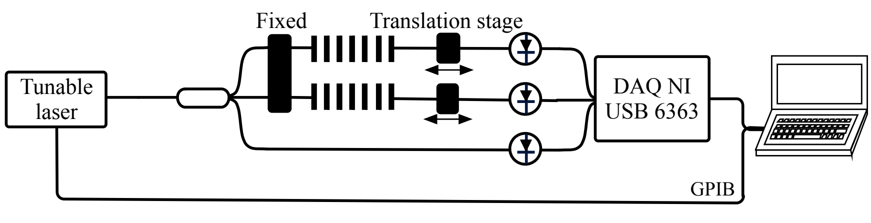

Figure 5.25 – Experimental setup for tuning the FBGs using a translation stage for each FBG and acquisition with the DAQ, used to retrieve simultaneously both transmission spectra.

A translation stage was used for each FBG allowing to tune both FBGs and consequently control the Bragg wavelength overlap. In Figure 5.26 it is shown the spectrum of the detuned FBGs with an overlap of 17.32 pm, at half power (-3 dB).

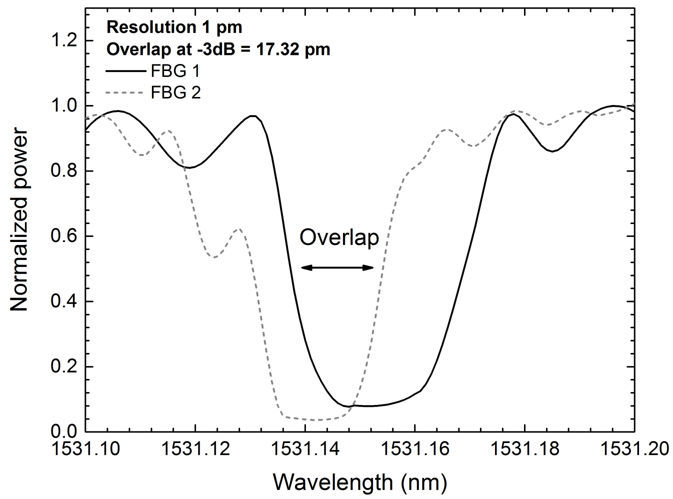

Figure 5.26 – Spectra of the cavity mirror FBGs with an overlap at half power set to 17.32 pm.

When the intended overlap was achieved, the FBGs were attached to the magnetostrictive rod using acrylate glue. After drying, the laser configuration shown in Figure 5.18 was then assembled, where 0.5 m segment of Fibercore M12 active fiber was used as the gain medium, resulting in total cavity length of 1.5 m. In Table 5.3 it is shown the laser linewidth and the optical power as function of the spectral overlap of the FBGs. As expected when the overlap raises the laser linewidth also increases and the peak optical power decreases because more modes are competing for the pump. The linewidth was measured using an ESA, a 50 GHz photodetector bandwidth and a laser tuned closed to the optical fiber laser emission wavelength.

Table 5.3 – Power and laser linewidth as function of the FBG spectral overlap.

Spectral overlap (pm)	Power (mW)	Laser linewidth (MHz / pm)
17.32	14.25	227 / 1.78
10.73	18	207 / 1.62
1	20	152 / 1.18

Power stability was also analyzed using a photodetector and an oscilloscope. For overlaps smaller than 1 pm, it was observed that any acoustic vibration into the laser cavity gave rise to an unstable emission regime. Moreover the ESA spectrum revealed only three longitudinal modes for this configuration. To minimize this effect, a coupled section of 2 m of SMF was introduced in the laser cavity (resulting in a cavity length of 3.5 m) with the goal of increasing the number of longitudinal modes. The results showed a more stable laser, with no pulsing but the power fluctuated (slow drift) up to ±10 %, with acoustic vibrations.

To reduce the power instability observed when reducing the detuning up to 1 pm a different active fiber was used. The setup is still the one shown in Figure 5.18 but the 0.5 m of M12 fibercore fiber were replaced with a peace of 6.8 m of M5 fibercore fiber, with much lower gain, increasing the cavity length and the number of longitudinal modes. In this configuration no drift or instability was observed in the presence of vibrations. Also, a detuning of 13.14 pm was adjusted for both FBGs by controlling the translation stages and then gluing them to the Terfenol-D rod, side by side and with the fixation points displaced 90 mm apart. A laser linewidth of 254 MHz, 1.99 pm at 1531.40 nm was obtained, with two orthogonal polarizations and several longitudinal modes. The laser threshold was reached with 21 mW pump power and the maximum optical output power was 110 mW with 546 mW pump. Furthermore, testing with vibrations induced to the laser cavity showed it was power stable. The FFT spectrum of the laser output revealed a SNR of -58 dB at 20 Hz.

5.5.1 Response to AC magnetic field

Following the laser characterization, the sensor response to magnetic field was inspected. Although the laser is power stable, when an AC magnetic field was present the reflectivity of the laser mirrors was modulated in wavelength and the laser output power was also modulated (but showing no pulsing behavior). Having this effect into account, several constant and alternating (DC and AC) magnetic fields were applied at 20 Hz and the power modulation was analyzed at 20 Hz and 40 Hz with and without a magnetic bias field, respectively. In these conditions the laser emits an amplitude modulated output. The ratio between the RMS value and the average value of the output signal is independent of the optical power and also independent on the transmission loss or pump instabilities. In Figure 5.27 it is shown the sensor response to alternating magnetic field with distinct bias magnetic fields. The curves correspond to polynomial fits of the average value of two independent measurements, and the standard deviation value, the error bars shown in the graph, represents the repeatability of both measurements. Better sensitivities are attained with no bias magnetic field applied, or for a bias magnetic field of 4.56 mT, enabling measurements of fields up to 8.67 mT_{RMS} and 12.02 mT_{RMS}, respectively. Moreover, for a bias field of 10.26 mT a more linear response is obtained ranging from 0 to 12.02 mT_{RMS}, however, the sensitivity is much lower than in the previous cases.

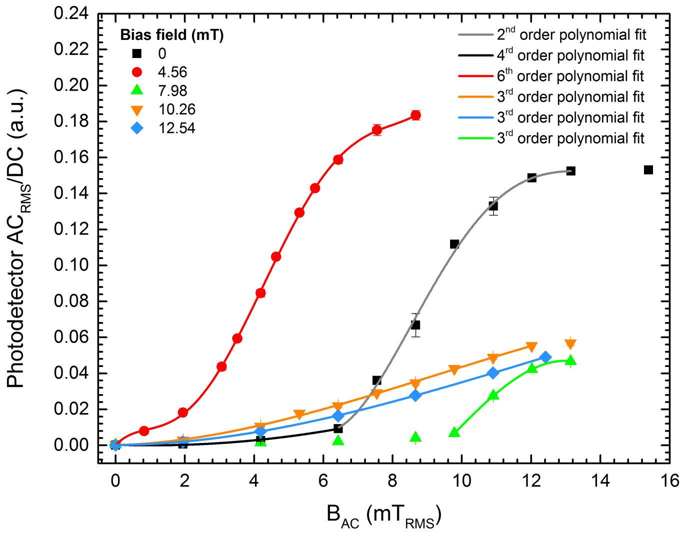

Figure 5.27 – Normalized AC output power change as function of the applied AC magnetic field, for several bias magnetic fields, obtained with the intensity modulated laser.

Considering the best result, obtained with a constant magnetic field bias of 4.56 mT, four independent measurements were repeated in order to study the sensor reproducibility (Figure 5.28). The worst resolution values registered in each measurement set are also shown with the resulting calibration curve. Overall, in the range between 1.93 mT_{RMS} and 5.29 mT_{RMS}, the worst resolution obtained was 51.2 μT_{RMS} (22.9 $\mu T_{RMS}\sqrt{Hz}$). This value is equivalent to a current resolution of 6.1 $A_{RMS}/\sqrt{Hz}$, assuming a relation of 266.54 A/mT, given by equation (5.6). This interval also corresponds to the region with higher sensitivity. Outside this scope, distortion increases drastically and the worst resolution was 592.7 μT_{RMS} (265 $\mu T_{RMS}\sqrt{Hz}$) for an applied AC magnetic field of 8.65 mT_{RMS}.

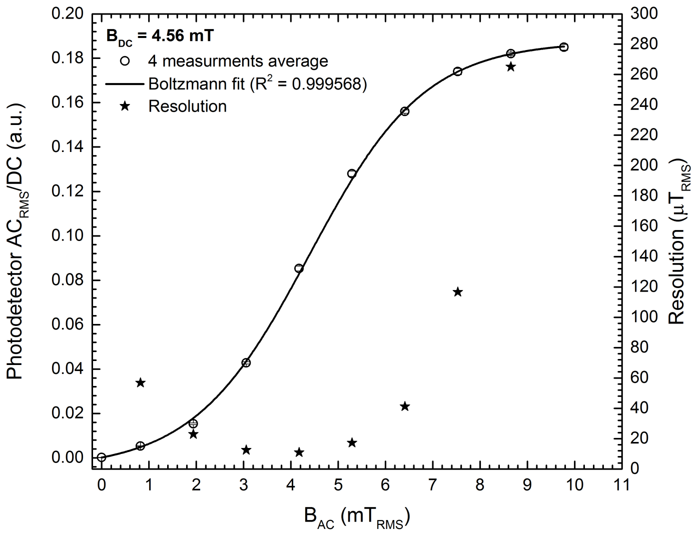

Figure 5.28 – Normalized AC power change as function of the applied AC magnetic field, for a DC magnetic field of 4.56 mT.

As obtained with the loop laser configuration, this configuration holds a very limited response, within the range of 1.93 mT_{RMS} and 5.29 mT_{RMS}, equivalent to the range of 514.4 A_{RMS} until 1410 A_{RMS}. In this case it was not possible to frame the sensor in any of the industry precision classes.

5.6 Narrow band configurations

Other compact optical fiber lasers have also been studied for detection of magnetic fields. One of the configurations tested is shown in Figure 5.20 and its named distributed feedback laser. It consists of a Phase shifted FBG written in a highly doped concentration, Fibercore M5. The phase shift was fabricated by a simple displacement of the phase mask (period 1067 nm) relative to the fiber during the beam scanning. The displacement necessary for obtaining a precise π-phase shift is a quarter of the phase mask period. The fiber holding setup was mounted on a piezoelectric transducer PZT stage with nanometer resolution that allowed to precisely control their relative position. By introducing a π-phase shift, a very narrow transmission window was opened at the Bragg wavelength of the grating.

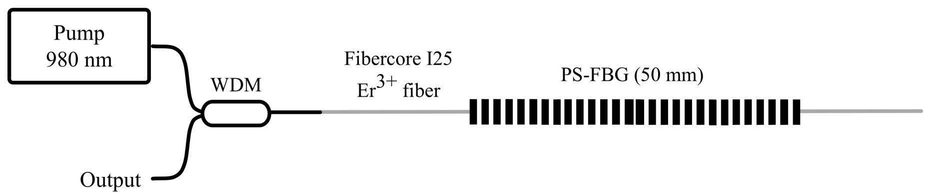

Figure 5.29 – DFB fiber laser setup.

The overall process is tricky. For a given FBG length it is essential to adjust the required reflectivity, by controlling the UV scan speed, in order to accomplish lasing. This configuration has resulted in a very narrow linewidth with just one mode and one polarization of 14.2 MHz, 0.11 pm at 1544 nm.

An alternative sensing configuration is show in Figure 5.30. It consists of a Fabry-Pérot interferometer build in a single piece of highly doped erbium fiber with two high reflectivity (82 % and 90 %) overlapped FBGs. The resulting spectral output has shown only one longitudinal mode with 5 MHz bandwidth but two orthogonal polarizations, spaced by 200 MHz (1.56 pm at 1532 nm).

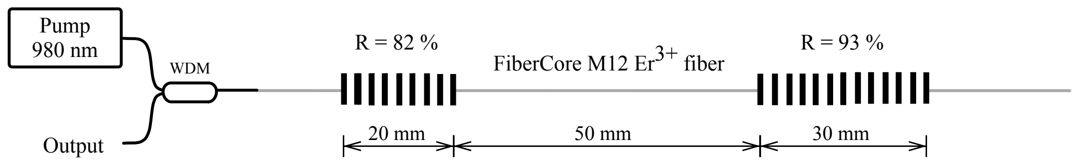

Figure 5.30 – Short Fabry-Perót optical fiber laser.

However due to a very narrow bandwidth these configurations were shown to be inadequate for magnetic field sensing, because they were very unstable, starting to pulse when modulated by the magnetostrictive element. This is true considering the standard interrogation techniques used in the previous lasers, however, with more advanced processing techniques, involving determination of the pulse amplitude and/or repetition rate, a very high accuracy system can be implemented. Unfortunately, due to time constrains, the investigation of such system was postponed for future work.

5.7 Summary

In this chapter optical fiber lasers combined with magnetostrictive materials were proposed and tested for magnetic field sensing, showing the influence of the laser bandwidth in its stability. In Table 5.4 it is present a comparison between the three best optical fiber laser configurations developed. Linking the first and second configuration, was the use of the same readout setup, a passive interferometer with a fixed OPD. However, in the second configuration much higher resolutions and SNR were achieved. This result was related with the mirrors spectral width, also affecting the laser linewidth. For a larger linewidth the laser cavity contains more longitudinal modes, which are affected differently according to the environment conditions and in average provide a more stable power output.

This effect was also observed in the third sensing configuration. Results showed that when the linewidth was too narrow, the laser becomes very susceptible to acoustic vibrations pick-up and can even show a pulsing behavior. Having this effect into account, the laser bandwidth was reduced, until power modulation was only attained in the presence of the magnetic field, with no pulsing behavior. Although the third laser configuration showed very limited dynamic range, in relation to the other two, in this case the alternating magnetic field information is encoded in the output power modulation, removing the need for the interferometer. However, the wavelength information may be extracted as well and combined with the power modulation information to improve the sensor resolution.

Although none of these sensors could be integrated in any precision class, its small size and ability to operate remotely can be useful in the detection of large currents inside complex machines such as generators.

Table 5.4 – Optical fiber lasers summary.

Sensor	Loop configuration	Wavelength modulated Fabry-Pérot	Intensity modulated configuration
Plaser [Ppump] (mW)	5.5 [380]	4.7 [560]	110 [546]
Wavelength (nm)	1544	1534	1531
Linewidth (MHz/pm)	25.8 / 0.2	1870 / 14.7	254 / 1.99
Readout system	Passive interferometer	Passive interferometer	AC_{RMS} / DC
Resolution ($\mu T_{RMS}/\sqrt{Hz}$)	57.76	6 or 20.93	22.9
Dianamic range (mT_{RMS})	4 up to 13	1.23 up to 9 or 0.97 up to 14	1.93 up to 5.29
Resolution ($A_{RMS}/\sqrt{Hz}$)	13.75	1.22 or 4.27	6.1
Dianamic range (A_{RMS})	950 up to 3100	250 up to 1840 or 200 up to 2860	510 up to 1410
SNR at 20Hz (dB)	39	63	58

Chapter 6 Detection of vibration and magnetic field using Long Period Gratings

In this chapter, a long-period grating (LPG) written on a standard single mode fiber is investigated as a fiber optic sensor for vibration and magnetic field. It is demonstrated the high sensitivity of the device to applied curvature and the possibility to monitor vibration in a wide range of frequencies from 30 Hz to 2000 Hz. The system was tested using intensity based and spectral scanning based interrogation schemes with the LPG sensor operating in a curvature or strain regime, with a frequency discrimination of 1 Hz. The goal of these tests is to evaluate the sensor as a passive vibration monitor to be employed in the electric grid, as the detection of changes in resonant vibration frequencies of support infrastructures can provide information on its degradation. Furthermore, taking advantage of the intrinsic sensitivity to micro curvature, alternating magnetic fields were also measured using an intensity-based interrogation scheme by coupling a Terfenol-D magnetostrictive rod to a pre-strained LPG sensor.

6.1 Vibration sensing with Long Period Gratings

A brief description concerning the state of the art of optical vibration sensors is given in the following section, in order to better frame the results obtained with the LPG sensor developed in this work for vibration sensing.

6.1.1 State of the art of vibration sensors

Nowadays, a large diversity of vibration sensors are being used for real-time structural health monitoring, in civil infrastructures and engineering systems, namely bridges, buildings and railway tracks [130]. In the case of large-scale structures like bridges, low frequency vibrations are the most commonly monitored. In this range of operation, however, traditional electromagnetic vibration sensors are usually very limited [131] and inadequate while operating in the presence of high magnetic fields, giving rise to faults. In contrast, optical sensors do not suffer from electromagnetic effects and therefore operate well in these environments [132].

Low frequency signals provide information about the presence of small cracks and discontinuities in the infrastructures [133]. In [134] it is referred, for an old arch bridge, that vibration frequencies in the range of 6 Hz to 44 Hz are the most suitable for the detection of signs of structural degradation. Furthermore, for a centenary iron arch bridge [135], bending and torsion of the structure present vibration frequencies within the 0.9 Hz to 9 Hz range. On the other hand, higher frequencies in the range of 1 kHz to 1.5 kHz enable the early detection of potential problems in electrical machines as bearing, eccentricity and broken rotor bars [136].

According to the working principle, fiber optic sensors to measure vibration can be based mostly on intensity or wavelength modulation schemes [137]. They can be implemented using different sensing elements such as fiber Bragg gratings (FBG) [138–140] or long-period gratings (LPGs) [141–143], mostly fabricated using conventional single mode fibers. Usually the former are interrogated in reflection and the later in transmission. However, FBGs and LPGs, fabricated in standard optical fibers, usually present a high cross-sensitivity to temperature. In LPGs, in addition, the refractive index of the external medium is also a major source of cross sensitivity, strongly affecting the sensor response [144,145] and requiring the use of low refractive index coatings that impact on the overall sensor response.

Concerning the optical sensors based on FBGs, in 2008, a vibration sensor having only one FBG was studied. The sensor is attached to a cantilever with a mass at one end and the interrogation system consists of a DFB laser tuned to the slope of the FBG transmission curve. When vibration is applied, the FBG wavelength is modulated and at the output, a proportional power change is detected using a photodetector [138]. This sensor was successfully tested in the range from 25 Hz to 50 Hz.

In order to compensate temperature fluctuations, in 2010, Nan [131] developed a low frequency vibration sensor operating in the range from 0.24 Hz to 50 Hz. It employs two FBGs sensors, one acting as the sensor (works in reflection) and the other like a transmission filter. The first FBG is attached to a oscillating cantilever plate with a mass in the edge. The reflected signal then follows through the filter FBG which is attached to a second cantilever of the same material. This cantilever, however, is not free to oscillate and its position can be adjusted by a screw that is used to define a fixed curvature. By adjusting the screw, the spectrum of the second FBG is tuned in wavelength, in order for its slope match with the reflective peak of the first FBG. Therefore, when vibration is applied to the first FBG, a proportional power fluctuation is detected in the photodetector. When temperature changes, however, both peaks move alike. Their relative position does not change, and the transmitted power is therefore independent of temperature.

On the other hand, LPG sensors for vibration measurement were also investigated in 2009 by Tanaka et al. [142]. The sensor consists of a symmetric LPG written by UV laser, exciting the 8^{th} order mode, and attached to a piezoelectric transducer. The sensor is illuminated by a laser source, coincident with the transmission slope of the LPG attenuation band, and when strain is applied to the piezoelectric transducer (using a 10.22 kHz modulation signal), the LPG only changes in wavelength, maintaining its spectral shape. At the output, a photodetector is used to detect the amplitude changes. Still, the LPG is dependent on the temperature and the external refractive index.

An LPG sensor was also used in the detection of acoustic waves, where small curvatures were induced by the propagating wave into the LPG (fabricated by UV), changing both the wavelength and the attenuation of the LPG transmission loss. The acquisition system uses a broadband source, and the integral of the optical power (as measured by a photodetector) is characterized as function of the acoustic waveform (1000 Hz to 2200 Hz). As expected different resonances (three in this case) were found for certain frequencies within the tested range [143].

In this chapter, a simpler approach, based on the previous configuration, is presented using a single LPG fabricated in a standard single mode fiber (SMF). Since the LPG was fabricated with a relatively long period, thus exciting lower order modes with a more internal power distribution, its sensitivity to external refractive index is very low. On the other hand, it sensitivity to vibration is preserved. The sensor device is therefore characterized and demonstrated as suitable for a high sensitivity curvature or vibration measurement applications.

6.1.2 Working principle

A long period grating consists of a refractive index perturbation inscribed along the fiber with a periodicity of hundreds of microns. The periodicity and amplitude of this refractive index variation determine the coupling of light between the guided core mode and the cladding modes, through the phase-matching condition. For long period gratings, the energy typically couples from the fundamental core mode to discrete forward-propagating cladding modes. The cladding modes are quickly attenuated and this results in a series of loss bands in the transmission spectrum of the grating, with peak wavelengths given by [146]

$$\lambda_p^{(m)} = \left(n_{eff} - n_{cl,eff}^{(m)}\right)\Lambda \tag{6.1}$$

In this expression, Λ is the grating period, n_{eff}, and $n_{cl,eff}^{(m)}$ are the effective refractive indices of the guided core mode and of the cladding mode, respectively. Typically, in LPGs fabricated in standard SMF fiber, the $n_{cl,eff}^{(m)}$ depends on the external refractive index and therefore $\lambda_p^{(m)}$ changes accordingly. In the proposed sensing head, the LPG excites internal cladding modes in order to have low sensitivity to refractive index.

According to literature [147] an LPG written in a SM fiber, when subject to curvature, undergoes changes in its resonance both in wavelength and transmission loss. Such behavior indicates this type of devices as an adequate candidate for a sensitive vibration sensor.

The LPG used in the experiment was fabricated by a research partner in UNICAMP, Brazil, using a CO_2 laser to locally heat the fiber with the desired periodicity. For this particular experiment a LPG with a period of 600 μm was produced and its transmission spectra is presented in Figure 6.1 (a). This fabrication technique creates LPGs which excites the asymmetric modes, typically the LP_{1m}, where m is the order of the mode. The refractive index modulation was introduced by closing and opening a shutter positioned in front of the laser, according to the period, while the pulsed beam is being focused along the fiber.

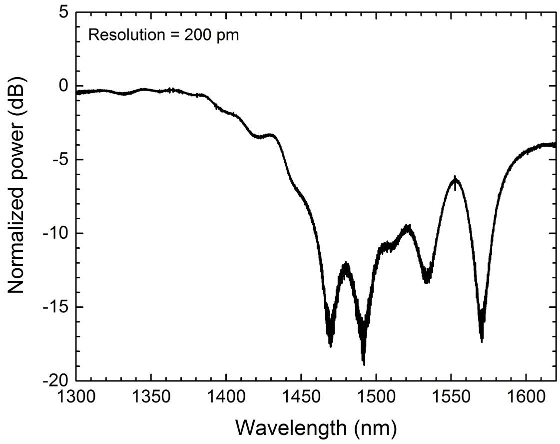

(a)

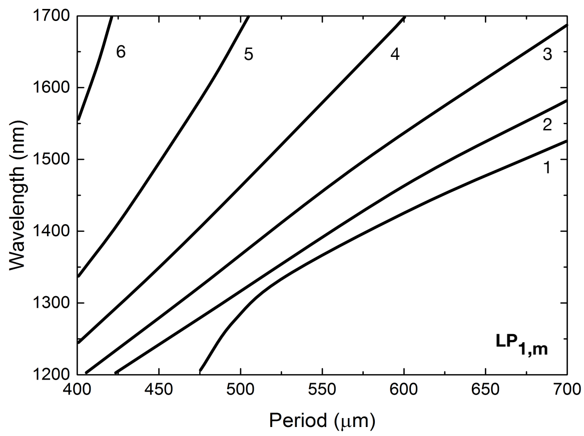

(b)

Figure 6.1 – (a) LPG spectrum measured with a white light source and (b) resonance wavelengths of cladding modes excited by an asymmetric arc-induced LPG.

The transmission spectrum obtained shows several resonant peaks between 1460 nm and 1570 nm, which are concordant with structures with relatively large period (around 600 μm) as can be seen in Figure 6.1 (b) [148], showing the resonance wavelengths of an asymmetrical LPG written by electric arc technique, which usually present similar modal distributions. Such observation is also in agreement with the measured periodicity as estimated by visual inspection under an optical microscope. Nevertheless, an uncommon overlap and increased loss in this spectral region is also observed which was attributed to random defects arising from a relatively unstable fabrication setup. Nevertheless, because the device tested showed both a low refractive index sensitivity and a relatively high sensitivity to micro curvature, further tests were carried out. The following tests were made considering the 1570 nm resonance, which was the dip with higher loss, in the 1500-1600 nm range, and also the range with greater equipment availability.

6.1.3 Temperature and refractive index characterization

The LPG was firstly characterized in temperature using an oven, with a setup as depicted in Figure 6.2. The sensing region was fixed carefully and with no torsion in an adequate support, inside the oven, where it was maintained with a constant applied strain by gravity with a 7 g weight.

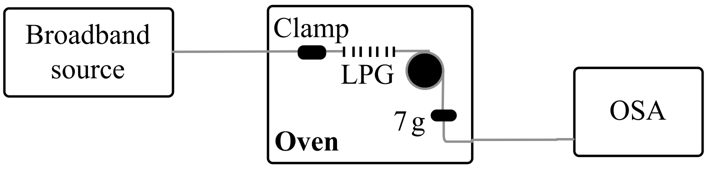

Figure 6.2 – Temperature characterization setup.

The sensor was submitted to a rising temperature between 30 ºC to 90 ºC. A linear red-shift was obtained in this range, from which it was possible to estimate a linear temperature sensitivity of 57.67 ± 0.26 pm/ºC (R^2 = 0.99892). The system was also let to cool down, and the sensor response registered during the lowering of temperature. No hysteresis was observed. This process was repeated two times with the results of both tests showing a good reproducibility.

In order to evaluate the cross sensitivity to refractive index, the response of the LPG to changes in the surrounding refractive index was also studied. Three independent experiments were carried out where the sensor was submitted to three measurements with refractive index changing between 1.0003 and 1.3355, measured at 589.3 nm and at 20 ^{o}C. The sensors showed a maximum change of the resonance peak of -1.074 ± 0.02 nm while changing from air to water, indicating a first order sensitivity of 3.2 nm/RIU. This is a value that is typical of low order modes and is quite low when compared with typical standard refractometer LPG where higher order modes are used (usually 5th or 6th) and this Figure is between 50 nm/RIU and 100 nm/RIU [149,150]. This feature contributes to minimize cross-sensitivity arising from surface contamination. Furthermore, the use of low refractive index coatings can also be employed to further reduce the sensor refractive index sensitivity. This change is also equivalent to a positive temperature variation of 18.62 ºC. Besides the observed wavelength shifting behavior of the resonance, its features remained otherwise preserved. Indeed, during temperature and refractive index tests, the shape and magnitude of the resonance transmission loss was preserved.

6.1.4 Curvature

In a preliminary stage, the sensor was characterized in curvature using the setup of Figure 6.3. The LPG was fixed carefully with no torsion on the fiber between a fixed pole and a moving pole, set on a micrometric translation stage with $\Delta L = 5$ µm resolution, where the fiber was stretched from the initial distance of $d = 326$ mm ($\Delta L = 0$). A rotation stage in each pole allows to spin the fiber, enabling testing the sensor response with curvature applied at different angles.

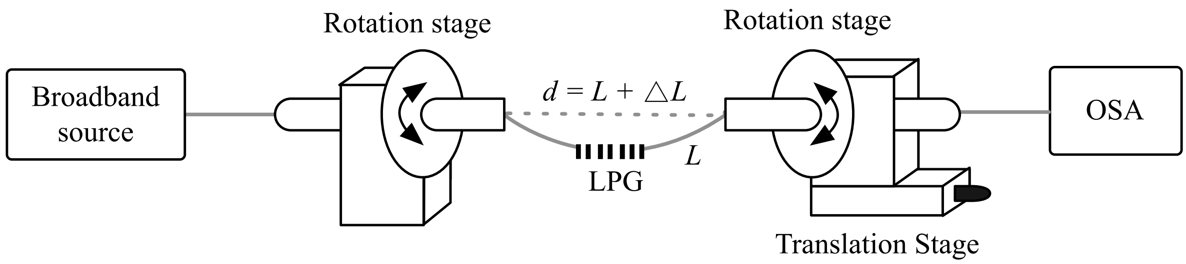

Figure 6.3 – Setup used for applying curvature to the LPG sensor at different angles by adjusting a rotation stage in each fixation pole.

Small curvatures were applied to the sensor by turning the moving screw of the translation stage in the micrometer range between -50 µm and 125 µm, while recording the transmission spectrum with an optical spectrum analyzer (OSA) with 20 pm resolution. In Figure 6.4 it is shown the behavior of the resonance peak with the fiber at 0 degrees. The negative and positive ranges correspond to applied curvature and strain, respectively (from now on referred as curvature mode and strain mode of operation). In addition, the transition point between these two regimes was established to have $\Delta L = 0$ µm, and is the limit where the fiber is stretched but has no applied strain. Results show that the position of the peak wavelength of the resonance dip is not affected but its depth changes significantly, with peak loss ranging between -38.0 dB and -20.9 dB.

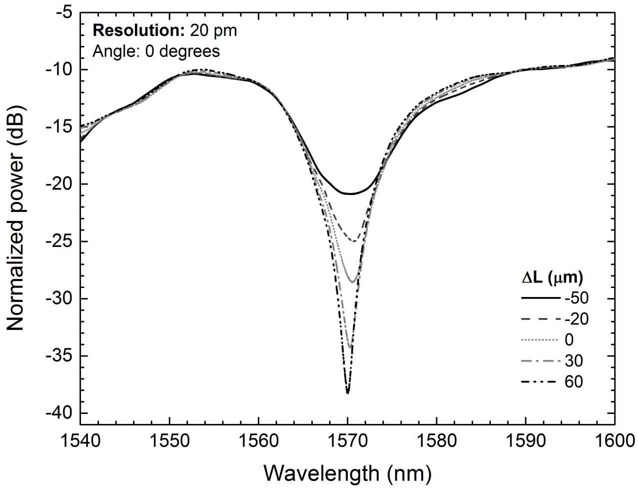

Figure 6.4 – LPG spectra obtained when the sensing region was submitted to different displacement values.

Variation of the transmitted optical power at a fixed wavelength, 1570 nm, was observed while changing the displacement with the fiber oriented at 0, 45, 90, 135 and 180 degrees. This test was performed in order to evaluate possible asymmetric behaviors of the LPG curvature response. In Figure 6.5 (a) it is shown the recorded average power variation and the corresponding standard deviation value, obtained from three independent tests, in a linear scale for each angle, while increasing the displacement. Results showed very good reproducibility, with very small deviations registered between tests. Furthermore, while decreasing the displacement to the initial value no hysteresis was observed. As noticed earlier, much higher power variation are observed in the region where curvature is applied to the LPG, i.e. for negative values of *ΔL*. Therefore, it is expected that any small perturbation in the curvature will be translated into a linear power fluctuation in the transmitted power. In particular, from the recorded data could be estimated a change of -148 ± 3.5 μW/μm (R^2 = 0.99396) between -55 μm and -10 μm. A logarithmic curve was also fitted to the data in the range between -40 μm to 50 μm with -0.17877 ± 0.00279 dB/μm (R^2 = 0.99781). A strain displacement sensitivity of 3.077 με/μm was calculated for positive values of *ΔL* and the behavior of the transmitted power and the corresponding radius of curvature is present in Figure 6.5 (b).

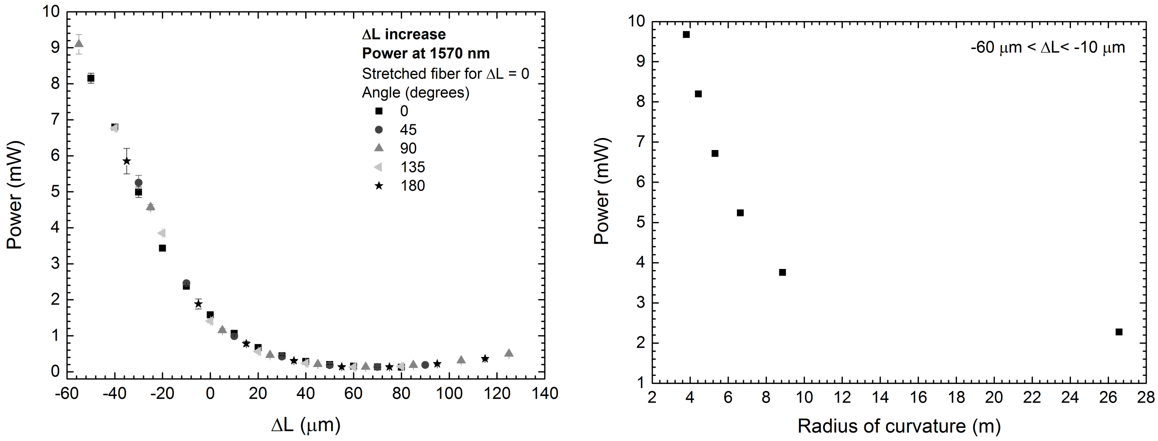

(a) (b)

Figure 6.5 – LPG power change at 1570 nm while increasing (a) ΔL between -55 µm and 125 µm or (b) the radius of curvature.

The behavior of the peak wavelength position was also characterized in the same range (Figure 6.6). The central wavelength of the resonance was calculated from the average value of the two points in the transmission curve, at lower and higher wavelengths, having +3 dB relative to the transmission minimum. In the strain regime a maximum change of 1 nm was observed between 0 µm and 125 µm, having a linear dependence with ΔL. In the curvature regime, however, linear dependence on ΔL was observed just for very small displacements, for $\Delta L > -55$ µm the spectral shift observed would rapidly decrease in magnitude, and eventually would turn from blue to red shift for $\Delta L > -20$ µm. In this regime the sensor response showed also a stronger dependence with the angle of applied curvature.

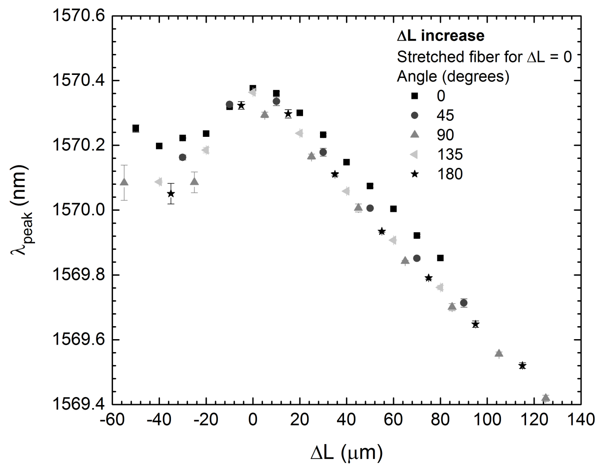

Figure 6.6 – Central wavelength of the LPG resonance according to the applied displacement with *ΔL* varying in the range between -55 μm and 125 μm.

6.1.5 Vibration monitoring based on a spectral scan

The high sensitivity to very small-applied curvatures (large radius of curvature) indicates that the LPG should also be responsive to acoustic vibration, because pressure variations will induce micro curvatures and strain in the fiber surface. Therefore, a preliminary evaluation of the sensor response was performed using the spectral scan of the FS2200SA Braggmeter from FiberSensing, in an arrangement schematically represented in Figure 6.7. The LPG was fixed with acrylate glue in two points to a solid acrylic plate (138 mm × 32 mm × 5 mm), with no torsion in the fiber, which in turn was glued to a loudspeaker. This way, a signal applied to the loudspeaker could be used to stimulate the LPG-Acrylic plate system in the 30 Hz to 18 kHz range. While this practical limitation on the frequency range tested leaves out an important range of lower frequencies, it is expected that the sensor will also be responsive in such range.

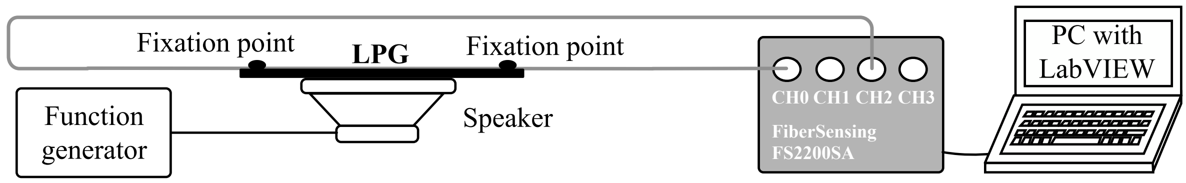

Figure 6.7 – Setup used to apply curvature to the LPG sensor consisted of a speaker connected to a function generator and a FiberSensing Braggmeter that reads the spectrum of the sensor.

As seen in Figure 6.5 (a) the sensitivity of the transmitted power, changes drastically from the curvature to the strain regime. Although it is expected to have more sensitivity in the former regime, the sensor will be tested in both operation modes. Since the Bragg meter system is based on a scanning laser, it was expected that time varying perturbations induced by micro curvature should show up as artefacts on the acquired spectra. To test this idea, the sensor was carefully glued with no torsion on the acrylic plate. Using the Optical Spectrum Analyzer (OSA), the operation point was set by adjusting the initial curvature of the sensor in order to obtain a resonance dip corresponding to ΔL = -30 μm (Figure 6.5 (a)). In this operation point, the sensor is expected to operate with maximum sensitivity, when small changes of curvature are introduced. The Bragg meter device was then connected to the LPG and the spectra as a function of frequency were recorded in the 30 Hz to 2000 Hz range.

In Figure 6.8 it is shown the apparent spectral modulation (normalized by the unperturbed spectrum of the LPG) imposed on the acquired signals when sinusoidal signals of 0.537 V_{RMS} were applied to the speaker with vibration frequencies of 600 Hz, 910 Hz and 1300 Hz, respectively. The results obtained shows that the vibration induced a change in the amplitude of the resonant loss yielding a spectral signal with a periodic perturbation in the wavelength scale. In the inset of Figure 6.8, it is exhibited the full resonance spectrum when a modulation at 600 Hz is applied (black curve) and when no vibration is applied (red curve). A modulation in the transmitted power is observed due to the micro curvatures induced by vibration. In general, the highest sensitivity is obtained in the vicinity of the resonance peak, changing slightly accordingly with the modulation frequency.

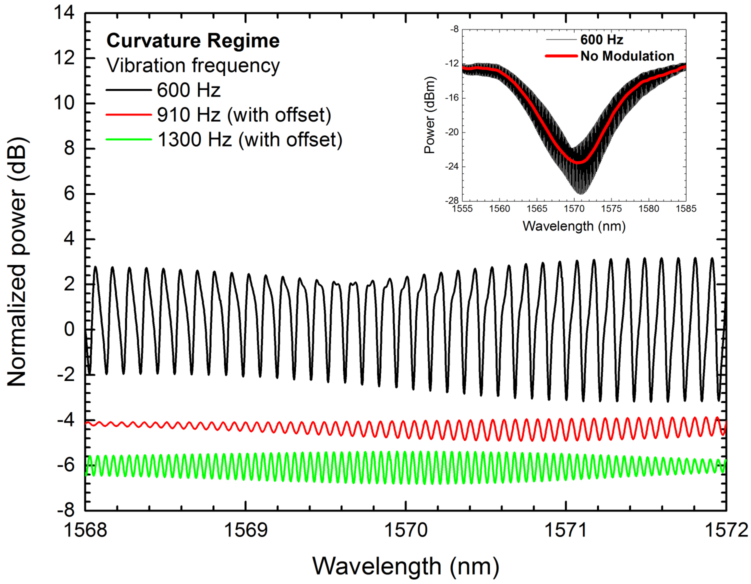

Figure 6.8 – Sensor response obtained with the Bragg meter, when the LPG is submitted to applied vibration at 600 Hz, 910 Hz and 1300 Hz, with the system operating in the curvature regime (ΔL = -55 µm).

In order to calculate the FFT of the acquired signals, it was first necessary to convert the wavelength information of the acquired spectrum to the corresponding time frame of the scanning laser. Since the unit scans a single spectrum from 1500 nm to 1600 nm in a time interval of 1.57 s, with a sampling wavelength of 2.5 pm, the wavelength yielded by the device can be directly converted to time by multiplying it by the conversion factor of 0.0157 s/nm. Also it was considered the spectrum ranging from 1565 nm to 1575 nm, where the sensitivity is higher. The results retrieved enough data, in all cases, to enable the calculation of the FFT. From the analysis of the results it can be seen the clear detection of peaks at the first harmonic of the imposed modulation as shown in Figure 6.9.

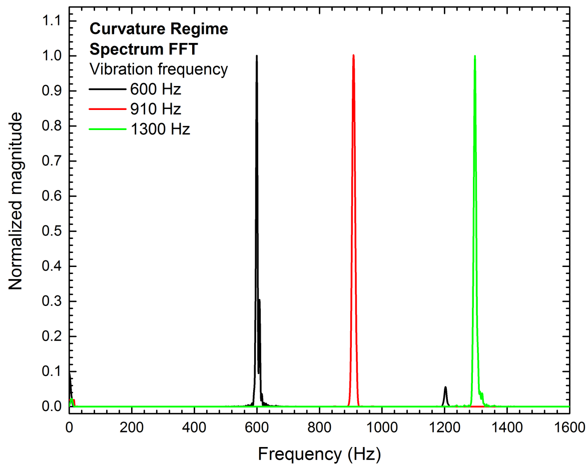

Figure 6.9 – FFT of the sensor spectrum obtained with the Bragg meter for three distinct modulation frequencies, with the sensor operating in the curvature regime (ΔL = -55 µm).

Considering the spectral region in the vicinity of the LPG resonant peak in an approximate range of 10 nm (a time frame of 0.157 s) and a minimum of four periods required in this time frame, the lowest detectable frequency by this method is 26 Hz. The number of periods is important in the FFT analysis, limiting the frequency resolution, so a minimum of four was considered. On the other hand, the maximum detectable frequency is limited by the sampling wavelength of the unit, which is 0.0025 nm. Converting this value into time and considering 10 samples for one period, the minimum required to recover the time varying signal, a maximum vibration frequency of 2547 Hz is calculated. Nevertheless, if the minimum sampling of two points per period is considered instead (Nyquist limit), the upper frequency limit rises to ~12 kHz.

The next step in sensor characterization using the Bragg meter consisted in stretching and gluing the LPG sensor to the acrylic plate in order for it to operate in the strain regime, corresponding to ΔL = 5 µm. As expected from the previous observed behavior (Figure 6.5 (a)) the results obtained in the strain regime, using the Bragg meter, show comparatively very little sensitivity. Detection of modulation was only possible in the vicinity of 600 Hz, corresponding to an acoustic resonance of the speaker plus acrylic plate system and fiber. This resonant behavior was confirmed by simultaneous measurement with another speaker working as a microphone.

In spite of these interesting details, the results obtained confirm the susceptibility of the sensor to applied vibration and demonstrate that, in a limited frequency range, certain type of spectral scanning methods can be used to retrieve the vibration frequency and amplitude. In practical applications, and to better characterize the sensor response, however, intensity based methods should be more appropriated.

6.1.6 Vibration analysis using an intensity modulation scheme

Foreseeing the possibility of using intensity-based systems in more practical applications, an alternative method using a tunable laser, Santec TSL-210V, was tested in the interrogation of the LPG vibration sensor with the setup shown in Figure 6.10. The tunable laser used has a line bandwidth of $\Delta\upsilon$ = 1 MHz ($\Delta\lambda$ = ~0.009 pm) and 15 mW of peak emission power. In this setup the sensor response to frequency is assessed using a tunable laser at a fixed wavelength, while recording the transmitted power using a photodetector, an analog-digital converter (DAQ NI USB 6363) system and a PC with appropriate LabVIEW software for signal acquisition and processing. The input channels of the DAQ had a resolution of 1.92 mV and the developed software was set to acquire the photodetector signal, searching for the most significant harmonic and recording its peak amplitude and frequency as a function of time. In the program, a vector of 10^5 samples and a sampling frequency of 10^5 Hz were defined. For each vibration frequency applied to the speaker, the AC optical signal, normalized by the DC value, was recorded during 60 s and its average and standard deviation values were calculated. This normalization makes the recovered signal independent of power fluctuations.

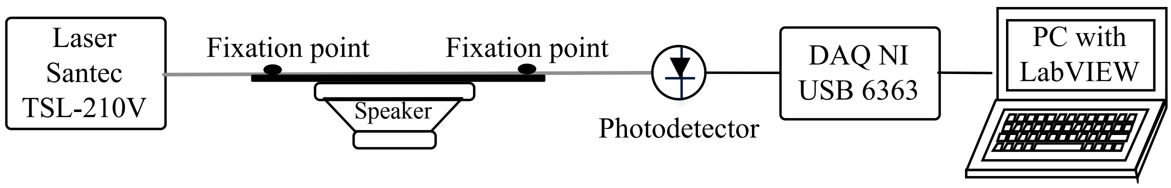

Figure 6.10 – Setup used for testing the sensor response to vibration.

As before, the sensor response to vibration was tested in the curvature and in the strain regime.

6.1.6.1 Vibration in the curvature regime

Firstly, the sensor response was characterized in the curvature regime (ΔL = -30 μm) from 30 Hz to 2000 Hz by applying an average vibration amplitude of 0.5 V_{RMS}. In Figure 6.11 it can be observed the normalized amplitude modulation of the signal read in the photodetector for 400 Hz, 650 Hz and 1000 Hz, showing different modulation amplitudes. During the measurements, the power of the laser was maintained constant. The main reason for the sensitivity dependence with frequency is the fact that, depending on the particular vibration modes excited on the surface, different vibration patterns with nodes and maxima, can be imposed on the fiber that condition the sensor response. The optimization of the arrangement of the fiber plus support plate and speaker ensemble, to explore further this mutual dependence, is a research topic by itself and will be explored in future work.

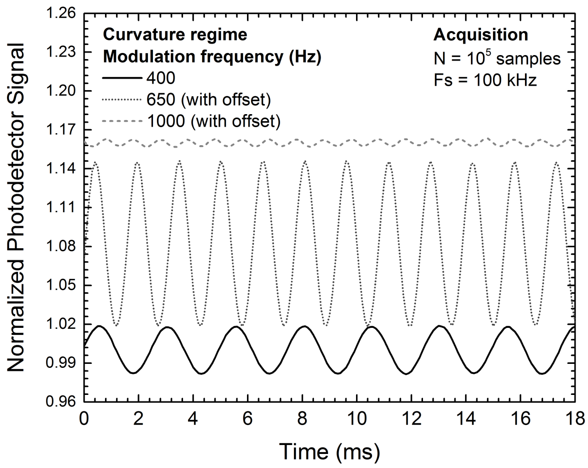

Figure 6.11 – Recovered optical output signals for several frequencies with the sensor operating in the curvature regime (ΔL = -30 μm).

From these tests resulted the data displayed in Figure 6.12, for frequencies from 30 Hz to 2000 Hz. The modulation amplitude defined by the function generator is fixed. However, because the speaker has lower impedance than the function generator and its impedance dependents on frequency, the speaker modulation amplitude changed 9.3 % from 30 Hz to 2000 Hz. Having this effect into account, the results shown in Figure 6.12 are also normalized as function of the function generator amplitude (Mod_{RMS}). Three independent tests were conducted, where some resonance peaks were detected at 300 Hz, 580 Hz and 1810 Hz, showing very high changes in amplitude.

While the same peaks were detected in all three independent tests, it was observed a great variability of the detected amplitude, particularly in the vicinity of the resonances. For instance, the resonance neighboring 300 Hz showed from the first to the second measurement an amplitude increase of 20.7 %. For the resonance at 580 Hz an amplitude increase of 200 % was observed between the first and the second measurements. On the other hand, off the resonances it can be observed that the sensors yielded very reproducible results. The frequency generator used during the experiment was manually configured, and although an effort was made to set the same frequencies in each measurement, very small changes and fluctuations could have taken place, inherent to the system limited resolution. As a result, slight changes in the frequency will result in amplitude differences, especially for the regions nearby the resonance where the rate of change of amplitude with frequency is much higher. Furthermore, changes in the laser input polarization may also affect the modulation amplitude of the optical signal. A change in the resonance dip of -3.2 dB (-52 %) was observed in the Bragg meter, while varying the input polarization.

Vibration of the structure was also simultaneously measured as function of frequency, using a microphone at 5 mm distance from the optical sensor. With this setup, a maximum positive variation of 2.4 % was observed at 580 Hz, much less than the one obtained with the optical sensor, with 200 %. This result indicates that the observed changes may be related with fluctuations of the resonant condition of the fiber-plate-speaker ensemble.

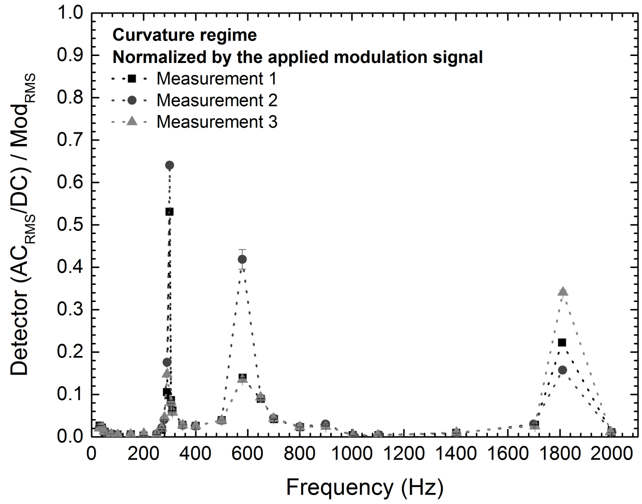

Figure 6.12 – Recovered AC amplitude as a function of the frequency generator for the sensor operating in the curvature regime (ΔL = -30 μm). Results are shown for three independent measurements.

In order to better understand the sensor behavior, the LPG transmission spectra was recorded before and after the vibration test. This way it was possible to evaluate if there was some spectral change that could justify part of the changing response. In Figure 6.13 are shown the spectra of the LPG sensor acquired without applied vibration, before and after the vibration tests. The values of the parameter *Depth,* considered as the contrast of the LPG and given by the difference between the transmission at the base and at the peak of the resonance are depicted in the graph and are respectively 17.21 dB and 21.07 dB, before and after the test, respectively. This corresponds to a change in the depth of the resonance of -3.82 dB, implying a change in the optimum operation point and consequently affecting the overall sensitivity. This effect may be related with changes in the input polarization and in the curvature due to the fiber being slightly loose in the support plate.

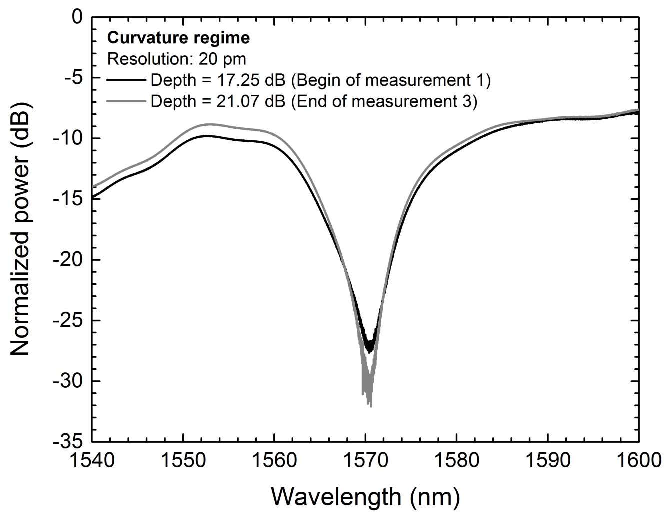

Figure 6.13 – Spectrum of the LPG sensor obtained with the OSA in the beginning and in the end of the measurements.

A detailed analysis of the LPG resonance peak during the tests was also investigated. The resonance depth could be tracked by evaluating the DC component of the signal read with the photodetector, as function of the frequency. The results of these tests can be seen in Figure 6.14. The data clearly indicates that changes in the amplitude of the resonance peak were taking place while varying the frequency, mostly in the vicinity of the resonances. The DC value in the beginning of first and last measurement, indicates an overall power increase in the order of 10.9 %. As previously mentioned, a linear fit was calculated in the range of -55 μm to -10 μm in Figure 6.5 (a). In this range, the sensitivity of the sensor to changes in curvature is constant and does not depends on the initial ΔL. According to Figure 6.5 (a), the sensitivity is constant in the range of -55 μm to -10 μm, so assuming an initial ΔL of -30 μm, a maximum positive and negative power variation of 110 % and 44 %, respectively, can occur without affecting the sensitivity.

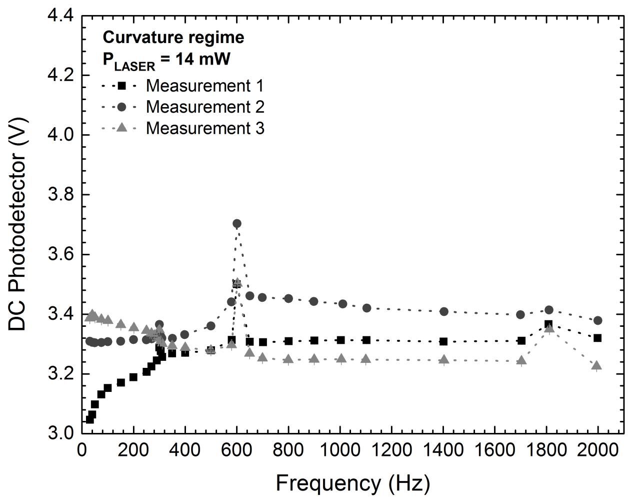

Figure 6.14 – DC part of the signal read with the photodetector as function of frequency, in the curvature regime (ΔL = -30 μm).

Linearity of the sensor response to the amplitude of modulation was also tested by fixing the modulation frequency and changing its amplitude. Tests were performed at 450 Hz and 700 Hz while changing the AC amplitude in the function generator from 0 to 0.7 V_{RMS}. A linear fit (R^2 = 0.9971) with a sensitivity of 0.2121 1/V was achieved at 700 Hz, however sensitivities were different depending on the frequency, with 0.0222 1/V at 450 Hz (9.6 times less) a result already expected according to Figure 6.12.

6.1.6.2 Vibration in the strain regime

Sensor AC response was also characterized in the strain regime from 30 Hz to 1800 Hz for ΔL = 5 μm. In Figure 6.15 it is shown the sensor output signals acquired during the application of modulation at three distinct frequencies. A residual low frequency signal, at 73 Hz was present in all frequencies, which was not observed in the curvature regime, nevertheless the strongest harmonic corresponds to the applied vibration frequency. In this case the fiber is under tension making it, in principle, more stable. On the other hand, the existence of the fixation points, together with a lower mobility make it more prone to pick up specific modulation at the surface of the acrylic support.

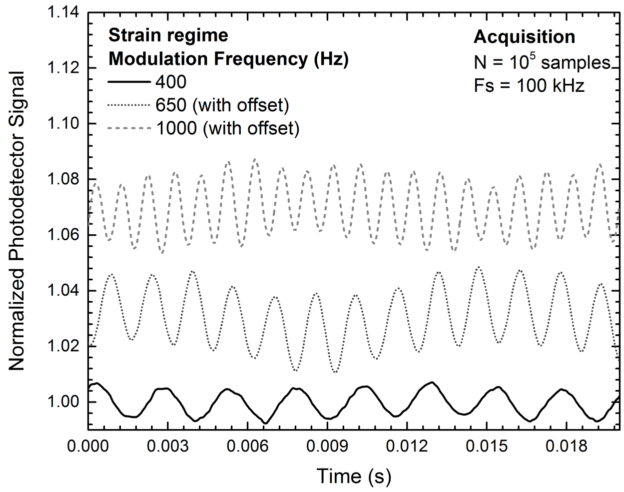

Figure 6.15 – Recovered optical output signals for several frequencies with the sensor operating in the strain regime (ΔL = 5 μm).

Three independent tests where the amplitude of modulation was registered while the frequency was scanned between 30 Hz and 1800 Hz were also carried out. The results for the three measurements are shown in Figure 6.16. The reproducibility of the tests is in general better than observed in the curvature regime, except at the resonance at 1100 Hz, where strong variability is registered from test to test. Again this amplitude changes occur at the resonant value where slight changes in the resonance frequency of the modulator or the resonant condition of the collective structure: fiber, acrylic plate and speaker, can result in mismatch and consequent reduction in sensitivity.

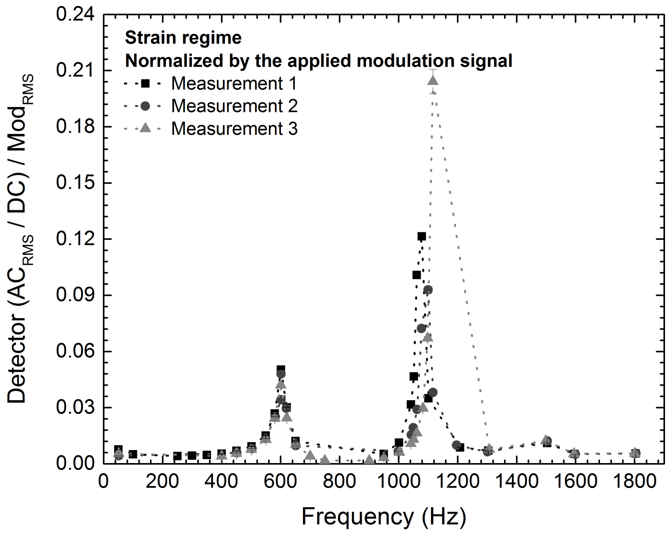

Figure 6.16 – Recovered AC amplitude as a function of the frequency generator for the sensor operating in the strain regime (ΔL = 5 µm).

Comparing this result with the one obtained in the curvature regime (Figure 6.12) a better reproducibility can be observed, particularly at the resonance at 600 Hz. This derives from the fact that the pre-tension in the LPG reduces its freedom to oscillate resulting in a more stable response to the acoustic stimulus. As before, the frequency determination athwart the amplitude of the signal read in the photodetector is the same as the one applied to the speaker. In the range of 150 Hz to 350 Hz, from 700 Hz to 900 Hz and for 2000 Hz in some tests it was not possible to recover the modulation signal because the AC modulation was too weak. In the curvature regime, Figure 6.12 shows three resonances, at 300 Hz, at 580 Hz and at 1810 Hz, while in the strain regime only two resonances were found at 600 Hz and at 1100 Hz. This change is related with the fiber being attached differently to the acrylic support, changing the acoustic response.

The acrylic plate response to vibration was also measured using a microphone at 5 mm distance, showing only a resonance at 600 Hz. Furthermore, at 1116 Hz between measurement number two and three, the optical sensor response increased 424 %, while the microphone showed a positive variation of 0.6 %. This result shows that the amplitude response of the optical signal was not constant for the same vibration frequency, probably due to fiber relaxation in the attachment points during the tests.

The optical sensor response was also compared between these two operating regimes at two distinct frequencies, 400 Hz and 900 Hz, unmatched with any resonances. The strain regime showed lower amplitude, with a decrease of 84 % and 94 %, respectively. A detailed analysis of the experimental points in Figure 6.16 indicate that in measurement number three it was not possible to recover the applied modulation frequency in the range of 150 Hz to 350 Hz, because the AC response decreased in relation to the other measurements.

In Figure 6.17 it is shown the DC signal read in the photodetector while varying the frequency, showing a positive power change of 35.4 % in the beginning of measurement 1 and 3. As in the curvature regime, the results are not reproducible and the peak power of the resonance is constantly changing along tests, resulting in different amplitude response, as shown in Figure 6.11.

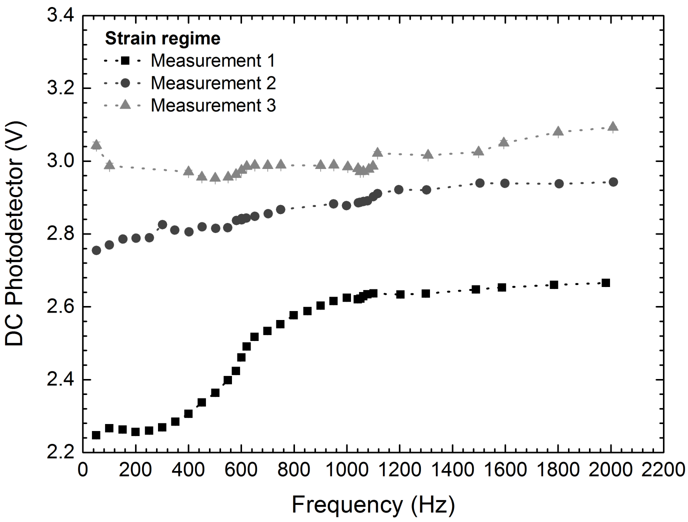

Figure 6.17 – DC part of the signal read with the photodetector as function of frequency, in the strain regime (ΔL = 5 μm).

Fixing the modulation frequency at 600 Hz and changing the AC function generator from 0 to 0.7 V_{RMS}, the linearity of the sensor response was tested. A linear fit with R^2 = 0.9943 was achieved for 600 Hz (resonance), with a sensitivity of 0.0475 1/V, 4.47 times less, a 77 % reduction in relation to the one obtained in the curvature regime at 700 Hz.

In order to assess the sensor response at lower frequencies a system using a Tira GmbH TV 52110 vibration column (property of Fibersensing) was used to generate sinusoidal vibration frequencies between 7 Hz and 15 Hz, with a peak to peak amplitude of 2.2 mm. Two independent measurements were performed, however in the second set of measurements it was not possible to detect any perturbation at these frequencies, indicating possible sliding of the fiber fixations. This result clearly shows how the coupling between the fiber and the holding plate is critical and needs optimization, in order to maximize the optical response to low frequencies. In spite of all, the test allowed to confirm that the sensor setup should be responsive also in the lower range of frequencies.

6.1.6.3 Sensor Resolution

To better characterize the sensor performance, the resolution and maximum measurement errors were estimated in different situations. The worst frequency resolution (calculated as two times the standard deviation of the measured frequency in 60 s samples intervals) and frequency errors (resolution divided by the average frequency of each sampling interval) were calculated for the three independent measurements presented in Figure 6.12 (curvature regime) and in Figure 6.16 (strain regime), and are shown in Figure 6.18. Comparing both operation regimes the results show overall quite similar resolutions values and measurement precision errors. Also, it can be seen that with increasing frequency the frequency resolutions are also degraded, but the frequency errors uphold around a relatively constant value and below ±0.08 %.

In the curvature regime the worst resolution achieved in the three independent tests was 913 mHz for 2000 Hz and the maximum precision error was ±0.049 % for 1700 Hz. On the other hand, for the sensor operating in the strain regime, where the sensitivity was 4.47 times lower than in the curvature regime, the resolution and precision errors were slightly higher with a maximum of 1 Hz at 1600 Hz and ±0.081 % for 600 Hz, respectively. In Table 6.1 it is presented a summary of the values obtained with the sensor operating in the two regimes.

Table 6.1 – Summary of the main parameters of the vibration sensor in the curvature and strain regime.

Regime	Frequency (Hz)	Sensitivity (1/V)	Resolution (Hz)	Frequency precision error (%)
Curvature	450	0.0222	0.913 Hz @ (2000 Hz)	±0.047 % @ (1700 Hz)
	700	0.2121		
Strain	600	0.0475	1 Hz @ (1600 Hz)	±0.081 % @ (600 Hz)

Having into account the frequency resolutions attained, the optical sensor is suitable for applications in structure monitoring only for frequency discrimination, where the amplitude of modulation is not critical. Moreover, it is important to position the sensor with curvature, where the sensitivity to vibrations is higher. In this regards, the proper fixation and positioning of the sensor in the structure can have a strong influence in its sensitivity and amplitude of response. This can be explored, by design of supports that can amplify or reduce the response of the sensor to given target frequencies.

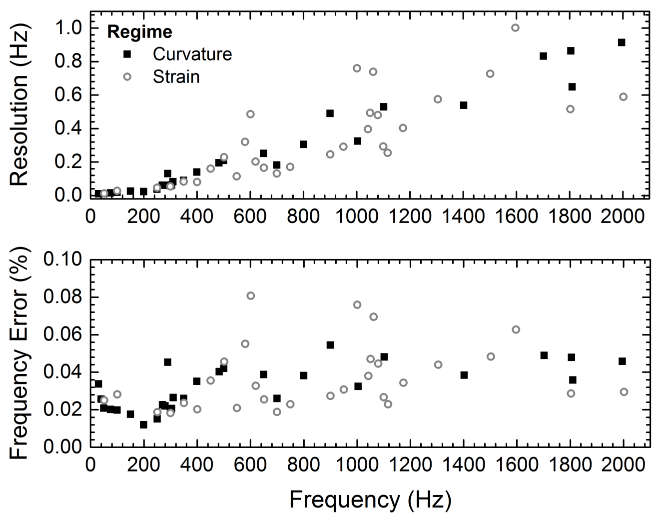

Figure 6.18 – Resolutions and measurement errors estimated as a function of the applied frequency for the LPG sensor operating in curvature (ΔL = -30 μm) and strain regime (ΔL = 5 μm).

6.1.6.4 Sensitivity dependence with wavelength

Although this sensor is intended to be used in frequency discrimination, if the vibration amplitude is too small it would not be possible to track the resonance frequency. This effect can occur due to temperature changes, with the LPG resonance shifting in wavelength as function of temperature 0.05767 nm/^{o}C. In order to evaluate the impact of the temperature in the sensitivity, a constant vibration amplitude and frequency was maintained. For each regime, three independent tests were conducted and presented in Figure 6.19, where each value is the average and standard deviation of the three measurements. Comparing both results, the strain regime is a little less sensitive to positive wavelength shifts at 600 Hz. Having into account the sensitivity of the LPG to temperature, an increase of 52 ºC will shift the resonance by 3 nm and consequently the sensitivity decreases 58 %, with the sensor operating in the strain regime. Also, for an increase of 86.70 ºC, the sensitivity decreases further 77 %. For the sensor operating in the curvature regime the results are worst. A change of 52 ºC and 86.70 ºC will reduce the sensitivity by 85 % and 91 %, respectively. Considering the curves in Figure 6.19 it was still possible to detect a minimum variation of the signal $(AC_{RMS}/DC)/Mod_{RMS}$ of 0.0014 1/V with the sensor operating in the curvature regime. This way, if the sensor is optimized for a given frequency range, it can withstand relatively large changes in temperature and still detect the target vibrations.

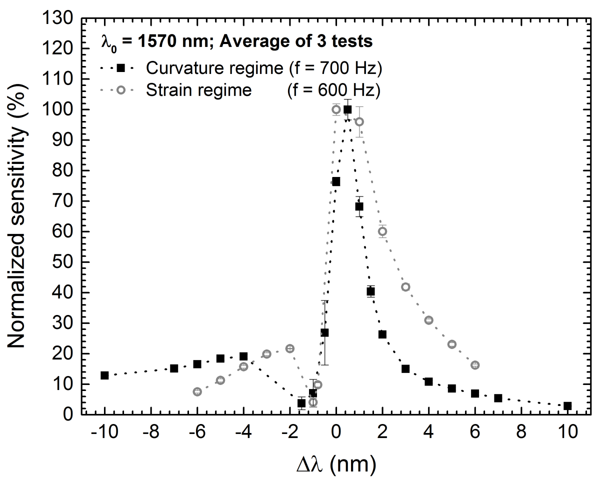

Figure 6.19 – Sensitivity of the LPG sensor as function of the laser wavelength operation change, for the LPG sensor operating in curvature (ΔL = -30 µm) and strain regime (ΔL = 5 µm).

6.2 LPG with a magnetostrictive material for magnetic field sensing

The previous vibrations tests, with the sensor operating in the strain regime, indicated that it could be used for magnetic field sensing, provided it is coupled with the right transducer element. In order to test this idea, the LPG was coupled to a rod of a magnetostrictive material (Terfenol-D). The sensor was pre-strained and glued in two fixation points, 52 mm apart. In these conditions, in the presence of a magnetic field, strain will be induced in the magnetorestritive rod which will modulate the LPG and impact the resonance dip accordingly. The experimental setup implemented to test this idea is shown in Figure 6.20 where the magnetic field is generated with an inductor with a relation of 9 mT/A, along the 52 mm extension of the sensor element. A specific LabVIEW program was designed for signal acquisition and processing. The transmitted optical signal and the current waveform applied to the inductor, were read with the analog digital converter from NI USB 6363, already used on the previous chapters. Due to electronic limitations of the current amplifier, the maximum alternating current that could be applied was of 3.5 mT_{RMS} at 20 Hz (no bias magnetic field could be set). Acquisition was done with a sample frequency of 1 kHz and filtering was performed at the second harmonic resulting from the symmetric response of the magnetostrictive material as function of the magnetic field, with a Butterworth band-pass filter with a 5 Hz bandwidth. As mentioned in Chapter 5, the 20 Hz modulation frequency was chosen for providing the best compromise between magnetic field amplitude and SNR.

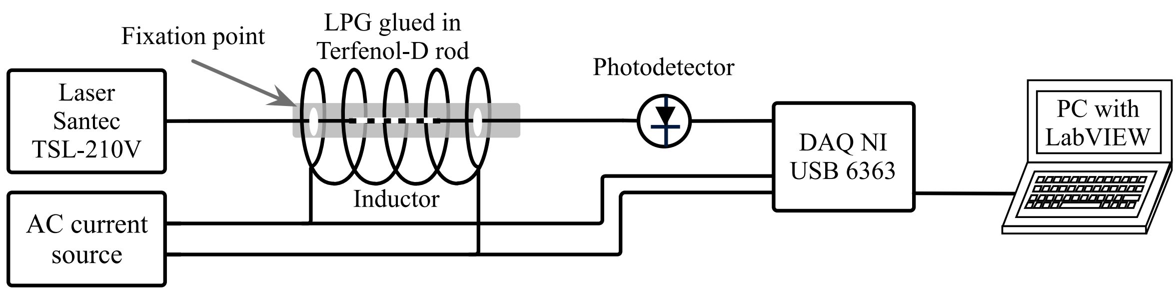

Figure 6.20 – Setup used to measure magnetic field with the LPG sensor glued to the magnetostrictive material.

Previous results showed that the sensitivity of the readout system to vibration is dependent on the relative wavelength position of the laser and the resonance dip. Hence the tests for the LPG based magnetic field sensor were carried out at two distinct wavelengths, near the resonance peak, at 1570 nm and 1569.7 nm, respectively.

6.2.1 Experimental results

The sensor was submitted to an increasing magnetic field between 0 and 3.3 $mT_{RMS,}$ by successively incrementing the applied alternating magnetic field with steps of approximately 0.25 mT with a duration of 30 s each. Three independent measurements were performed. The results obtained can be observed in Figure 6.21 (a) showing a behavior that can be fit by a 3rd order polynomial up to the 2.52 mT_{RMS} range. In this Figure, the average and standard deviation of the three measurements are also shown, revealing a good agreement between independent measurements. Furthermore, the waveform of the applied magnetic field and the corresponding photodetected sensor output is shown for 3.28 mT_{RMS} in Figure 6.21 (b). The photodetected signal presents a high level of distortion, with a SNR of 36.15 dB, measured with a 10 Hz bandwidth. The distortion is related with the magnetostrictive material response and primarily due to the LPG amplitude modulation dependence with wavelength, already observed in Figure 6.8.

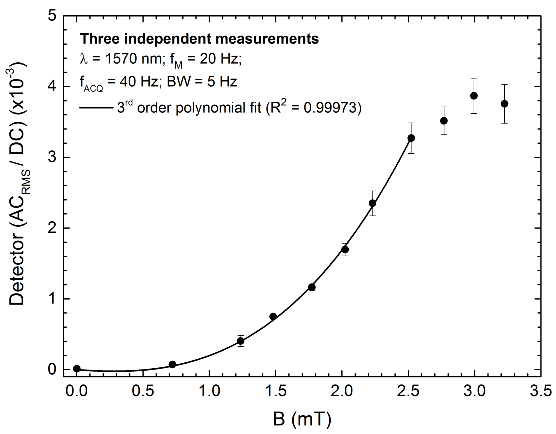

(a)

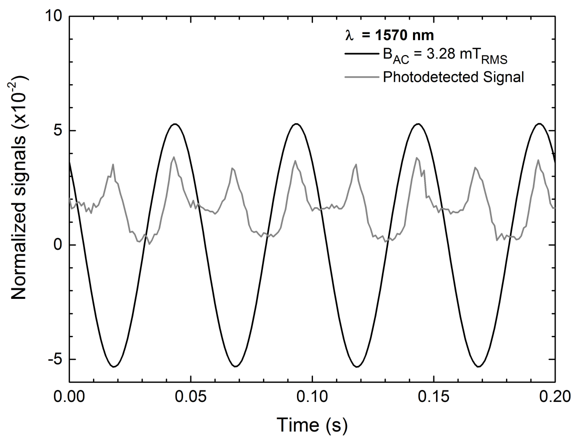

(b)

Figure 6.21 – (a) Normalized photodetected AC response as function of the magnetic field and in (b) the applied magnetic field and the corresponding photodetected signals (with gain) obtained at 1570 nm.

The same measurements were performed with the laser operating at 1569.7 nm where much better results could be obtained as demonstrated in Figure 6.22. The recovered optical signal present much less noise, containing only the distortion due to the magnetostrictive material, showing the frequency doubling. In Figure 6.22 (a) a 4th order polynomial curve provided a good fit ($R^2 = 0.99996$) to the experimental data where the maximum response registered was 4.2 times higher than in the previous test (Figure 6.21 (a)). The SNR was also calculated at 10 Hz bandwidth yielding a value of 40.71 dB, which represents an improvement of 4.56 dB relatively to the previous test performed at 1570 nm.

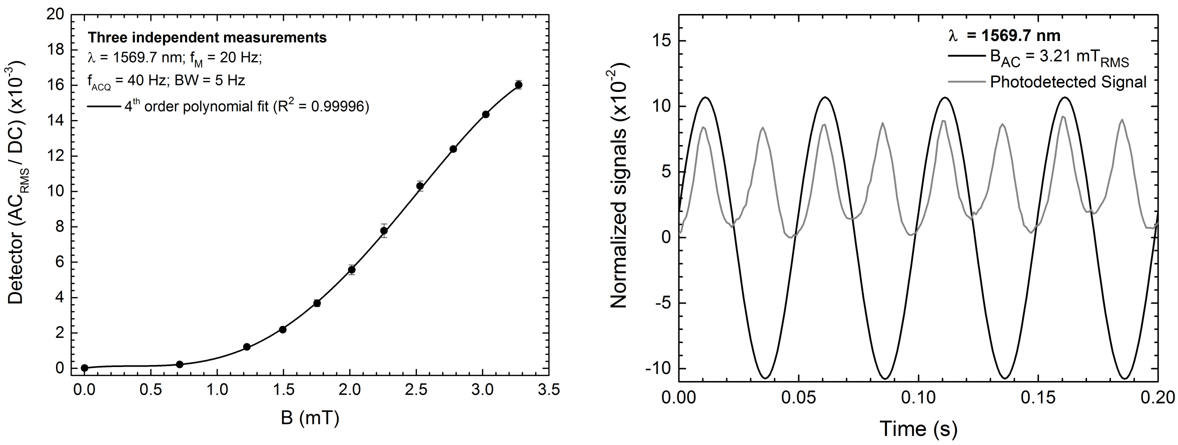

(a) (b)

Figure 6.22 – (a) Normalized photodetected AC response in relation to the DC component and in (b) the applied magnetic field and the corresponding photodetected signals (with gain), obtained for 1569.7 nm.

Resolutions were also analyzed as a function of the magnetic field and the values corresponding to maximum errors are shown in Figure 6.23. As expected, better results were attained for the 1569.7 nm wavelength, because the sensitivity is higher. The best resolution values registered were 2.06 $\mu T_{RMS}/\sqrt{Hz}$ and 7.41 $\mu T_{RMS}/\sqrt{Hz}$ for 1569.7 nm and 1570 nm, respectively.

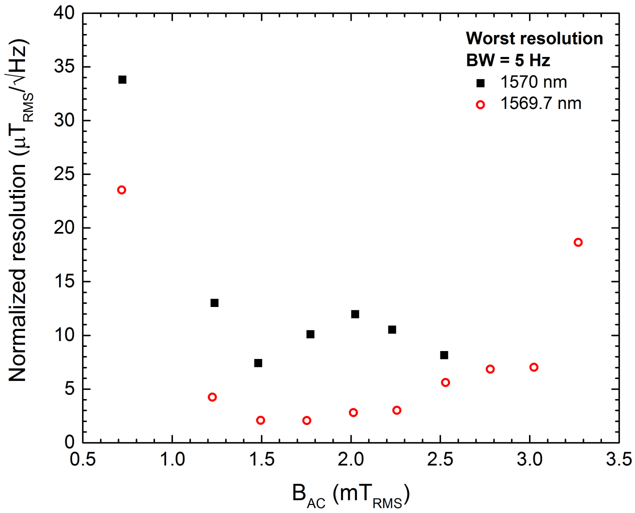

Figure 6.23 – LPG sensor magnetic field resolution as function of the applied AC magnetic field, with the laser operating at 1570 nm and 1569.3 nm.

Comparison with previous optical current sensors can be done by estimating the equivalent current for a conductor at 40 mm distance, through equation (5.6) providing a relation of 225 A/mT. Having into account the sensor operation only responds to magnetic fields higher than 1.2 mT, an equivalent current of 495 A_{RMS}, it is not possible to satisfy class 1 operation. However, the minimum detected value can be improved by the use of a bias magnetic field, but at the time of the experiment there was no available equipment, capable of generating simultaneously a DC and an AC field.

6.3 Summary

An LPG fabricated in a standard fiber was implemented and tested for vibration and magnetic field sensing. The sensor was shown to be highly sensitive to the applied curvature yielding a change in the resonant peak amplitude without affecting too much its peak wavelength position.

The sensor was tested in the curvature and strain regime and interrogated using both a spectral scan and a laser source tuned to the resonant peak. Using the spectral scan laser source and the sensor operating in the strain regime it was only possible to detect the vibration resonance at 600 Hz. However, in the curvature regime, it was possible to detect a wider range of frequencies, because the sensitivity was higher. For instance, in the curvature regime, 4.47 times more sensitivity was obtained at 700 Hz, than in the strain regime at 600 Hz, corresponding to a resonance peak.

On the other hand, using the intensity-based scheme it was demonstrated the possibility to detect vibration in structures with frequencies ranging from 30 Hz to 2000 Hz with a maximum resolution of 913 mHz and 1 Hz, in the curvature and strain regime, respectively. However, the recovered modulation amplitude was not stable, especially in the vicinity of the resonance peaks. In the curvature regime differences between measurements of up to 200 % were observed in the detected amplitude near a resonance peak, at 580 Hz. High errors were also found in the strain regime, at 1116 Hz with an increase of 424 %. Despite the instability observed in amplitude determination, the results suggest the sensor can successfully be used in identification of the vibration frequency.

The LPG was also tested in temperature where a sensitivity of 57.67 pm/^{o}C in the resonant peak was found. Nevertheless, while the wavelength shift can reduce the sensitivity to applied vibration, it still allows retrieving the signal frequency in a broad range of temperatures. For the sensor operating in the curvature regime a change of 52 ^{o}C will reduce the sensitivity by 85 %, nevertheless, still enabling frequency identification. Overall the results indicate that the sensor is highly sensitive to the way it is coupled to the system under monitoring. This way, working on the optimization of material, shape and disposition of the fixation system, the sensor can be tailored to monitor specific frequencies with much higher sensitivity.

Finally, the LPG sensor was also tested in the detection of magnetic fields. A Terfenol-D rod was attached to the sensor and results presented resolutions of 2.06 $\mu T_{RMS}/\sqrt{Hz}$ and 7.41 $\mu T_{RMS}/\sqrt{Hz}$ for 1569.7 nm and 1570 nm wavelength, respectively. Classification of the sensor according to the electric grid requirements was not possible because the minimum equivalent current is too high and the range was somewhat limited. Nevertheless, the sensor small size and remote sensing ability can be useful to monitor large current inside complex systems such as generators.

Chapter 7 Conclusion

In this doctoral thesis a set of different optical fiber sensor technologies was explored aiming its future application in high power grids, in the context of a project with Brazilian industry. In particular, different optical fiber current sensors, using both bulk and all fiber sensing heads, were implemented and tested. Several promising features, as well as critical problems were identified in each of the technologies explored. While several technological problems should still be addressed, overall, fiber optics technology presents several highly attractive features that make it an enabling technology for truly smart grids.

In this document, a detailed description of the fiber optic magnetic field sensors has been presented, using distinct sensing mechanisms, such as Faraday effect, magnetostrictive effects and Lorentz force for constant and alternating magnetic fields.

Sensors based on Faraday effect were developed, using bulk and fiber optic materials. The first sensor was present in chapter number three and consists of a pre-industrial prototype developed for the TECCON project, including a clamp-on portable bulk sensing head and an acquisition system. The sensing head is constituted by a high Verdet constant diamagnetic material of low birefringence and low elasto-optic coefficient, in order to improve the sensitivity, avoid saturation effects and be practically immune to induced linear birefringence effects due to packaging.

Experimental results obtained at 830 nm revealed the possibility to reject most of the common-mode noise while using the quadrature processing scheme, improving the resolution by at least 4.6 %, when compared with the basic polarimetric detection. The sensor was classified as a 1 class device considering nominal currents equal or greater than 900 A_{RMS}. Moreover, detection of transient pulses was demonstrated where several pulses under 10 μs were detected, expressing the viability of the single prism bulk optical sensor to be used both as a metering and a protection device in high power systems applications. However, in its present form, the arrangement of prims and coupling lens its still very susceptible to misalignments with temperature. A more stable version will require setting up a monolithic sensing head with all optical components glued together with adequate optical epoxy glues.

Simulation of an electric grid configuration, as proposed in project TECCON, was analytically studied by positioning the clamp-on sensing head in distinct locations around the conductor. Results demonstrate that a minimal amplitude error do not always corresponds to a minimal phase error. Either way, considering distinct sensor positioning and the three conductors, it was possible to minimize the amplitude error to ±0.68 % with a phase error of 0.57 degrees. This result indicates that without proper shielding of the sensor, it can only operate as a class 1 sensor, enabling its operation only in protection systems, in high power lines for transient detection. Nevertheless, a more stable monolithic approach, proper shielding and positioning in the power line, should enable a device suitable both for high accuracy metering and protection applications.

Closed loop configurations, easily obtained with fibers, can easily overcome the hindrance of external fields. This way, all-fiber current sensor based on the Faraday effect were also studied using a polarimetric detection schemes. For the sensing coil, three distinct fibers were used: one of them was a standard SMF and the other two were spun HiBi fibers, elliptically stressed fiber from IVG and a spun photonic crystal fiber (PCF) developed by Gleb Wataghin physics institute from the University of UNICAMP, Brazil. Both the SMF and IVG fibers were tested in a transmission and in a reflection configuration, using a polarimetric interrogation scheme. The PCF fiber, however, could only be tested in transmission due to experimental constrains. In the first transmission configuration the results were very poor (with the all three fibers) because in a transmission configuration there is no compensation of the SOP drift due to reciprocal effects, such as induced birefringence due to temperature and pressure variations of the fiber against the coiling support. Furthermore, with the spun HiBi fibers a high degradation of the DOP was observed when increasing the optical source bandwidth, especially with the 50 nm bandwidth optical source, where no Faraday rotation could be measured because the SOP decreased to 0.5 %.

Nevertheless, in the reflection configuration, with the FRM, where the reciprocal linear and circular birefringence effects are compensated, good results were achieved. The conventional SMF fiber showed lower sensitivity and much more susceptibility to induced linear birefringence due to winding, than the commercial spun HiBi fiber. While overall results with the IVG fiber were much better, still, the need to splice a short 2 m section of SMF in the setup (from the FRM) greatly limited the sensor stability due to the sensitivity of the SMF to linear birefringence.

Nevertheless, results obtained showed that the SMF fiber could be used as an accuracy class 1 sensor for nominal currents equal or higher than 700 A_{RMS}, while the spun IVG fiber complied, instead, with accuracy class 0.5 operation for nominal currents of 600 A_{RMS} or higher, enabling its application in metering and protection systems. In many of the tests performed, the intrinsic sensor precision seemed to indicate a better performance was possible. However, the poor stability of the high current source, with fluctuations often exceeding the sensor precision, limited more accurate characterization. In order to better classify and optimize the sensor systems a high accuracy current generator and meter are needed. In spite of all, it was possible to observe that, increasing the number of turns allows to improve the sensitivity and resolution for the spun HiBi fiber, increasing its potential for precision metering.

Results also confirm that such sensor configurations will not work properly in the field unless highly birefringent spun fibers are used. Indeed, susceptibility of the sensing coil to pressure was also studied by deforming the sensing coil with a 12 mm cross-section rod. The IVG fiber proved to be weakly dependent, decreasing the sensor sensitivity by 4% with 4 mm deformation, against the 50 % decrease attained with the standard fiber with 3 mm deformation. Still, in order to ensure the sensor will comply with the errors limit requirements in precision metering, when the sensor is placed in the harsh environment conditions, it is necessary to further protect the sensing coil inside a capillary and immerse it in oil, or a controlled atmosphere, to avoid friction, as mentioned in the state of the art. Susceptibility to vibrations were also analyzed for the conventional SMF and the IVG fiber, where no perturbation was found on the sensor signal (no harmonics at the perturbation frequencies were found in the frequency spectrum of the acquired optical signal).

Although the HiBi PCF fiber could not be tested in a reflection configuration, it is a very promising candidate to be used in current sensing, because its expected to have very low induced linear birefringence temperature dependence, contrary to the commercial IVG HiBi fiber, which is made of two distinct materials.

In the fifth chapter, a different class of sensors was tested. In particular, three distinct optical fiber lasers configurations were developed for magnetic field sensing, employing a magnetostrictive material, a Terfenol-D rod bar, acting as the magnetic-strain transducer. The loop and the wavelength modulated Fabry Pérot lasers both required a passive interferometer acting as a wavelength-intensity converter. Although the first configuration needed only one FBG, the second configuration provided better SNR and a more stable output power, when the laser Bragg mirrors were being modulated by the magnetic field. This effect was related with the laser spectral width because each mode is affected differently and when the cavity length is reduced, less modes exist and the overall effect translates into additional power instability. Best resolution values obtained were 13.75 $A_{RMS}/\sqrt{Hz}$ and 1.22 $A_{RMS}/\sqrt{Hz}$, for the first and second configuration, respectively. However, for this particular kind of sensors, none of the configuration would comply with any of the measurement accuracy classes. Besides having slightly larger errors, it measurement range was also very limited when compared with the Faraday sensors. In particular, the sensors did not respond to currents below 495 A_{RMS}, with the exception of the wavelength modulated Fabry-Pérot laser, but accuracy errors exceeded ±1 %. Although the magnetostrictive element is subject to saturation effects it may also be also used in protection, for cases where the shape of the pulse is not important, with bandwidth up to 100 kHz. Nevertheless, if the application is only for protection, the distance between the sensor and the conductor can also be increased, enabling the sensor to detect higher currents, with the disadvantage of increasing the minimal current. Also, the small dimensions of these sensors, together with the possibility of remote interrogation, can make then suitable alternatives for measurement of large currents inside complex devices such as high power generators.

An LPG interrogation scheme was also tested as an alternative interrogation method but demonstrated not to be a viable alternative, because its spectral width was quite wide in relation to the interferometer, limiting the overall sensitivity. Furthermore, due to practical fabrication limitations it cannot be reduced.

Exploiting the laser power stability dependence with its spectral width, the intensity modulated laser configuration, whose bandwidth was controlled with two narrow band fiber Bragg mirrors, partial overlapped, allowed to develop a sensor whose magnetic field information was encoded in power. This sensor presented a solution, which did not require the use of an interferometer, achieving a minimal resolution of 6.1 $A_{RMS}/\sqrt{Hz}$. These three configurations can be used for protection, however its expected saturation related with the magnetostrictive material. Other two narrow bandwidth configurations were explored but the unstable behavior related with the magnetic field modulation were undesirable.

In the last chapter, a LPG was proposed for vibration and magnetic field sensing by recording the changes in the resonance peak amplitude with an intensity-based scheme. The sensor was tested by positioning the LPG sensor on the plate and operating it in strain and curvature regimes, where in the latter mode, higher sensitivity was attained. It was demonstrated the possibility to detect vibration in structures with frequencies ranging from 30 Hz to 2000 Hz with a maximum resolution of 913 mHz. The results indicated good frequency discrimination but the amplitude instability observed suggests the fiber/support plate ensemble needs further study, potentially being adjusted to maximize the response in the pretended frequency range.

The next step consisted on evaluating the LPG sensor in magnetic field recognition. A Terfenol-D rod was attached to the sensor providing a resolution of 4.61 μT_{RMS} at 1569.7 nm wavelength. In this case the sensor did not fit any of the accuracy class requirements. As previously, further investigation in the fiber/support assemble is required to optimize the structure response as function of the alternating magnetic field.

In summary, a prototype clamp-on optical sensor was developed which is a promising candidate to be used in the high power grid for precision current measurement and protection applications, provided improvements in the alignment and fixation of the components are established. This work will be carried out in a project TECCON II, which aims to incorporate the bulk sensor in a high power insulator, establishing a truly industrial prototype that will be tested in high power laboratories and in a field application.

It was also established that the polarimetric sensor with spun fibers has suitable characteristics for metering applications, provided careful designed with polarization maintaining fibers and components are setup. Overall, to perform a real evaluation of the sensor configurations a more stable current source and meter are required. The PCF spun fiber showed to have some of the required characteristics in terms of resilience to birefringence effects. However, several improvements are required concerning fiber fragility, and low loss guiding at higher wavelengths.

Finally, several new sensor configurations based in laser systems and LPG, were tested for vibration and magnetic field. While the configuration tested showed limited range of operation, its features show them as promising devices for monitoring large currents in complex system such as high power generators.

7.1 Future works

The results presented along this thesis were performed in the laboratory, a controlled environment. The next stage consists on developing prototypes of each of the sensors and test it in the field. For instance, the clamp-on optical current sensor prototype needs to be improved by gluing the GRIN lens to the bulk sensing head using a suitable optical epoxy, before it can be tested in real scenario, of an electric power grid. Additionally, it is required to compensate the Verdet constant temperature dependence, with the introduction of a waveplate (a birefringent material) with a certain retardance that still needs to be calculated. Alternatively, a FBG sensor can be included in the sensing head enclosure and its information can be used to compensate the optical sensor response, with the advantage of also providing the temperature of the conductor.

Concerning the polarimetric sensor with the fiber acting as the sensing medium, the implementation of an interferometric configuration can be adopted using commercial spun HiBi fibers or new spun HiBi fibers with higher Verdet constants. Furthermore, new spun HiBi PCF fibers are also required in order to study the sensor dependence with temperature and its susceptibility to induced linear birefringence, in a reflection configuration.

The laser sensors can also be improved by etching the fiber Bragg gratings mirrors to increase the grating sensitivity to magnetostriction. Another enhancement involves replacing the magnetostrictive rod with a film deposition with distinct layers of magnetostrictive materials, as demonstrated in reference [97]. The passive interferometer with the 3x3 coupler can also be upgraded by implementing a reflection configuration with two FRMs, similar to the configuration in reference [111], eliminating the need of a polarization controller in one of the interferometer arms. Relatively to the intensity modulated laser, the wavelength and power modulation information may be combined in order to improve the magnetic field resolution. The narrow band configurations lasers might also provide information concerning the magnetic field by implementing advanced algorithms that uses the information of pulse amplitude and repetition rate to retrieve the magnetic field information.

The LPG sensor developed for vibration can also be improved by writing the LPG sensor in a PCF fiber, delivering intrinsic immunity to temperature variations. However, for magnetic field measurement, the temperature dependence of the magnetostrictive material cannot be removed. Additionally, material deposition on the LPG surface will surely change the LPG resonance dip and its sensitivity to the induced strain. The optimization of the fiber/support plate ensemble is also required to explore further this mutual dependence and enhance the sensor sensitivity to vibration.

Chapter 8 References

1. H. J. El-Khozondar, M. S. Muller, R. J. El-Khozondar, and A. W. Koch, "Magnetic field inhomogeneity induced on the Magneto-optical current sensors," in *Information Photonics* (2011), pp. 1–2.

2. F. Rahmatian, "High-Voltage Current and Voltage Sensors for a Smarter Transmission Grid and their Use in Live-Line Testing and Calibration," in *Power and Energy Society General Meeting* (2010), pp. 10–12.

3. "Transformer Accuracy," http://www.itl-uk.com/en/services/knowledge-bridge/accuracy-class/.

4. B. Gholamzadeh and H. Nabovati, "Fiber Optic Sensors," World Acad. Sci. Eng. Technol. **42**, 297–307 (2008).

5. S. Yin, P. B. Ruffin, and F. T. S. Yu, *Fiber Optic Sensors*, Second edi (CRC Press, 2008).

6. M. Majumder, T. K. Gangopadhyay, A. K. Chakraborty, K. Dasgupta, and D. K. Bhattacharya, "Fibre Bragg gratings in structural health monitoring-Present status and applications," Sensors Actuators A Phys. **147**, 150–164 (2008).

7. P. Antunes, H. Lima, N. Alberto, H. Rodrigues, P. Pinto, J. Pinto, R. Nogueira, H. Varum, A. Costa, and P. André, "Optical fiber accelerometer system for structural dynamic monitoring," IEEE Sens. J. **9**, 1347–1354 (2009).

8. Y. Zhao, J. Chang, Q. Wang, J. Ni, Z. Song, H. Qi, C. Wang, P. Wang, L. Gao, Z. Sun, G. Lv, T. Liu, and G. Peng, "Research on a novel composite structure Er3+ -doped DBR fiber laser with a π-phase shifted FBG," Opt. Express **21**, 22515–22522 (2013).

9. W. G. Zhang and J. Zhang, "Study on Practical FBG Acceleration System," Adv. Mater. Res. **346**, 546–550 (2011).

10. K. Bohnert, P. Gabus, J. Kostovic, and H. Brändle, "Optical fiber sensors for the electric power industry," Opt. Lasers Eng. **43**, 511–526 (2005).

11. J. Chen, J. Zhou, and Z. Jia, "High-Sensitivity Displacement Sensor Based on a Bent Fiber Mach-Zehnder Interferometer," IEEE Photonics Technol. Lett. **25**, 2354–2357 (2013).

12. R. Garg, S. M. Tripathi, K. Thyagarajan, and W. J. Bock, "Long period fiber grating based temperature-compensated high performance sensor for bio-chemical sensing applications," Sensors Actuators B Chem. **176**, 1121–1127 (2013).

13. Y. N. Ning, Z. P. Wang, A. W. Palmer, K. T. V. Grattan, and D. A. Jackson, "Recent progress in optical current sensing techniques," Rev. Sci. Instrum. **66**, 3097 (1995).

14. H. Lin, W. Lin, and M. Chen, "Modified in-line Sagnac interferometer with passive demodulation for environmental immunity of a fiber-optic current sensor," Appl. Opt. **38**, 2760–2766 (1999).

15. G. Frosio and R. Dandliker, "Reciprocal reflection interferometer for a fiber-optic Faraday current sensor," Appl. Opt. **33**, 6111–6122 (1994).

16. W. Na and W. Quan, "Application of the Fiber Optical Current Transformer in the 110kV Smart Substation," in *Power and Energy Engineering Conference* (2012), pp. 1–4.

17. E. Hecht, *Optics*, 4th ed. (Addison Wesley, 2001).

18. R. Alan, *Polarization in Optical Fibers* (Artech House, 2008).

19. G. Westenberger, H. J. Hoffmann, W. W. Jochs, and G. Przybilla, "The Verdet constant and its dispersion in optical glasses," in *Passive Materials for Optical Elements* (1991), Vol. 1535, pp. 113–120.

20. M. J. Weber, "Handbook of Laser Science and Technology Supplement 2: Optical Materials," in (CRC Press, 1994).

21. C. M. M. van den Tempel, "Model of a new temperature-compensated optical current sensor using BI12SIO20," Appl. Opt. **32**, 4869–4874 (1993).

22. V. P. Gubin, V. A. Isaev, S. K. Morshnev, A. I. Sazonov, N. I. Starostin, Y. K. Chamorovsky, and A. I. Oussov, "Use of Spun optical fibres in current sensors," Quantum Electron. **36**, 287–291 (2006).

23. R. Ulrich, S. C. Rashleigh, and W. Eickhoff, "Bending-induced birefringence in single-mode fibers," Opt. Lett. **5**, 273–275 (1980).

24. N. F. Borrelli and R. A. Miller, "Determination of the individual strain-optic coefficients of glass by an ultrasonic technique," Appl. Opt. **7**, 745–750 (1968).

25. R. M. Silva, H. Martins, I. Nascimento, J. M. Baptista, A. L. Ribeiro, J. L. Santos, P. Jorge, and O. Frazão, "Optical Current Sensors for High Power Systems: A Review," Appl. Sci. **2**, 602–628 (2012).

26. C. D. Perciante and J. A. Ferrari, "Magnetic Crosstalk Minimization in Optical Current Sensors," IEEE Trans. Instrum. Meas. **57**, 2304–2308 (2008).

27. G. A. Woolsey, N. E. Fisher, and D. A. Jackson, "Control of the Critical Angle of Reflection in an Optical Current Sensor," in *12th International Conference on Optical Fiber Sensors* (1997), Vol. 16, pp. 237–240.

28. S. P. Bush and D. A. Jackson, "Numerical investigation of the effects of birefringence and total internal reflection on Faraday effect current sensors," Appl. Opt. **31**, 5366–5374 (1992).

29. T. Sato, G. Takahashi, and Y. Inui, "Method and apparaturs for optically measuring a current," (1986).

30. N. Fisher and D. Jackson, "Vibration Immunity for a Triangular Faraday Current Sensor," Fiber Integr. Opt. **16**, 321–328 (1997).

31. B. C. Chu, Y. N. Ning, and D. A. Jackson, "Faraday current sensor that uses a triangular-shaped bulk-optic sensing element," Opt. Lett. **17**, 1167–1169 (1992).

32. B. Yi, B. C. B. Chu, and K. S. Chiang, "Magneto-optical electric-current sensor with enhanced sensitivity," Meas. Sci. Technol. **13**, N61–N63 (2002).

33. Y. N. Ning, B. C. Chu, and D. A. Jackson, "Miniature Faraday current sensor based on multiple critical angle reflections in a bulk-optic ring," Opt. Lett. **16**, 1996–1998 (1991).

34. Y. N. Ning, Z. P. Wang, A. W. Palmer, and K. T. V Grattan, "A Faraday current sensor using a novel multi-optical-loop sensing element," Meas. Sci. Technol. **6**, 1339–1342 (1995).

35. Z. P. Wang, Q. Bo Li, Y. Qi, Z. Jun Huang, and J. Hui Shi, "Wavelength dependence of the sensitivity of a bulk-glass optical current transformer," Opt. Laser Technol. **38**, 87–93 (2006).

36. Z. P. Wang, X. Wang, X. Liu, C. Ouyang, and Q. Tan, "Effect of the spectral width of optical sources upon the output of an optical current sensor," Meas. Sci. Technol. **16**, 1588–1592 (2005).

37. Z. P. Wang, Q. Bo Li, and Q. Wu, "Effects of the temperature features of linear birefringence upon the sensitivity of a bulk glass current sensor," Opt. Laser Technol. **39**, 8–12 (2007).

38. S. D. Targonski, "Compensation for temperature dependence of faraday effect in diamagnetic materials: application to optical fibre sensors," Electron. Lett. **27**, 1131–1132 (1991).

39. A. Cruden, C. Michie, I. Madden, P. Niewczas, J. R. McDonald, and I. Andonovic, "Optical current measurement system for high-voltage applications," Measurement **24**, 97–102 (1998).

40. P. Menke and T. Bosselmann, "Temperature compensation in magnetooptic AC current sensors using an intelligent AC-DC signal evaluation," J. Light. Technol. **13**, 1362–1370 (1995).

41. A. H. Rose, M. N. Deeter, and G. W. Day, "Submicroampere-per-root-hertz current sensor based on the Faraday effect in Ga:YIG," Opt. Lett. **18**, 1471–1473 (1993).

42. M. N. Deeter, "High sensitivity fiber-optic magnetic field sensors based on iron garnets," IEEE Trans. Instrum. Meas. **44**, 464–467 (1995).

43. "Powersense," http://www.powersense.com/images/Download/Datasheets/DataSheet_Indoor_Current_Sensor_5111.pdf.

44. "Airak," http://www.airak.com/OCS.htm.

45. P. G. Duncan and S. Mastro, "Fiber Optic Current and Potential Sensors for Naval Shipboard Use," in *Intelligent Ships Symposium VI* (2005), pp. 1–8.

46. J. Blake, P. Tantaswadi, and R. T. de Carvalho, "In-line Sagnac interferometer current sensor," IEEE Trans. Power Deliv. **11**, 116–121 (1996).

47. K. Sasaki, M. Takahashi, and Y. Hirata, "Temperature-insensitive Sagnac-type optical current transformer," J. Light. Technol. **33**, 2463–2467 (2015).

48. M. Takahashi, K. Sasaki, A. Ohno, Y. Hirata, and K. Terai, "Sagnac interferometer-type fibre-optic current sensor using single-mode fibre down leads," Meas. Sci. Technol. **15**, 1637–1641 (2004).

49. K. Böhm, P. Marten, E. Weidel, and K. Petermann, "Direct rotation-rate detection with a fibre-optic gyro by using digital data processing," Electron. Lett. **19**, 997 (1983).

50. K. B. Rochford, G. W. Day, and P. R. Forman, "Polarization Dependence of Response Functions in 3x3 Sagnac Optical Fiber Current Sensors," **12**, 1504–1509 (1994).

51. K. Kurosawa, "Optical current transducers using flint glass fiber as the faraday sensor element," Opt. Rev. **4**, A38–A44 (1997).

52. K. Kurosawa, K. Yamashita, and T. Sowa, "Flexible Fiber Faraday Effect Current Sensor Using Flint Glass Fiber and Reflection Scheme," IEICE Trans. Electron. **E83-C**, 326–330 (2000).

53. K. Hotate, "Comparison between flint glass fiber and twisted/bent single-mode fiber as a Faraday element in an interferometric fiber optic current sensor," in *European Workshop on Optical Fibre Sensors* (1998), Vol. 3483, pp. 233–237.

54. K. Barczak, T. Pustelny, D. Dorosz, and J. Dorosz, "New Optical Glasses with High Refractive Indices for Applications in Optical Current Sensors," **116**, 247–249 (2009).

55. L. Sun, S. Jiang, J. D. Zuegel, and J. R. Marciante, "Effective Verdet constant in a terbium-doped-core phosphate fiber," Opt. Lett. **34**, 1699–1701 (2009).

56. L. Sun, S. Jiang, and J. R. Marciante, "Compact all-fiber optical Faraday components using 65-wt%-terbium-doped fiber with a record Verdet constant of -32 rad/(Tm)," Opt. Express **18**, 12191–12196 (2010).

57. M. Segura, N. Vukovic, N. White, T. May-Smith, W. H. Loh, F. Poletti, and M. N. Zervas, "Low birefringence measurement and temperature dependence in metre-long optical fibers," J. Light. Technol. **8724**, (2015).

58. A. H. Rose, Z. B. Ren, and G. W. Day, "Twisting and annealing optical fiber for current sensors," J. Light. Technol. **14**, 2492–2498 (1996).

59. R. I. Laming and D. N. Payne, "Electric current Sensors employing Spun Highly Birefringent Optical Fibers," J. Light. Technol. **7**, 2084–2094 (1989).

60. "Fibercore," http://fibercore.com/product/spun-hibi-fiber.

61. N. Peng, Y. Huang, S. Wang, T. Wen, W. Liu, Q. Zuo, and L. Wang, "Fiber optic current sensor based on special spun highly birefringent fiber," IEEE Photonics Technol. Lett. **25**, 1668–1671 (2013).

62. D. Tang, a. H. Rose, G. W. Day, and S. M. Etzel, "Annealing of linear birefringence in single-mode fiber coils: application to optical fiber current sensors," J. Light. Technol. **9**, 1031–1037 (1991).

63. A. H. Rose, S. M. Etzel, and C. M. Wang, "Verdet constant dispersion in annealed optical fiber current sensors," J. Light. Technol. **15**, 803–807 (1997).

64. P. Drexler, P. Fiala, and R. Kadlec, "Utilization of Faraday Mirror in Fiber Optic Current Sensors and Experiments," in *Progress In Electromagnetics Research Symposium* (2009), pp. 137–141.

65. S. Zhou and X. Zhang, "Simulation of Linear Birefringence Reduction in Fiber-Optical Current Sensor," IEEE Photonics Technol. Lett. **19**, 1568–1570 (2007).

66. A. D. Kersey and M. J. Marrone, "Fiber Bragg Grating High-Magnetic-Field Probe," in *Tenth International Conference on Optical Fibre Sensors* (1994), pp. 53–56.

67. P. Orr and P. Niewczas, "An optical fibre system design enabling simultaneous point measurement of magnetic field strength and temperature using low-birefringence FBGs," Sensors Actuators A Phys. **163**, 68–74 (2010).

68. A. C. Zimmermann, M. Besen, L. S. Encinas, and R. Nicolodi, "Improving Optical Fiber Current Sensor Accuracy using Artificial Neural Networks to Compensate Temperature and Minor Non-Ideal Effects," in *21st International Conference on Optical Fiber Sensors*, W. J. Bock, J. Albert, and X. Bao, eds. (2011), Vol. 7753, pp. 1–4.

69. K. Bohnert, H. Brändle, M. G. Brunzel, P. Gabus, and P. Guggenbach, "Highly accurate fiber-optic dc current sensor for the electrowinning industry," IEEE Trans. Ind. Appl. **43**, 180–187 (2007).

70. ABB, "MOCT Optical Current Transformer System for Metering," http://www.tdproducts.com/files/36371861.pdf.

71. F. Rahmatian and J. N. Blake, "Applications of high-voltage fiber optic current sensors," in *Power Engineering Society General Meeting* (Ieee, 2006), pp. 1–6.

72. "Arteche SDO OCT," www.arteche.com.

73. "Terfenol-D," http://www.etrema.com/core/.

74. R. Angara, "High Frequency High Amplitude Magnetic Field Driving System for Magnetostrictive Actuators," ProQuest (2009).

75. A. Yariv and H. V. Winsor, "Proposal for detection of magnetic fields through magnetostrictive perturbation of optical fibers," Opt. Lett. **5**, 87–89 (1980).

76. A. Dandridge, A. B. Tveten, G. H. Sigel, E. J. West, and T. G. Giallorenzi, "Optical fibre magnetic field sensors," Electron. Lett. **16**, 408–409 (1980).

77. J. Jarzynski, J. H. Cole, J. A. Bucaro, and C. M. Davis, "Magnetic field sensitivity of an optical fiber with magnetostrictive jacket," Appl. Opt. **19**, 3746–3748 (1980).

78. H. I. Heaton, "Thermal straining in a magnetostrictive optical fiber interferometer," Appl. Opt. **19**, 3719–3720 (1980).

79. S. C. Rashleigh, "Magnetic-field sensing with a single-mode fiber," Opt. Lett. **6**, 19–21 (1981).

80. K. P. Koo and G. H. Sigel, "Characteristics of fiber-optic magnetic-field sensors employing metallic glasses," Opt. Lett. **7**, 334–336 (1982).

81. A. D. Kersey, M. Corke, D. A. Jackson, and J. D. C. Jones, "Detection of DC and low-frequency AC magnetic fields using an all single-mode fibre magnetometer," Electron. Lett. **19**, 469–471 (1983).

82. K. P. Koo, A. Dandridge, A. B. Tveten, and G. H. Sigel, "A Fiber-optic DC Magnetometer," J. Light. Technol. **LT-1**, 524–525 (1983).

83. A. D. Kersey, "Phase Shift nulling DC-field fibre-optic magnetometer," Electron. Lett. **20**, 573–574 (1984).

84. A. Kersey, D. Jackson, and M. Corke, "Single-mode fibre-optic magnetometer with DC bias field stabilization," J. Light. Technol. **3**, 836–840 (1985).

85. F. Bucholtz, "Mixing and detection of RF signals in fibre-optic magnetostrictive sensor," Electron. Lett. **25**, 1285–1286 (1989).

86. H. Uesugi, T. Kimura, Y. Kawama, and M. E. Corporation, "High-frequency fibre-optic magnetometer with 70 fT/ square root (Hz) resolution," Electron. Lett. **25**, 1719–1721 (1989).

87. M. Sedlar, I. Paulicka, and M. Sayer, "Optical fiber magnetic field sensors with ceramic magnetostrictive jackets," Appl. Opt. **35**, 5340–5344 (1996).

88. K. D. Oh, J. Ranade, V. Arya, A. Wang, and R. O. Claus, "Optical Fiber Fabry – Perot Interferometric Sensor for Magnetic Field Measurement," IEEE Photonics Technol. Lett. **9**, 797–799 (1997).

89. P. Pérez-Millán, L. Martínez-León, A. Díez, J. L. Cruz, and M. V. Andrés, "A fiber-optic current sensor with frequency-codified output for high-voltage systems," IEEE Photonics Technol. Lett. **14**, 1339–1341 (2002).

90. D. Reilly, A. J. Willshire, G. Fusiek, P. Niewczas, and J. R. McDonald, "A Fiber-Bragg-Grating-Based Sensor for Simultaneous AC Current and Temperature Measurement," IEEE Sens. J. **6**, 1539–1542 (2006).

91. Z. Djinovic, M. Tomic, and C. Gamauf, "Fiber-optic interferometric sensor of magnetic field for structural health monitoring," in *Proc. Eurosensors XXIV* (Elsevier, 2010), Vol. 5, pp. 1103–1106.

92. J. Mora, A. Diez, J. L. Cruz, and M. V. Andres, "A magnetostrictive sensor interrogated by fiber gratings for DC-current and temperature discrimination," IEEE Photonics Technol. Lett. **12**, 1680–1682 (2000).

93. B. Yi, B. C. B. Chu, and K. S. Chiang, "Temperature compensation for a fiber-bragg-grating-based magnetostrictive sensor," Microw. Opt. Technol. Lett. **36**, 211–213 (2003).

94. M. L. M. Li, J. Z. J. Zhou, Z. X. Z. Xiang, and F. L. F. Lv, "Giant magnetostrictive magnetic fields sensor based on dual fiber Bragg gratings," IEEE Networking, Sens. Control 490–495 (2005).

95. J. Mora, L. Martínez-León, a. Díez, J. L. Cruz, and M. V. Andrés, "Simultaneous temperature and ac-current measurements for high voltage lines using fiber Bragg gratings," Sensors Actuators A Phys. **125**, 313–316 (2006).

96. D. Davino, C. Visone, C. Ambrosino, S. Campopiano, A. Cusano, and A. Cutolo, "Compensation of hysteresis in magnetic field sensors employing Fiber Bragg Grating and magneto-elastic materials," Sensors Actuators A Phys. **147**, 127–136 (2008).

97. M. Yang, J. Dai, C. Zhou, and D. Jiang, "Optical fiber magnetic field sensors with TbDyFe magnetostrictive thin films as sensing materials," Opt. Express **17**, 20777–20782 (2009).

98. H. Liu, S. W. Or, and H. Y. Tam, "Magnetostrictive composite-fiber Bragg grating (MC-FBG) magnetic field sensor," Sensors Actuators A Phys. **173**, 122–126 (2012).

99. F. Chen, Y. Jiang, and L. Jiang, "3x3 coupler based interferometric magnetic field sensor using a TbDyFe rod," Appl. Opt. **54**, 1–6 (2015).

100. S. Y. Yang, Y. P. Chiu, B. Y. Jeang, H. E. Horng, C. Y. Hong, and H. C. Yang, "Origin of field-dependent optical transmission of magnetic fluid films," Appl. Phys. Lett. **79**, 2372–2374 (2001).

101. S. Y. Yang, J. J. Chieh, H. E. Horng, C. Y. Hong, and H. C. Yang, "Origin and applications of magnetically tunable refractive index of magnetic fluid films," Appl. Phys. Lett. **84**, 5204–5206 (2004).

102. T. Liu, X. Chen, Z. Di, J. Zhang, X. Li, and J. Chen, "Tunable magneto-optical wavelength filter of long-period fiber grating with magnetic fluids," Appl. Phys. Lett. **91**, 2005–2008 (2007).

103. T. Hu, Y. Zhao, X. Li, and J. Chen, "Novel optical fiber current sensor based on magnetic fluid," Chinese Phys. Lett. **8**, 392–394 (2010).

104. J. Dai, M. Yang, X. Li, H. Liu, and X. Tong, "Magnetic field sensor based on magnetic fluid clad etched fiber Bragg grating," Opt. Fiber Technol. **17**, 210–213 (2011).

105. H. V. Thakur, S. M. Nalawade, S. Gupta, R. Kitture, and S. N. Kale, "Photonic crystal fiber injected with Fe3O4 nanofluid for magnetic field detection," Appl. Phys. Lett. **99**, 22–25 (2011).

106. P. Zu, C. C. Chan, L. W. Siang, Y. Jin, Y. Zhang, L. H. Fen, L. Chen, and X. Dong, "Magneto-optic fiber Sagnac modulator based on magnetic fluids," Opt. Lett. **36**, 1425–1427 (2011).

107. Y. Zhao, R. Lv, Y. Ying, and Q. Wang, "Hollow-core photonic crystal fiber Fabry–Perot sensor for magnetic field measurement based on magnetic fluid," Opt. Laser Technol. **44**, 899–902 (2012).

108. X. Li and H. Ding, "All-fiber magnetic-field sensor based on microfiber knot resonator and magnetic fluid," Opt. Lett. **37**, 5187–5189 (2012).

109. Y. Zhao, D. Wu, and R.-Q. Lv, "Magnetic Field Sensor Based on Photonic Crystal Fiber Taper Coated With Ferrofluid," IEEE Photonics Technol. Lett. **27**, 26–29 (2015).

110. J. S. Park, S. H. Yun, S. J. Ahn, and B. Y. Kim, "Polarization- and frequency-stable fiber laser for magnetic-field sensing," Opt. Lett. **21**, 1029–1031 (1996).

111. G. A. Cranch, G. M. H. Flockhart, and C. K. Kirkendall, "DFB Fiber Laser Magnetic Field Sensor Based on the Lorentz Force," in *Optical Fiber Sensors* (2006), pp. 1–4.

112. L. Cheng, Z. Guo, J. Han, L. Jin, and B. Guan, "Ampere force based magnetic field sensor using dual-polarization fiber laser," Opt. Express **21**, 13419–13424 (2013).

113. A. Masoudi and T. P. Newson, "Distributed optical fiber dynamic magnetic field sensor based on magnetostriction," Appl. Opt. **53**, 2833–2838 (2014).

114. Y. N. Ning, T. Y. Liu, and D. A. Jackson, "Two low-cost robust electro-optic hybrid current sensors capable of operation at extremely high potential," Am. Inst. Phys. **63**, 5771–5773 (1992).

115. Z. Gang, L. Shaohui, Z. Zhipeng, and C. Wei, "A novel electro-optic hybrid current measurement instrument for high-voltage power lines," IEEE Trans. Instrum. Meas. **50**, 59–62 (2001).

116. Y. N. Ning, B. C. Chu, and D. A. Jackson, "Interrogation of a conventional current transformer by a fiber-optic interferometer," Opt. Lett. **16**, 1448–1450 (1991).

117. P. A. Williams, A. H. Rose, G. W. Day, T. E. Milner, and M. N. Deeter, "Temperature dependence of the Verdet constant in several diamagnetic glasses," Appl. Opt. **30**, 1176–1178 (1991).

118. A. C. S. Brigida, I. M. Nascimento, S. Mendonça, J. C. W. A. Costa, M. a. G. Martinez, J. M. Baptista, and P. A. S. Jorge, "Experimental and theoretical analysis of an optical current sensor for high power systems," Photonic Sensors **3**, 26–34 (2012).

119. "Epoxy Technology Inc.," http://www.epotek.com/site/component/products/productdetail.html?cid[0]=231.

120. A. Michie, J. Canning, K. Lyytikäinen, M. Aslund, and J. Digweed, "Temperature independent highly birefringent photonic crystal fibre," Opt. Express **12**, 5160–5 (2004).

121. A. Michie, J. Canning, I. Bassett, J. Haywood, K. Digweed, B. Ashton, M. Stevenson, J. Digweed, A. Lau, and D. Scandurra, "Spun elliptically birefringent photonic crystal fibre for current sensing," Meas. Sci. Technol. **18**, 3070–3074 (2007).

122. P. Russell, "Photonic crystal fibers," Science **299**, 358–362 (2003).

123. J. Noda, T. Hosaka, and Y. Sasaki, "Dispersion of verdet constant in stress-birefringent silica fibre," Electron. Lett. **20**, 20–22 (1984).

124. X. Wang, X. Dong, and Z. Xie, "Measurement and analysis of the birefringence of photonic crystal fiber with wavelength scanning method," Opt. Quantum Electron. **39**, 1081–1090 (2007).

125. O. Frazão, J. M. T. Baptista, and J. L. Santos, "Recent Advances in High-Birefringence Fiber Loop Mirror Sensors," Sensors **7**, 2970–2983 (2007).

126. D. A. Brown, C. B. Cameron, R. M. Keolian, D. L. Gardner, and S. L. Garrett, "A symmetric 3x3 coupler based demodulator for fiber optic interferometric sensors," in *Fiber Optic and Laser Sensors IX* (1991), Vol. 1584, pp. 328–335.

127. M. D. Todd, G. A. Johnson, and C. C. Chang, "Passive light intensity-independent interferometric method for fiber Bragg grating interrogation," Electron. Lett. **35**, 1970–1971 (1999).

128. M. Nazarathy, W. V. Sorin, D. M. Baney, and S. a. Newton, "Spectral analysis of optical mixing measurements," J. Light. Technol. **7**, 1083–1096 (1989).

129. D. M. Dagenais, F. Bucholtz, K. P. Koo, and A. Dandridge, "Detection of Low-Frequency Magnetic Signals in a Magnetostrictive Fiber-Optic Sensor With Suppressed Residual Signal," J. Light. Technol. **7**, 881–887 (1989).

130. S. Zheng, Y. Zhu, and S. Krishnaswamy, "Temperature insensitive all-fiber accelerometer using a photonic crystal fiber long-period grating interferometer," in *Nondestructive Characterization for Composite Materials, Aerospace Engineering, Civil Infrastructure*, A. L. Gyekenyesi, ed. (2012), Vol. 8347, pp. 83470A–1 – 83470A–10.

131. Q. Nan, "Development and Application of Low-frequency FBG Vibration Sensor," in *5th International Symposium on Advanced Optical Manufacturing and Testing Technologies: Smart Structures and Materials in Manufacturing and Testing*, L. Yang, Y.-D. Jiang, W. Jiang, Y. Zhang, T. Ye, X. Luo, G. von Freymann, S. Han, J. Sasián, M. K. Cho, B. Kippelen, Y. Namba, D. D. Walker, J. Yu, F. Wu, L. Xiang, M. Kameyama, S. Hu, S. Li, and S. To, eds. (2010), Vol. 7659, pp. 76590L–1 – 76590L–7.

132. T. K. Gangopadhyay, "Non-contact vibration measurement based on an extrinsic Fabry–Perot interferometer implemented using arrays of single-mode fibres," Meas. Sci. Technol. **15**, 911–917 (2004).

133. G. Park, D. J. Inman, W. R. Group, and L. Alamos, "Impedance-based health monitoring of civil structural components," J. Infrastruct. Syst. **6**, 153–160 (1995).

134. J. Bien, T. Kaminski, M. Kuzawa, P. Rawa, and J. Zwolski, "Dynamic tests of two old masonry arch bridges over the Odra river in Wrocław," in *EVACES 2011: Proceedings of the International Conference on Experimental Vibration Analysis for Civil Engineering Structures* (2011), pp. 79–86.

135. C. Gentile and A. Saisi, "Structural Health Monitoring of a centenary iron arch bridge: Ambient vibration tests and condition assessment," in *EVACES 2011: Proceedings of the International Conference on Experimental Vibration Analysis for Civil Engineering Structures* (2011), pp. 121–130.

136. H. A. Toliyat, "Condition monitoring and fault diagnosis of electrical machines-a review," in *Industry Applications Conference, 1999. Thirty-Fourth IAS Annual Meeting* (1999), pp. 197–204.

137. B. Lee, "Review of the present status of optical fiber sensors," Opt. Fiber Technol. **9**, 57–79 (2003).

138. J. Chang, D. Huo, L. Ma, X. Liu, T. Liu, and C. Wang, "Interrogation a Fiber Bragg Grating vibration sensor by narrow line width light," in *Optical Fiber Sensors Conference, 2008. APOS '08. 1st Asia-Pacific* (Ieee, 2008), pp. 1–4.

139. T. C. Liang and Y. L. Lin, "Ground vibrations detection with fiber optic sensor," Opt. Commun. **285**, 2363–2367 (2012).

140. J. Chang, Q. Wang, X. Zhang, L. Ma, H. Wang, S. Zhang, Q. Wang, J. Ni, and Y. Wu, "Fiber-optic vibration sensor system," Laser Phys. **18**, 911–913 (2008).

141. S. Tanaka, A. Wada, and N. Takahashi, "Highly sensitive operation of LPG vibration sensor using bending-induced spectral change," in *21st International Conference on Optical Fiber Sensors, Ottawa, Canada, 2011, Pp. 1-4*, W. J. Bock, J. Albert, and X. Bao, eds. (2011), Vol. 7753, pp. 1–4.

142. S. Tanaka, H. Somatomo, A. Wada, and N. Takahashi, "Sensitivity enhancement of LPG vibration sensor using higher-order cladding mode," in *20th International Conference on Optical Fibre Sensors*, J. D. C. Jones, ed. (2009), Vol. 7503, p. 75033C–75033C–4.

143. J. O. Gaudron, F. Surre, T. Sun, and K. T. V. Grattan, "LPG-based optical fibre sensor for acoustic wave detection," Sensors Actuators A Phys. **173**, 97–101 (2012).

144. S. W. James and R. P. Tatam, "Optical fibre long-period grating sensors : characteristics and application," Meas. Sci. Technol. **14**, 49–61 (2003).

145. A. Lim, W. Bin Ji, and S. C. Tjin, "Improved refractive index sensitivity utilizing long-period gratings with periodic corrugations on cladding," in *Photonics Research Centre, School of Electrical and Electronic Engineering* (2012), pp. 1–5.

146. V. Bhatia, "Applications of long-period gratings to single and multi-parameter sensing," Opt. Express **4**, 457–466 (1999).

147. Z. He, Y. Zhu, and H. Du, "Effect of macro-bending on resonant wavelength and intensity of long-period gratings in photonic crystal fiber.," Opt. Express **15**, 1804–1810 (2007).

148. G. Rego, O. V Ivanov, and P. V. S. Marques, "Demonstration of coupling to symmetric and antisymmetric cladding modes in arc-induced long-period fiber gratings," Opt. Express **14**, 9594–9599 (2006).

149. A. Cusano, A. Iadicicco, P. Pilla, A. Cutolo, M. Giordano, and S. Campopiano, "Sensitivity characteristics in nanosized coated long period gratings," Appl. Phys. Lett. **89**, 87–90 (2006).

150. I. M. Nascimento, C. Gouveia, S. Jana, S. Bera, J. M. Baptista, P. Moreira, P. Biwas, S. Bandyopadhyay, and P. A. S. Jorge, "High refractive index and temperature sensitivity LPGs for high temperature operation," 8th Iberoam. Opt. Meet. 11th Lat. Am. Meet. Opt. Lasers, Appl. 1–5 (2013).

Appendix A Summary of the sensors presented in state of the art

In the following tables it is presented the main characteristics of the optical current sensors presented in the state of the art.

Tab. A.1 – Main characteristics of the bulk current sensors

Configuration	Optical source	Interrogation	Current source	Sensitivity	Range	Accuracy
Triangular shape [31]	Single mode laser 633 nm	Polarimetric	Inductor	-	Up to 3 kA Up to 10 kHz	20 mA/√Hz
Circular shape [33]	Single mode laser 780 nm	Polarimetric	Inductor	-	50 Hz	1 A/√Hz
Square shape [34]	Single mode laser 633 nm	Polarimetric	Inductor	6.57×10^{-5} rad/A	360 Hz	11.3 mA/√Hz
Square shape [40]	LED 850 nm	Polarimetric	-	-	-20 to 80 ºC	0.2 %
Ferromagnetic Square [41]	633 nm	Polarimetric	Conductor	-	Up to 10 A	220 nA/√Hz
Commercial DISCOS [43]	-	Polarimetric	Conductor	-	20 A to 20 kA	2 %
Commercial AIRAK [44]	-	Polarimetric	Conductor	-	30 A to 30 kA	±1 %

Tab. A.2 – Main characteristics of the all-fiber current sensors

Configuration	Optical source	Interrogation	Current source	Sensitivity	Range	Accuracy
Sagnac with mirror [47]	SLD	Interferometric	Conductor	-	-40 to 80 ºC Up to 7 kHz 0.8 to 4 kA	0.1 % (IEC 60044-8 class 0.2S)
Sagnac with SM fibers [48]	SLD 850 nm	Interferometric	Conductor	-	Up to 100 kA	0.2 % (IEC class 0.5)
Flint glass fiber [51]	SLD 840 nm	Polarimetric	Conductor	-	-10 to 70 ºC Up to 4 A_{RMS}	<1 % (JEC1201-1PS class)
Flint glass fiber [52]	SLD 1550 nm	Polarimetric	Conductor	-	Up to 1 kA	0.1 % JEC1201-1PS class
Fibercore spun Panda fiber with mirror [59]	Multimode laser 780 nm	Polarimetric	Conductor	-	Up to 450 Hz	0.5 % 1 $mA_{RMS}\sqrt{Hz}$
Fibercore spun Panda HiBi fiber Sagnac with mirror [22]	SLD 1550 nm	Interferometric	Conductor	-	Up to 3 kA	±0.6 % 70 mA/√Hz
Spun HiBi fiber [61]	SLD 1550 nm	Interferometric	Conductor	-	Up to 6 k_{ARMS} -40 to 70 ºC	±0.1 %
FBG [66]	SLD 1300 nm	Reflection	Inductor	200 pm/mT	400 Hz Up to 100 T (theoretical)	0.1 mT (estimated)
Low birefringence Fiber transmission) [68]	SLD (unknown wavelength)	Polarimetric	Conductor	-	22 to 55 ºC Up to 1.2 kA	0.1 % (±2 A)
Commercial ABB [69]	SLD 820 nm	Interferometric	Conductor	-	Up to 500 kA	±0.1 %
Commercial ABB MOCT [70]	-	Interferometric	Conductor	-	1 A to 4 kA (for 800 kV)	IEC Class 0.2S and ANSI Class 0.15 s
Commercial NXCT from NxtPhase (now	-	Interferometric	Conductor	-	362 kV	IEC Class 0.2S and IEEE Class

Alstom) [71]						0.3
Arteche SDO OCT [72].		Interferometric	Conductor	-	100 A_{RMS} to 5000 A_{RMS} Up to 550 kV	IEC class 0.2/0.2s

Tab. A.3 – Main characteristics of the magnetostrictive current sensors

Configuration	**Optical source**	**Interrogation**	**Current source**	**Sensitivity**	**Range**	**Accuracy**
Strain in SMF (Nickel coating) [75]	-	-	-	-3×10^{-4} με/mT	-	-
Birefringence induced by strain due to Nickel cylinder [79]	HeNe laser 633 nm	Polarimetric	-	1.76×10^{-1} rad/(mT.m)	-10^{-4} mT up to 0.1 mT	4.4×10^{-7} mT/m
Metallic glass [80]		Interferometric	Inductor		0.03 mT up to 1 mT	5×10^{-10} mT/m
Nickel rod or Metallic glass [81]	Laser 830 nm	Interferometric	Inductor	-	20 Hz	Nickel: 1×10^{-4} mT/m Metallic glass: 1×10^{-7} mT/m
2 μm thick NCF_2 (Cobalt doped nickel ferrite) [87]	HeNe laser 633 nm	Interferometric	Inductor	-	1 kHz Up to 1.76×10^{-2} mT	4.02×10^{-6} mT/m
FBG and Bulk Terfenol-D [92].	-	Wavelength shift	Inductor	2.31×10^{-10} nm/($A^2.m^{-2}$)	Up to 59 mT	-
FBG and Bulk Terfenol-D [94]	1548 nm	Wavelength shift	Inductor	18 pm/mT	Up to 70 mT	-
FBG coated with Terfenol-D films [97]	-	Wavelength shift	Inductor	Terfenol-D: 0.95 pm/mT FeNi and Terfenol-D: 1.08 pm/mT	Up to 50 mT	-
FBG coated with Spurr epoxy-bonded Terfenol-D [98]	1548 nm	Wavelength shift	Inductor	0.68 nm with 183 mT (almost linear)	Up to 183 mT	-

Terfenol-D [99]	DFB laser 1550	Interferometer	Inductor	-	200 Hz 5 µT up to 75 µT	2.14 nT/√Hz
CO_2 400 µm period LPG and magnetic fluid [102]	1525 nm	OSA	Inductor	7.4 nm with 166.1 mT (non linear dependence)	Up to 166.1 mT	-
Etched FBG with 8.5 µm diameter and magnetic fluid [104]	-	OSA	Inductor	86 pm with 25 mT (non linear dependence)	Up to 25 mT	
PCF filled with Fe_3O_4 (0.6 mg/ml) [105]	-	OSA	Inductor	242 pm/mT	Up to 47 mT	
Interferometer with Hollow core PCF filled with magnetic fluid [107]	-	OSA	Inductor	5.5 nm with 28 mT (non linear dependence)	Up to 28 mT	
Fiber laser and Lorentz force [111]	1549 nm	Interferometer	Inductor	-	144 Hz 0.05 mT up to 0.6 mT	1.5 µT/√Hz
Laser with Nickel for distributed sensing [112]	1550 nm	Interferometer	Inductor	-	0.1 mT up to 0.9 mT 50 Hz up to 5000 Hz	1 m (special resolution)

Tab. A.4 – Main characteristics of the magnetostrictive current sensors

Configuration	**Optical source**	**Interrogation**	**Current source**	**Sensitivity**	**Range**	**Accuracy**
Optical fiber only to transmit data [13]	LED	-	-	-	-	0.5 %/ºC
CT used as primary transducer [13]	Laser (Unknown)	Interferometer	Conductor	-	Up to 3 kA 10 kHz	1 %

Appendix B Dimensions of the sensor enclosure

A more detailed schematic of the sensor enclosure with all the dimensions in mm is shown in the three following figures. In Fig. B.1 and in Fig. B.2 it is exhibited the bottom and top nylon plates, respectively.

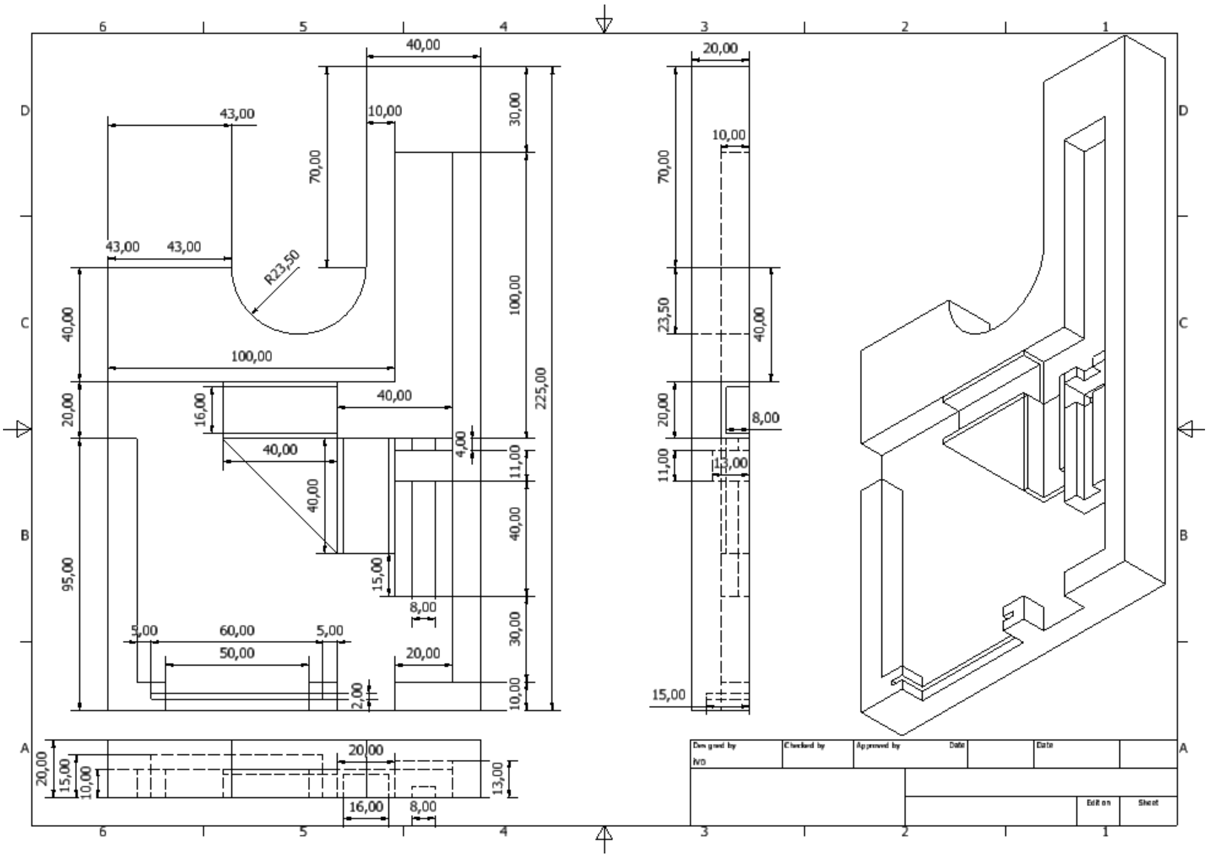

Fig. B.1 – Bottom enclosure plate with measurements in mm.

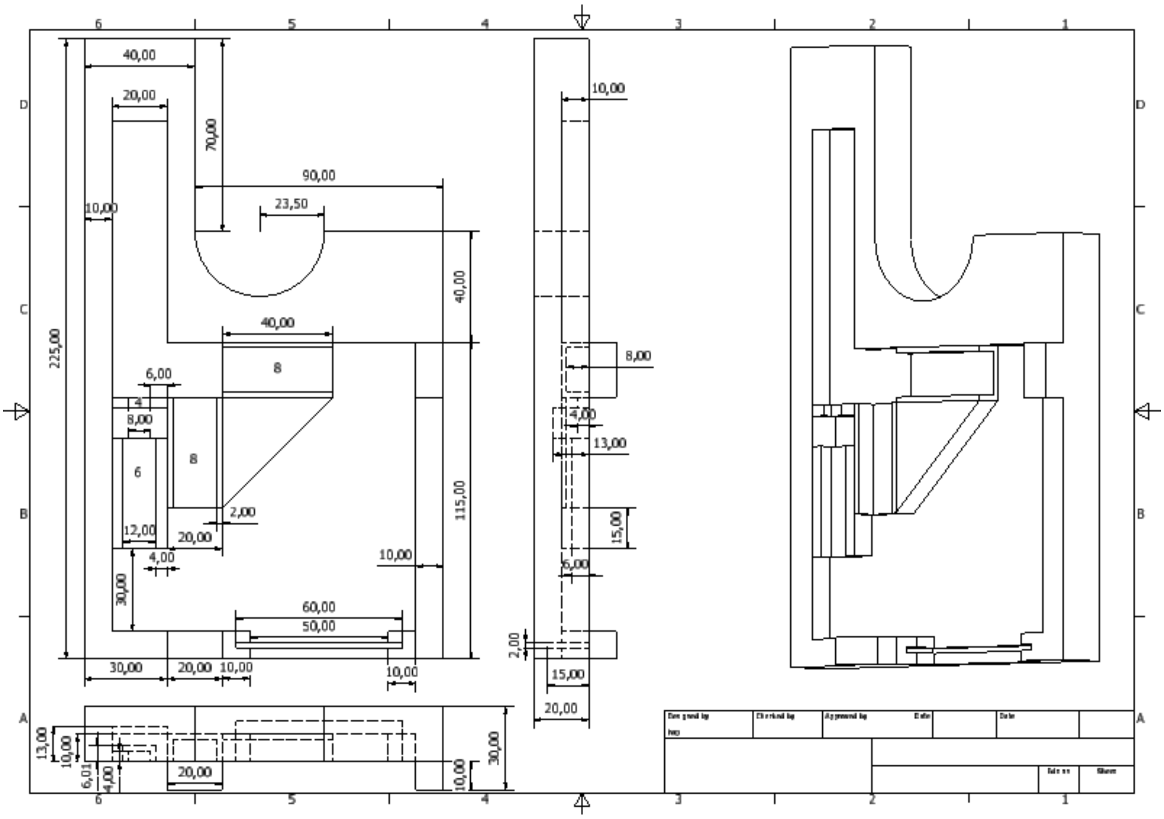

Fig. B.2 - Top enclosure plate with measurements in mm.

The rest of the enclosure components are also shown in Fig. B.3. On the left it is represented the component responsible for attaching the sensing head to the conductor, in right up a PVC plate with three holes where the three FC/APC connectors are attached and on right below an example of half of the internal ring design to attach the sensing head to a 27 mm diameter conductor.

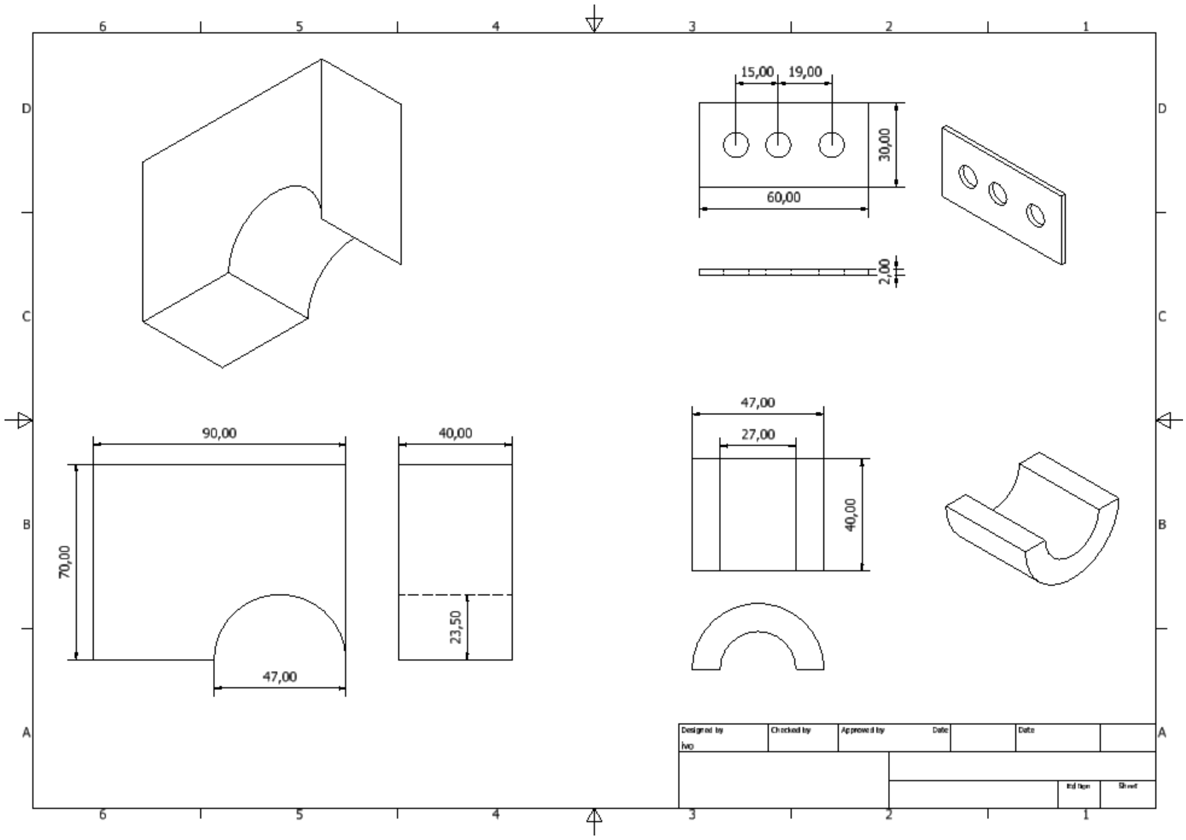

Fig. B.3 – Schematic of the components that attach the sensing head to the conductor, internal ring adapter for smaller diameter conductors and a plate where the three FC/APC inputs and outputs are placed.

Appendix C Enclosure assembly

In Fig. C.1 it is shown the bottom and top nylon plates after machining that are the main parts for sensor enclosure, with the first to be used to position the components, including the bulk glass components, input polarizer and the three GRIN lens.

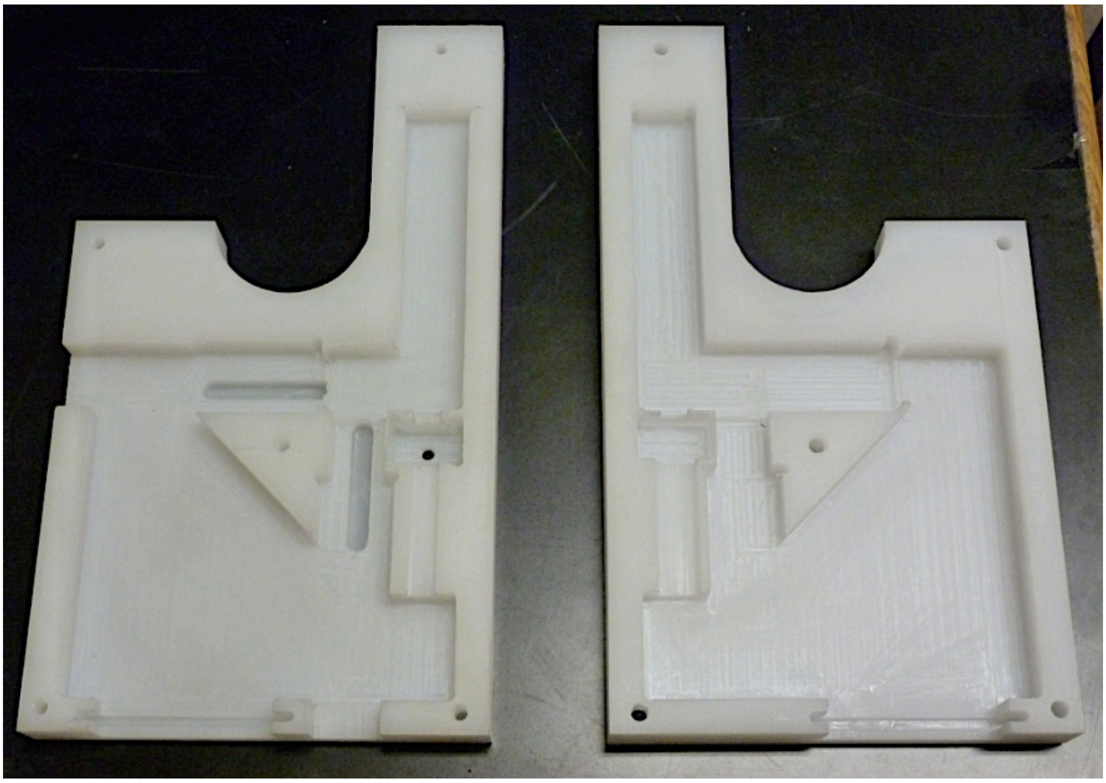

Fig. C.1 – Bottom and top Nylon supports used for the sensor enclosure after machining.

In Fig. C.2 (a) a photo of the sensor in the lower plate is exhibited with the three optical components glued together with the optical epoxy EPO-TEK 301. The input GRIN lens were also glued to the nylon plate and the input polarizer was mounted in a 360 degrees rotating support, Thorlabs RSP05, ensuring both outputs are at ± 45 ° in relation to the input polarizer and consequently operating with maximum sensitivity.

The outputs GRIN lens are aligned using a XYZ position stage with two adjustment angles, as exhibited in Fig. C.2 (b), reducing the injection losses. Although the sensor is maximized to operate at 830 nm, an SLD source at 650 nm, in the visible spectral range, was used to facilitate the first alignment. The objective is to only glue the lens to the nylon plate using a hot melt adhesive and after drying the alignment setup is removed (Fig. C.3 (a)).

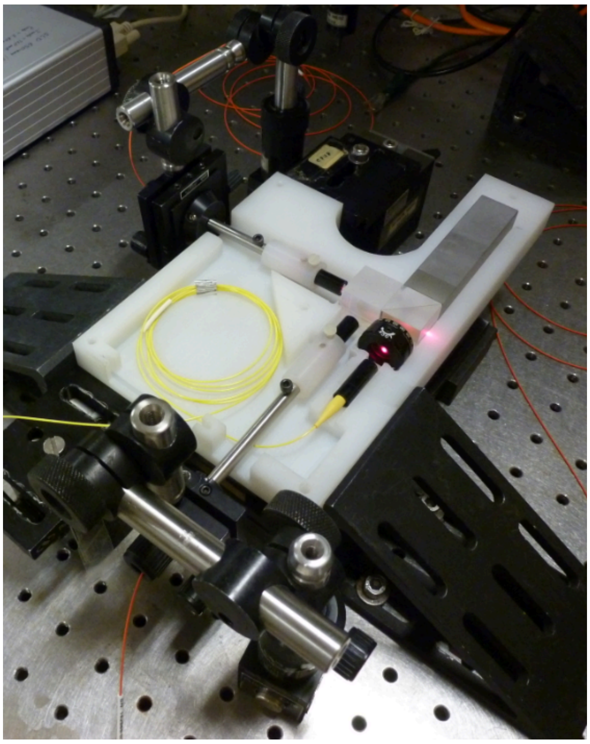

(a)

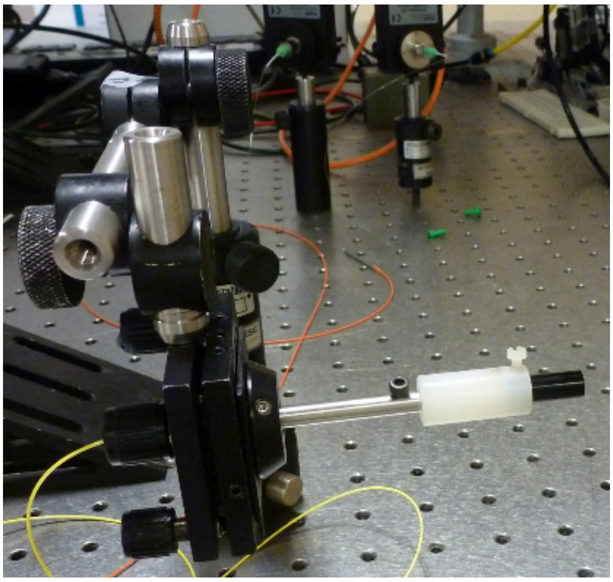

(b)

Fig. C.2 – (a) Lower plate with the optical components and in (b) the XYZ position stage with two adjustment angles.

The next step consisted on splicing all the three GRIN lens to fiber pigtails and connect them to the grey support with the FC/APC connectors exhibited in Fig. C.3 (a). However, disalignment of the lens was observed due to temperature variations. Another glue, an epoxy capable of withstand temperatures from -30 ºC to 120 ºC from Ceys was also tested to attach the GRIN lens to the lower support but the disalignment problem persisted showing the problem was due to expansion of the nylon enclosure with temperature.

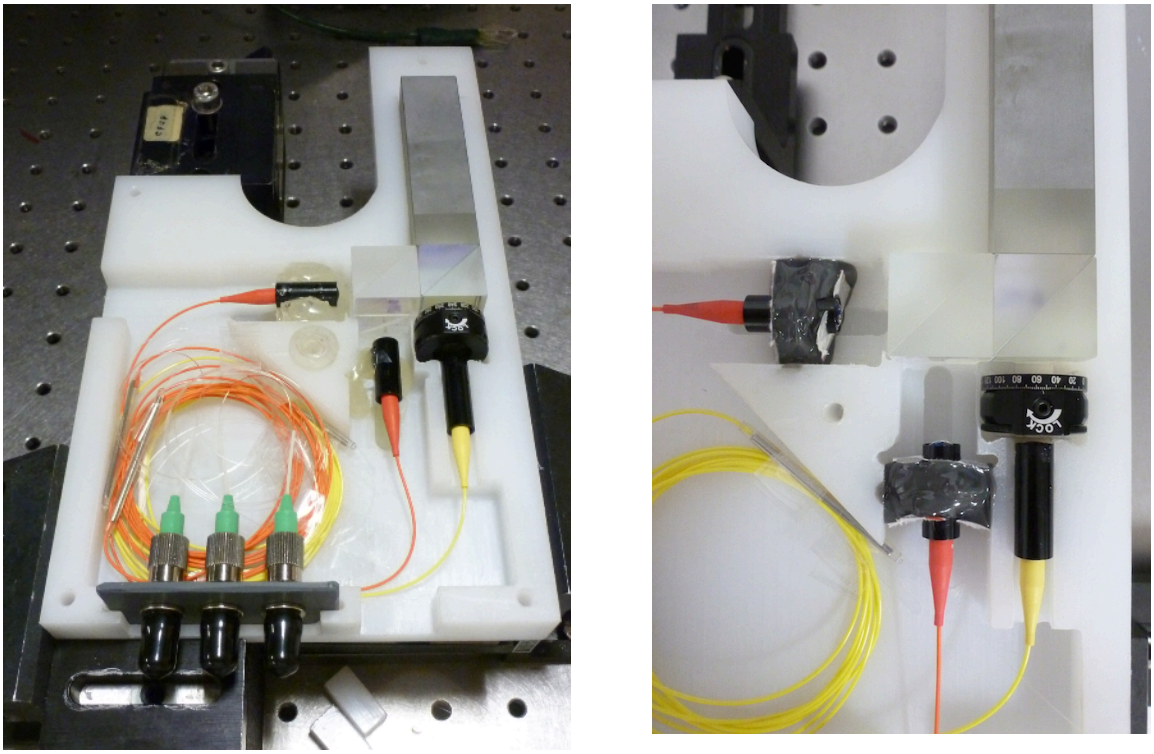

(a) (b)

Fig. C.3 – GRIN lens glued to the inferior support with (a) hot-melt adhesive and with a (b) High temperature epoxy.

In Fig. C.4 (a) it is shown the support used to attach the sensor to the conductor and in Fig. C.4 (b) the rings to fix it to a 27 mm diameter cable.

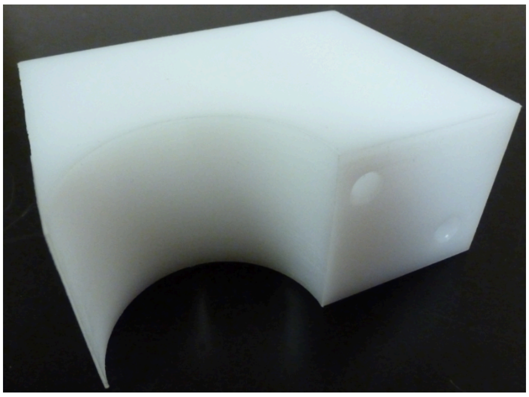

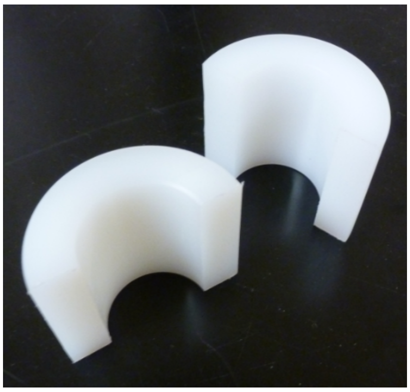

(a) **(b)**

Fig. C.4 – (a) Support used to fix the sensor to the conductor and (b) the rings to adapt the sensor enclosure to the desirable conductor diameter.

In Fig. C.5 (a) and (b) it is shown the sensor prototype before and after the attachment to the conductor. In (b) are shown the three cables used to inject and collect the light from the sensing head.

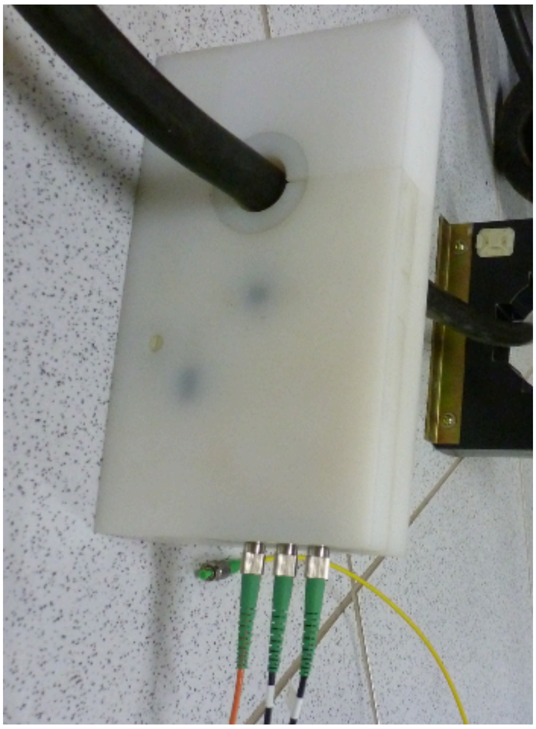

(a) **(b)**

Fig. C.5 – Sensor enclosure (a) before and (after) being attached to a conductor.

Appendix D Photodetector circuit

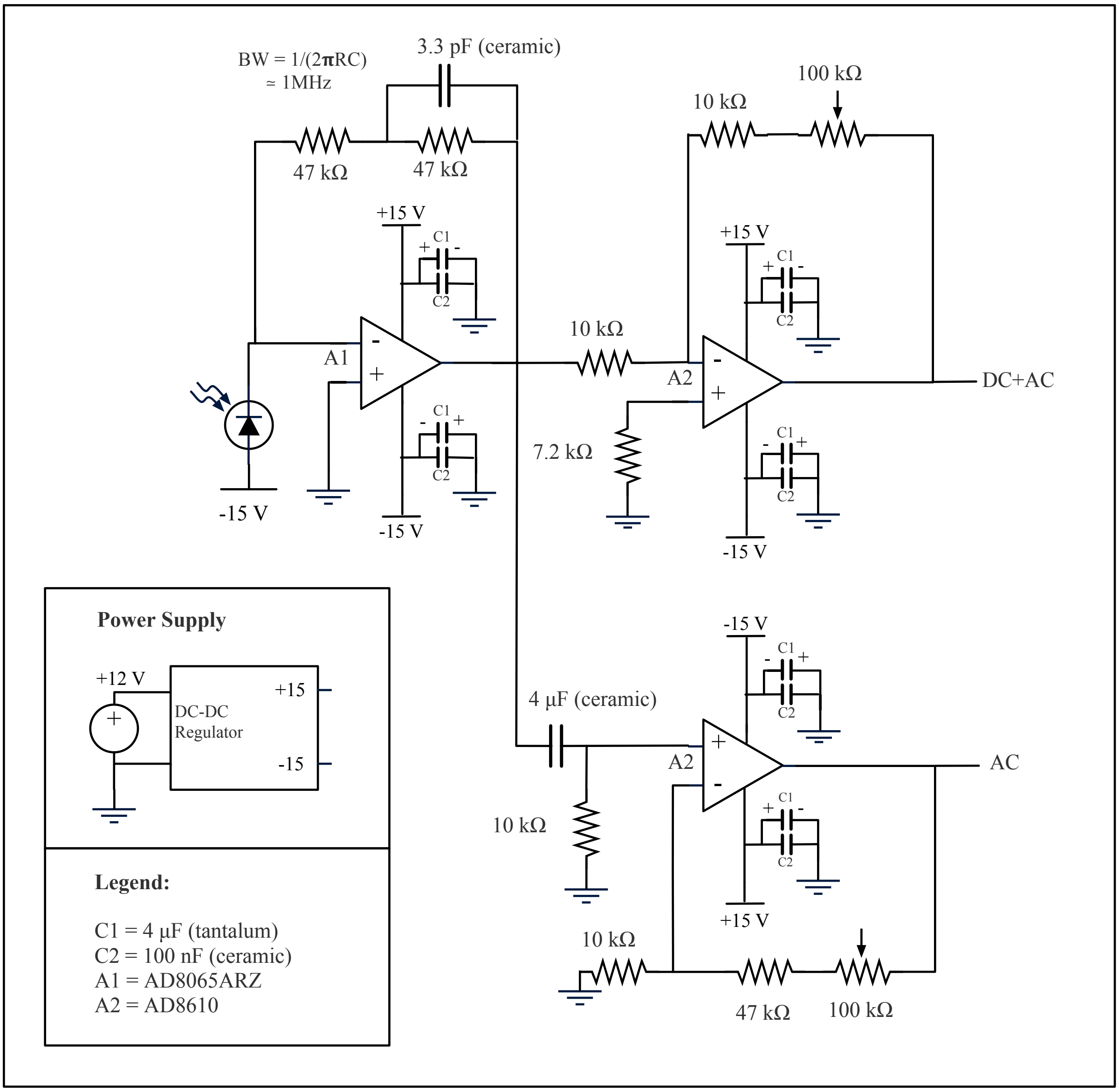

Fig. D.1 – Photodetector circuit with 1 MHz bandwidth, including a transimpedance circuit with a low noise amplifier and two adjustable amplification circuits, one for the DC+AC component and the other, with higher gain, just for the AC part.

Appendix E Schematic of the different geometries of sensor / conductor arrangements

In the following tables the Faraday rotation parameters to be used in equation (3.11) and schematic for each sensor are presented.

Tab. E.1 – Faraday rotation parameters, due to all conductors, for the sensing head in position *ij*=11 and 12.

θ_{ijz}	r	h	Schematic
θ_{111}	r	0	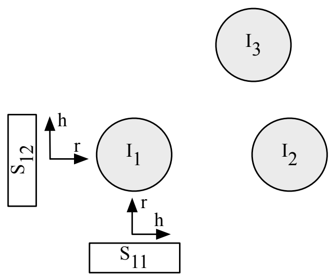
θ_{112}	r	d_{12}	
θ_{113}	r + d_{23}	d_{13}	
θ_{121}	r	0	
θ_{122}	r + d_{12}	0	
θ_{123}	r + d_{13}	d_{23}	

Tab. E.2 – Faraday rotation parameters, due to all conductors, for the sensing head in position *ij*=13 and 14.

θ_{ijz}	r	h	Schematic
θ_{131}	r	0	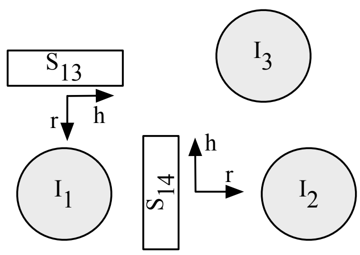
θ_{132}	r	d_{12}	
θ_{133}	r - d_{23}	d_{13}	
θ_{141}	-r	0	
θ_{142}	d_{12} - r	0	
θ_{143}	d_{13} - r	d_{23}	

Tab. E.3 – Faraday rotation parameters, due to all conductors, for the sensing head in position *ij*=21 and 22.

θ_{ijz}	r	h	Schematic
θ_{211}	r	d_{12}	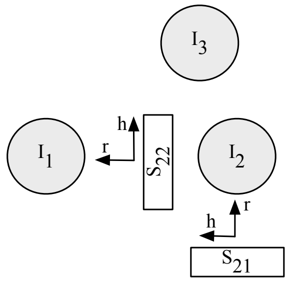
θ_{212}	r	0	
θ_{213}	r + d_{23}	$d_{12} - d_{13}$	
θ_{221}	d_{12} - r	0	
θ_{222}	-r	0	
θ_{223}	$d_{12} - d_{13}$	d_{23}	

Tab. E.4 – Faraday rotation parameters, due to all conductors, for the sensing head in position *ij=23* and 24.

θ_{ijz}	r	h	Schematic
θ_{231}	-r	d_{12}	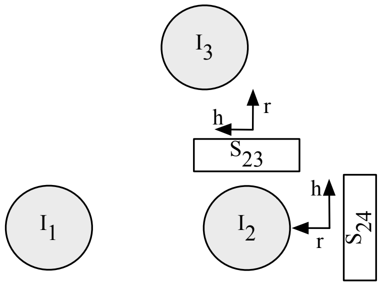
θ_{232}	-r	0	
θ_{233}	d_{23} - r	$d_{12} - d_{13}$	
θ_{241}	r + d_{12}	0	
θ_{242}	r	0	
θ_{243}	r + d_{12} - d_{13}	d_{23}	

Tab. E.5 – Faraday rotation parameters, due to all conductors, for the sensing head in position *ij*=31 and 32.

θ_{ijz}	r	h	Schematic
θ_{311}	r – d_{23}	d_{13}	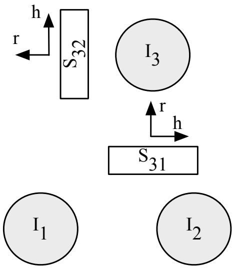
θ_{312}	r – d_{23}	$d_{13} - d_{12}$	
θ_{313}	r	0	
θ_{321}	d_{13} - r	d_{23}	
θ_{322}	d_{13} – r – d_{12}	d_{23}	
θ_{323}	-r	0	

Tab. E.6 – Faraday rotation parameters, due to all conductors, for the sensing head in position *ij*=33 and 34.

θ_{ijz}	r	h	Schematic
θ_{331}	$r + d_{23}$	d_{13}	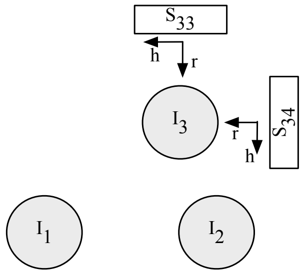
θ_{332}	$r + d_{23}$	$d_{13} - d_{12}$	
θ_{333}	r	0	
θ_{341}	$r + d_{13}$	d_{23}	
θ_{342}	$r + d_{13} - d_{12}$	d_{23}	
θ_{343}	r	0	